Two-nucleon knockout from ^{4}He in a translationally invariant model

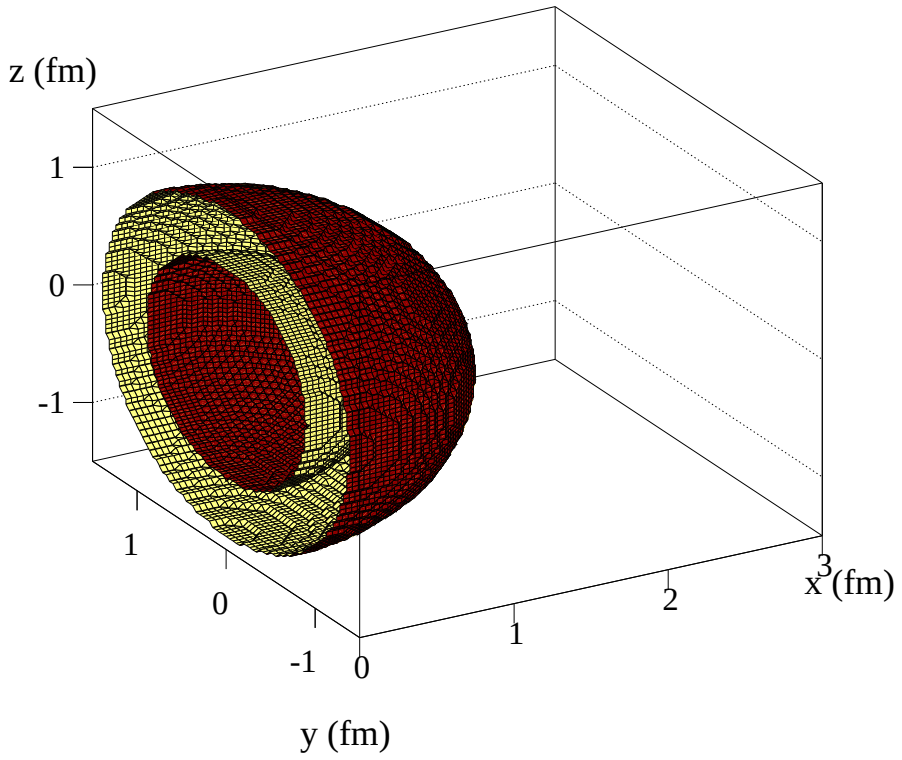

Wim Van Nespen

Two-nucleon knockout from ^{4}He in a translationally invariant model

Wim Van Nespen

Proefschrift ingediend tot het behalen
van de academische graad van
Doctor in de Wetenschappen : Natuurkunde

Promotor : Prof. Dr. J. Ryckebusch

Universiteit Gent
Faculteit Wetenschappen
Vakgroep Subatomaire en Stralingsfysica
2003-2004

Contents

List of Figures

List of Tables

Chapter I

Introduction

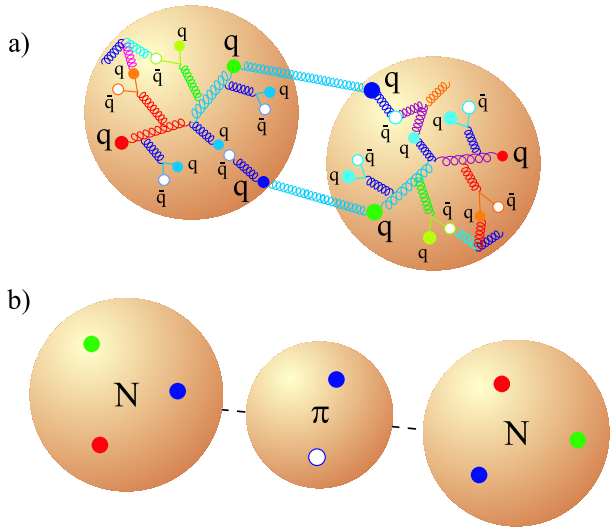

Figure I-1: *The upper panel (a) shows a QCD picture of two interacting nucleons, i.e. a color exchange diagram. The lower panel (b) describes the same process in terms of effective degrees of freedom, namely by means of pions and nucleons.*

The atomic nucleus is a quantum many-body system governed by the strong interaction. The study and final understanding of the nucleus in all its complexity is the genuine justification for the mere existence of nuclear physics.
The discovery in the early 20th century, of the nucleus by Rutherford, Geiger and Marsden [1] followed by the discovery of the neutron a few years later [2] may be considered as the birth of nuclear physics. Since the early days, a lot of data have been collected culminating in a whole range of models trying to describe the features of the nucleus.
At low excitation energies, typically of the order of a few MeV, the nucleus can, to a good approximation, be described in terms of nucleonic degrees of freedom. The nuclear shell-model, introduced by Mayer and Jensen in the fifties, is the common tool to interpret the enormous richness of nuclear spectroscopy. The shell model is very successful in explaining a lot of low-energy nuclear properties like

the appearance of magic numbers, ground-state energies, transition probabilities between low-lying excited states, ...
At a more fundamental level, one could hope to explain the basic features of nuclei at low energies in terms of quarks and gluons which constitute the basic building blocks of the hadronic universe as described by quantum chromo dynamics (QCD) (see Fig. I-1). Unfortunately, QCD can not be directly used to do calculations at nuclear physics temperatures ($\approx$ MeV-scale). Indeed, this misdemeanor of QCD is caused by its running coupling constant ($\alpha_s = \frac{12\pi}{(33-2n_f)\log q^2/\Lambda^2}$) which grows infinitely large at low energies ($\approx$ 1 GeV). One refers to this property as the anti-screening effect of QCD. In short, only at very small distances where it is not meaningful anymore to think of matter in terms of nuclei or nucleons, the strong coupling constant is sufficiently small so that QCD can be solved perturbatively using a Feynmann-diagram expansion.

In this dissertation, an attempt is made to improve our knowledge about the nuclear dynamics up to distance scales of 0.5 fm. To that purpose we study processes in which an electromagnetic probe and energy transfers ranging from 100 up to 600 MeV are involved. The research described in this thesis belongs to a particular branch in physics, denoted hadron physics. Neither QCD nor the nuclear shell-model are fully applicable to model the reaction processes at the length scales covered in hadron physics. Indeed, at short distances one would expect the influence of quark and gluon degrees of freedom to persist while on the other hand nuclei are still described as manifolds of nucleons. A hybrid model is adopted which describes the nucleus in terms of nucleonic degrees of freedom, though corrected for the short-range features of the nucleon-nucleon interaction. To describe these effects accurately one has to modify the high-momentum components of the nuclear wave function as conceived with a nuclear shell-model technique.
Summarizing, hadron physics studies the transition regime between the typical high-energy behavior of subatomic matter governed by QCD and the low-energy phenomena which can be efficiently described by the nuclear shell model. The most important questions which will be addressed are: What are the relevant degrees of freedom? Which Feynman diagrams play a role? Do the various symmetries persist?

The meeting ground of those two regimes is formed by the so-called effective field theories. During the last decades several techniques have been developed to derive the nuclear wave function starting from some "effective" field theory. Effective field theory is a more natural way to describe nature, because at every energy scale it is formulated in terms of the relevant degrees of freedom. All higher energy properties are absorbed in suitably chosen form factors (see Fig. I-1). In this thesis, we wish to explore how the nuclear interior looks like at photon energies of a few hundreds of MeV or equivalently at a distance of around 0.5 fm. At this energy scale, it can be anticipated that other relevant degrees of freedom,

like mesons (e.g. $\pi, \rho, \cdots$) and low-lying excited baryon states (e.g. $\Delta^+, \cdots$) play a role. The aforementioned particles are not explicitly incorporated in nuclear-structure calculations, though the specific functional form of the NN-potential is a direct consequence of their presence. For example, the tensor part of the NN-force is attributed to the one-pion exchange graphs. To study the nuclear system at short distances one needs a high-quality wave function which goes beyond those produced in an independent-particle model. Recent computational advances made the exact calculation of the ground-state wave function for few-body nuclei ($A \leq 8$) feasible. This is however not the case for medium and heavy nuclei. In this dissertation we focus on the ^{4}He nucleus.

Since the experimental work by Lyman and Hofstadter [3] [4], who introduced electron scattering as an alternative to nucleon transfer reactions (e.g. (α, d) or (t, p)-reactions [5]) nuclear physics entered into a new era. Studies of the nucleus with the aid of an electromagnetic probe were made possible thanks to the progress made in accelerator and detector technology. On the theoretical side, the development of quantum electrodynamics (QED) by Tomonaga, Schwinger and Feynman is of crucial importance for the correct interpretation of the experimental results. In contrast to QCD, QED has the major advantage of having a weak coupling constant at MeV-scale ($\alpha_e \approx \frac{1}{137}$) making the first Born expansion of the scattering matrix a good approximation. The electromagnetic interaction which has a highly penetrating potential in nuclear matter, can be used to map the electric and magnetic charge- and current distributions in the nucleus.

From the very start, some deficiencies of the nuclear shell-model showed up. First, the early elastic electron scattering experiments revealed the presence of sub-nuclear degrees of freedom in the nucleus masked as meson exchange currents (e.g. modifications of the charge form factor). Further, an (e, e')-experiment to measure the charge distribution of the $3s$-proton in ^{206}Pb, performed in the seventies at Mainz [6] and independently at Saclay [7], provided the first unambiguous experimental evidence for the depletion of the nuclear shell model states near the Fermi level. This marked the onset of the quest for short- as well as long-range correlations.
Later on, with the advent of high duty-cycle electron accelerators, double coincidence measurements came within experimental reach. A wide spectrum of single nucleon-knockout experiments of the $A(e, e'p)$ type have been the subject of investigation at various laboratories. The one-nucleon knock-out data pointed toward the necessity of having a better description for the nuclear interior (e.g. high momentum components) [8] and for incorporating meson and baryon exchange currents (e.g., the delta peak at an invariant mass of $\pm$ 1200 MeV) in the scattering matrix [9]. The presence of short-lived delta particles in the nucleus could already be inferred from (e, e') reactions where they give rise to a broad structure above the quasi-elastic peak.

Improvements to the wave functions advocated by these experiments concerned the inclusion of nucleon-nucleon short-range dynamics and can be jus-

tified by the observation that most of the time the nucleons overlap inside the nucleus. Early theoretical models folded the shell model wave function with some correlation function (Jastrow ansatz). This has the effect of introducing a form factor thereby modifying the short-range or high-momentum physics. To impose further constraints on the size and shape of the correlation functions, direct two-nucleon knock-out reactions were asserted to be a particularly sensitive tool [11]. During the last decade a fair amount of two-nucleon knock-out data haven been collected at several accelerator facilities (e.g. Tokyo, NIKHEF, MAMI, ELSA, JLAB, LEGS) for a variety of kinematical settings with medium-heavy nuclei as target (i.e. ^{12}C, ^{16}O, ^{40}Ca, $\cdots$). These experimental efforts have gradually learned us where to look or not to look for signatures of the short-range correlations. An analysis of $^{12}\mathrm{C}(e,e'pp)$ and $^{16}\mathrm{O}(e,e'pp)$ data [12] taught us that signals from the SRC can only be detected when the photon gets absorbed on a dinucleon with "large" relative and "small" COM-momentum [9][12]. Due to its high central density of approximately two times nuclear matter density, ^{4}He can be expected to be a good target nucleus with the eye on detecting signals from the SRC's.

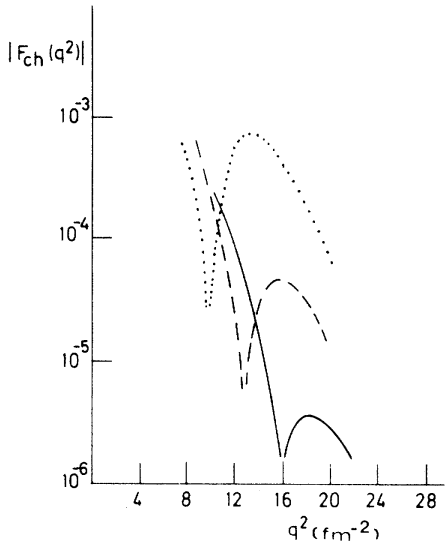

Figure I-2: *The effect of the center-of-mass spuriosity on the ^{4}He charge form factor. The dotted line has been obtained using the Tassie-Barker correction whereas the solid and dashed lines are two different solutions of the Gartenhaus-Schwartz prescription (see Ref. [10]) i.e. $G(\vec{R}) = \delta(\vec{R})$ or 1 respectively.*

Until now the major part of the two-nucleon knock-out reaction calculations have been performed in a CBF inspired approach for the nuclear wave function and neglect all recoil effects. Correlated Basis Function theory (CBF) is a technique to incorporate short-range correlations into the wave function by means of correlation functions and operators.
Ciofi degli Atti [13] already pointed out the importance of the recoil effects for light nuclear systems. A shell-model derived form factor contains the residual center-of-mass motion in addition to the internal nucleon motion. From now

on we will refer to a form factor which is not corrected for the COM-motion as a non-intrinsic form factor. A standard procedure to correct for the center-of-mass motion is to multiply the non-intrinsic form factor with the so-called Tassie-Barker correction factor [10]. The non-intrinsic form factor is referred to the center of the potential instead of to the COM of the nucleus. Adjusting the non-intrinsic Slater determinant by means of this factor ($= e^{b_0^2 q^2/4A}$) is only well-founded for harmonic oscillator (b_0 equals the oscillator strength) single-particle wave functions (see Fig. I-2). The recoil effects do not only alter the kinematical phase space but also the wave function. To investigate whether modern nuclear wave functions are able to explain the two-nucleon knock-out data, a proper treatment of the center-of-mass motion is in order. The removal of the center-of-mass coordinate from the non-intrinsic wave function inserts, apart from the short-range correlations, so-called center-of-mass correlations into the intrinsic wave function. Eliminating the center-of-mass motion from the wave function and incorporating all recoil diagrams in the dynamical picture of a two-hadron knockout process is a formidable task which can only be performed for light nuclei. For the deuteron this problem can be solved trivially. For the ^{3}He and ^{3}H nuclei the Bochum group computed several observables by solving the Faddeev equations to derive the wave functions [14][15]. In this thesis, an attempt will be made to treat the COM effects in the four-body breakup of the ^{4}He nucleus.

These days, a lot of experimental efforts are directed to the study of correlations in light nuclei. A fair amount of one-nucleon emission data has been collected [16] [17] [18]. Since the mid-eighties two-nucleon knock-out experiments on the target nucleus ^{4}He have been performed. A pioneering $^4\mathrm{He}(\gamma, NN)$ experiment was performed at the TagX facility in Tokyo [19][20]. Both three- and four-body break-up reactions were studied for photon energies ranging from 135 to 455 MeV. The TagX data showed a broad structure at photon energies of about 350 MeV. At MAMI-A, low photon energy four-body break-up data where collected by Doran et al. [21] showing a less significant probability for a photon to be absorbed on a proton-proton pair than predicted by the calculations. A comparative study of the photon asymmetry has been performed by Adamian et al. [22] measuring the photon asymmetry for the $\mathrm{d}(\gamma, pn)$, $^6\mathrm{Li}(\gamma, pn)X$ and $^4\mathrm{He}(\gamma, pn)X$-processes for a photon energy ranging from 200 up to 900 MeV. In the near future $^4\mathrm{He}(\vec{\gamma}, pp)nn$ and $^4\mathrm{He}(\vec{\gamma}, pn)X$ data from the PIP-TOF collaboration in Mainz will become available. Complementary to the photon induced reactions a $^4\mathrm{He}(e, e'pp)nn$-experiment has been performed at the ELSA facility in Bonn. This work has been described in the PH.D. thesis by de Vries [16].

In this work, the influence of recoil effects and short-range correlations on the $^4\mathrm{He}(\gamma^*, NN)X$ process is studied. Chapter 2 reviews a number of models which have been successfully applied to construct the four-nucleon ground-state. Special attention will be paid to the effect of ground-state correlations and center-of-mass motion. The derivation of the $^4\mathrm{He}(\gamma, NN)$ and $^4\mathrm{He}(e, e', NN)$ observables will be the subject of Chapter 3. Apart from the differential cross section, also the

polarization observables (i.e. asymmetries, induced polarizations and transferred polarizations) are derived in this context. Theoretical results for the ^{4}He$(e, e'NN)$ and ^{4}He(γ, NN) reaction will be summarized in Chapter 4 and compared to the available experimental data. The role played by short-range correlations and recoil effects is discussed. The definitions and the more technical parts of the derivations are summarized in the appendices.

Chapter II

The ^{4}He Wave Function

It goes without saying that a good knowledge of the wave function is crucial for doing nuclear-reaction calculations. The acquainted tool to compute nuclear wave functions is the nuclear shell model which works remarkably well, despite the fact that the nucleus is a high density strongly interacting medium. The shell model is capable of explaining most of the measured nuclear observables because of their surface character. The ^{4}He nucleus can't be described in terms of the shell-model wave function consisting of s-wave single-particle states only. This deficiency comes along when trying to explain the diffractive nature of the ^{4}He charge form factor. For the study of few-body (≤ 8) nuclei, techniques to determine the wave function directly from the NN-interaction have been developed. In this chapter, we will describe these techniques and define the most important features of the ^{4}He wave function.

§1 Introduction

Solving the A-body Schrödinger equation

$$(\sum_{i=1}^{A} \hat{T}_i + \sum_{i<j=1}^{A} \hat{V}_{ij})\Psi(x_1, x_2, \cdots, x_A) \;=\; E_A\Psi(x_1, x_2, \cdots, x_A) \qquad \text{(II-1)}$$

with $x_i = (\vec{r}_i, s_i, t_i)$, for a realistic nucleon-nucleon potential is one of the major goals in present-day nuclear physics. It remains a challenging task to understand how nuclear structure and the observed symmetries come along from the underlying interaction between nucleons or, at an even deeper level in terms of quarks and gluons. The first major challenge, one encounters when trying to solve this problem is to determine a suitable functional form for the realistic nucleon-nucleon potential. A large amount of NN-scattering data have been accumulated (some 1787 pp- and 2514 np-scattering data [23]) over the last decades. Several research groups (e.g. the Nijmegen group [24][25]) have derived effective NN potentials from these data sets. Up to now, no one has succeeded in deriving an expression for the NN potential from first principles, i.e. QCD. In that respect, all of the available potential models are fully or at best semi-phenomenological. To our

present knowledge, the radial dependence of the nuclear potential can be subdivided in three regions each characterized by a particular interaction mechanism. A schematic picture is shown in Fig. II-1.

Agreement has been reached on the nature of the long-range part of the potential which is entirely due to one-pion exchange. The latter gives rise to a large tensor component in the NN-interaction at distances comparable to the inverse pion mass ($\frac{1}{m_\pi} \approx 1.4$ fm). Due to the tensorial character of the nuclear potential, spin and spatial degrees of freedom get intertwined. An illustrative example of this is the spin-dependence of the deuteron nucleon density as displayed in Fig. II-2. The long-range part of the nuclear potential is fairly well established. This is not the case for short and intermediate distances. The intermediate range of the NN-potential can be modeled using medium and heavy meson exchange as well as multiple pion exchange diagrams, though there is no consensus on which diagrams to include to properly describe the medium range of the NN-force. In the long run, the repulsive core, which refers to strongly overlapping interacting nucleons, needs to be understood in terms of quark and gluon degrees-of-freedom. Recently, the existence of six-quark clusters have been put forward as a possible explanation for some unsolved problems like the EMC-effect [27] and the hole in the particle density of ^{4}He [28][29], $\cdots$. The particle density emerges when the nuclear charge density is corrected for the nucleon charge density. Summarizing, most of the commonly used nucleon-nucleon potentials contain a phenomenological parameterization for the short and intermediate-range part, in addition to a long-range pion-exchange force.

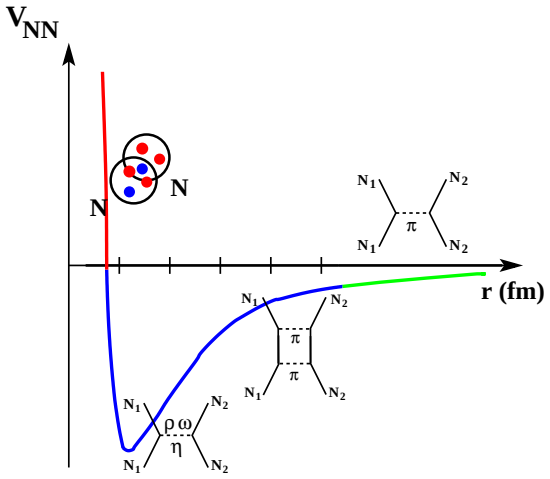

Figure II-1: *The NN-potential is shown indicating its three different regions. The green region is the long-range part of the potential while its intermediate range is located in the blue region. The short range repulsion is marked in red.*

Some groups claim to have found important effects from relativistic corrections and three-body forces in the nuclear potential [30] [31]. Both corrections, although small, have some effect on the nuclear ground-state energy due to large cancellations between kinetic and two-body potential energy. Though, they are of minor importance, especially the three-body potential, for the calculation of the response functions.

Ignoring relativistic corrections, the most general operator structure for the

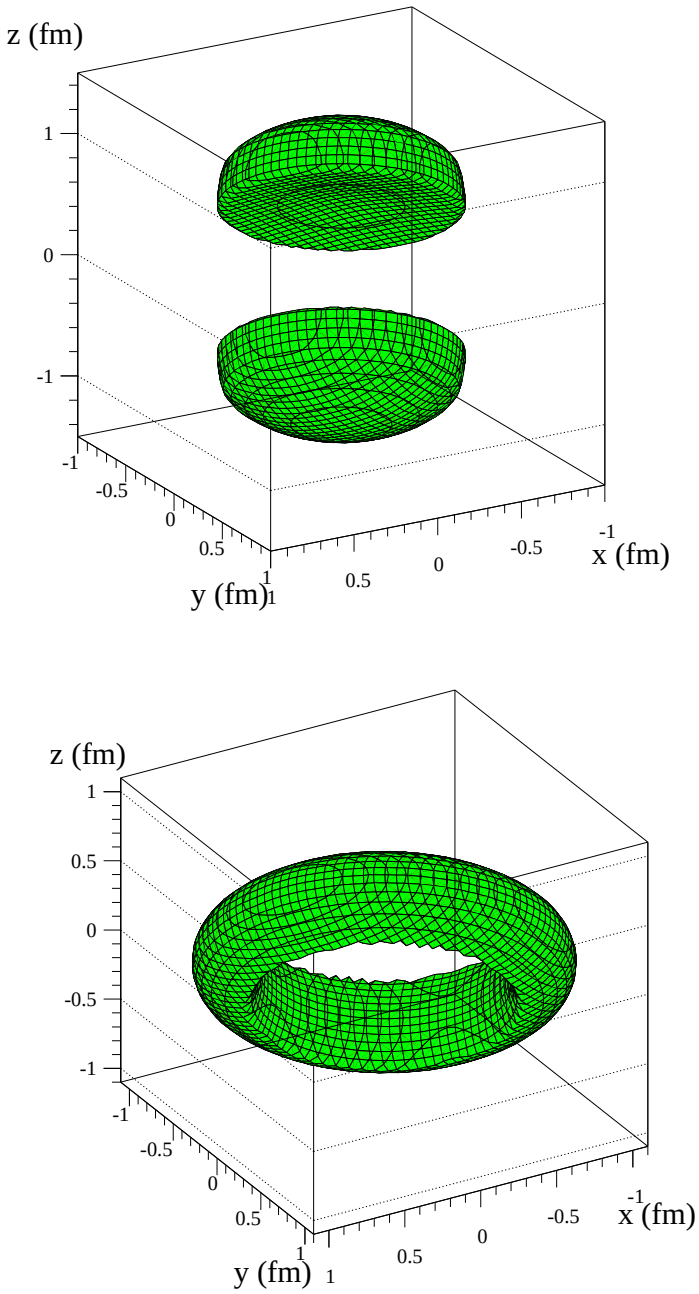

Figure II-2: *The deuteron nucleon density $\rho^{M_J}_{J=1}(\vec{r})$ for an angular momentum projection $M_J = \pm 1$ (upper panel) and $M_J = 0$ (lower panel). The resulting geometrical structures are dubbed a "dumbbell" and a "torus" [26].*

nuclear Hamiltonian reads :

$$\hat{H} = \sum_{i=1}^{A} \frac{\hat{\vec{p}_i}^{\,2}}{2m_i} + \sum_{i<j=1}^{A} \hat{V}_{ij} + \sum_{i<j<k=1}^{A} \hat{V}_{ijk} + \cdots , \qquad \text{(II-2)}$$

which contains one-, two-, three and possibly many-body interactions. The two-body force can be formally written as :

$$\hat{V}_{ij}(\vec{r}_{ij}) = \sum_{p=1}^{18} v^p(\vec{r}_{ij}) \hat{O}^p_{ij} , \qquad \text{(II-3)}$$

where the operators $\hat{O}^p_{ij}$ are contained in

$$\begin{aligned} \hat{O}^p_{ij} \in\ & [1, \vec{\sigma}_i.\vec{\sigma}_j, S_{ij}, (\vec{L}.\vec{S})_{ij}, \vec{p}_{ij}{}^2, \vec{p}_{ij}{}^2 \vec{\sigma}_i.\vec{\sigma}_j, (\vec{L}.\vec{S})^2_{ij}] \otimes [1, \vec{\tau}_i.\vec{\tau}_j] \\ & \oplus [T_{ij}, T_{ij}\vec{\sigma}_i.\vec{\sigma}_j, S_{ij}T_{ij}, (\tau_{iz} + \tau_{j_z})] \end{aligned} \qquad \text{(II-4)}$$

with $\vec{r}_{ij} = \vec{r}_i - \vec{r}_j$ and $\vec{p}_{ij} = \vec{p}_i - \vec{p}_j$. The tensor operator takes on its standard form : $S_{ij} = 3\vec{\sigma}_i.\vec{r}_{ij}\vec{\sigma}_j.\vec{r}_{ij}/r^2_{ij} - \vec{\sigma}_i.\vec{\sigma}_j$ while the isotensor operator looks like : $T_{ij} = 3\tau_{iz}\tau_{j_z} - \vec{\tau}_i.\vec{\tau}_j$. Apart from a two-pion exchange diagram, there is no agreement on what other terms should be incorporated into the three-nucleon potential. Given an expression for the nuclear Hamiltonian, one still needs to solve the Schrödinger equation to obtain the nuclear bound-state wave function. Over the years, some techniques have been developed.

Since long, the Nuclear Shell Model (SM) [32] [33] has been the standard technique to tackle the A-body nuclear problem. At first, the success of the SM for understanding nuclei (e.g. explaining the magic numbers) may seem counterintuitive until one realizes that the Pauli exclusion principle suppresses the hard nucleon-nucleon collisions at low energy. Most static nuclear observables are dominated by the surface properties of nuclei due to the occurrence of a r^2 factor in their definition. At the surface, the nucleons are further apart favoring a SM-approach. In a first order approximation, the nuclear SM method amounts to solving the Hartree-Fock equation for a good chosen NN-potential which does not possess a hard core (the so-called mean field-approach). In a next step, the residual interactions can be incorporated as particle-hole excitations in an inert core. The way to proceed is to diagonalize the nuclear Hamiltonian in a truncated model space P. The truncation of the model space gives rise to the introduction of an "effective interaction" [34][35]. The solutions of the eigenvalue problem formulated in terms of the effective Hamiltonian, approach the real solutions for an infinitely large model space (i.e. all p-h excitations). The main argument against such an approach lies in its mean field (MF) character. A MF or independent-particle model (IPM) approach has two major drawbacks. First, any mean-field potential manifestly violates translation invariance [36][37]. Second, by treating the nucleons as moving independently from each other in an average potential a

lot of inter nucleon correlations (short, as well as long-range) are neglected. Over the years, a lot of experimental evidence has been accumulated which advocates the importance of these correlations. The IPM does not, for example, account for the small spectroscopic factors ($\approx 0.6 - 0.7$) which are systematically extracted from $A(e, e'p)$ experiments [38]. An early, rather clumsy, attempt to explain this observation was to introduce a spherical square well NN-potential shifted over some distance relative to the origin. This potential could be tuned so as to reproduce the ^{4}He charge form factor or the dip in the inter nucleon separation distribution at the origin. This approach was not popular due to the unrealistic character of the potential and the big COM spuriosity [13].
A popular technique that goes beyond the IPM, is the correlated-basis function approach (CBF) [39] [40]. In this approach, the IPM wave function is multiplied by a series of ascending powers in some correlation function. The central correlation function models the repulsive effect of the short-range piece of the nucleon-nucleon potential (see Fig. II-1) while the overall long-range part is accounted for by the mean field potential. Although the introduction of correlation functions is rather effective in correcting MF wave functions, it does not restore translation invariance. The latter deficiency has an effect on the physical observables going as $\frac{1}{A}$, i.e. having a bigger effect on light nuclei then on medium or heavy nuclei. Several COM effects have been studied throughout the years, ranging from the modification of the energy spectrum [41] over a change of the charge form factor [13][42] and a broadening of the coordinate as well as the momentum density [43] to the altering of the spectroscopic factors ($n_{k<k_F} \approx 0.6 - 0.7$) [44][38][45]. Lipkin [36] pointed out that only for the harmonic oscillator potential there exists an unambiguous method to eliminate the center-of-mass motion from the wave function. Several methods e.g. a Gartenhaus-Schwartz transformation [37], have been developed to project out the COM coordinate for an arbitrary wave function. It is possible to construct a CBF wave function which is translationally invariant [46] provided that harmonic-oscillator states are used when constructing the uncorrelated reference state. Harmonic oscillator one-particle states are, however, unsuitable to correctly implement the short-range behavior of the NN-potential.

§2 Model calculations: a survey

These days, most nuclear physics studies involving the electromagnetic probe use light nuclei as a target. For these systems one can hope to find exact methods to solve the nuclear A-body problem, thereby overcoming the shortcomings of the shell model. Since long, only the two- and three-body problem could be solved exactly for a realistic potential. Recently, different groups have developed methods to perform ab initio calculations for the ground state of ^{4}He. All of these calculations are translationally invariant and account for the nuclear interaction in

its full complexity [47]. These methods are the Faddeev-Yakubovsky (FY) equations, the variational methods (VM), the so-called "no-core Shell Model method" and the Greens Function Monte Carlo (GFMC) technique. A recent paper [47] by Kamada et al. showed all these wave functions giving more or less the same predictions for the nuclear properties. Hereafter, we will highlight the features of each technique separately.

§2.1 Shell-model inspired techniques

The no-core Shell Model calculations (NCSM) [48] are based on the standard Shell Model techniques. To reduce the dimensionality of the problem, one diagonalizes the bare Hamiltonian into some finite (truncated) model space introducing an effective Hamiltonian :

$$\hat{H}_{eff} = [P(1+\omega^\dagger\omega)P]^{-1/2}(P+P\omega^\dagger Q)H(Q\omega P+P)[P(1+\omega^\dagger\omega)P]^{-1/2} , \quad \text{(II-5)}$$

where, P is the projection operator onto the model space while $Q \equiv 1-P$ is the complementary operator. The Lee-Suzuki similarity transformation ω implements the transition from the model space into the excitation space [34][35]. The two main differences with the ordinary scheme is the usage of a center-of-mass corrected model space and the fact that all particles are supposed to be active, in contradistinction to the standard SM calculations that involve an inert core. In these calculations, it is crucial to impose the right anti-symmetrization properties on the wave function which is a function of the relative coordinates only (i.e. Jacobi coordinates, see App. B-1). Two different approaches have been adopted. In the first one, the model space is spanned by HO-wave functions [49]. Alternatively, hyperspherical harmonics, which are generalizations of the spherical harmonics [50][51], have been used. These schemes do not explicitly implement the short-range NN-behavior into the wave function. Therefore, a huge amount of basis states is required to account for all the dynamical features of the ^{4}He nucleus.

§2.2 Faddeev-Yakubovski equations

The Faddeev-Yakubovsky (FY) equations [52][53][54][55][56][57][58] are a generalization of the Faddeev equations [59][60][61]. The Faddeev-Yakubovski equations can be obtained by expanding the total wave function in terms of six Faddeev amplitudes each referring to a particular interacting pair :

$$\Psi \equiv \sum_{i<j=1}^{4} \psi_{ij} = \psi_{12}+\psi_{13}+\psi_{14}+\psi_{23}+\psi_{24}+\psi_{34} , \quad \text{(II-6)}$$

these amplitudes are solutions of six Schrödinger-like differential equations :

$$(\hat{T}-E)\psi_{ij} = -\hat{V}_{ij}\sum_{k<l=1}^{4}\psi_{kl} . \quad \text{(II-7)}$$

In their turn, each of these amplitudes can be rewritten as a sum of three wave functions corresponding to the different two-body breakup channels :

$$\psi_{ij} \;=\; \psi^{l}_{ij,k} + \psi^{k}_{ij,l} + \psi_{ij,kl} \;\text{ with }\; (i<j, k<l)\;. \tag{II-8}$$

This refinement gives rise to a threefold multiplication of the number of basis states and correspondingly of the number of differential equations which leads to 18 equations.

$$\left\{\begin{array}{rcl} (\hat{T}+\hat{V}_{ij}-E)\psi^{l}_{ij,k} &=& -\hat{V}_{ij}\left(\psi^{l}_{ik,j}+\psi^{j}_{ik,l}+\psi_{ik,lj}+\psi^{l}_{jk,i}+\psi^{i}_{jk,l}+\psi_{jk,il}\right) \\ (\hat{T}+\hat{V}_{ij}-E)\psi^{k}_{ij,l} &=& -\hat{V}_{ij}\left(\psi^{k}_{il,j}+\psi^{j}_{il,k}+\psi_{il,kj}+\psi^{k}_{jl,i}+\psi^{i}_{jl,k}+\psi_{jl,ik}\right) \\ (\hat{T}+\hat{V}_{ij}-E)\psi_{ij,kl} &=& -\hat{V}_{ij}\left(\psi^{j}_{kl,i}+\psi^{i}_{kl,j}+\psi_{kl,ij}\right) \end{array}\right. \tag{II-9}$$

The different amplitudes are written in terms of Jacobi coordinates. K-type coordinates for the twelve $\psi^{l}_{ij,k}$ channels and H-type coordinates for the six $\psi_{ij,kl}$ wave functions (see App. B-1). Eventually, the original Schrödinger equation can be reformulated in terms of 18 differential equations. These manipulations on the Schrödinger equation reduce the complexity of the original problem because in every differential equation only one pair undergoes an interaction. When spin and isospin degrees of freedom are introduced, the proton and neutron with their respective spin projection s_z can be seen as different appearances of one and the same object. This allows one to reduce the 18 FY-equations to two equations (i.e., a K and a H-type: see App. B-1) by the introduction of permutation operators,

$$\begin{array}{rcl} (\hat{T}+\hat{V}_{12}-E)\psi^{4}_{12,3} &=& -\hat{V}_{12}[(1+P_{34})(P_{13}+P_{23})\psi^{4}_{12,3}-(P_{13}+P_{23})\psi_{12,34}] \\ (\hat{T}+\hat{V}_{12}-E)\psi_{12,34} &=& -\hat{V}_{12}[(P_{13}P_{24}+P_{14}P_{23})\psi^{4}_{12,3}+P_{13}P_{24}\psi_{12,34}]\;, \end{array} \tag{II-10}$$

where, P_{ij} interchanges the particles i and j. The complete four-body wave function of Eq. (II-6) can now be written as :

$$\Psi \;=\; \Psi_{3+1}+\Psi_{2+2} \tag{II-11}$$

$$\Psi_{3+1} \;=\; [1-(P_{13}+P_{23})][1-(P_{14}+P_{24}+P_{34})]\psi^{4}_{12,3} \tag{II-12}$$

$$\Psi_{2+2} \;=\; [1-(P_{13}+P_{23}+P_{14}+P_{24})+P_{13}P_{24}]\psi_{12,34}\;, \tag{II-13}$$

where, Ψ_{3+1} and Ψ_{2+2} denote the two two-body breakup channels of ^{4}He.
To solve the set of Yakubovski equations one projects the chain wave function components ($\psi^{4}_{12,3}$ or $\psi_{12,34}$) onto a partial-wave basis depending on the type of chain. The partial-wave expansion is usually expressed in terms of tripolar harmonics which are defined according to :

$$\mathcal{Y}_{[l_x l_y l_z, LM]} \;=\; [[Y_{l_x}(\hat{\vec{x}})\otimes Y_{l_y}(\hat{\vec{y}})]_{l_{xy}}\otimes Y_{l_z}(\hat{\vec{z}})]_{LM}\;, \tag{II-14}$$

with, l_x the angular momentum of the pair defined by $\vec{x}$. For the 2+2 fragmentation, l_y is the angular momentum of the pair defined by $\vec{y}$ while l_z is the relative angular momentum of the two two-particle systems. In the case of the 3+1 chain, l_y is the angular momentum of the third particle relative to the center of mass of the pair which determines $\vec{x}$ and l_z is the angular momentum of the fourth particle relative to the three-body cluster. In practice, one accounts for a certain restricted number of relative and total angular momenta. The spin-isospin channels, on the other hand, are treated in their full complexity. The eigenvalue problem in the truncated angular momentum space has to be solved for every chain and spin-isospin configuration which is a non-trivial task that could only be done with the aid of super-computers. To arrive at the solution of the original problem one has to sum the computed energy eigenvalues and radial wave function eigenvectors according to the formula's contained in Eqs. (II-11)-(II-13).

§2.3 Variational methods

The variational methods start from an educated guess for the ground-state wave function $|\Psi_0\rangle$ and solve for a set of parameters which minimize the nuclear ground-state energy. The crucial point in the variational method is the proper choice for the trial wave function. Three approaches have been followed. First, one can choose the most appropriate functional form to describe the short- as well as the long-range behavior and solve the matrix elements to find the best values for the non-linear parameters. Second, facilitating the calculation of the matrix elements, a large and simple basis can be chosen and one can solve the equations for the expansion coefficients. Third, assuming a particular form for the wave function (e.i. $\Psi = \sum_{\mu=n,m,l,s,t} u_\mu(\rho) Y_\mu(\Omega)$) one arrives at a differential equation which needs to be solved in order to derive the radial component of the wave function. All approaches make use of the Rayleigh-Ritz variational principle

$$\delta(< \Psi_0 | \hat{H} - E | \Psi_0 >) \;\; = \;\; 0 \qquad \text{(II-15)}$$

to determine the free parameters or to derive the differential equation.
An example of the second approach is the Coupled-Rearrangement-Channel Gaussian-Basis Variational method [62] developed to solve the Coulomb three-body problem. The ground-state wave function is expanded in a Gaussian basis using the two types of Jacobian coordinates which are the natural coordinate frames to describe the relative four-body state. The main disadvantage of this method is the slow convergence caused by the strong short-range repulsion of the NN-potential which is not contained in the adopted basis states. One possibility to correct for this shortcoming, is to introduce an additional correlation function in front of the Gaussians. In Ref. [63] a Gaussian correlation function has been adopted.
In order to solve the four-body problem, the authors of Ref. [63] adopted a

Stochastic Variational Method (SVM). In this approach, the non-linear parameters, for each basis function added, are generated randomly from a predefined domain while the expansion coefficients are determined to minimize the energy eigenvalue. A general basis function looks like :

$$\Psi_{(LS)JMTM_T} = \mathcal{A}\left\{e^{\frac{1}{2}x^\dagger Ax}\left[\mathcal{Y}_{[l_xl_yl_z,LM_L]}\xi_{SM_S}\right]_{JM_J}\chi_{TM_T}\right\} \qquad \text{(II-16)}$$

with, $\mathcal{Y}_{[l_xl_yl_z,LM_L]}$ the tripolar harmonics defined in Eq. (II-14). The spin and isospin wave functions are denoted by ξ_{SM_S} and χ_{TM_T} respectively. The exponential has a matrix argument of dimension 3×3. The SVM uses a basic property of the variational method i.e. enlarging the model space makes the computed spectrum to move closer to the real spectrum. When more advanced correlation functions are used one has to resort to other techniques.
One of these other techniques is the Correlated Hyperspherical Harmonics Variational method (CHH) [64] [65]. The ground-state wave function is expressed as a sum over the different spin-, isospin- and angular momentum channels, as well as over the different Jacobi rearrangement channels

$$\Psi = \sum_i \left\{\psi^i_H(x,y,z) + \psi^i_K(x,y,z)\right\}, \qquad \text{(II-17)}$$

with, H and K the two types of Jacobi arrangements (Appendix B-1). Also here, the wave function is written in terms of the tripolar harmonics but an additional expansion of the radial part of the wave function $\psi(|\vec{x}|,|\vec{y}|,|\vec{z}|)$ is performed. Before doing this, a coordinate transformation is pursued

$$\begin{aligned} \rho &= \sqrt{|\vec{x}|^2+|\vec{y}|^2+|\vec{z}|^2} \\ \cos\phi &= \frac{|\vec{x}|}{\rho} \\ \cos\eta &= \frac{|\vec{y}|}{\rho\sin\phi}\,, \end{aligned} \qquad \text{(II-18)}$$

with, (ρ,ϕ,η) the hyperspherical coordinates referring to the original Cartesian coordinates $(|\vec{x}|,|\vec{y}|,|\vec{z}|)$. The two coordinates (ϕ,η) can be interpreted as some hyper solid angle making an expansion of the radial wave function in terms of spherical harmonics possible :

$$\psi(|\vec{x}|,|\vec{y}|,|\vec{z}|) = \sum_{n,l,m} u_{n,l}(\rho)Y_{lm}(\phi,\eta) \qquad \text{(II-19)}$$

The radial hyperspherical component of the wave function $u_{n,l}(\rho)$ is a solution of a differential equation showing up as a result of the Rayleigh-Ritz variation to obtain the correct ground-state.

The presence of large amounts of correlations in the exact ground state makes all aforementioned methods to suffer from the same shortcoming, namely a large

model space is mandatory in order to predict the experimental ground-state energy with some acceptable accuracy.
As alluded to earlier in the discussions, there exists an alternative approach which circumvents this shortcoming. Instead of expanding the nuclear wave function in a large model space of relatively simple functions, the correlation function in its full operatorial complexity can be included. Evaluating the matrix elements for such a wave function becomes a very involving task. Monte Carlo techniques are used to perform the numerical quadratures which show up in the energy minimizing procedure. The A-particle probability distribution is used as a weighting function to perform the Monte Carlo quadratures. This approach is called the Variational Monte Carlo (VMC) method. The ^{4}He trial wave function has the following form :

$$|\Psi >= \left[\mathcal{S} \prod_{i<j<k=1}^{4} F_{ijk}\right] \left[\mathcal{S} \prod_{i<j=1}^{4} F_{ij}\right] |\Phi > \qquad \text{(II-20)}$$

where F_{ij} and F_{ijk} are correlation functions with the same operatorial structure as the two- and three-body potential. In general, the central, spin-isospin and tensor isospin correlations are the most important ones. Because of the $(S = 0, T = 0)$ character of the ^{4}He nucleus, the spin-spin and isospin-isospin operators induce the same effect on the wave function. The uncorrelated wave function Φ is a spin-isospin slater determinant corresponding with an $(S = 0, T = 0)$ spin-isospin state. Once the non-linear parameters, which minimize the energy, are fixed all physical observables can be calculated.

The Argonne-Urbana group has developed a method to calculate the ground-state properties starting from a general ground-state wave function. This method projects out of the trial wave function the exact ground-state by means of an iteration process.
The Diffusion or Greens Function Monte Carlo (GFMC) [66] [67][68][30][69][31] method can be used as a further refinement for each of the previously obtained wave functions using one of the various techniques enlisted above. Typically, one resorts to the ground-state wave function obtained by the VMC-method, as an input wave function. A Greens function operator is used to describe the projection process

$$\Psi(\tau) = e^{-\frac{1}{\hbar}(\hat{H}-E_0)\tau}\Psi_T \qquad \text{(II-21)}$$

$$\Psi = \lim_{\tau\to\infty} \Psi(\tau) \qquad \text{(II-22)}$$

where, τ is the imaginary time. The GFMC method does not specifically alter the expansion coefficients or non-linear parameters in the trial wave function, it actually provides an alternative way of calculating expectation values :

$$< \hat{O}(\tau) > = \frac{< \Psi(\tau)|\hat{O}|\Psi(\tau) >}{< \Psi(\tau)|\Psi(\tau) >}$$

$$= \frac{< \Psi_T \left[e^{-\frac{1}{\hbar}(\hat{H}-E_0)\Delta\tau}\right]^n |\hat{O}| \left[e^{-\frac{1}{\hbar}(\hat{H}-E_0)\Delta\tau}\right]^m \Psi_T >}{< \Psi_T \left[e^{-\frac{1}{\hbar}(\hat{H}-E_0)\Delta\tau}\right]^n | \left[e^{-\frac{1}{\hbar}(\hat{H}-E_0)\Delta\tau}\right]^m \Psi_T >} \quad \text{(II-23)}$$

with, $\Delta\tau$ a small imaginary time interval and $m(n)$ a parameter which is gradually increased till convergence is approached. The crucial point in these calculations is the derivation for every spin-isospin channel of the A-body propagator $G(\vec{R},\vec{R}') =< \vec{R}|e^{-\frac{1}{\hbar}(\hat{H}-E_0)\Delta\tau}|\vec{R}' >$ in r-space ($\vec{R} \equiv (\vec{r}_1,\ldots,\vec{r}_A)$). To suppress the errors induced by the approximations made to derive G, $\Delta\tau$ has to be made small.

§2.4 Cluster-expansion techniques

Calculating matrix elements with wave functions which account for the full complexity of nucleon-nucleon correlations is not an easy task. Cluster expansion techniques which are known from classical liquid and gas calculations, have been adopted to the nuclear problem by Clark and Ristig [70] [71][72]. The A-body correlation function is written in a functional form which lends itself easily to expansions in a cluster series i.e. $\mathcal{F} = e^{-i\sum_{i<j=1}^{A}\hat{S}_{ij}}$ [73][74][46] or $= \prod_{i<j=1}^{A} f_{ij}$ [75][76][77]. The cluster expansion method is suited to study the effect of two-, three-, ... body correlation effects on the physical observables. The major drawback of this approach is that with every order in the cluster expansion the wave functions have to be renormalized and even re-orthogonalized [39].

An alternative way, circumventing the normalization pitfall, is to cluster expand the density functions instead of the wave function. The density functions will be defined in the next section. The cluster expansion is performed in terms of $g_c = f_c^2 - 1$ with f_c the Jastrow correlation function defined at the level of the wave functions. The major advantage of this perturbation expansion is that when including only linked diagrams the correct normalization can be guaranteed. The latter feature is also well-known from field theory.

§3 The four-nucleon wave function

Throughout this work we will make use of a hybrid GFMC wave function for the ^{4}He ground state. The GFMC wave function contains central an tensor correlations. In order to implement the effect of correlations we will adopt a cluster expansion. The GFMC wave function as it has been calculated by the Argonne-Urbana group [66] has the following functional form

$$\Psi_{^4He}\Big(x_1,x_2,x_3,x_4\Big) = \frac{1}{(2\pi)^{3/2}}\, e^{\mathbf{i}\vec{P}.\vec{R}}\, \psi\Big(\vec{r}_{\rm rel}{}^1,\vec{r}_{\rm rel}{}^2,\vec{r}_{\rm rel}{}^3\Big)$$

$$\times\frac{1}{\sqrt{4!}}\begin{vmatrix} \chi_{m_s=1/2,m_t=1/2}(1) & \chi_{m_s=1/2,m_t=-1/2}(1) & \chi_{m_s=-1/2,m_t=1/2}(1) & \chi_{m_s=-1/2,m_t=-1/2}(1)\\ \chi_{m_s=1/2,m_t=1/2}(2) & \chi_{m_s=1/2,m_t=-1/2}(2) & \chi_{m_s=-1/2,m_t=1/2}(2) & \chi_{m_s=-1/2,m_t=-1/2}(2)\\ \chi_{m_s=1/2,m_t=1/2}(3) & \chi_{m_s=1/2,m_t=-1/2}(3) & \chi_{m_s=-1/2,m_t=1/2}(3) & \chi_{m_s=-1/2,m_t=-1/2}(3)\\ \chi_{m_s=1/2,m_t=1/2}(4) & \chi_{m_s=1/2,m_t=-1/2}(4) & \chi_{m_s=-1/2,m_t=1/2}(4) & \chi_{m_s=-1/2,m_t=-1/2}(4) \end{vmatrix}, \tag{II-24}$$

where, ψ describes the internal excitation of the four-body system and the slater determinant denotes the spin-isospin part. Equation (II-24) is an eigenvector of a translationally invariant Hamiltonian, irrespective of the presence of correlations. The internal wave function ψ reflects the specific nature of the NN-interaction and has been cast in the following format within the GFMC framework

$$\psi\Big(\vec{r}_{\rm rel}{}^1,\vec{r}_{\rm rel}{}^2,\vec{r}_{\rm rel}{}^3\Big) = \frac{1}{\sqrt{\mathcal{N}}}\mathcal{S}\prod_{i<j=1}^{4}\Big(1+u_{t\tau}\left(|\vec{r}_i-\vec{r}_j|\right) \times\left[3\frac{(\vec{\sigma}_i.\vec{r}_{ij})(\vec{\sigma}_j.\vec{r}_{ij})}{r_{ij}^2}-\vec{\sigma}_i.\vec{\sigma}_j\right]\vec{\tau}_i.\vec{\tau}_j\Big)\prod_{k<l=1}^{4}\phi_c\left(|\vec{r}_k-\vec{r}_l|\right)\ . \tag{II-25}$$

From the complete GFMC trial wave function (II-20) only the central and tensor correlations have been retained because they are by far the dominant correlations. To simplify the calculations of the matrix elements, a cluster expansion has been adopted when computing the effect of the tensor correlations :

$$\psi\Big(\vec{r}_{\rm rel}{}^1,\vec{r}_{\rm rel}{}^2,\vec{r}_{\rm rel}{}^3\Big) = \frac{1}{\sqrt{\mathcal{N}}}\mathcal{S}\Big(\prod_{i<j=1}^{4}f_c\left(|\vec{r}_i-\vec{r}_j|\right)+ \sum_{i<j=1}^{4}f_{t\tau}\left(|\vec{r}_i-\vec{r}_j|\right)\left[3\frac{(\vec{\sigma}_i.\vec{r}_{ij})(\vec{\sigma}_j.\vec{r}_{ij})}{r_{ij}^2}-\vec{\sigma}_i.\vec{\sigma}_j\right]\vec{\tau}_i.\vec{\tau}_j+\ldots\Big)\prod_{k<l=1}^{4}\phi_{\rm ho}\left(|\vec{r}_k-\vec{r}_l|\right)\ , \tag{II-26}$$

with, $\phi_{\rm ho}(|\vec{r}|)$ the $1s$ Harmonic oscillator (HO) wave function (with oscillator parameter $\nu = 0.4/fm^2$) upon which the short range dynamics is imposed by means of the central ($f_{\rm c}(|\vec{r}|)$) and tensor ($f_{t\tau}(|\vec{r}|)$) correlation function. The correlation functions as used in our calculations are displayed in Fig II-3. The dip in the central correlation function ($f_c(r)$) around zero NN-separation comes from the hard-core repulsion in the NN-potential. The central correlation function behaves as a form factor for the NN-potential cutting out its short range repulsive part which reduces the binding energy. The tensor correlation function, although small compared to the central one, enhances the effect of the pion and two-pion exchange parts of the potential and contribute negatively to the binding energy.

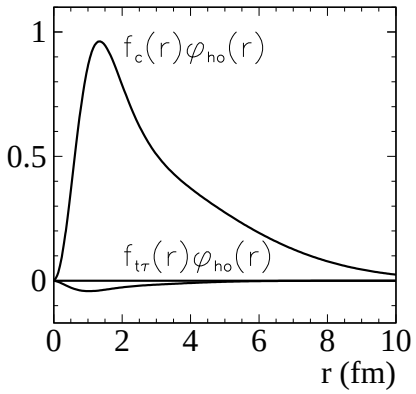

Figure II-3: *The central and tensor correlation functions derived using a GFMC-technique multiplied with a* $1s$ *HO-relative pair wave function.*

Although very important in deriving the binding energy, the tensor correlations do not contribute, in lowest order, to the particle coordinate- as well as momentum densities. Some studies exploring the effect of state dependent correlations have been reported. The authors of Ref. [78] observed only a minor modification for scalar quantities (e.g. mass density, momentum density, form factor) stemming from the tensor correlations in next-to-leading order. Non-scalar quantities (e.g. response functions) are, already in lowest order, slightly altered by the tensor part of the NN-potential [79][80].

Incorporating the tensor correlations in a consistent manner into the calculations is a challenging task. The mechanism that the tensor correlations shift some strength in the momentum density from low to higher nucleon momenta can be partly simulated by a proper increase of the Jastrow correlation function. In order to keep the four-body breakup calculations manageable, tensor correlations will be discarded in the remainder of this work. To compensate for the small increase of high momentum components induced by the tensor correlations, we adopt a more repulsive Jastrow ansatz as the one deduced by the Argonne-Urbana group [66]. The Jastrow correlation function has been altered as to reproduce the one-body momentum density which is measured up to a momentum of 600 MeV/c [81][17][82].

§3.1 Density operators

For an A-body system, the A-particle density matrix contains an equal amount of information as the wave function. In atomic-, molecular- and solid state physics it is common practice to use the density matrix instead of the wave function (e.g. Density Functional Theory). The density matrices can be written as :

$$\begin{aligned} \rho_1(x_1;x_1') &= \int \Psi(x_1,x_2,\cdots,x_A)^\dagger \Psi(x_1',x_2,\cdots,x_A) dx_2 \ldots dx_A \\ \rho_2(x_1,x_2;x_1',x_2') &= \int \Psi(x_1,x_2,\cdots,x_A)^\dagger \Psi(x_1',x_2',\cdots,x_A) dx_3 \cdots dx_A \\ &\vdots \quad , \end{aligned} \tag{II-27}$$

where, the variable x_i denotes the coordinate space variables as well as spin and isospin degrees of freedom. The diagonal part of the density operator is a physical observable which is equal to the so-called N-body probability density. To extract information about the off-diagonal elements a fourier transform can be performed. The latter gives rise to the density matrix in momentum space. Again, the diagonal elements give rise to an N-body probability distribution.
In what follows, we will restrict ourselves to the one- and two-particle density operators. The one-body equidensity surfaces in coordinate space as well as in momentum space become experimentally accessible quantities once some approximations have been made. Usually, these approximations involve considerable simplifications with respect to the treatment of possible reaction mechanisms, for example neglect of particle distortions, in electromagnetically induced processes. For example, in the first Born approximation, the (e,e') cross-section is proportional to the charge form factor which can be used to extract the charge density. In a symmetrical nucleus ($N=Z$) and to first order in the charge operator (i.e. neglecting all kind of sub nuclear contributions to the charge density e.g. from pion exchange) the latter is just half the particle density.
In a Plane Wave Impulse Approximation (PWIA) description, the $A(e,e'p)$ cross section can be cast in the following factorized form [83]:

$$\frac{d^5\sigma}{dE_{e'}d\Omega_{e'}d\Omega_p} = K\sigma_{ep}S(|\vec{p}_m|,E_x) \tag{II-28}$$

where K is a kinematical factor and σ_{ep} is the half off-shell electron proton scattering cross section. Further, $S(|\vec{p}_m|,E_x)$ is the spectral function which reduces after an integration over the excitation energy (E_x) of the residual nucleus to the momentum density corresponding with the specific quantum numbers of the struck proton.
As for the momentum density there's no model independent way to extract the two-particle density matrices from the experimental data. The two-nucleon knockout cross-section does not factorize unless some additional approximations

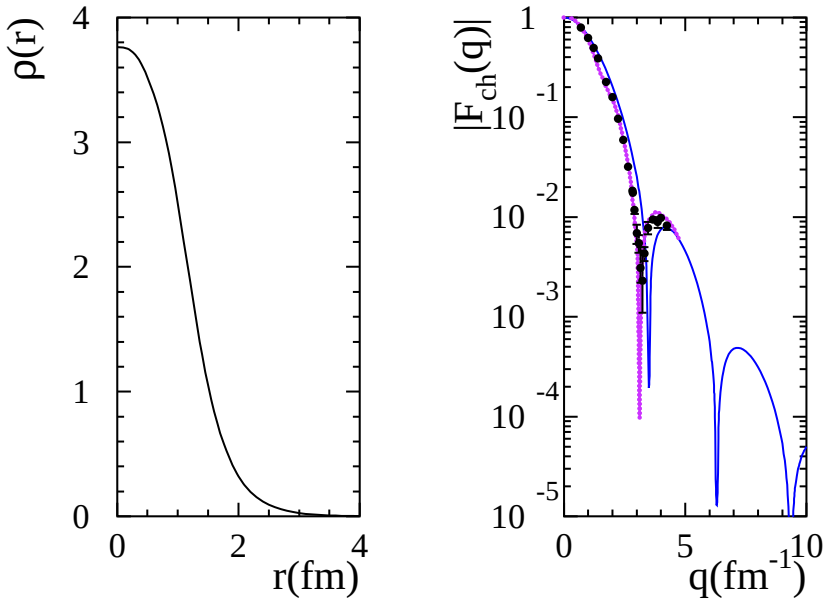

Figure II-4: *The one-particle point density (left panel) and the ^{4}He charge form factor (right panel). Rescaled to unity, the form factor data are from Refs. [86] and [87]. The purple dotted curve is a full calculation, including meson exchange and isobar excitation currents, taken from Ref. [88]. The full curve is obtained with the ^{4}He wave function used throughout this work (see App. C-1 for more details).*

are made. The pair momentum distribution factorizes out in the $(e, e'NN)$-cross section once one adopts the Gottfried approximation [11] i.e. a plane-wave description of the reaction process adopting additionally a spectator approximation for the residual nucleons while describing the active pair as a quasi deuteron [84]:

$$\frac{d^8\sigma}{dE_{e'}d\Omega_{e'}dE_{N_1}d\Omega_{N_1}d\Omega_{N_2}} \;=\; K\sigma_{eNN}F_{\rm pair}(\vec{P}) \;\;, \qquad \text{(II-29)}$$

where $K = E_{N_1}P_{N_1}E_{N_2}P_{N_2}$ and $F_{\rm pair}(\vec{P})$ is the pair momentum function [11][85]. The pair momentum function denotes the probability of finding a nucleon pair in some particular two-particle state with a COM momentum $\vec{P}$.

In Appendix C-1.1 and C-1.2 analytical expressions for the coordinate and momentum space density matrices have been derived for the ^{4}He case. Many ^{4}He(e, e') experiments have probed the charge form factor [86][87].

The charge form factor is determined as follows :

$$F_{\rm ch}(\vec{q}) \;=\; \left[\frac{d\sigma}{d\omega}(e,e')/\left(\frac{d\sigma}{d\omega}\right)_p(e,e')\right] \;\;, \qquad \text{(II-30)}$$

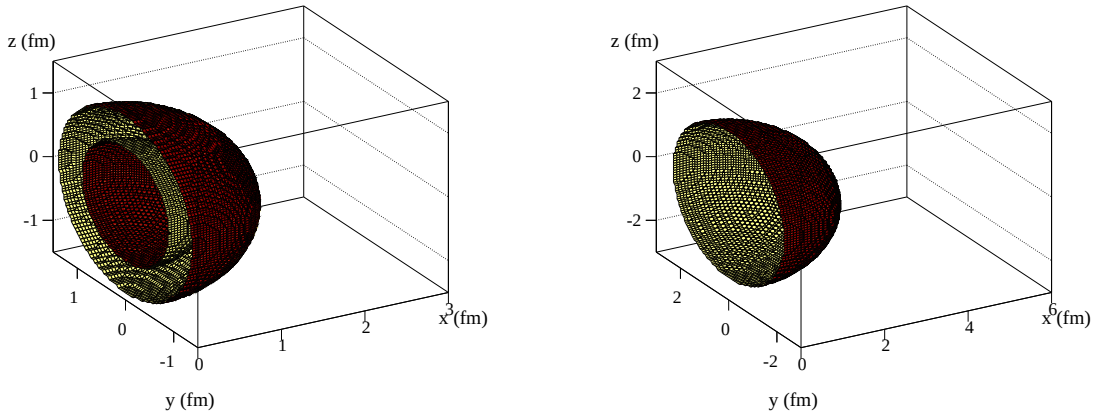

Figure II-5: *A 3D plot of the internucleon separation distribution for ^{4}He. The left panel shows the 10% equiprobability surface while the right panel depicts the 1.3% surface.*

where, $(d\sigma/d\omega)_p$ is the cross section for elastic electron scattering from a point particle.
Assuming that the meson and isobar contributions to the charge operator can be neglected, it's straightforward to obtain, in the first Born approximation for the electromagnetic field, the charge form factor by a Fourier transform of the one-body density.

$$F_{\rm ch}(\vec{q}) \;=\; \int d^3\vec{r}\rho(\vec{r})e^{-i\vec{q}\cdot\vec{r}}\,. \qquad \text{(II-31)}$$

Before comparing the experimental and theoretical results one has to make sure that the experimental nuclear form factor has been corrected for the finite extension of the nucleon (i.e. $F_{\rm ch}^{\rm exp}(\vec{q})=F_{\rm ch}^{\rm proton}(\vec{q})\,.\,F_{\rm ch}^{\rm nucleus}(\vec{q})$).

Fig. II-4 displays the one-particle point density and the ^{4}He charge form factor. Looking at the particle density, one observes, after dividing out the entire solid angle (4π), a central density ($\approx 0.35 fm^{-3}$) of almost twice nuclear matter density ($\approx 0.17 fm^{-3}$) pointing to the possibility of finding strong correlation effects in ^{4}He. The theoretical charge form factor reproduces the experimental data within a few percent. Including the meson as well as the isobar currents [88] shifts the charge form factor to the left, on top of the data points.

Just as for the deuteron (see Fig. II-2) one can calculate the 3D surfaces of equal relative density (see also Eq. C-6) :

$$\rho_{rel}(\vec{r}) \;=\; \frac{1}{2}\int d^3\vec{R} < \Psi| \sum_{i\neq j=1}^{4} \delta^3(\vec{r}-\vec{r}_{ij})\delta^3(\vec{R}-(\frac{\vec{r}_i+\vec{r}_j}{2}-\vec{R}_{\rm com}))|\Psi >$$

Fig. II-5 displays the equiprobability surface for finding two nucleons in the nucleus at a particular (x, y, z) from each other with a probability of 10% (left

panel) or 1.3% (right panel). As opposed to the deuteron, there's only one type of structure (i.e. a hybrid dumbbell toroidal structure) because the helium ground state is an S=0 state. The typical deuteron dumbbell structure comes about from the quadrupole character of the tensor correlations. Neglecting those one ends up with a double sphere instead, as can be observed from Fig. II-5. When the probability is lowered smaller nuclear densities are probed and the inner sphere disappears giving rise to a spherical density as in the classical IPM description. This can be explained by observing that when going to smaller nuclear densities, the nucleons become less sensitive to the short range dynamics and only feel some average field.

Although most wave functions are derived in coordinate space, their momentum space counterparts are more relevant when it comes to calculating cross-sections. In electromagnetically induced breakup reactions, one gets information about the momentum distributions. One-nucleon knockout experiments are sensitive to the nucleon momentum distribution $n(\vec{p})$ (see Eq. (II-28)) while two-body knockout experiments offer the possibility to obtain information about the relative pair- $\rho_{rel}(\vec{q})$ and center-of-mass pair $\rho_{com}(\vec{Q})$ momentum distribution. All three momentum distributions are plotted in Fig. II-6 for the ^{4}He case. In a factorized approach, the cross section even scales with the pair momentum function. Realistic calculations reproduce the experimental data nicely in the case of the nucleon momentum distribution. The difference between the theoretical curve and the model-dependent experimental data obtained by Ciofi et al. [82] is resolved by including the tensor correlations. The major impact of the latter is to enhance the momentum distribution at intermediate momenta ($\approx 400 - 500$ Mev/c).

We now discuss two peculiar aspects of the ^{4}He wave function which will prove to be of the utmost importance for the remainder of this thesis.

§3.2 Short-range correlations

Elastic scattering of high-energy electrons from nuclei has revealed features (e.g., the diffraction dip in the charge form factor) in the nuclear form factor which are incompatible with naive IPM wave functions. When trying to explain the data, the incorporation of short-range correlations appears indispensable.

In order to estimate the influence of short-range correlations one needs a reference model wave function which lacks the correlations. A suitable candidate is the harmonic oscillator wave function (see Appendix C -2). Before proceeding it is worth stressing that the realistic wave function is translationally invariant, therefore the outcome of the realistic calculations have to be compared to the results obtained with the COM-corrected harmonic oscillator wave function (oscillator parameter $\nu = 0.4/fm^2$).

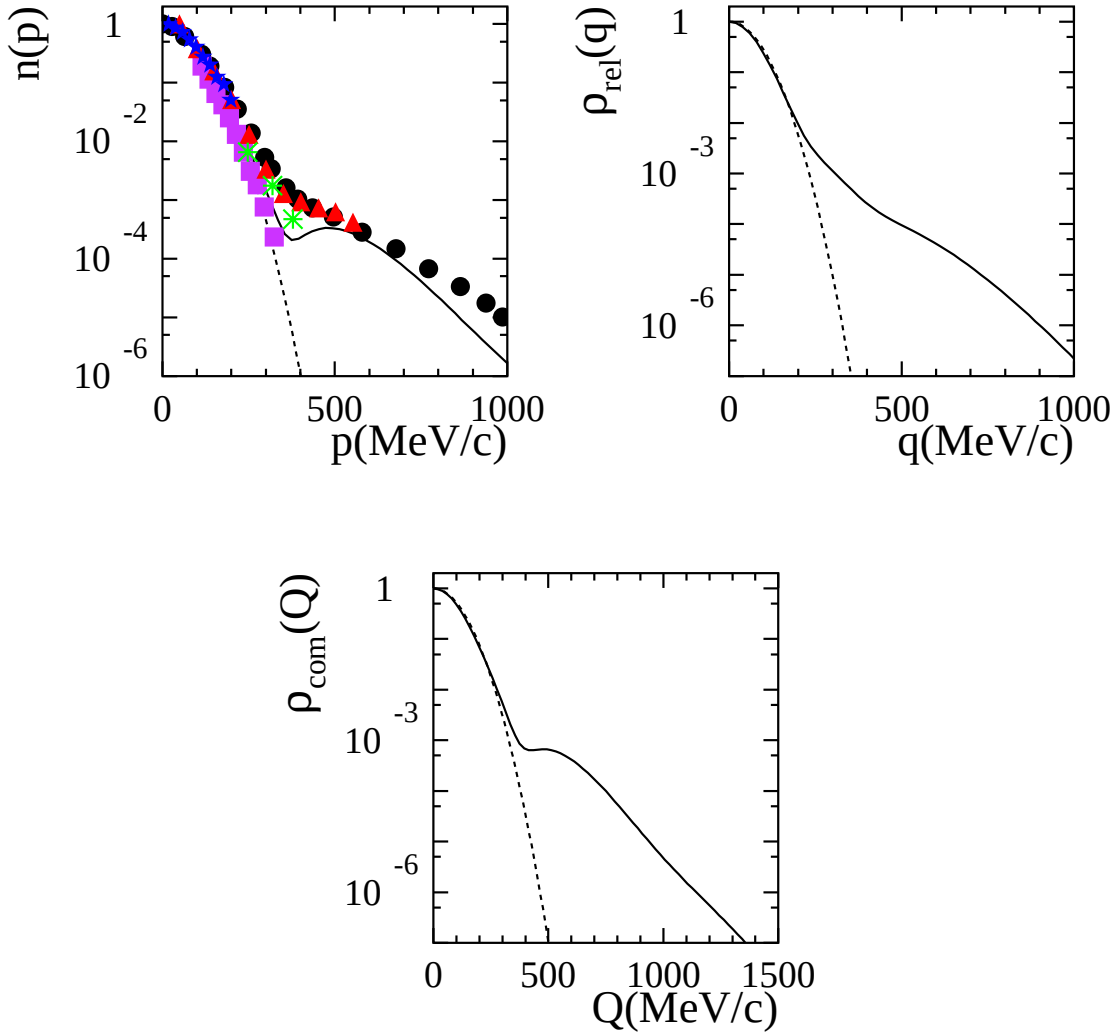

Figure II-6: *The ^{4}He momentum distributions as obtained with different wave functions. The solid curve corresponds to the realistic wave function defined in App. C-1.2, the dashed curve is a HO-calculation (see App. C-2). For both calculations the densities are averaged over the solid angle and normalized to unity. The three data sets are from : Refs [17] (★), [17] (■) and [81] (✳). The red triangles (▲) have been extracted from the experimental spectral function in a model-dependent [82] while the black dots (●) represent a full calculation by the Argonne-Urbana group including tensor correlations up to all orders [89].*

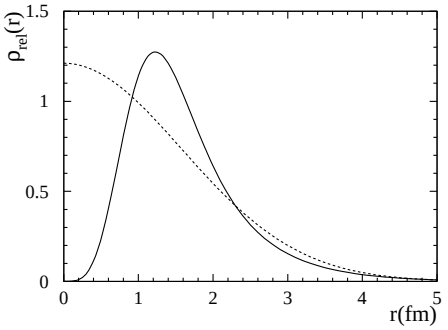

Figure II-7: *The inter-particle separation distribution for an harmonic oscillator wave function (dashed curve) as well as for a realistic description (solid curve) (see App. C-1.1).*

In coordinate space, the inter-particle separation distribution $\rho_{rel}(\vec{r})$ will give us information about the impact of short-range correlations (see Fig. II-7). At zero distance they push the nucleons away from each other. For inter-particle distances exceeding 4 fm both curves more or less overlap indicating that the short-range correlations do hardly alter the long-range behavior of the nucleons. This is dubbed the healing process. For heavy and intermediate nuclei the healing distance is about $2fm$ indicating that all nucleons feel to a greater extent the self-consistent field rather than the correlation effects. In a 3D-picture the former dip gives rise to an exclusion sphere as earlier explained when discussing Fig. II-5.

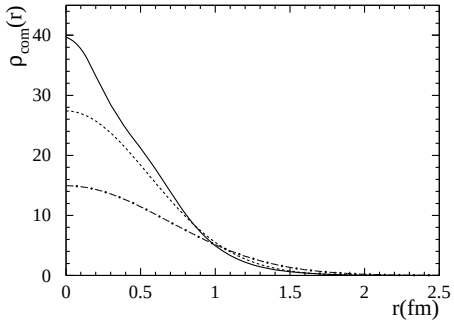

Figure II-8: *The pair distribution in ^{4}He calculated for three different model wave functions i.e. a realistic wave function (solid curve), a translationally invariant HO-wave (dashed curve) and a genuine IPM harmonic oscillator wave function (dash-dotted curve) (see App. C-1.1).*

Another sign indicating the presence of SRC is obtained by comparing the average nuclear radius $< |\vec{r}| >$ with the average nucleon-nucleon separation $< |\vec{r}_1 - \vec{r}_2| >$ in the nucleus. The former equals 1.5 fm while the latter is equal to 2.4 fm which forces us to conclude that most of the particles of a pair are located at opposite sides of the COM. Those pairs make up for almost 50% of the total amount of pairs. The cumulative inter-particle separation distribution $\Phi_{rel}(\vec{r}) = \int_{\vec{0}}^{\vec{r}} \vec{x}^2 \cdot \rho_{rel}(\vec{x}) d^3\vec{x}$ confirms this statement. The presence of short-range correlations can also be inferred from the momentum densities. In general they induce a shift of strength from the low to the high momentum components as can be observed from Fig. II-6. The three dashed curves in Fig.II-6, representing the HO-momentum densities, all undergo a similar modification when short-range correlations come into play. The

alteration of the pair momentum density will produce an amplification of the 2-body knock-out cross-section at large missing momenta while for the 1-body knock-out cross-section also an enlargement will be observed due to a larger high momentum component in the one-body momentum density. These implications can be deduced from the functional form of the respective cross sections II-28 II-29. Although they are only approximately correct, they still can be used to infer some general tendencies.

§3.3 Center-of-mass corrections

Translational invariance of physical laws, imposed by the requirment of momentum conservation, leads to the observation that the COM movement of a system can not have any physical relevance and must therefore be discarded when describing the intrinsic properties of a composite system. To impose translational invariance on a general wave function it must be separable into an internal and COM part. A crucial issue is imposing, in addition, the correct anti-symmetrization.

As alluded to in Sec. §1, spurious COM contributions can alter some of the experimental accessible quantities such as spectroscopic factors, charge form factors, particle densities, etc. Already in 1958 Lipkin pointed out [36] that only for the harmonic oscillator potential the COM coordinate can be separated out in an unambiguous way. Techniques to remove the COM coordinate for an arbitrary mean-field potential have been developed [37][41]. They have the disadvantage of producing non-unique results and there is no criterion to decide which technique is favorable [37][41]. Therefore, in what follows we will use the harmonic-oscillator wave function with and without COM-corrections to estimate the impact of the COM motion on the computed observables. The physically relevant quantities which we will study to pin down the recoil-effects, are the coordinate as well as the momentum density operators. The analytical expressions have been derived in Appendix C -2.

For the realistic, uncorrected Slater wave function C-15 the densities are all referred relative to the center of the potential while they are referred to the center of the nucleus for the recoil-corrected wave function. In coordinate space one expects to observe the largest effects on the pair COM distribution function. From Fig. II-8 it's clear that eliminating the COM motion reduces the width of the distribution function as one would expect. The difference between the solid and the dashed curve can be attributed to the short-range correlations. One can state that the COM-corrected HO-wave function is a much better approximation to the realistic one then the IPM wave.
In our approach, the charge form factor is not altered because we adjusted the one-particle density so it reproduces the rms charge radius inducing the same one-particle density for both descriptions.

Fig. II-9 displays the equivalent momentum distributions from Fig. II-6 but uses different wave functions. All the curves in Fig. II-9 are obtained with

HO-wave functions. The first set of curves refer to a translationally invariant description (dashed curves). The second set (dash-dotted) is obtained when not projecting out spurious COM effects. Both descriptions are obtained using an IPM harmonic oscillator wave function. The relative momentum density $\rho_{rel}(\vec{q})$ stays more or less the same as one would expect. Eliminating the recoil from the wave function decreases the one nucleon $n(\vec{p})$ and pair momentum $\rho_{com}(\vec{Q})$ distribution with a few orders of magnitude at intermediate momenta (≈ 500 MeV/c). A similar reduction will be observed in the one- and two-nucleon knockout cross-sections for missing momenta of the same magnitude, because the cross-section is proportional to the respective density functions.

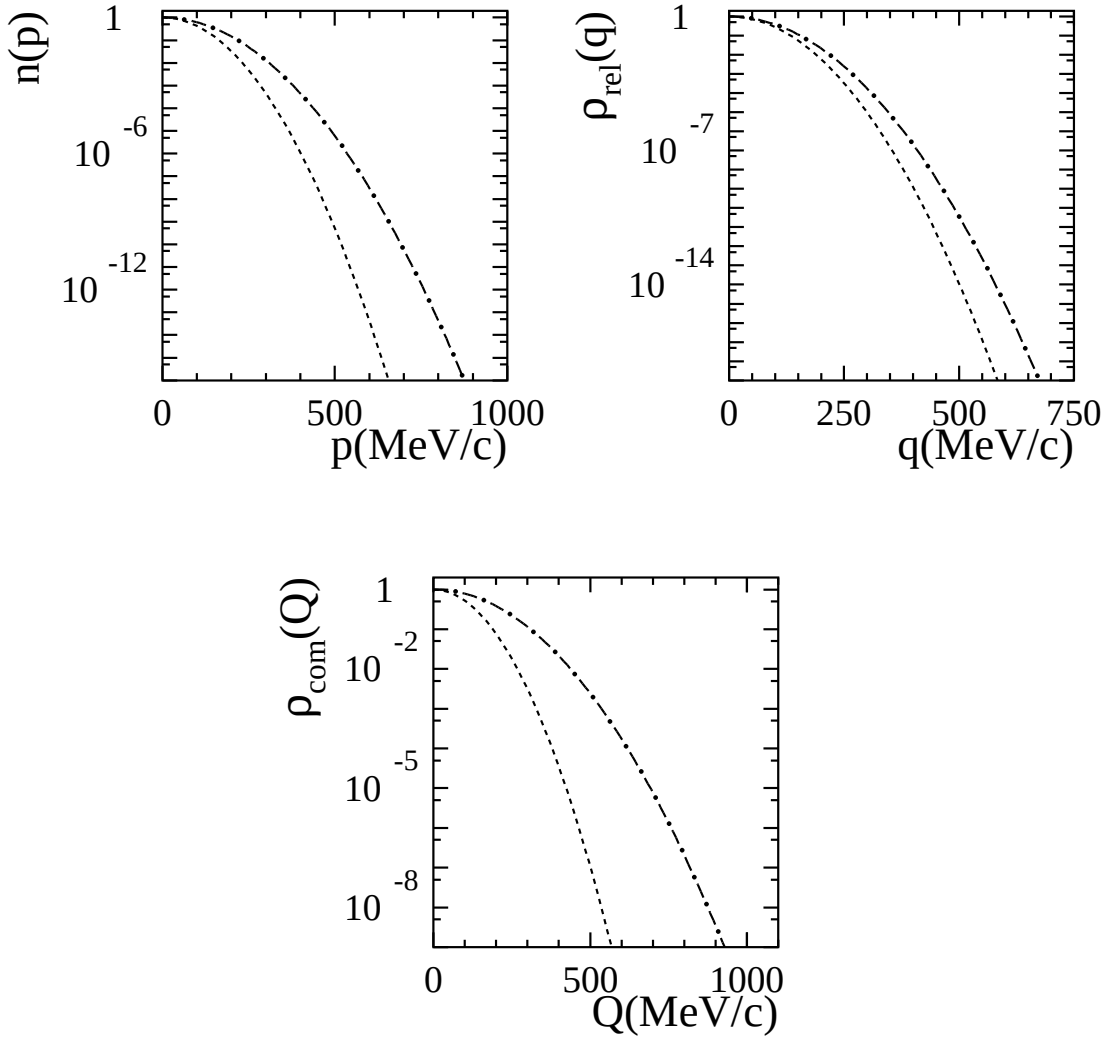

Figure II-9: *Three momentum distributions for ^{4}He as derived with HO-wave functions. The dashed curves are obtained with a translationally invariant wave function. The dot-dashed curves are the results when neglecting this correction. The HO-parameters used, are $\nu = 0.4$ for the dashed and $\nu = 0.5$ for the dot-dashed curves (see App. C-2).*

Chapter III

Two Nucleon-Knockout Observables

When exploring the nuclear interior one needs a microscope. For several reasons an electromagnetic probe (electron or photon beam) is, apart from the low associated counting rates preferable above a hadronic beam. Not only is the theory of electromagnetic interactions well understood, the smallness of the electromagnetic coupling constant, makes the exchanged photon (real or virtual) to scan the entire nuclear volume.

§1 Introduction

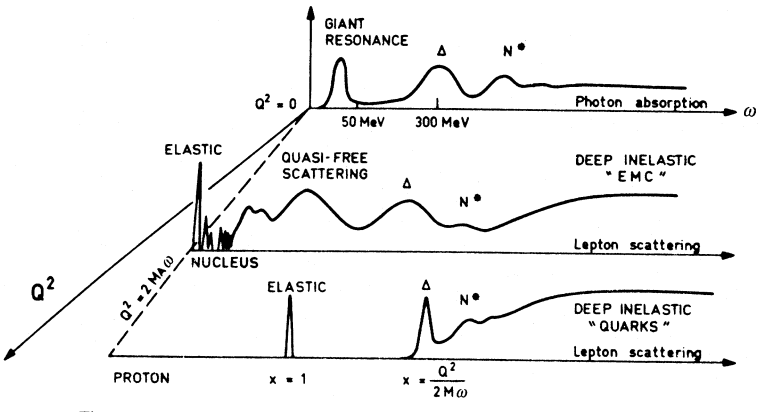

Figure III-1: *Schematic picture of the inclusive scattering cross section of a photon (real or virtual) from a proton or a nucleus [83].*

To gain more insight in the relevant reaction mechanisms contributing to the measured electron-scattering cross section, a little historical survey will be undertaken in this section.

In the early days of nuclear-structure research, one remained in the conviction that the $A(e,e')$ experiments would provide us with all the relevant information. Those experiments produced, over the years, a huge amount of data ranging from the elastic scattering peak up to the deep inelastic region. Fig. III-1 shows a typical inclusive electron scattering $A(e,e')$ cross section as a function of transferred energy (ω) and four-momentum (Q^2). These one-arm experiments could

be explained quite well in terms of independent nucleons swirling around in the nucleus. Those nucleons reside in a particular state or have a particular momentum. The former model is commonly known as the shell model while the latter is usually referred to as the Fermi gas model for nuclear matter. When we focus on these $A(e, e')$ experiments which survey the quasi-elastic peak (QE), most of the experimental results can be described within the context of the Fermi gas framework. The low-energy scattering experiments, on the other hand, could be well described in a shell-model approach. The shell model is well suited to explain the sharp peaks in the scattering cross section, which can be related to the particle-hole excitation spectrum. In the transition region where the giant resonances reside, one adopts a hybrid liquid drop model to describe the nucleus. The existence of the giant resonances can be explained by considering deformations of the nucleus as a whole.

When, over the years, the quality of the beams as well as the sensitivity of the detectors improved, an L/T-separation of the (e, e') cross section came within experimental reach. A Rosenbluth separation can be accomplished by measuring the cross section for different polarizations of the virtual photon. The Fermi gas model, which did so well in explaining the total cross section in the QE-region, failed in reproducing simultaneously the longitudinal and transverse response function. A major quenching of the experimental longitudinal response function in comparison with theory was observed. Moreover, a violation of the Coulomb sum rule emerged from these experiments. The Coulomb sum rule states that the integrated longitudinal response should equal the total nuclear charge.
Over the years, people searched for explanations of these observed discrepancies. One proposed the inclusion of other reaction mechanisms such as meson exchange and isobar currents as well as a better treatment of nuclear structure to remedy those shortcomings. As yet still no single theory has succeeded in describing simultaneously the longitudinal and the transverse inclusive response functions starting from first principles.

Although still open, this problem has triggered a lot of theoretical and experimental efforts.
To improve on our knowledge $A(e, e'p)(A-1)$ experiments were conducted at several accelerator facilities. These experiments revealed the depletion of the independent particle states just beneath the Fermi level in comparison to predictions made by the genuine shell model. The theoretical answer in this matter was the introduction of spectroscopic factors having a value of around 0.6 instead of 1 for the valence states. A spectroscopic factor gives the probability of finding a nucleon in a particular state within the nucleus. Short- as well as long-range correlations were called into play to explain these features. With the advent of the proof of existence of strong correlations, the naive shell-model picture of the nucleus had to be adjusted. Several techniques were introduced to implement the correlations in the wave function. In the previous chapter, a wave function for the ^{4}He nucleus is proposed, incorporating these features in a generic way.

Apart from nuclear structure effects also the possible reaction mechanisms are explored in the search to explain the quenching of the longitudinal response function. The aforementioned $A(e,e'p)(A-1)$ experiments revealed some other caveats in our description. In analogy to the $A(e,e')$ case also the $A(e,e'p)$ cross section can be rewritten in terms of structure functions. It became clear that theory could not fully account for all the structure functions at the same time [91] whenever energies above the two-particle emission threshold are probed. In 1990 Ulmer [90] conducted a ^{12}C$(e,e'p)$-experiment and extracted the longitudinal and transverse response as a function of missing energy (see Fig. III-2). The response functions reveal some distinctive behavior. At missing energies above 50 MeV the transverse and longitudinal response function evolve along different lines as indicated by the rise in the function $S_T - S_L$ around 30 MeV ($S_i = R_i/K\sigma_{ep}^{CC1}, i = T, L$ the reduced response, where K is a kinematical factor). This missing energy value coincides with the two-nucleon emission threshold alluding to some two-body current contributions in the transverse channel. These conclusions concerning the L/T separation reached in the ^{12}C$(e,e'p)$ experiments at Bates by Ulmer et al. have recently been confirmed in a ^{12}C$(e,e'p)$ experiment at Jefferson Lab [92].

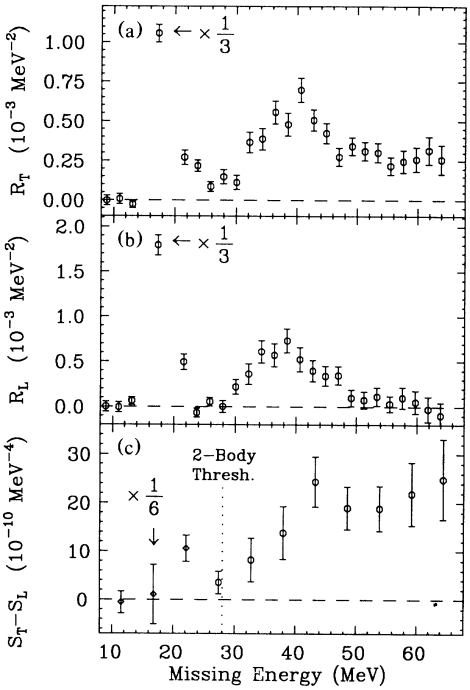

Figure III-2: *The missing-energy dependence of the longitudinal and transverse response functions for the $^{12}C(e,e'p)$ reaction at $q = 397$ MeV/c and $\omega = 122$ MeV [90].*

Also in the dip region a substantial amount of $A(e,e'p)$ strength is observed at high missing energies [93]. Models based on the IPM cannot account for this strength.

Summarizing, the semi-exclusive $A(e,e'p)$ data appear to advocate the need for many-body currents in addition to the dominant one body currents. An excellent tool to study the two-nucleon mechanisms are the two-nucleon knockout reactions $(e,e'NN)$ and (γ,NN). Due to the advent of high-duty cycle accelerators and the advances made in detector technology, two- and even threefold coincidence measurements (e.g. $^{12}C(\gamma,ppn)$ [94]) with e.m. probes came

within experimental reach. During the last decade several accelerator facilities have performed $(e, e'NN)$ and (γ, NN) experiments on a variety of target nuclei [95][96][97][12][98].

The various physical observables for the $(e, e'NN)$ and (γ, NN) reactions will be derived in the course of forthcoming sections. At the same time a detailed discussion of the current operators corresponding with the contributing electromagnetic reaction mechanism is included. The current operators will be, starting from an effective-field framework, derived in momentum space.

§2 Cross section

§2.1 Scattering matrix and cross section

The scattering matrix describes the evolution of a system from an initial ($t = -\infty$) into a final ($t = +\infty$) asymptotic state. Over the years, it became common practice to define the scattering matrix in the interaction or Dirac picture. This picture has the advantage of allowing to discriminate between the free evolution of the fields and the distortions attributable to the interactions. The latter picture is convenient with the eye on performing a perturbation expansion. In what follows, we adopt the interaction picture. The scattering matrix $\hat{S}$ reads

$$S_{fi} = \left\langle \Phi_f | \hat{S} | \Phi_i \right\rangle \quad ,$$

with

$$\begin{aligned} \hat{S} &= e^{-\frac{i}{\hbar}\int d^4x \hat{\mathcal{H}}_{int}(x)} \\ &= \sum_{n=0}^{\infty} \frac{1}{n!} (-\frac{i}{\hbar})^n \int d^4x_1 \ldots \int d^4x_n T(\hat{\mathcal{H}}_{int}(x_1) \ldots \hat{\mathcal{H}}_{int}(x_n)) \ , \end{aligned} \quad \text{(III-1)}$$

where, Φ_i and Φ_f are the initial and final non-interacting states, while $\hat{\mathcal{H}}_{int}(x)$ denotes the electromagnetic interaction Hamiltonian. In the one-photon exchange approximation, only the first two terms of Eq. (III-1) are taken into account :

$$S_{fi} \to \delta_{fi} - \frac{i}{\hbar} \left\langle \Phi_f \right| \int d^4x \hat{\mathcal{H}}_{int}(x) \left| \Phi_i \right\rangle \quad \text{(III-2)}$$

The electromagnetic interaction Hamiltonian has the following general form

$$\hat{\mathcal{H}}_{int}(x) = \hat{J}^{\mu}_N(x) \hat{A}^{\gamma}_{\mu}(x) \ , \quad \text{(III-3)}$$

with $\hat{J}_N(x)$ and $\hat{A}^{\gamma}(x)$ respectively the nuclear current and the electromagnetic field associated with real or virtual photon exchange. A cross section contains all features of a general scattering process $1 + 2 \to 3 + 4 + \ldots$.
Three elements have to be introduced before a general expression for the cross

section can be derived. First, using translational invariance a typical operator in Minkowski space $\hat{O}(x)$ can be rewritten as $e^{-i\hat{P}x/\hbar}\hat{O}(0)e^{i\hat{P}x/\hbar}$ and every wave function has to be a 4-momentum eigenstate. Second, in a volume V the number of momentum final states (normal modes) in the range defined by $[\vec{k}, \vec{k}+d\vec{k}]$ equals $Vd^3\vec{k}/(2\pi)^3$. Third, the momentum eigenstates are to be normalized properly. To do so in an unambiguous way we will derive the cross section in a box. Therefore each wave function ψ has to be replaced by

$$\psi_V \;=\; [(2\pi)^3/V]^{1/2}\psi \quad . \tag{III-4}$$

In the one-photon exchange approximation the scattering matrix defined in a box of volume V looks like :

$$\begin{aligned} S_{fi}^V &= \delta_{fi} - \frac{i}{\hbar}\int_V d^4x e^{-i(K_N^f - K_N^i - q_{\gamma^*})x}\left[\frac{(2\pi)^3}{V}\right]^{N/2}\left\langle \Phi_f\middle|\hat{J}_N^\mu(0)\hat{A}_\mu^\gamma(0)\middle|\Phi_i\right\rangle\left[\frac{(2\pi)^3}{V}\right]^{2/2} \\ &= \delta_{fi} - \frac{i}{\hbar}VT\delta^3_{\vec{K}_N^f,\vec{K}_N^i+\vec{q}_{\gamma^*}}\delta_{\Omega_N^f,\Omega_N^i+\omega_{\gamma^*}}\left[\frac{(2\pi)^3}{V}\right]^{(N+2)/2} M_{fi}\;, \end{aligned} \tag{III-5}$$

where, N is the number of particles in the final channel. The momentum and energy of the c.o.m motion in respectively the initial and final state is denoted by $(\vec{K}_N^i, \Omega_N^i)$ and $(\vec{K}_N^f, \Omega_N^f)$. The transition matrix element $M_{fi} = \left\langle \Phi_f|\hat{J}_N^\mu(0)\hat{A}_\mu^\gamma(0)|\Phi_i\right\rangle$ contains all the dynamical features of the reaction process under study. In Eq. (III-5) we replaced Φ_f^V and Φ_i^V by their renormalized versions (see Eq. III-4). The transition rate is proportional to the squared scattering matrix and reads

$$\begin{aligned} d\Gamma_{fi}^V &= \frac{|S_{fi}^V|^2}{T}\times\prod_{n=1}^N\frac{V}{(2\pi)^3}d^3\vec{k}_n^f \\ &= \left[\frac{(2\pi)^3}{V}\right]^2\frac{V^2T}{\hbar^2}\delta^3_{\vec{K}_N^f,\vec{K}_N^i+\vec{q}_{\gamma^*}}\delta_{\Omega_N^f,\Omega_N^i+\omega_{\gamma^*}}|M_{fi}|^2\prod_{n=1}^N d\vec{k}_n^f\;. \end{aligned} \tag{III-6}$$

To arrive at the transition rate, the squared scattering matrix was multiplied with the density of final states ($\vec{k}^f$ are the momenta of the outgoing particles). Eventually, the cross section is defined as the transition rate per incoming flux. In a non-relativistic approximation, the incoming flux can be written as $\phi = v_{\rm rel}/V$, with $v_{\rm rel}$ the relative velocity of the projectile to the target. In a relativistic treatment, the relative velocity is given by

$$v_{\rm rel} \;=\; c\sqrt{(p_t.p_p)^2 - m_t^2c^2m_p^2c^2}/[(E_t/c).(E_p/c)] \quad ,$$

with (p_t, m_t, E_t) and (p_p, m_p, E_p) denoting the target and projectile variables. The differential scattering cross section reads

$$d\sigma_{fi} \;=\; \lim_{V,T\to\infty}\frac{d\Gamma_{fi}^V}{\phi}\quad .$$

$$
\begin{aligned}
d\sigma_{fi} &= \lim_{V,T\to\infty}\left[\frac{(2\pi)^3}{V}\right]^2 \frac{\frac{E_p}{c}\frac{E_t}{c}V}{\hbar^2 c\sqrt{(p_t.p_p)^2 - m_t^2c^2m_p^2c^2}} \\
&\qquad \times V^2 T\delta^3_{\vec{K}_N^f,\vec{K}_N^i+\vec{q}_{\gamma^*}}\delta_{\Omega_N^f,\Omega_N^i+\omega_{\gamma^*}}|M_{fi}|^2\prod_{n=1}^{N}d\vec{k}_n^f \\
&= (2\pi)^{10}\delta^4(K_N^f - K_N^i - q_{\gamma^*})\frac{\frac{E_p}{c}\frac{E_t}{c}}{\hbar^2 c\sqrt{(p_t.p_p)^2 - m_t^2c^2m_p^2c^2}}|M_{fi}|^2\prod_{n=1}^{N}d\vec{k}_n^f
\end{aligned}
\tag{III-7}
$$

where use has been made of the identity

$$
\lim_{V,T\to\infty}\delta_V^p\delta_T^E \to \frac{(2\pi)^4}{VT}\delta^3(p)\delta(E)\ . \tag{III-8}
$$

In the one-photon exchange approximation, the photon and nuclear parts of the squared transition matrix element can be separated

$$
\begin{aligned}
|M_{fi}|^2 &= |\left\langle \Psi_f^N\middle|\hat{J}_N^\mu(0)\hat{A}_\mu^\gamma(0)\middle|\psi_i^\gamma,\Psi_i^N\right\rangle|^2 \\
&= |J_N^\mu A_\mu^\gamma|^2 \\
&= \Gamma_{\mu\nu}W^{\mu\nu}\ ,
\end{aligned}
\tag{III-9}
$$

with, $J_N^\mu = \left\langle \Psi_f^N\middle|\hat{J}_N^\mu(0)\middle|\Psi_i^N\right\rangle$ and $A_\mu^\gamma = \left\langle 0\middle|\hat{A}_\mu^\gamma(0)\middle|\psi_i^\gamma\right\rangle$. The electromagnetic ($\Gamma_{\mu\nu}$) and hadronic ($W_{\mu\nu}$) tensor are products of the expectation values

$$
\Gamma_{\mu\nu} = A_\mu^\gamma[A_\nu^\gamma]^\dagger \tag{III-10}
$$

and

$$
W^{\mu\nu} = J_N^\mu[J_N^\nu]^\dagger\ . \tag{III-11}
$$

In the following subsections we will derive expressions for the electromagnetic tensor for the particular case of electro- and photo-induced four-body breakup of ^{4}He.

§2.1.1 $(\vec{e},e'\vec{N}N)$ Cross section

Fig. III-3 displays the four-body breakup reaction $^4\mathrm{He}(e,e'NN)NN$. The incoming electron has an energy E_e, momentum $\vec{p}_e$ and spin projection s_e. The outgoing electron has energy $E_{e'}$, momentum $\vec{p}_{e'}$ and spin projection $s_{e'}$. Absorption of the virtual photon $(E_\gamma,\vec{p}_\gamma)$ leads to the breakup of the entire nucleus, resulting in four escaping nucleons of which two are detected. The latter are denoted as nucleon "one" and "two". One refers to the peculiar situation that

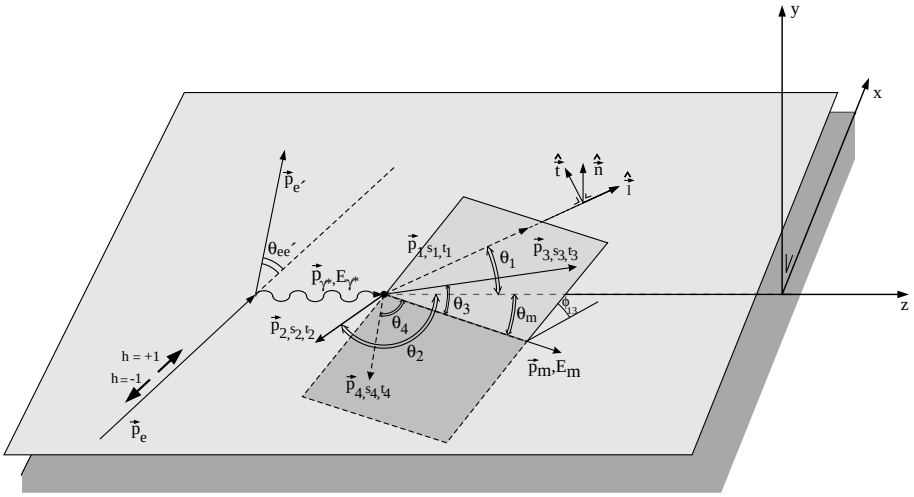

Figure III-3: *Pictorial representation of the kinematical variables used to describe the $^4He(e,e'NN)NN$ cross section in coplanar kinematics.*

both ejected nucleons are detected in the electron scattering plane as coplanar kinematics. The conventions adopted to denote the outgoing nucleon energies, momenta, spin and isospin projections are displayed in Fig. III-3.

Now, we shall derive the electromagnetic tensor for the specific case of electron scattering. In terms of classical source theory, the electromagnetic field generated by the electron current $\hat{j}^e_\mu(x)$ (i.e. the Möller potential) is a solution of the following differential equation

$$\begin{aligned} \Box A^{\gamma^*}_\mu(x) &= -e\mu_0 \left\langle f \left| \hat{j}^e_\mu(x) \right| i \right\rangle \quad (e>0) \\ &= -\frac{ec\mu_0}{(2\pi)^3} e^{i(k^f_e - k^i_e)x} \bar{u}(\vec{k}^f_e, m_{s_f}) \gamma_\mu u(\vec{k}^i_e, m_{s_i}) \; . \end{aligned} \tag{III-12}$$

This equation can be solved for the electromagnetic field using a Greens' function technique :

$$\begin{aligned} A^{\gamma^*}_\mu(x) &= -\frac{ec\mu_0}{(2\pi)^3} \bar{u}(\vec{k}^f_e, m_{s_f}) \gamma_\mu u(\vec{k}^i_e, m_{s_i}) \int d^4y G(x-y) e^{i(k^f_e - k^i_e)y} \quad , \\ &= \frac{ec\mu_0}{(2\pi)^3} e^{i(k^f_e - k^i_e)x} \frac{\bar{u}(\vec{k}^f_e, m_{s_f}) \gamma_\mu u(\vec{k}^i_e, m_{s_i})}{(k^f_e - k^i_e)^2} \; , \end{aligned} \tag{III-13}$$

with, μ_0 the permeability of vacuum and

$$G(x-y) = -\frac{1}{(2\pi)^4} \int d^4k \frac{e^{-ik(x-y)}}{k^2} \quad .$$

Inserting this expression for the electromagnetic field into $\Gamma_{\mu\nu}$ and putting $x = 0$, leads to the definition of the leptonic tensor :

$$\begin{aligned}\Gamma_{\mu\nu} &= \left[\frac{ec\mu_0}{(2\pi)^3}\right]^2 \frac{1}{(k_e^f - k_e^i)^4}\Big(\bar{u}(\vec{k}_e^f, m_{s_f})\gamma_\mu u(\vec{k}_e^i, m_{s_i})\Big)^\dagger.\Big(\bar{u}(\vec{k}_e^f, m_{s_f})\gamma_\nu u(\vec{k}_e^i, m_{s_i})\Big) \\ &= \left[\frac{ec\mu_0}{(2\pi)^3}\right]^2 \frac{1}{(k_e^f - k_e^i)^4} L_{\mu\nu} \ , \end{aligned} \tag{III-14}$$

where, $L_{\mu\nu}$ is the lepton tensor. The lepton tensor for the most general case of incoming and outgoing electron polarization, is derived in Appendix C -3, and reads, in the ultra-relativistic limit :

$$L_{\mu\nu} = \frac{2c^2}{4E_e^f E_e^i}\left\{(p_e^f)_\mu(p_e^i)_\nu + (p_e^f)_\nu(p_e^i)_\mu - g_{\mu\nu}(p_e^f.p_e^i) + ih\epsilon_{\mu\nu\alpha\beta}(p_e^f)^\alpha(p_e^i)^\beta\right\} \ , \tag{III-15}$$

with, h the electron helicity (initial helicity = final helicity) and $\epsilon^{\mu\nu\rho\sigma}$ the Levi-Civita tensor defined as follows : $\epsilon^{0123} = 1$.
Relying on the above expression for the lepton tensor, it is convenient to reformulate the contraction of the lepton and hadron tensor in a spherical basis.

$$\begin{aligned} & L_{\mu\nu}W^{\mu\nu} \\ &= \frac{2c^2}{4E_e^f E_e^i}\Big\{(p_e^f)_\mu(p_e^i)_\nu + (p_e^f)_\nu(p_e^i)_\mu - g_{\mu\nu}(p_e^f.p_e^i) + ih\epsilon_{\mu\nu\alpha\beta}(p_e^f)^\alpha(p_e^i)^\beta\Big\} W^{\mu\nu} \\ &= \left[\cos\frac{\theta_{ee'}}{2}\right]^2 e^2c^2\Big\{v_L W_L + v_T W_T + v_{LT} W_{LT} + v_{TT} W_{TT} + \\ &\qquad\qquad h\left(v'_{LT} W'_{LT} + v'_{TT} W'_{TT}\right)\Big\} \ , \end{aligned} \tag{III-16}$$

where, the common factor ec has been extracted from the nuclear current and

the different lepton and hadron structure functions read :

$$
\begin{aligned}
v_L &= \left[\frac{p^\mu_\gamma c p_{\gamma_\mu} c}{|\vec{p}_\gamma c|^2}\right]^2 & W_L &= \rho\,[\rho]^\dagger \\
v_T &= \left[\left[\tan\frac{\theta_{ee'}}{2}\right]^2 - \frac{1}{2}\frac{p^\mu_\gamma c p_{\gamma_\mu} c}{|\vec{p}_\gamma c|^2}\right] & W_T &= \left[\vec{J}_-\left[\vec{J}_-\right]^\dagger + \vec{J}_+\left[\vec{J}_+\right]^\dagger\right] \\
& & &= \left[\vec{J}_x\left[\vec{J}_x\right]^\dagger + \vec{J}_y\left[\vec{J}_y\right]^\dagger\right] \\
v_{LT} &= \frac{p^\mu_\gamma c p_{\gamma_\mu} c}{\sqrt{2}|\vec{p}_\gamma c|^3}\left(E^i_e + E^f_e\right)\tan\frac{\theta_{ee'}}{2} & W_{LT} &= 2\Re\left[[\rho]^\dagger\,\vec{J}_- - [\rho]^\dagger\,\vec{J}_+\right] \\
& & &= 2\sqrt{2}\Re\left[[\rho]^\dagger\,\vec{J}_x\right] \\
v_{TT} &= \frac{p^\mu_\gamma c p_{\gamma_\mu} c}{2|\vec{p}_\gamma c|^2} & W_{TT} &= 2\Re\left[\vec{J}_+\left[\vec{J}_-\right]^\dagger\right] \\
& & &= -\left(\vec{J}_x\left[\vec{J}_x\right]^\dagger - \vec{J}_y\left[\vec{J}_y\right]^\dagger\right) \\
v'_{LT} &= \frac{p^\mu_\gamma c p_{\gamma_\mu} c}{|\vec{p}_\gamma c|^2\sqrt{2}}\tan\frac{\theta_{ee'}}{2} & W'_{LT} &= -2\Re\left[[\rho]^\dagger\,\vec{J}_+ + [\rho]^\dagger\,\vec{J}_-\right] \\
& & &= -2\sqrt{2}\Im\left[[\rho]^\dagger\,\vec{J}_y\right] \\
v'_{TT} &= \frac{E^i_e + E^f_e}{|\vec{p}_\gamma|c}\left[\tan\frac{\theta_{ee'}}{2}\right]^2 & W'_{TT} &= \left[\vec{J}_+\left[\vec{J}_+\right]^\dagger - \vec{J}_-\left[\vec{J}_-\right]^\dagger\right] \\
& & &= 2\Im\left[\vec{J}_x\left[\vec{J}_y\right]^\dagger\right]
\end{aligned}
\qquad \text{(III-17)}
$$

where, use has been made of the conservation of nuclear current and the ultra-relativistic limit ($m_e/E_e \to 0$) has been adopted. Further, the electron scattering plane is chosen as the xz-plane.

With the transition matrix of Eq. (III-9) and the lepton tensor of Eq. (III-15), the general N-particle knockout cross section of Eq. (III-7) reduces to the following form for the electro-induced two-nucleon knockout reaction in the LAB-frame

$$
\begin{aligned}
d^9\sigma &= \int_3 d^3\vec{k}_3 \int_4 d^3\vec{k}_4 (2\pi)^4 \delta^4(k_1 + k_2 + k_3 + k_4 + k^f_e - K_{^4He} - k^i_e) \\
&\quad \frac{\frac{E^i_e}{c}\frac{E_{4_{He}}}{c}}{c\sqrt{(p^i_e . p_{4_{He}})^2 - m^2_e c^2 m^2_{^4He} c^2}} \left[\frac{ec\mu_0}{\hbar(k^f_e - k^i_e)^2}\right]^2 L_{\mu\nu} W^{\mu\nu} d^3\vec{k}^f_e d^3\vec{k}_1 d^3\vec{k}_2 \\
&= (2\pi)^4 \int d^2\Omega_3 \frac{|\vec{k}_3| E_3}{\hbar c^2} f^{-1}_{rec} \frac{E^i_e}{|\vec{p}^{\,i}_e| c^2} \left[\frac{ec\mu_0}{\hbar(k^f_e - k^i_e)^2}\right]^2 L_{\mu\nu} W^{\mu\nu} d^3\vec{k}^f_e d^3\vec{k}_1 d^3\vec{k}_2 \,, \qquad \text{(III-18)}
\end{aligned}
$$

where the flux has been evaluated in the LAB-frame. In the LAB-frame the flux:

$$
\frac{\frac{E^i_e}{c}\frac{E_{4_{He}}}{c}}{c\sqrt{(p^i_e . p_{4_{He}})^2 - m^2_e c^2 m^2_{^4He} c^2}}
$$

reduces to

$$\frac{E_e^i}{|\vec{p}_e^{\,i}|c^2} \ .$$

The recoil factor f_{rec} is derived in Appendix C-4 and reads

$$f_{rec} \ = \ \left| 1 + \frac{E_3}{E_4}(1 - \frac{|\vec{p}_m| \cos{(\theta_{3m})}}{|\vec{p}_3|}) \right| \ , \tag{III-19}$$

where the missing momentum $\vec{p}_m$ is defined as $\vec{p}_m = \vec{p}_e^{\,i} - \vec{p}_e^{\,f} - \vec{p}_1 - \vec{p}_2$. In the ultra-relativistic limit, one has $E_e \approx |\vec{p}_e|c$. With this substitution and Eq. (III-16), the final expression for the nine-fold differential electro-induced two nucleon knockout cross section reads :

$$\frac{d^9\sigma}{d|\vec{k}_1|d^2\Omega_1 d|\vec{k}_2|d^2\Omega_2 d|\vec{k}_e^{\,f}|d^2\Omega_e} = (2\pi)^4 \int d^2\Omega_3 f_{rec}^{-1} \frac{e^4c^4\mu_0^2}{16\hbar c {E_e^i}^2 \left[\sin\frac{\theta_{ee'}}{2}\right]^4} \left[\cos\frac{\theta_{ee'}}{2}\right]^2$$
$$\times |\vec{k}_1|^2|\vec{k}_2|^2|\vec{k}_3| E_3 \Big\{ v_L W_L + v_T W_T + v_{LT} W_{LT} + v_{TT} W_{TT} + h\,(v'_{LT} W'_{LT} + v'_{TT} W'_{TT}) \Big\} \ , \tag{III-20}$$

when inserting the Mott cross section :

$$\left(\frac{d\sigma}{d\Omega}\right)_M = \frac{(\alpha\hbar c Z)^2 \left[\cos\frac{\theta_{ee'}}{2}\right]^2}{4{E_e^i}^2 \left[\sin\frac{\theta_{ee'}}{2}\right]^4} \ ,$$

with $\alpha = e^2\mu_0 c/4\pi\hbar \approx 1/137$ in Eq. (III-20) the differential cross section takes on the following form :

$$\frac{d^9\sigma}{d|\vec{k}_1|d^2\Omega_1 d|\vec{k}_2|d^2\Omega_2 d|\vec{k}_e^{\,f}|d^2\Omega_e} = \frac{(2\pi)^6}{4\hbar c} \left(\frac{d\sigma}{d\Omega}\right)_M \int d^2\Omega_3 f_{rec}^{-1} |\vec{k}_1|^2|\vec{k}_2|^2|\vec{k}_3| E_3$$
$$\times \Big\{ v_L W_L + v_T W_T + v_{LT} W_{LT} + v_{TT} W_{TT} + h\,(v'_{LT} W'_{LT} + v'_{TT} W'_{TT}) \Big\} \ . \tag{III-21}$$

§2.1.2 $(\vec{\gamma}, \vec{N}N)$ Cross section

The photo-induced four-body breakup reaction is sketched in Fig. III-4. For the hadronic kinematical variables we adopt the same conventions as for the complementary electro-induced reaction. With a real photon beam only the transverse part of the nuclear current can be probed whereas an electron beam is also sensitive to the longitudinal nuclear current. Because nature is gauge invariant it does not matter what gauge we choose to do our calculations in. From now on we will use the Coulomb or physical gauge ($A_0 = 0$ and $\vec{\nabla}.\vec{A} = 0$) which keeps only

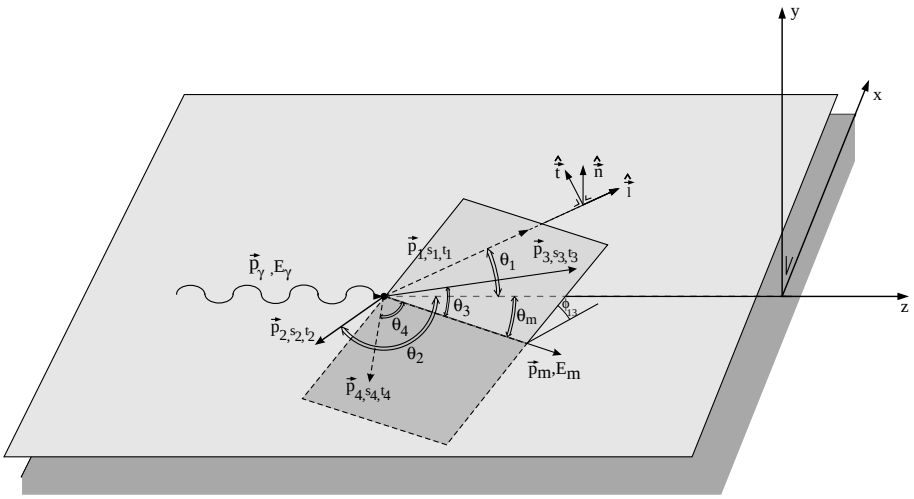

Figure III-4: *Photo-induced four-body breakup* $^4He(\gamma, NN)NN$ *in coplanar kinematics.*

the physically relevant degrees of freedom. The electromagnetic field is defined by the following expression :

$$A^\mu = (0, \vec{A}) \tag{III-22}$$

$$\vec{A} = \sum_{\vec{q},r} N_{\vec{q}} \Big\{ \vec{\epsilon}_r(\vec{q}) \hat{a}(\vec{q}, r) e^{-iqx} + \vec{\epsilon}_r(\vec{q})^* \hat{a}(\vec{q}, r)^\dagger e^{iqx} \Big\} , \tag{III-23}$$

where, $N_{\vec{q}} = \sqrt{\frac{\hbar\mu_0 c^2}{2\omega_\gamma (2\pi)^3}}$ denotes the normalization constant while the $\hat{a}(\vec{q}, r)$ are annihilation operators for a photon with momentum $\vec{q}$ and polarization denoted by r. The $\vec{\epsilon}_r(\vec{q})$ vectors with $r = 1, 2$ constitute a polarization basis which spans the plane perpendicular to $\vec{k}$ as required by the Coulomb gauge condition $\vec{\nabla} \cdot \vec{A} = 0$.
Concerning the polarization vectors, two different basis sets are in use namely a linear and circular basis. In both cases the photon propagates along the z-axis. With this choice one gets

$$\text{linear basis :} \quad \vec{\epsilon}_{r=1,2} = (\vec{e}_x, \vec{e}_y)$$

$$\text{circular basis :} \quad \vec{\epsilon}_{r=\pm} = (\vec{e}_+ = -\tfrac{1}{\sqrt{2}}(\vec{e}_x + i\vec{e}_y), \vec{e}_- = \tfrac{1}{\sqrt{2}}(\vec{e}_x - i\vec{e}_y))$$

Irrespective of the choices made regarding the polarization basis, the electromagnetic tensor reduces to

$$\Gamma^{ij} = \frac{\hbar\mu_0 c^2}{2\omega_\gamma (2\pi)^3} [(\vec{\epsilon}_r)^i]^* (\vec{\epsilon}_r)^j . \tag{III-24}$$

As in the electron case, one can evaluate the contraction between the photonic and hadronic tensors in the spherical basis. The final expressions depend on whether one deals with linearly or circularly polarized photons.

For a linearly polarized photon beam

$$\begin{aligned}\Gamma_{\mu\nu}W^{\mu\nu} &= \frac{\hbar\mu_0 c^2}{2\omega_\gamma(2\pi)^3}[(\vec{\epsilon}_r)_i]^*(\vec{\epsilon}_r)_j W^{ij} \\ &= \frac{\hbar\mu_0 e^2 c^4}{4\omega_\gamma(2\pi)^3}\left(W_T + (-1)^r W_{TT}\right) \quad (r=1,2)\,; \end{aligned} \tag{III-25}$$

For a circularly polarized photon beam

$$\begin{aligned}\Gamma_{\mu\nu}W^{\mu\nu} &= \frac{\hbar\mu_0 c^2}{2\omega_\gamma(2\pi)^3}[(\vec{\epsilon}_r)_i]^*(\vec{\epsilon}_r)_j W^{ij} \\ &= \frac{\hbar\mu_0 e^2 c^4}{4\omega_\gamma(2\pi)^3}\left(W_T + r W'_{TT}\right)\,, \end{aligned} \tag{III-26}$$

with, $r \in \{-1,+1\}$. In deriving Eqs. (III-25) and (III-26) the factor ec has been extracted from the expression for the nuclear current. The nuclear response functions W_T, W_{TT} and W'_{TT} are defined in Eqs. (III-17) and are also part of the electro-induced two nucleon knockout cross section.

After inserting Eq. (III-24), the photo-induced two nucleon knockout cross section becomes

$$d^6\sigma = \int_3 d^3\vec{k}_3 \int_4 d^3\vec{k}_4 (2\pi)^{10}\delta^4(K_N^f - K_N^i - q_\gamma)\frac{1}{\hbar^2 c}\frac{\hbar\mu_0 c^2}{2\omega_\gamma(2\pi)^3}[\vec{\epsilon}_r^{\,i}]^*\vec{\epsilon}_r^{\,j} W_{ij} d^3\vec{k}_1 d^3\vec{k}_2\,, \tag{III-27}$$

where the photon flux is equal to c/V.
Discriminating between both photon polarizations and replacing $[\vec{\epsilon}_r^{\,i}]^*\vec{\epsilon}_r^{\,j}W_{ij}$ by the relations (III-25) and (III-26) gives rise to the following expressions for the differential cross sections :

For linearly polarized photons ($r = 1, 2$)

$$\frac{d^6\sigma}{d|\vec{k}_1|d^2\Omega_1 d|\vec{k}_2|d^2\Omega_2} = (2\pi)^8\frac{\alpha}{2E_\gamma}\int d^2\Omega_3 |\vec{k}_1|^2|\vec{k}_2|^2|\vec{k}_3|E_3 f_{rec}^{-1}\left(W_T + (-1)^r W_{TT}\right) \tag{III-28}$$

For circularly polarized photons ($h = \pm$)

$$\frac{d^6\sigma}{d|\vec{k}_1|d^2\Omega_1 d|\vec{k}_2|d^2\Omega_2} = (2\pi)^8\frac{\alpha}{2E_\gamma}\int d^2\Omega_3 |\vec{k}_1|^2|\vec{k}_2|^2|\vec{k}_3|E_3 f_{rec}^{-1}\left(W_T + h W'_{TT}\right)\,, \tag{III-29}$$

with, f_{rec}^{-1} defined by Eq. (III-19).

§2.2 The hadronic tensor

In this subsection, a general expression for the hadronic tensor will be derived for the specific reaction with two ejected nucleons in the final channel, one of them being polarized. The kinematical variables of Fig. III-3 and III-4 hint at the symmetry constraints which the hadronic tensor has to obey. The hadronic tensor is a hermitian, second rank Lorentz tensor which has to satisfy gauge invariance and parity conservation and is at most linear in the spin of one of the outgoing nucleons [99][100]. The hadronic tensor $W_{\mu\nu}$ receives contributions from vectors that combine the Levi-Civita tensor with five four-vectors belonging to $\{p_\gamma, p_1, s_1, p_2, p_A\}$. The manifold of possible four-vectors has as cardinal number 15. A possible representation looks like :

$$\begin{aligned}
&\Big\{\ p_\gamma^\mu,\ p_1^\mu,\ s_1^\mu,\ p_2^\mu,\ p_A^\mu,\\
&\zeta_1^\mu = \epsilon^{\mu\nu\rho\sigma}(p_\gamma)_\nu(p_1)_\rho(p_2)_\sigma,\\
&\zeta_2^\mu = \epsilon^{\mu\nu\rho\sigma}(p_\gamma)_\nu(p_1)_\rho(p_A)_\sigma,\\
&\zeta_3^\mu = \epsilon^{\mu\nu\rho\sigma}(p_\gamma)_\nu(p_1)_\rho(s_1)_\sigma,\\
&\zeta_4^\mu = \epsilon^{\mu\nu\rho\sigma}(p_\gamma)_\nu(p_2)_\rho(p_A)_\sigma,\\
&\zeta_5^\mu = \epsilon^{\mu\nu\rho\sigma}(p_\gamma)_\nu(p_2)_\rho(s_1)_\sigma,\\
&\zeta_6^\mu = \epsilon^{\mu\nu\rho\sigma}(p_\gamma)_\nu(p_A)_\rho(s_1)_\sigma,\\
&\zeta_7^\mu = \epsilon^{\mu\nu\rho\sigma}(p_1)_\nu(p_2)_\rho(p_A)_\sigma,\\
&\zeta_8^\mu = \epsilon^{\mu\nu\rho\sigma}(p_1)_\nu(p_2)_\rho(s_1)_\sigma,\\
&\zeta_9^\mu = \epsilon^{\mu\nu\rho\sigma}(p_1)_\nu(p_A)_\rho(s_1)_\sigma,\\
&\zeta_{10}^\mu = \epsilon^{\mu\nu\rho\sigma}(p_2)_\nu(p_A)_\rho(s_1)_\sigma\Big\}\ .
\end{aligned} \tag{III-30}$$

As the Minkowski space is four-dimensional, only four linearly independent four-vectors out of (III-30) are required to decompose a general four-vector (i.e., $p_\gamma^\mu, p_1^\mu, p_2^\mu, \zeta_1^\mu$). The hadronic tensor can be decomposed using these four four-vectors. Regarding the previously mentioned constraints i.e. gauge invariance, parity conservation and linearity in the spin coordinate, the following expressions for the hadronic tensor emerge:

$$W^{\mu\nu} = W_S^{\mu\nu} + W_A^{\mu\nu} \tag{III-31}$$

$$\begin{aligned}
W_S^{\mu\nu} &= W_1 G^{\mu\nu} + W_2 V_1^\mu V_1^\nu + W_3[V_1, V_2]_+^{\mu\nu} + W_4 V_2^\mu V_2^\nu + \\
&\quad \bar{W}_5[V_1, \zeta_1]_+^{\mu\nu} + \bar{W}_6[V_2, \zeta_1]_+^{\mu\nu}
\end{aligned} \tag{III-32}$$

$$W_A^{\mu\nu} = W_7[V_1, V_2]_-^{\mu\nu} + \bar{W}_8[V_1, \zeta_1]_-^{\mu\nu} + \bar{W}_9[V_2, \zeta_1]_-^{\mu\nu}\ , \tag{III-33}$$

with, $G^{\mu\nu} = g^{\mu\nu} - p_\gamma^\mu p_\gamma^\nu / p_\gamma^2$ and $V_i^\mu = p_i^\mu - (p_i.p_\gamma)p_\gamma^\mu / p_\gamma^2$. These combinations of p_γ, p_1 and p_2 are introduced to ensure gauge invariance. The hadronic tensor is the sum of a symmetric ($W_S^{\mu\nu}$) and anti-symmetric ($W_A^{\mu\nu}$) term. The W_i and $\bar{W}_i$ are hadronic structure functions depending on scalar and pseudo-scalar variables

constructed with the four-vectors of manifold (III-30). The W_i structure functions are scalar quantities while the $\bar{W}_i$ are pseudo-scalars. In order to further expand the structure functions, we first need to define the possible Lorentz scalars and pseudo-scalars with the four-vectors of manifold (III-30) :

$$\begin{aligned} \text{Scalar :} \quad & \{p_\gamma^2,\, p_\gamma.p_1,\, p_\gamma.p_2,\, p_\gamma.p_A,\, p_1.p_2,\, p_1.p_A,\, p_2.p_A, \\ & \qquad \zeta_1.s_1,\, \zeta_2.s_1,\, \zeta_4.s_1,\, \zeta_7.s_1\} \qquad \text{(III-34)} \\ \text{Pseudo-scalar :} \quad & \{p_\gamma.s_1,\, p_2.s_1,\, p_A.s_1,\, \zeta_1.p_A\}\ . \qquad \text{(III-35)} \end{aligned}$$

Using these scalar and pseudo-scalar quantities and remembering that the structure functions depend at most linear on s_1, we can rewrite them as follows :

$$\begin{aligned} W_x &= F_x^0 + F_x^1\zeta_1.s_1 + F_x^2\zeta_2.s_1 + F_x^3\zeta_4.s_1 + F_x^4\zeta_7.s_1 \qquad \text{(III-36)} \\ \bar{W}_x &= \bar{F}_x^1 p_\gamma.s_1 + \bar{F}_x^2 p_2.s_1 + \bar{F}_x^3 p_A.s_1 \qquad \text{(III-37)} \end{aligned}$$

Each of the newly introduced functions F_x and $\bar{F}_x$ is a function of seven scalar (i.e. $\{p_\gamma^2,\, p_\gamma.p_1,\, p_\gamma.p_2,\, p_\gamma.p_A,\, p_1.p_2,\, p_1.p_A,\, p_2.p_A\}$) and one pseudo-scalar (i.e. $\zeta_1.p_A$) quantities. These variables can be reexpressed in the laboratory reference system using the kinematical variables as they were defined in Figs. III-3 and III-4.

$$\begin{aligned} p_\gamma^2 &= \frac{E_\gamma^2}{c^2} - |\vec{p}_\gamma|^2 \\ p_\gamma.p_1 &= \frac{E_\gamma.E_1}{c^2} - |\vec{p}_\gamma||\vec{p}_1|\cos\theta_1 \\ p_\gamma.p_2 &= \frac{E_\gamma.E_2}{c^2} - |\vec{p}_\gamma||\vec{p}_2|\cos\theta_2 \\ p_\gamma.p_A &= E_\gamma.M_A \\ p_1.p_2 &= \frac{E_1.E_2}{c^2} - |\vec{p}_1|.|\vec{p}_2|(\sin\theta_1\sin\theta_2\cos(\phi_1-\phi_2) + \cos\theta_1\cos\theta_2) \\ p_1.p_A &= E_1.M_A \\ p_2.p_A &= E_2.M_A \\ \zeta_1.p_A &= -\vec{p}_\gamma.(\vec{p}_1\times\vec{p}_2)M_A\ . \qquad \text{(III-38)} \end{aligned}$$

From these expressions one can infer that the hadronic structure functions F and $\bar{F}$ depend on $(|\vec{p}_\gamma|, E_\gamma, |\vec{p}_1|, \theta_1, |\vec{p}_2|, \theta_2, \phi_{12} = \phi_1 - \phi_2)$ but not on the azimuthal angle $\Phi = \frac{\phi_1+\phi_2}{2}$, assigned to the COM of the two ejectiles "1" and "2".

Also expressions for the spin-dependent expansion variables of the structure functions can be derived

$$\begin{aligned} \zeta_1.s_1 &= -\vec{p}_\gamma.(\vec{p}_1\times\vec{p}_2).s_0 + \left[\frac{E_\gamma}{c}(\vec{p}_1\times\vec{p}_2) - \frac{E_1}{c}(\vec{p}_\gamma\times\vec{p}_2) + \frac{E_2}{c}(\vec{p}_\gamma\times\vec{p}_1)\right] \\ &\quad \times\left(\vec{s}_1 + \frac{(\vec{s}_1.\vec{p}_1 c).\vec{p}_1 c}{m_N c^2(E_1 + m_N c^2)}\right) \qquad \text{(III-39)} \end{aligned}$$

$$\zeta_2.s_1 = M_A c^2(\vec{p}_\gamma \times \vec{p}_1).\vec{s}_1 \quad \text{(III-40)}$$

$$\zeta_4.s_1 = M_A c^2(\vec{p}_\gamma.\vec{p}_2).\left(\vec{s}_1 + \frac{(\vec{s}_1.\vec{p}_1 c).\vec{p}_1 c}{m_N c^2(E_1 + m_N c^2)}\right) \quad \text{(III-41)}$$

$$\zeta_7.s_1 = M_A c^2(\vec{p}_1 \times \vec{p}_2).\vec{s}_1 \quad \text{(III-42)}$$

$$p_\gamma.s_1 = \frac{E_\gamma.s_0}{c} - \vec{p}_\gamma.\left(\vec{s}_1 + \frac{(\vec{s}_1.\vec{p}_1 c).\vec{p}_1 c}{m_N c^2(E_1 + m_N c^2)}\right) \quad \text{(III-43)}$$

$$p_2.s_1 = \frac{E_2.s_0}{c} - \vec{p}_2.\left(\vec{s}_1 + \frac{(\vec{s}_1.\vec{p}_1 c).\vec{p}_1 c}{m_N c^2(E_1 + m_N c^2)}\right) \quad \text{(III-44)}$$

$$p_A.s_1 = \frac{M_A c^2.s_0}{c}\ . \quad \text{(III-45)}$$

Making use of the unity vectors ($\vec{e}_l = \vec{p}_1/|\vec{p}_1|$, $\vec{e}_n = (\vec{p}_\gamma \times \vec{p}_1)/|\vec{p}_\gamma \times \vec{p}_1|$, $\vec{e}_t = (\vec{p}_1 \times \vec{e}_n)/|\vec{p}_1 \times \vec{e}_n|$), the expansion variables derived in Eqs. (III-39)-(III-45) read in coplanar kinematics

$$\zeta_1.s_1 \rightarrow \vec{e}_n.\vec{s}_1 \quad \text{(III-46)}$$

$$\zeta_2.s_1 \rightarrow \vec{e}_n.\vec{s}_1 \quad \text{(III-47)}$$

$$\zeta_4.s_1 \rightarrow \vec{e}_n.\vec{s}_1 \quad \text{(III-48)}$$

$$\zeta_7.s_1 \rightarrow \vec{e}_n.\vec{s}_1 \quad \text{(III-49)}$$

$$p_\gamma.s_1 \rightarrow \vec{e}_l.\vec{s}_1 + \vec{e}_t.\vec{s}_1 \quad \text{(III-50)}$$

$$p_2.s_1 \rightarrow \vec{e}_l.\vec{s}_1 + \vec{e}_t.\vec{s}_1 \quad \text{(III-51)}$$

$$p_A.s_1 \rightarrow \vec{e}_l.\vec{s}_1\ . \quad \text{(III-52)}$$

A further simplification for the special case of super-parallel kinematcs, where the two nucleons are ejected along the direction of the momentum transfer $\vec{p}_\gamma$ ([101])

$$\zeta_1.s_1 \rightarrow 0 \quad \text{(III-53)}$$

$$\zeta_2.s_1 \rightarrow 0 \quad \text{(III-54)}$$

$$\zeta_4.s_1 \rightarrow 0 \quad \text{(III-55)}$$

$$\zeta_7.s_1 \rightarrow 0 \quad \text{(III-56)}$$

$$p_\gamma.s_1 \rightarrow \vec{e}_l.\vec{s}_1 \quad \text{(III-57)}$$

$$p_2.s_1 \rightarrow \vec{e}_l.\vec{s}_1 \quad \text{(III-58)}$$

$$p_A.s_1 \rightarrow \vec{e}_l.\vec{s}_1\ . \quad \text{(III-59)}$$

From now on, we will restrict ourselves to coplanar kinematics unless otherwise specified. With the aid of the expressions for the structure functions (Eqs. III-36 and III-37) and their specific spin dependence (Eqs. III-46 - III-52), the symmetric and anti-symmetric hadronic tensor (Eqs. III-32 and III-33) read :

$$W_S^{\mu\nu} = [F_1 + F_1^n \vec{e}_n.\vec{s}_1]G^{\mu\nu} + [F_2 + F_2^n \vec{e}_n.\vec{s}_1]V_1^\mu V_1^\nu + [F_3 + F_3^n \vec{e}_n.\vec{s}_1][V_1, V_2]_+^{\mu\nu} +$$

$$
\begin{aligned}
& [F_4 + F_4^n \vec{e}_n.\vec{s}_1]V_2^\mu V_2^\nu + [F_5^l \vec{e}_l.\vec{s}_1 + F_5^t \vec{e}_t.\vec{s}_1][V_1, \zeta_1]_+^{\mu\nu} + \\
& [F_6^l \vec{e}_l.\vec{s}_1 + F_6^t \vec{e}_t.\vec{s}_1][V_2, \zeta_1]_+^{\mu\nu} \qquad \text{(III-60)} \\
W_A^{\mu\nu} \;=\; & [F_7 + F_7^n \vec{e}_n.\vec{s}_1][V_1, V_2]_-^{\mu\nu} + [F_8^l \vec{e}_l.\vec{s}_1 + F_8^t \vec{e}_t.\vec{s}_1][V_1, \zeta_1]_-^{\mu\nu} + \\
& [F_9^l \vec{e}_l.\vec{s}_1 + F_9^t \vec{e}_t.\vec{s}_1][V_2, \zeta_1]_-^{\mu\nu} \;, \qquad \text{(III-61)}
\end{aligned}
$$

where all of the 18 functions $F_i^x (i = 1, 9, x = l, n, t)$ are scalar functions of the variables $(|\vec{p}_\gamma|, E_\gamma, |\vec{p}_1|, \theta_1, |\vec{p}_2|, \theta_2, \phi_{12} = \phi_1 - \phi_2)$.

In what follows, we will rewrite the hadronic tensor in a spherical basis. This formulation is more suitable to describe the interaction with the electromagnetic field. A definition of the spherical basis in terms of the Cartesian frame of reference is contained in Appendix B -2. Due to hermiticity and gauge invariance constraints, the number of independent elements of the hadronic tensor reduces from 16 to only 6, namely W_S^{00}, W_S^{01}, W_S^{02}, W_S^{11}, W_S^{12}, W_S^{22}. Whereas for the symmetric case only 4 independent elements remain leaving just two anti-symmetric structure functions. Reformulated in a spherical basis, the 6 components read :

$$
\begin{aligned}
W_L &= W_S^{00} && \text{(III-62)} \\
W_T &= -(W_S^{+-} + W_S^{-+}) && \text{(III-63)} \\
W_{LT} &= W_S^{0-} - W_S^{0+} && \text{(III-64)} \\
W_{TT} &= -(W_S^{--} + W_S^{++}) && \text{(III-65)} \\
W'_{LT} &= W_A^{0+} + W_A^{0-} && \text{(III-66)} \\
W'_{TT} &= W_A^{+-} - W_A^{-+} \;, && \text{(III-67)}
\end{aligned}
$$

with, $W^{\lambda\lambda'} = W \cdot [\vec{e}_\lambda \otimes \vec{e}_{\lambda'}]$.
The different terms of the hadronic tensor, Eqs. (III-32) and (III-33), contribute to some or more of the response functions, Eqs. (III-62) - (III-67), as can be observed from Appendix B -5.

From Eqs. (B-24) - (B-29) it can be observed that the response functions W_L, W_T and W'_{TT} do not depend on the average azimuthal angle $\Phi = (\phi_1 + \phi_2)/2$ while W_{LT} and W'_{LT} are a function of Φ whereas W_{TT} contains 2Φ as a functional variable. In coplanar kinematics the response functions (B-24) - (B-29) can be rewritten, using Eq. (III-60) and Eq. (III-61), as follows :

$$
\begin{aligned}
W_L(E_\gamma, |\vec{p}_\gamma|, |\vec{p}_1|, \theta_1, |\vec{p}_2|, \theta_2, \phi_{12}) &= R_L + R_L^n \vec{e}_n.\vec{s}_1 && \text{(III-68)} \\
W_T(E_\gamma, |\vec{p}_\gamma|, |\vec{p}_1|, \theta_1, |\vec{p}_2|, \theta_2, \phi_{12}) &= R_T + R_T^n \vec{e}_n.\vec{s}_1 && \text{(III-69)} \\
W_{LT}(E_\gamma, |\vec{p}_\gamma|, |\vec{p}_1|, \theta_1, |\vec{p}_2|, \theta_2, \phi_{12}, \Phi) &= R_{LT} + R_{LT}^n \vec{e}_n.\vec{s}_1 && \text{(III-70)} \\
W_{TT}(E_\gamma, |\vec{p}_\gamma|, |\vec{p}_1|, \theta_1, |\vec{p}_2|, \theta_2, \phi_{12}, 2\Phi) &= R_{TT} + R_{TT}^n \vec{e}_n.\vec{s}_1 && \text{(III-71)} \\
W'_{LT}(E_\gamma, |\vec{p}_\gamma|, |\vec{p}_1|, \theta_1, |\vec{p}_2|, \theta_2, \phi_{12}, \Phi) &= {R'_{LT}}^l \; \vec{e}_l.\vec{s}_1 + {R'_{LT}}^t \; \vec{e}_t.\vec{s}_1 && \text{(III-72)} \\
W'_{TT}(E_\gamma, |\vec{p}_\gamma|, |\vec{p}_1|, \theta_1, |\vec{p}_2|, \theta_2, \phi_{12}) &= {R'_{TT}}^l \; \vec{e}_l.\vec{s}_1 + {R'_{TT}}^t \; \vec{e}_t.\vec{s}_1 && \text{(III-73)}
\end{aligned}
$$

where, in super-parallel kinematics only those terms survive which do not depend on the spin and which depend on the longitudinal spin component only.

$$
\begin{aligned}
W_L(E_\gamma,|\vec{p}_\gamma|,|\vec{p}_1|,\theta_1,|\vec{p}_2|,\theta_2,\phi_{12}) &= R_L && \text{(III-74)}\\
W_T(E_\gamma,|\vec{p}_\gamma|,|\vec{p}_1|,\theta_1,|\vec{p}_2|,\theta_2,\phi_{12}) &= R_T && \text{(III-75)}\\
W_{LT}(E_\gamma,|\vec{p}_\gamma|,|\vec{p}_1|,\theta_1,|\vec{p}_2|,\theta_2,\phi_{12},\Phi) &= R_{LT} && \text{(III-76)}\\
W_{TT}(E_\gamma,|\vec{p}_\gamma|,|\vec{p}_1|,\theta_1,|\vec{p}_2|,\theta_2,\phi_{12},2\Phi) &= R_{TT} && \text{(III-77)}\\
W'_{LT}(E_\gamma,|\vec{p}_\gamma|,|\vec{p}_1|,\theta_1,|\vec{p}_2|,\theta_2,\phi_{12},\Phi) &= {R'_{LT}}^{\,l}\ \vec{e}_l.\vec{s}_1 && \text{(III-78)}\\
W'_{TT}(E_\gamma,|\vec{p}_\gamma|,|\vec{p}_1|,\theta_1,|\vec{p}_2|,\theta_2,\phi_{12}) &= {R'_{TT}}^{\,l}\ \vec{e}_l.\vec{s}_1\ , && \text{(III-79)}
\end{aligned}
$$

To finish this section, an important property of the hadronic tensor will be derived. It translates the principle of parity conservation and time symmetry into a symmetry for the hadronic tensor. The influence of the previous symmetries can be studied starting from the general expression for the nuclear electromagnetic tensor $W^{\mu\nu}$:

$$
\begin{aligned}
W^{\mu\nu}(p_\gamma,P,p_1,s_1,p_2,(-)) &= \sum_F \Big\langle p_1,s_1,p_2,s_2,p_3,s_3,p_4,s_4,(-)\Big|(\hat{J}^\mu(p_\gamma))^\dagger\Big|I,P\Big\rangle\\
&\quad\times\Big\langle I,P\Big|\hat{J}^\nu(p_\gamma)\Big|p_1,s_1,p_2,s_2,p_3,s_3,p_4,s_4,(-)\Big\rangle\ , \qquad \text{(III-80)}
\end{aligned}
$$

where, the sum over F implies an integration over the momenta of the third and fourth particle and in addition a sum over the spin projection of nucleons two, three and four. The minus sign, showing up in the final state wave function, refers to the fact that the final waves evolve outward. The initial state has four-momentum P and is non-degenerate in case of the ^{4}He-ground state making it a parity eigenstate due to the space reflection invariance of the strong interaction. First we will examine the transformation properties of the nuclear tensor under a parity transformation $\mathcal{P}$. Inserting the identity $\mathcal{P}^{-1}\mathcal{P}$ in Eq. (III-80) gives rise to the following relation :

$$
\begin{aligned}
&W^{\mu\nu}(p_\gamma,P,p_1,s_1,p_2,(-))\\
&= \sum_F \Big\langle p_1,s_1,p_2,s_2,p_3,s_3,p_4,s_4,(-)\Big|\mathcal{P}^{-1}\left[\mathcal{P}\hat{J}^\mu(p_\gamma)\mathcal{P}^{-1}\right]^\dagger\mathcal{P}\Big|I,P\Big\rangle\\
&\qquad\times\Big\langle I,P\Big|\mathcal{P}^{-1}\left[\mathcal{P}\hat{J}^\nu(p_\gamma)\mathcal{P}^{-1}\right]\mathcal{P}\Big|p_1,s_1,p_2,s_2,p_3,s_3,p_4,s_4,(-)\Big\rangle\\
&= g_{\mu\mu}g_{\nu\nu}\sum_F \Big\langle p'_1,-s'_1,p'_2,s_2,p_3,s_3,p_4,s_4,(-)\Big|\hat{J}^\mu(p'_\gamma)^\dagger\Big|I,P'\Big\rangle\\
&\qquad\times\Big\langle I,P'\Big|\hat{J}^\nu(p'_\gamma)\Big|p'_1,-s'_1,p'_2,s_2,p_3,s_3,p_4,s_4,(-)\Big\rangle\\
&= g_{\mu\mu}g_{\nu\nu}W^{\mu\nu}(p'_\gamma,P',p'_1,-s'_1,p'_2,(-))\ , \qquad \text{(III-81)}
\end{aligned}
$$

where, we did not indicate the transformed values of the momenta and spins of the second, third and fourth particle because they are summed over a complete basis. The primed four-vectors are the space reflected counterparts of the original ones and are in more detail given by the expression $x' = (x_0, -\vec{x})$. The nuclear current operator is a four-vector and transforms as such giving rise to the coefficients $g_{\alpha\alpha} = \pm$. The nuclear current operator as well as the momentum four-vectors transform the same way under a time reflection $\mathcal{T}$. Therefore the previously derived expression for the hadronic tensor (Eq. (III-81)) becomes :

$$\begin{aligned}
&W^{\mu\nu}(p_\gamma, P, p_1, s_1, p_2, (-)) \\
&= \sum_F \left\langle p_1', -s_1', p_2', s_2, p_3, s_3, p_4, s_4, (-) \middle| \mathcal{T}\hat{J}^\mu(p_\gamma)^\dagger \mathcal{T}^{-1} \middle| I, P' \right\rangle \\
&\qquad \times \left\langle I, P' \middle| \mathcal{T}\hat{J}^\nu(p_\gamma)\mathcal{T}^{-1} \middle| p_1', -s_1', p_2', s_2, p_3, s_3, p_4, s_4, (-) \right\rangle \\
&= \sum_F \left\langle p_1, -s_1, p_2, s_2, p_3, s_3, p_4, s_4, (+) \middle| \hat{J}^\nu(p_\gamma)^\dagger \middle| I, P \right\rangle \\
&\qquad \times \left\langle I, P | \hat{J}^\mu(p_\gamma) | p_1, -s_1, p_2, s_2, p_3, s_3, p_4, s_4, (+) \right\rangle \\
&= W^{\nu\mu}(p_\gamma, P, p_1, -s_1, p_2, (+)) \; , \qquad \text{(III-82)}
\end{aligned}$$

the interchange of the indices (μ, ν) is invoked by the anti-linearity of the time reflection operator. In addition this property causes the interchange of the in going and outgoing evolution operator resulting in the replacement of retarded wave solution with an advanced wave solution. In the plane wave limit the differences between the in going and outgoing solutions can be ignored resulting in the relation :

$$W^{\mu\nu}(p_\gamma, P, p_1, s_1, p_2) = W^{\nu\mu}(p_\gamma, P, p_1, -s_1, p_2) \; . \qquad \text{(III-83)}$$

From Eq. (III-83) one can draw as general conclusion in a plane wave approximation : any terms linear in spin must vanish in the symmetric part of the tensor and any terms not linear in the spin must vanish in the anti-symmetric part of the tensor.

Combining this theorem with the expression of the nuclear electromagnetic tensor in coplanar kinematics results in the final expressions for the nuclear response functions :

$$\begin{aligned}
W_L(E_\gamma, |\vec{p}_\gamma|, |\vec{p}_1|, \theta_1, |\vec{p}_2|, \theta_2, \phi_{12}) &= R_L & \text{(III-84)} \\
W_T(E_\gamma, |\vec{p}_\gamma|, |\vec{p}_1|, \theta_1, |\vec{p}_2|, \theta_2, \phi_{12}) &= R_T & \text{(III-85)} \\
W_{LT}(E_\gamma, |\vec{p}_\gamma|, |\vec{p}_1|, \theta_1, |\vec{p}_2|, \theta_2, \phi_{12}, \Phi) &= R_{LT} & \text{(III-86)} \\
W_{TT}(E_\gamma, |\vec{p}_\gamma|, |\vec{p}_1|, \theta_1, |\vec{p}_2|, \theta_2, \phi_{12}, 2\Phi) &= R_{TT} & \text{(III-87)} \\
W'_{LT}(E_\gamma, |\vec{p}_\gamma|, |\vec{p}_1|, \theta_1, |\vec{p}_2|, \theta_2, \phi_{12}, \Phi) &= R'_{LT}{}^{l}\vec{e}_l.\vec{s}_1 + R'_{LT}{}^{t}\vec{e}_t.\vec{s}_1 & \text{(III-88)} \\
W'_{TT}(E_\gamma, |\vec{p}_\gamma|, |\vec{p}_1|, \theta_1, |\vec{p}_2|, \theta_2, \phi_{12}) &= R'_{TT}{}^{l}\vec{e}_l.\vec{s}_1 + R'_{TT}{}^{t}\vec{e}_t.\vec{s}_1 \; , & \text{(III-89)}
\end{aligned}$$

while,in super parallel kinematics, the side-ways polarized components of the W'_{LT} and W'_{TT} structure functions disappear also as indicated above.

§3 Polarization observables

As alluded to in section §1, as of now no theoretical model appears to be able to simultaneously describe the longitudinal and the transverse (e, e') nuclear response (for light nuclei the authors of Ref. [102] claim to have succeeded in describing both response functions). In an attempt to solve this shortcoming one should focus on the exclusive and semi-exclusive counterparts of the inclusive experiments. Those reactions offer better opportunities to study the single and multi-nucleon contributions to the inclusive cross section. Studying the unpolarized photo- and electro-induced multi-nucleon knockout reaction, will provide detailed information on the features of the principal mechanisms driving the reaction. Complementary to the multi-coincidence measurements, polarization experiments can help to elucidate the role played by the subnuclear degrees of freedom and their contributions to the nine structure functions. Due to the dramatic fall off of the reaction rates, coincidence and polarization experiments became only feasible with the advent of high duty cycle accelerators and a new generation of detectors. Polarization observables have the advantage of being rather insensitive to various kinds of corrections which are an essential ingredient of a typical data analysis. In subsections §3.1 and §3.2 we review the different polarization observables for electro- and photo-induced two-nucleon knockout reactions.

§3.1 $(\vec{e}, e'\vec{N}N)$-polarization observables

For a 0^+ target nucleus, one can consider three types of measurements involving a polarized beam and the possibility to determine one of the ejectile's polarization : first, a two-nucleon knockout reaction induced by a polarized electron beam $((\vec{e}, e'NN))$; second, the polarization of one ejectile is detected $((e, e'\vec{N}N))$ and third, the polarization transfer is measured $((\vec{e}, e'\vec{N}N))$. The electron, being ultra-relativistic, is spontaneously polarized along its propagation direction. The nucleon spin, though, can in principle be directed along any axis in three dimensional space. The nucleon polarization basis is usually attached to its rest frame (= baryocentric basis).

$$\vec{e}_l = \frac{\vec{p}}{|\vec{p}|} \tag{III-90}$$

$$\vec{e}_n = \frac{\vec{p}_\gamma \times \vec{p}}{|\vec{p}_\gamma \times \vec{p}|} \tag{III-91}$$

$$\vec{e}_t = \frac{\vec{p} \times \vec{e}_n}{|\vec{p} \times \vec{e}_n|} \, . \tag{III-92}$$

The polarization vectors are displayed in Figs. III-3 and III-4.
The seventh structure function W_7 (Eq. III-33) can be extracted from the cross section by measuring the electron polarization. The $(\vec{e}, e'NN)$-experiments can determine the so-called electron analyzing power A_e defined as

$$A_e \;=\; \frac{\sigma(h=+1)-\sigma(h=-1)}{\sigma(h=+1)+\sigma(h=-1)}\;. \tag{III-93}$$

As becomes obvious from Eqs. (B-28) and (B-29) a non-vanishing value for the electron analyzing power requires an out-of-plane experiment. In addition, our discussion about the transformation properties of the nuclear electromagnetic tensor under a space-time reflection reveals that in a plane-wave approximation (PWA) the analyzing power will always vanish as a plane-wave doesn't depend on the nuclear spin. Therefore, the A_e variable is an excellent tool to study the spin-dependence of final state interactions (FSI).

Alternatively, one can measure the outgoing nucleon polarization instead of the electron helicity ($(e, e'\vec{N}N)$). To describe the hadron tensor for a polarized final nucleon, the nucleon spin vector has to be projected in the nucleon baryocentric basis defined in Eqs. (III-90) - (III-92). Three different polarization observables can be defined, i.e. the three induced polarizations $P_i (i = l, n, t)$:

$$P_i \;=\; \frac{\sigma(m_{s_i}=\uparrow)-\sigma(m_{s_i}=\downarrow)}{\sigma(m_{s_i}=\uparrow)+\sigma(m_{s_i}=\downarrow)} \qquad \text{(i=l,n,t)}\;. \tag{III-94}$$

In coplanar kinematics only the normal (n) component of the induced polarization is accessible. The latter can be inferred from equations III-68 - III-71. The longitudinal (l) and the transverse (t) induced polarization P_i can only be measured in an out-of-plane measurement (See Eqs. III-72 and III-73). A more stringent condition on the induced polarization is imposed by the FSI. Without FSI all three induced polarizations will be identical to zero. As for the electron analyzing power the nucleon induced polarization can give us a clue of the effects induced by FSI.

The only electron polarization observables which survive in the plane-wave approximation for the ejectiles, are the so-called polarization transfer coefficients (P'_l, P'_n, P'_t) lying along one of the three nucleon-polarization axes. To measure these one has to setup a double-polarization experiment $(\vec{e}, e'\vec{N}N)$. The $P'_i, (i = l, n, t)$ are defined according to :

$$P'_i = \frac{\Big(\sigma(h{=}+1,m_{s_i}{=}\uparrow)-\sigma(h{=}-1,m_{s_i}{=}\uparrow)\Big)-\Big(\sigma(h{=}+1,m_{s_i}{=}\downarrow)-\sigma(h{=}-1,m_{s_i}{=}\downarrow)\Big)}{\Big(\sigma(h{=}+1,m_{s_i}{=}\uparrow)+\sigma(h{=}-1,m_{s_i}{=}\uparrow)\Big)+\Big(\sigma(h{=}+1,m_{s_i}{=}\downarrow)+\sigma(h{=}-1,m_{s_i}{=}\downarrow)\Big)}\;. \tag{III-95}$$

In coplanar kinematics the normal polarization transfer observable P'_n vanishes while in super-parallel kinematics also the P'_t component vanishes.

Using Eqs. (III-93), (III-94) and (III-95), the doubly-polarized differential cross section can be casted into the form

$$\frac{d^9\sigma}{d|\vec{k}_1|d^2\Omega_1 d|\vec{k}_2|d^2\Omega_2 d|\vec{k}_e^{\,f}|d^2\Omega_e} = \frac{1}{2}\sigma_0\left[1+\vec{P}.\vec{\sigma}+h\left(A_e+\vec{P}'.\vec{\sigma}\right)\right] , \quad \text{(III-96)}$$

with, $\vec{\sigma}$ a unit vector in spin space. The unpolarized cross section σ_0 is obtained from Eq. (III-21) by summing over the electron and nucleon spin projections. For the peculiar of coplanar kinematics and neglecting all forms of FSI mechanisms, the above expression reduces to :

$$\frac{d^9\sigma}{d|\vec{k}_1|d^2\Omega_1 d|\vec{k}_2|d^2\Omega_2 d|\vec{k}_e^{\,f}|d^2\Omega_e} = \frac{1}{2}\sigma_0\left[1+h\left(\cos\theta_1 P_l'+\sin\theta_1 P_t'\right)\right] , \quad \text{(III-97)}$$

with, θ_1 approaching zero in super-parallel kinematics.

In the PWA some of the polarization observables mentioned to vanish in coplanar kinematics. We wish to stress that these properties are only valid under the condition of strict hermiticity of the employed current operators. Once the hermiticity condition is violated, by introducing a finite width for the in-medium delta for example, some of the statements made are to be softened.

§3.2 $(\vec{\gamma},\vec{N}N)$-polarization observables

For processes involving polarized photons, one can either start from a linear or from a circular photon polarization basis [103]. In the case of a linearly polarized beam, the photon asymmetry determines the difference in the nuclear response to a photon polarized in ($\sigma_{||}$) or perpendicular ($\sigma_\perp$) to the reaction plane

$$\Sigma_l = \frac{\sigma_{||}-\sigma_\perp}{\sigma_{||}+\sigma_\perp} = -\frac{W_{TT}}{W_T} . \quad \text{(III-98)}$$

For a circularly polarized incident photon, on the other hand, the asymmetry reflects the difference in cross section for the absorption of a left- ($\sigma(h=-1)$) or a right-handed ($\sigma(h=+1)$) photon

$$\Sigma_c = \frac{\sigma(h=+1)-\sigma(h=-1)}{\sigma(h=+1)+\sigma(h=-1)} = \frac{W'_{TT}}{W_T} . \quad \text{(III-99)}$$

In coplanar kinematics, only the linear asymmetry survives. Even in the PWA it does not vanish. An out-of-plane measurement is required to determine the circular asymmetry Σ_c. The circular asymmetry vanishes in any plane-wave model.

As for the electro-induced case, it is possible to define an induced polarization and a polarization transfer coefficient. The induced polarization ($P_i, (i=l,n,t)$), as defined in Eq. (III-94), looks identical in the photo- and electro-induced case. In coplanar kinematics, only the component perpendicular to the reaction plane

Reaction		out-of-plane DWIA	out-of-plane PWIA	in-plane DWIA	in-plane PWIA	super parallel DWIA	super parallel PWIA
$(\vec{e}, e'NN)$	A_e	X	0	0	0	0	0
$(e, e'\vec{N}N)$	P_l	X	0	0	0	0	0
	P_n	X	0	X	0	X	0
	P_t	X	0	0	0	0	0
$(\vec{e}, e'\vec{N}N)$	P'_l	X	X	X	X	X	X
	P'_n	X	X	0	0	0	0
	P'_t	X	X	X	X	0	0
$(\vec{\gamma}_l, NN)$	Σ_l	X	X	X	X	X	X
$(\vec{\gamma}_c, NN)$	Σ_c	X	0	0	0	0	0
$(\gamma, \vec{N}N)$	P_l	X	0	0	0	0	0
	P_n	X	0	X	0	X	0
	P_t	X	0	0	0	0	0
$(\vec{\gamma}_l, \vec{N}N)$	P'_l	X	0	0	0	0	0
	P'_n	X	0	X	0	X	0
	P'_t	X	0	0	0	0	0
$(\vec{\gamma}_c, \vec{N}N)$	P'_l	X	X	X	X	X	X
	P'_n	X	X	0	0	0	0
	P'_t	X	X	X	X	0	0

Table III-1: *The polarization observables for electromagnetically induced two-nucleon knockout under some specific kinematical and dynamical conditions. For each observable we indicate wether it will vanish (0) or not (X) under the specific conditions.*

has a value different from zero. In the plane-wave approximation for the outgoing nucleons also the component directed along $\vec{e}_n$ vanishes.

With a linearly polarized photon beam the transfer polarization coefficients $(P'_i, (i = l, n, t))$ look like :

$$P'_i = \frac{\left(\sigma_{||}(m_{s_i=\uparrow}) - \sigma_{\perp}(m_{s_i=\uparrow})\right) - \left(\sigma_{||}(m_{s_i=\downarrow}) - \sigma_{\perp}(m_{s_i=\downarrow})\right)}{\left(\sigma_{||}(m_{s_i=\uparrow}) - \sigma_{\perp}(m_{s_i=\uparrow})\right) + \left(\sigma_{||}(m_{s_i=\downarrow}) - \sigma_{\perp}(m_{s_i=\downarrow})\right)} \ . \quad \text{(III-100)}$$

Only the normal component is assessible in coplanar kinematics. To get access to P'_l and P'_t an out-of-plane measurement is required. In a plane wave approximation also the component normal to the scattering plane vanishes, making it a tool to probe the influence of FSI mechanisms on the reaction cross section. A totally different picture arises for the circularly polarized photon beam where the transfer polarization observable is defined as in Eq. (III-95). As for Eq. (III-95) the same conclusions can be drawn regarding the effects of selecting coplanar kinematics and of including FSI. In brief, in a PWA approximation only the longitudinal P'_l and transverse P'_t transfer polarization coefficients survive. Where the latter disappear in super parallel kinematics.

The differential cross sections can be rewritten in terms of the aforementioned polarization observables. We will restrict ourselves to the case of coplanar kinematics and for a plane-wave approximation. The differential cross sections look like :

For a linearly polarized photon

$$\frac{d^6\sigma(\vec{\gamma}, NN)}{d|\vec{k}_1|d^2\Omega_1 d|\vec{k}_2|d^2\Omega_2} = \frac{1}{2}\sigma_0 \left[1 + (-1)^h \Sigma_l\right] \ , \quad \text{(III-101)}$$

where, h equals 1 for a photon polarized in the reaction plane while it is equal to 2 in the case of a perpendicular polarized photon.

For a circularly polarized photon

$$\frac{d^6\sigma(\vec{\gamma}, NN)}{d|\vec{k}_1|d^2\Omega_1 d|\vec{k}_2|d^2\Omega_2} = \frac{1}{2}\sigma_0 \left[1 + h\left(\cos\theta_1 P'_l + \sin\theta_1 P'_t\right)\right] \ , \quad \text{(III-102)}$$

where h equals $+1$ for a right-handed photon and -1 for a left-handed one. θ_1 refers to the polar angle of the polarized ejectile.

The different polarization observables for several kinematical and dynamical situations are summarized in Table III-1.

§4 Two-nucleon knockout mechanisms

The ingredients determining the hadronic structure functions $W^{\mu\nu}$ are the nuclear initial and final wave functions and the nuclear electromagnetic current operator. Chapter II dealt with the initial ^{4}He wave function. All of the calculations

presented in this work are performed within the PWA for the ejectiles. The discussion of the implications of this approximation will be postponed until section §5. In this section we will derive the different terms contributing to the nuclear current and discuss the impact of electromagnetic and hadronic form factors as well as the role played by the short-range correlations.
Adopting an effective field formalism the nuclear current is rewritten as an expansion of Feynman diagrams. In an effectieve field theory the nucleons as well as the mesons are treated as elementary particles. To account for the internal structure of the hadrons, form factors are introduced. In an effective field theory one should start from the most general possible Lagrangian density consistent with the symmetries of the theory and expressed in terms of the relevant degrees of freedom. To plug the electromagnetic field into the nuclear effective lagrangian, use has been made of the minimal substitution method ($\partial_\mu \rightarrow \partial_\mu - iqA_\mu$). In the one-photon exchange approximation, it is straightforward to derive the nuclear current based on the effective lagrangian density. In our calculations, only the tree diagrams for the nuclear current are retained. All higher order diagrams are, on the one hand considered as final state interactions and on the other hand included in some sense in the initial state nuclear wave function. Summarized, apart from the common one-body convection- and magnetization current, lowest order meson exchange and delta excitation diagrams are included into the current operator.
Quantum electrodynamics being a gauge theory, the nuclear current operator has to fulfill the Ward-Takahashi identities or, equivalently, the nuclear current $< \hat{J}^\mu >$ is a conserved quantity.The latter condition constrains the longitudinal part of the nuclear current operator once the NN-potential is known, through the following relation :

$$\vec{q}_\gamma \cdot \hat{\vec{J}}_N = \left[\hat{\rho}_N, \hat{H}_{NN}\right] \ . \tag{III-103}$$

Apart from the model independent longitudinal current, the unconstraint transverse part of the nuclear current has to be derived on the basis of some microscopic model assumptions with respect tot the nuclear dynamics.

§4.1 Meson exchange currents

Our calculations implement the pion exchange currents [104]. Heavier meson exchange currents are neglected. These currents are suppressed by the short-range correlations which tend to keep the nucleons apart. Moreover, the theoretical description of short-range heavy-meson exchange is not free of ambiguities. The existence of pions in the nucleus as a natural explanation for the NN-force was already pointed out in the thirties by Yukawa. The exchange of a finite mass pion explains the long-range character of the NN-potential, as well as its tensorial component. The meson-exchange currents (MEC) consisting of the pion seagull

and in-flight terms, can be derived from the pion-nucleon interaction Lagrangian density

$$\begin{aligned}\mathcal{L}^{PV} &= \bar{\psi}(\not{p} - m_N c)\psi + \frac{1}{2}\partial_\mu\vec{\phi}.\partial^\mu\vec{\phi} - \frac{1}{2}\left(\frac{m_\pi c}{\hbar}\right)^2\vec{\phi}.\vec{\phi} + \\ &\quad \frac{g^{PV}_{\pi NN}}{m_\pi}\sqrt{\frac{\hbar^3}{c}}\bar{\psi}\gamma^\mu\gamma^5\partial_\mu(\vec{\phi}.\vec{\tau})\psi\ , \end{aligned} \tag{III-104}$$

where the pseudo-vector πNN coupling scheme has been adopted and the corresponding coupling constant is determined by $\left(g^{PV}_{\pi NN}\right)^2/4\pi = 0.079$.
The nuclear current induced by the pion-exchange graphs shown in Fig. III-5 can be obtained from the Lagrangian density $\mathcal{L}^{PV}$ by means of the minimal substitution technique : $\partial^\mu \to \partial^\mu + i\frac{q}{\hbar}A^\mu$ (with q the electromagnetic charge of the active particle). The resulting expression for the above Lagrangian density is

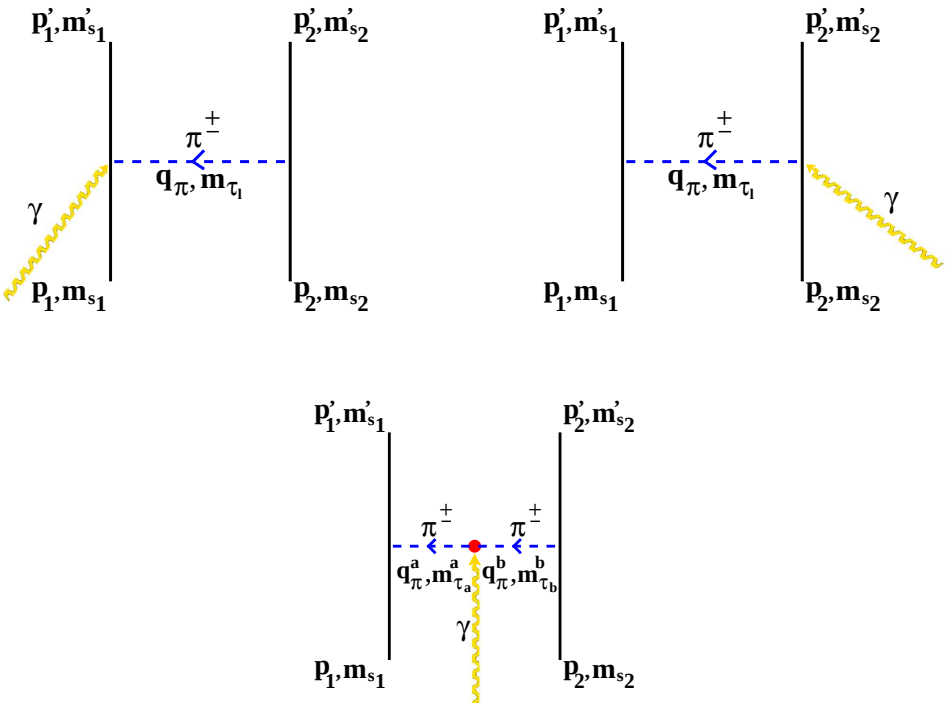

Figure III-5: *The pion seagull and in-flight diagrams.*

$$\begin{aligned}\mathcal{L}^{PV}_A &= \mathcal{L}^{PV} - \frac{e}{\hbar}\left(\vec{\phi}\times\partial_\mu\vec{\phi}\right)_z A^\mu - e\bar{\psi}\not{A}\frac{1+\tau_z}{2}\psi + \\ &\quad \frac{e}{\hbar}\frac{g^{PV}_{\pi NN}}{m_\pi}\sqrt{\frac{\hbar^3}{c}}\bar{\psi}\gamma^\mu\gamma^5\left(\vec{\tau}\times\vec{\phi}\right)_z\psi A_\mu\ , \end{aligned} \tag{III-105}$$

where, the quadratic terms in the electromagnetic field vector are neglected and with the elementary charge $e > 0$. After some algebra, one arrives at the following expressions for the pion seagull and in-flight current

$$\hat{J}^{\mu}_{seagull}(0) = iec\left(\frac{g^{PV}_{\pi NN}}{m_\pi c^2}\right)^2(\hbar c)^3\left(\frac{(\not{p}^{\,r}c\gamma^5)_{(2)}(\gamma^\mu\gamma^5)_{(1)}}{(p^r_2c)^2-m^2_\pi c^4}-\frac{(\not{p}^{\,r}c\gamma^5)_{(1)}(\gamma^\mu\gamma^5)_{(2)}}{(p^r_1c)^2-m^2_\pi c^4}\right) \times\left[\vec{\tau}_{(1)}\times\vec{\tau}_{(2)}\right]_z \quad \text{(III-106)}$$

$$\hat{J}^{\mu}_{in-flight}(0) = iec\left(\frac{g^{PV}_{\pi NN}}{m_\pi c^2}\right)^2(\hbar c)^3\frac{(\not{p}^{\,r}c\gamma^5)_{(1)}(\not{p}^{\,r}c\gamma^5)_{(2)}(p^r_2c-p^r_1c)^\mu}{((p^r_1c)^2-m^2_\pi c^4).((p^r_2c)^2-m^2_\pi c^4)}\left[\vec{\tau}_{(1)}\times\vec{\tau}_{(2)}\right]_z\ , \quad \text{(III-107)}$$

with, $p^r_1 = p^f_1 - p^i_1$ equal to the four-momentum transfer to particle 1 for example. In the absence of any relativistic description for the ^{4}He nucleus, it is convenient to use the non-relativistic limit of these currents. In the static and non-relativistic limit the current operators of Eqs. (III-106) and (III-107) reduce to :

$$\hat{\vec{J}}_{seagull}(0) = iec\left(\frac{g^{PV}_{\pi NN}}{m_\pi c^2}\right)^2(\hbar c)^3\left(\frac{\vec{\sigma}_{(1)}.\vec{p}^{\,r}_1c}{(\vec{p}^{\,r}_1c)^2+m^2_\pi c^4}.\vec{\sigma}_{(2)}-\vec{\sigma}_{(1)}.\frac{\vec{\sigma}_{(2)}.\vec{p}^{\,r}_2c}{(\vec{p}^{\,r}_2c)^2+m^2_\pi c^4}\right) \times\left[\vec{\tau}_{(1)}\times\vec{\tau}_{(2)}\right]_z \quad \text{(III-108)}$$

$$\hat{\vec{J}}_{in-flight}(0) = iec\left(\frac{g^{PV}_{\pi NN}}{m_\pi c^2}\right)^2(\hbar c)^3\frac{\vec{\sigma}_{(1)}.\vec{p}^{\,r}_1c}{(\vec{p}^{\,r}_1c)^2+m^2_\pi c^4}.\frac{\vec{\sigma}_{(2)}.\vec{p}^{\,r}_2c}{(\vec{p}^{\,r}_2c)^2+m^2_\pi c^4}.(\vec{p}^{\,r}_1c-\vec{p}^{\,r}_2c) \left[\vec{\tau}_{(1)}\times\vec{\tau}_{(2)}\right]_z\ , \quad \text{(III-109)}$$

where, the nucleon energy was replaced by the nucleon mass and the perturbation expansion was carried out up to lowest order in $\vec{p}/m$. By construction these currents obey current conservation for the nucleon charge density operator $\rho(\vec{r}) = \frac{1}{2}(1+\tau_z)e^{-i\vec{q}\cdot\vec{r}}$ and the one-pion exchange potential

$$V_{OPEP} = -\frac{g^{PV}_{\pi NN}}{m_\pi c^2}\sqrt{\frac{\hbar^3}{c}}\frac{\vec{\sigma}_{(1)}.\vec{p}_\pi\vec{\sigma}_{(2)}.\vec{p}_\pi}{p^2_\pi+m^2_\pi c^2}\vec{\tau}_{(1)}.\vec{\tau}_{(2)}\ .$$

In lowest non-relativistic order, the pion seagull and in-flight diagrams do not contribute to the charge density operator.

It is a common practice in non-renormalizable effective-field theories to introduce hadronic form factors $F_\pi(p^2_\pi)$ to effectively incorporate the physics at very-short distance scales. The hadronic form factors are purely phenomenological and are commonly assumed to be of a monopole form

$$F_\pi(p^2_\pi) = \frac{\Lambda^2_\pi - m^2_\pi c^2}{\vec{p}^{\,2}_\pi + \Lambda^2_\pi}\ .$$

The standard range for the values of the cut-off mass Λ_π is 800-1250 MeV/c. In practice, the inclusion of a form factor $F_\pi(p^2_\pi)$ amounts to neglecting all

high-momentum contributions to the transition matrix elements. The softer the form factor (i.e. the smaller the value of Λ_π) the lower the upper-limit in the momentum-space integrations. Both pion-exchange currents have to be altered, always reminding to preserve gauge invariance, and the following final expressions arise :

$$\hat{\vec{J}}_{seagull}(0) = iec\left(\frac{g^{PV}_{\pi NN}}{m_\pi c^2}\right)^2(\hbar c)^3\left(F_\pi(\vec{p}_1^{\,r})\frac{\vec{\sigma}_{(1)}.\vec{p}_1^{\,r}c}{(\vec{p}_1^{\,r}c)^2+m_\pi^2c^4}.\vec{\sigma}_{(2)} - \vec{\sigma}_{(1)}.F_\pi(\vec{p}_2^{\,r})\frac{\vec{\sigma}_{(2)}.\vec{p}_2^{\,r}c}{(\vec{p}_2^{\,r}c)^2+m_\pi^2c^4}\right)\left[\vec{\tau}_{(1)}\times\vec{\tau}_{(2)}\right]_z \tag{III-110}$$

$$\begin{aligned}\hat{\vec{J}}_{in-flight}(0) = {} & iec\left(\frac{g^{PV}_{\pi NN}}{m_\pi c^2}\right)^2(\hbar c)^3(\vec{\sigma}_{(1)}.\vec{p}_1^{\,r}c)\\ & \left(F_\pi(\vec{p}_1^{\,r})\frac{1}{(\vec{p}_1^{\,r}c)^2+m_\pi^2c^4}.F_\pi(\vec{p}_2^{\,r})\frac{1}{(\vec{p}_2^{\,r}c)^2+m_\pi^2c^4}+\right.\\ & F_\pi(\vec{p}_1^{\,r})\frac{1}{(\vec{p}_1^{\,r}c)^2+m_\pi^2c^4}.F_\pi(\vec{p}_2^{\,r})\frac{1}{(\vec{p}_1^{\,r}c)^2+\Lambda_\pi^2c^2}+\\ & \left.F_\pi(\vec{p}_1^{\,r})\frac{1}{(\vec{p}_2^{\,r}c)^2+\Lambda_\pi^2c^2}.F_\pi(\vec{p}_2^{\,r})\frac{1}{(\vec{p}_2^{\,r}c)^2+m_\pi^2c^4}\right)\\ & (\vec{\sigma}_{(2)}.\vec{p}_2^{\,r}c).(\vec{p}_1^{\,r}-\vec{p}_2^{\,r})\left[\vec{\tau}_{(1)}\times\vec{\tau}_{(2)}\right]_z\ ,\end{aligned} \tag{III-111}$$

In the actual calculations, the last two terms in the above expression for the pion-in-flight current have been neglected. The fast fall-off of the corrected pion-in-flight propagator justifies this approximation despite the fact that gauge invariance with respect to the pion exchange potential will be slightly violated.

§4.2 Delta isobar excitation

A meson-exchange current of a different kind is the isobar current (IC). This current is associated with the excitation of an intermediate delta Δ_{33} i.e. the spin and isospin $\frac{3}{2}$ excited state of the nucleon. The need for incorporating delta degrees-of-freedom in realistic models of the nucleus, was prompted by photo- and electro-pion production experiments showing a broad bump at a transferred energy equal to approximately the mass of the delta [105] [106]. Some properties of the delta particle are outlined in Appendix B-4. In contrast to pion-exchange currents, isobar currents are model dependent. Indeed gauge invariance does not constrain the delta current operator. As illustrated in Fig. III-6, the delta excitation current consists of two topologically different diagrams namely an s-channel (or, resonant diagram) and a u-channel (or, non-resonant diagram). In order to derive the delta current associated with the diagrams of Fig. III-6 one

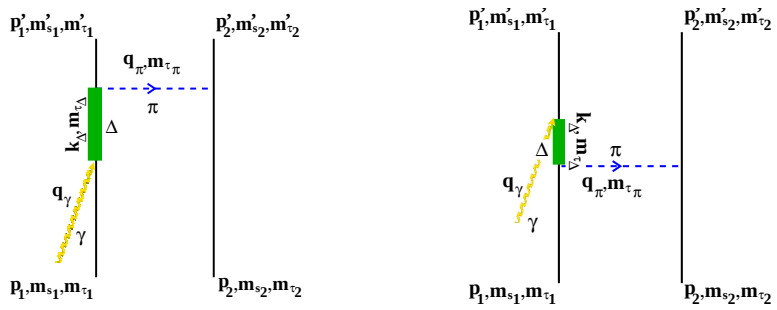

Figure III-6: *The resonant (left) and non-resonant (right) diagram which constitute the delta current.*

needs apart from the $\mathcal{L}_{\pi NN}$- also the $\mathcal{L}_{\gamma\Delta N}$ and $\mathcal{L}_{\pi N\Delta}$ Lagrangian densities :

$$\mathcal{L}_{\gamma\Delta N}(x) = -e\frac{\hbar f_{\gamma N\Delta}}{2m_\pi}\bar{\Psi}^\mu_\Delta(x)\epsilon^{\mu\nu\rho\sigma}\gamma^\sigma T_3^\dagger \partial^\nu A^\rho(x)\psi(x) + h.c. \quad \text{(III-112)}$$

$$\mathcal{L}_{\pi N\Delta}(x) = \frac{f_{\pi N\Delta}}{m_\pi}\sqrt{\frac{\hbar^3}{c}}\bar{\psi}(x)\partial_\mu(\vec{\phi}(x).\vec{T})\Psi^\mu_\Delta(x) + h.c.\,, \quad \text{(III-113)}$$

where, $\mathcal{L}_{\gamma\Delta N}$ is manifestly gauge invariant. The electromagnetic coupling constant $f_{\gamma N\Delta}$ equals 0.12 while the hadronic coupling constant is defined as $(f_{\pi N\Delta})^2/4\pi = 0.37$. Throughout this work, the small non-magnetic terms in the $\gamma\Delta N$ Lagrangian density will be neglected. As explained in more detail in Appendix B-4, the isospin projection operator $\vec{T}$ projects an isospin $\frac{3}{2}$-state on an isospin $\frac{1}{2}$-state. The $\pi N\Delta$-Lagrangian has been taken from Refs. [107] [108] where we only retained the on-shell part (discarding terms proportional to $\gamma_\mu\Psi^\mu_\Delta$) of the chiral invariant Lagrangian proposed by the authors of Refs. [107] [108]. In the static or non-relativistic limit, the interaction Lagrangian densities reduce to :

$$\mathcal{L}_{\pi NN}(x) \approx -\frac{g^{PV}_{\pi NN}}{m_\pi}\sqrt{\frac{\hbar^2}{c}}\psi^\dagger(x)\vec{\sigma}.\left[\vec{\nabla}\left(\vec{\phi}.\vec{\tau}\right)\right]\psi(x) \quad \text{(III-114)}$$

$$\mathcal{L}_{\gamma\Delta N}(x) \approx \frac{e\hbar}{2m_\pi}f_{\gamma N\Delta}\Psi^\dagger_\Delta(x)T_3^\dagger\vec{S}^\dagger.(\vec{\nabla}\times\vec{A}(x))\psi(x) + h.c. \quad \text{(III-115)}$$

$$\mathcal{L}_{\pi N\Delta}(x) \approx -\frac{f_{\pi N\Delta}}{m_\pi}\sqrt{\frac{\hbar^3}{c}}\Psi^\dagger_\Delta(x)\vec{S}^\dagger.\left[\vec{\nabla}\left(\vec{\phi}.\vec{T}^\dagger\right)\right]\psi(x) + h.c.\,, \quad \text{(III-116)}$$

where, use has been made of the non-relativistic expressions for the spin 1 (see Appendix B-4) and $\frac{1}{2}$ (see Appendix B-3) wave functions. The spin projection operator $\vec{S}$ appears in a natural way in the theory when taking the non-relativistic limit. The nucleon (ψ) and delta isobar (Ψ_Δ) wave functions, as they appear in Eqs. (III-114), (III-115) and (III-116), are reduced to their spin-isospin content

only :

$$\psi(x) = \sum\!\!\!\!\!\!\int \frac{d^3\vec{k}}{(2\pi)^{3/2}} a(\vec{k}) \chi_{(\frac{1}{2},m_s)} \eta_{(\frac{1}{2},m_t)} e^{-ikx} + h.c. \qquad \text{(III-117)}$$

$$\Psi_\Delta(x) = \sum\!\!\!\!\!\!\int \frac{d^3\vec{k}}{(2\pi)^{3/2}} a(\vec{k}) \chi_{(\frac{3}{2},m_{s_\Delta})} \eta_{(\frac{3}{2},m_{t_\Delta})} e^{-ikx} + h.c. \; . \qquad \text{(III-118)}$$

The final expression for the interaction Lagrangian which is needed to deduce the matrix elements associated with the diagrams depicted in Fig. III-6 reads :

$$\begin{aligned} \mathcal{L}_{int}(x) = & -\frac{g^{PV}_{\pi NN}}{m_\pi} \sqrt{\frac{\hbar^2}{c}} \psi^\dagger(x) \vec{\sigma}. \left[\vec{\nabla} \left(\vec{\phi}. \vec{\tau} \right) \right] \psi(x) + \\ & \frac{e\hbar}{2m_\pi} f_{\gamma N\Delta} \Psi^\dagger_\Delta(x) T_3^\dagger \vec{S}^\dagger . (\vec{\nabla} \times \vec{A}(x)) \psi(x) + h.c. \\ & -\frac{f_{\pi N\Delta}}{m_\pi} \sqrt{\frac{\hbar^3}{c}} \Psi^\dagger_\Delta(x) \vec{S}^\dagger . \vec{\nabla} \vec{\phi} . \vec{T}^\dagger \psi(x) + h.c. \; . \end{aligned} \qquad \text{(III-119)}$$

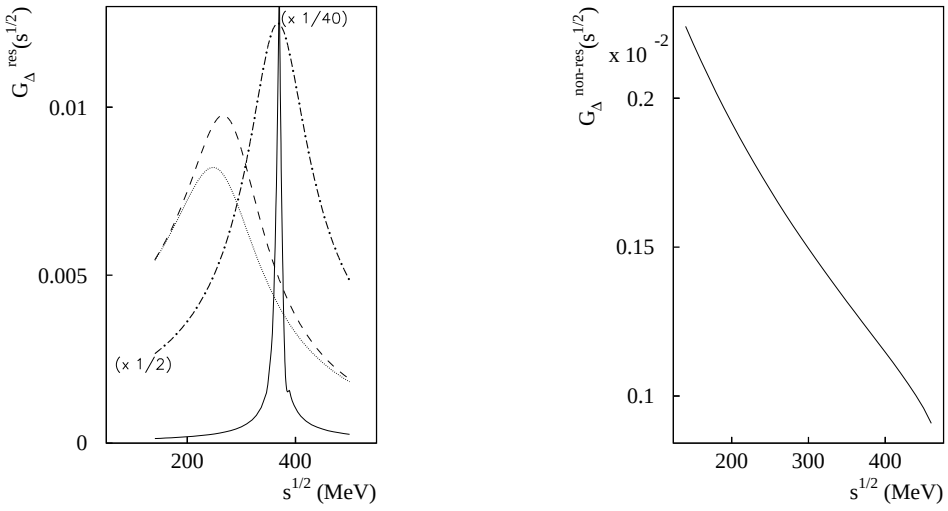

Figure III-7: *The left panel depicts the resonant delta propagator III-122 while in the right panel its non-resonant III-124 counterpart is shown. The different graphs in the left panel represent several approaches for the delta decay width : zero width (full), fixed width Σ_I of 80 MeV (dot-dashed), only pion-nucleon decay width $\Gamma_{\pi N}$ (dashed) and the full width i.e. $\Gamma_{\pi N} - 2\Sigma_I$ (dotted).*

In order to construct a current operator from these $\mathcal{L}_{int}(x)$, a non-relativistic free delta propagator associated with the quantized field $\Psi_\Delta(x)$ is required. The

obvious need for having realistic descriptions for the delta propagator was stressed in Refs. [109], [110] and [111]. In essence, the free relativistic delta propagator from Appendix B -4 has to be modified for the finite delta decay width and the medium corrections. With the aid of Eqs. B-22 and B-23, the spin and isospin dependence of the propagator can be ignored which leads to the following general expression for the non-relativistic delta propagator :

$$G_{\Delta}(\sqrt{s}) \;=\; \frac{1}{(m_{\Delta}c^2+\Sigma_R)-\sqrt{s}-i\frac{\Gamma_{\pi N}-2.\Sigma_I}{2}}\;, \qquad \text{(III-120)}$$

where, $\sqrt{s}$ equals the total energy in the delta c.o.m. system. The two quantities Σ_R and Σ_I are the real and imaginary parts of the in-medium delta self-energy where the pion-nucleon decay channel ($\Gamma_{\pi N}$) has been lifted out of the imaginary part of the self-energy. In Appendix C -5 an expression (C-33) for the pion-nucleon delta decay width, which is the most important decay channel in free space, has been derived assuming that all participating particles are on-shell. The in-medium delta propagator depends on the Mandelstam variable s, therefore it will undergo a shift of the position of the delta resonance in addition to a broadening as can be observed from Fig. III-7. The off-shell mass correction Σ_R is effectively implemented in our calculations through the off-shellness of the excited nucleon as well as by its Fermi motion. Therefore, we set Σ_R equal to zero when computing the Δ propagator. The imaginary part of the self-energy (Σ_I), receives contributions stemming from the in-medium decay channels on one side, and the Pauli-blocking of these channels on the other side [112] [113]. In Ref. [114], Oset and Salcedo used an RPA approach including up to 3p3h contributions to calculate the self-energy diagrams for a general spin-isospin NN potential. The results of their calculations could be parametrized as follows

$$-\Sigma_I \;=\; C_Q(\rho/\rho_0)^{\alpha}+C_{A_2}(\rho/\rho_0)^{\beta}+C_{A_3}(\rho/\rho_0)^{\gamma}\;, \qquad \text{(III-121)}$$

with, the nuclear matter density $\rho_0 = 0.17/fm^3$. In our calculations we used the density averaged version of the imaginary self-energy III-121. Therefore we folded the above expression with the ^{4}He density function C-3 and averaged over 3-dimensional space. The photon energy dependence of this width is shown in Fig. III-8.

Accounting for both the off-shellness and the imaginary self-energy of the in-medium delta gives rise to a broadening and a shift towards lower energies for the in-medium delta resonance (see Fig. III-7).
One can write the energy-dependence of the delta propagator in terms of the Mandelstam variable s

$$G^{res}_{\Delta}(\sqrt{s}) \;=\; \frac{1}{m_{\Delta}c^2-\sqrt{s_{res}}-i\frac{\Gamma_{\pi N}-2.\Sigma_I}{2}}\;, \qquad \text{(III-122)}$$

with,

$$\sqrt{s_{res}} \;=\; \sqrt{(m_Nc^2-\epsilon_h)^2+p_{\gamma}^2c^2+2(m_Nc^2-\epsilon_h)E_{\gamma}}\;, \qquad \text{(III-123)}$$

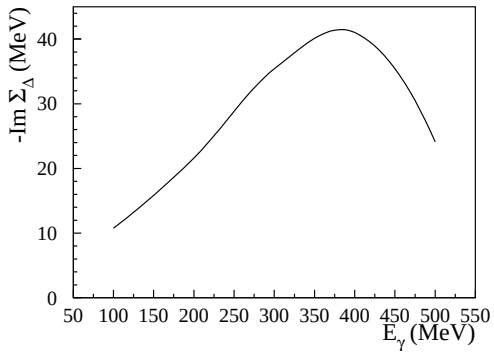

Figure III-8: *Imaginary part of the delta self-energy obtained by averaging expression (III-121) with the ^{4}He density.*

where, ϵ_h is the binding energy of the active nucleon. For the Δ propagator in the u channel on obtains

$$G_\Delta^{non-res}(\sqrt{s}) \;=\; \frac{1}{m_\Delta c^2 - \sqrt{s_{non-res}}}\;, \tag{III-124}$$

with,

$$\sqrt{s_{non-res}} \;=\; \sqrt{|\vec{p}_\gamma|^2 c^2 + m_N^2 c^4} - E_\gamma\;. \tag{III-125}$$

As can be observed from Fig. III-7, the nonresonant propagator has the tendency to decrease the relative impact of the nonresonant diagram at higher values of the Mandelstam variable s.

At this point, one can derive an expression for the delta-excitation current associated with the diagrams displayed in Fig. III-6. Starting from the interaction Lagrangian density of Eq. (III-119) and adopting the quantum field theory formalism, after some algebra one arrives at the following expression for the nonrelativistic delta current :

$$\begin{aligned}
\hat{\vec{J}}_\Delta(0) \;=\; & iec\frac{(\hbar c)^3}{9}\frac{f_{\pi NN}^{PV} f_{\pi N\Delta} f_{\gamma N\Delta}}{(m_\pi c^2)^3} G_{\gamma N\Delta}(Q^2) \\
& \Big\{ \left[G_\Delta^{res} + G_\Delta^{non-res}\right] F_\pi(\vec{p}_2^{\,r}) \frac{\vec{\sigma}_2.\vec{p}_2^{\,r} c}{|\vec{p}_2^{\,r}|^2 c^2 + m_\pi^2 c^4} \\
& \qquad (4\tau_2^z\,(\vec{p}_2^{\,r} \times \vec{q})c - (\vec{\tau}_1 \times \vec{\tau}_2)_z (\vec{\sigma}_1 \times \vec{p}_2^{\,r} c) \times \vec{q}c) + \\
& \left[G_\Delta^{res} - G_\Delta^{non-res}\right] F_\pi(\vec{p}_2^{\,r}) \frac{\vec{\sigma}_2.\vec{p}_2^{\,r} c}{|\vec{p}_2^{\,r}|^2 c^2 + m_\pi^2 c^4} \\
& \qquad (- 2i\tau_2^z (\vec{\sigma}_1 \times \vec{p}_2^{\,r} c) \times \vec{q}c - 2i(\vec{\tau}_1 \times \vec{\tau}_2)_z (\vec{p}_2^{\,r} \times \vec{q})c) + 1 \leftrightarrow 2 \Big\}\;,
\end{aligned} \tag{III-126}$$

where, pion hadronic form factors $F_\pi(p)$ are introduced to account for the short range physics. An electromagnetic form factor $G_{\gamma N\Delta}$ is inserted at the $\gamma N\Delta$-vertex. It accounts for the finite extension of the Δ particle. As the Δ is a more extended object then a nucleon, the following parameterization for the form factor is adopted (see Ref. [115])

$$G_{\gamma N\Delta}(Q^2) = \left(\frac{1}{1+\frac{Q^2}{\Lambda_1^2}}\right)^2 \frac{1}{\sqrt{1+\frac{Q^2}{\Lambda_2^2}}}\,,$$

with $\Lambda_1 = 840$ MeV/c, $\Lambda_2 = 1200$ MeV/c and $Q^2 = -p_\gamma^2$. Some final remark concerning the inclusion of these form factors remains to be made. Due to the transverse nature of the delta current and the particular way of including the form factors, gauge invariance is not violated for the delta current.

§4.3 Dynamical and kinematical correlations

With "correlations" we refer to dynamical, induced by the short-range part of the nucleon-nucleon force, as well as kinematical correlations. The latter emerge when the center-of-mass motion is treated properly. In an IPM treatment for the initial and final wave function, the one-body reaction mechanisms (introduced in subsection (§4.3.1)) have vanishing contributions to the two-nucleon knockout process due to the orthogonality of the initial and final state. The one-body current is only capable of altering one of the outgoing nucleon states leaving the other nucleon state unaltered. Therefore this final state will be orthogonal to the initial state. Another point is the appearance of so-called recoil diagrams into the scattering matrix because of the action of short range and COM correlations. The former account for the short-range behavior of the nucleon-nucleon potential. The COM correlations arise in a natural way when treating the COM-motion in a proper manner. In the next two subsections, we will focus, in more detail, on both corrections to the scattering process.

§4.3.1 One-body current

The dominant contribution to the exclusive $A(e,e'p)$ one-nucleon knockout reaction stems from the one-body nuclear current. For a two-nucleon knockout reaction, the one-body current contribution vanishes in an IPM picture. Taking the correlations into account reintroduces the one-body current in the two-nucleon knockout reaction process. The initial bound nucleon, which absorbs the photon, is definitely off-shell ($p^2 \neq m_N^2c^2$) whereas the detected nucleon has to be on-shell. The major issue now is to find a parameterization for the half off-shell $NN\gamma$-vertex.
Guided by the principle of Lorentz invariance, in the sixties Bincer ([116]) derived

a general form for the off-shell $NN\gamma$-vertex :

$$\begin{aligned}\Gamma^{\mu}(p^f,p^i) &= e\left\{\Lambda_+(p^f)\left[f_1^{++}\gamma^{\mu}+if_2^{++}\sigma^{\mu\nu}(p_\gamma)_\nu/2m_N+f_3^{++}p_\gamma^{\mu}\right]\Lambda_+(p^i)+\right.\\ &\quad \Lambda_+(p^f)\left[f_1^{+-}\gamma^{\mu}+if_2^{+-}\sigma^{\mu\nu}(p_\gamma)_\nu/2m_N+f_3^{+-}p_\gamma^{\mu}\right]\Lambda_-(p^i)+\\ &\quad \Lambda_-(p^f)\left[f_1^{-+}\gamma^{\mu}+if_2^{-+}\sigma^{\mu\nu}(p_\gamma)_\nu/2m_N+f_3^{-+}p_\gamma^{\mu}\right]\Lambda_+(p^i)+\\ &\quad \left.\Lambda_-(p^f)\left[f_1^{--}\gamma^{\mu}+if_2^{--}\sigma^{\mu\nu}(p_\gamma)_\nu/2m_N+f_3^{--}p_\gamma^{\mu}\right]\Lambda_-(p^i)\right\}\ ,\end{aligned} \tag{III-127}$$

with, $\Lambda_\pm(p)=(W\pm p.\gamma)/2W, (W=+(p^2)^{1/2})$ and $p_\gamma=p^f-p^i$. With the final nucleon on-shell, gauge invariance can be imposed with the aid of the Ward-Takahashi identity :

$$q_\mu\Gamma^{\mu}(p^f,p^i)=eS_0^{-1}(p^f)\left[S(p^i)-S(p^f)\right]S_0^{-1}(p^i)\ ,$$

where, the bare and full nucleon propagator are represented by $S_0(p)$ and $S(p)$ respectively. The electromagnetic vertex reads :

$$\begin{aligned}\bar{u}(\vec{p}^f,m_{s_f})\Gamma^{\mu}(p^f,p^i) &= e\bar{u}(\vec{p}^f,m_{s_f})\left\{\left[f_1^{++}\gamma^{\mu}+if_2^{++}\sigma^{\mu\nu}(p_\gamma)_\nu/2m_N\right]\Lambda_+(p^i)+\right.\\ &\quad \left.\left[f_1^{+-}\gamma^{\mu}+if_2^{+-}\sigma^{\mu\nu}(p_\gamma)_\nu/2m_N\right]\Lambda_-(p^i)\right\}\ .\end{aligned} \tag{III-128}$$

In Eq. (III-128) we neglected the terms proportional to q^μ because they vanish once coupled to a conserved electron current or to a real photon field. A measure for the off-shellness of the form factors $f^{\lambda\lambda'}(p_\gamma^2,{p^i}^2)$ is given by how much ${p^i}^2$ differs from $m_N^2c^2$. Many authors have stressed the fundamental impossibility to assess off-shell properties of particles. The major argument is that it is always possible to perform a field transformation which does not change the scattering matrix albeit modifying the off-shell parameters (see for example Refs. [117] [118]). We are not aware of a theoretical model giving precise predictions for these off-shell form factors although some attempts have been made (see Ref. [119]). A possible way out of this, is to adopt the same operatorial form as for the on-shell vertex, but adjusting the kinematical parameters that enter it. Concerning the latter remark, the inserted momenta are the off-shell nucleon momenta while the energies are the associated on-shell extrapolations satisfying the relativistic dispersion relation : $E=\sqrt{\vec{p}^2c^2+{m_N^*}^2c^2}$ (with $m_N^*=m_N-\epsilon_h$ and ϵ_h the nucleon binding energy). All results contained in this work are obtained with the so-called CC2-prescription for the $NN\gamma$-vertex :

$$\Gamma^{\mu}_{CC2} = F_1^N(Q^2)\gamma^{\mu}+i\kappa_N\frac{F_2^N(Q^2)}{2m_Nc}\sigma^{\mu\nu}(p_\gamma)_\nu\ , \tag{III-129}$$

where, κ_N denotes the anomalous magnetic moment of the nucleon N. Two different recipes to impose current conservation will be adopted : the Coulomb

gauge ($J_z \equiv \frac{\omega}{q}\rho$) and the Weyl gauge ($\rho \equiv \frac{q}{\omega}J_z$). Estimates of the uncertainties induced by the gauge ambiguities on $A(\vec{e}, e'\vec{p})$ observables can be found in Refs. [120] and [121].
The on-shell form factors appearing in Eq. (III-129) can be expressed in terms of the nucleon electric ($G_E^N(Q^2)$) and magnetic ($G_M^N(Q^2)$) form factors (or, Sachs form factors) through

$$G_E^N(Q^2) = F_1^N(Q^2) - \frac{Q^2}{4m_N^2c^2}\kappa_N F_2^N(Q^2) \quad \text{(III-130)}$$

$$G_M^N(Q^2) = F_1^N(Q^2) + \kappa_N F_2^N(Q^2)\ , \quad \text{(III-131)}$$

where a dipole parameterization has been used for the Sachs form factors

$$G_E^p(Q^2) = \frac{1}{\left(1+\frac{Q^2}{\beta^2}\right)^2} \qquad \text{with } \beta^2 = 0.71(GeV/c)^2 \quad \text{(III-132)}$$

$$G_M^p(Q^2) = \mu_p G_E^p(Q^2) \qquad \text{with } \mu_p = 1+\kappa_p = 2.793 \quad \text{(III-133)}$$

$$G_E^n(Q^2) = \frac{\tau}{1+5.6\tau}\left|G_M^n(Q^2)\right| \qquad \text{with } \tau = \frac{Q^2}{4m_N^2c^2} \quad \text{(III-134)}$$

$$G_M^n(Q^2) = \mu_n \frac{1}{\left(1+\frac{Q^2}{\beta^2}\right)} \qquad \text{with } \mu_n = \kappa_n = -1.913\ . \quad \text{(III-135)}$$

The finite size of the nucleon, imposing the use of form factors, gives rise to an additional form factor $G^V(Q^2)$ in the meson exchange current. Making use of the relation III-103, one can prove that $G^V(Q^2)$ depends on the nucleon form factor :

$$G^V(Q^2) = 2F_1^V(Q^2) = F_1^p(Q^2) - F_1^n(Q^2)\ . \quad \text{(III-136)}$$

Due to the non-relativistic nature of the nuclear wave function used in our calculations, we need a reduction scheme to derive from the general relativistic nucleon current an effective two-component hadronic current. Two different approaches appear in literature. First, the Pauli reduction scheme evaluates the relativistic operator between free positive energy Dirac spinors (see Eq. (B-4)) and reduces the operator to a two-component form acting on the Pauli wave functions. Second, the Foldy-Wouthuysen transformation which casts the operator in a block-diagonal form up to some higher order (in $|\vec{p}^N|/m_N$) correction term. Only for the lowest order terms, the two techniques provide identical results (see Ref. [117]). The lowest order non-relativistic one-body nuclear current, as derived in Appendix C-6 using the Pauli reduction method, reads :

$$\hat{\rho}_{1-body}(0) = eG_E^p(Q^2)\frac{1+\tau_z}{2} \quad \text{(III-137)}$$

$$\hat{\vec{J}}_{1-body}(0) = ec\left\{G_E^p(Q^2)\frac{\vec{p}^f c+\vec{p}^i c}{2m_N c^2}\frac{1+\tau_z}{2}+ i\left[G_M^p(Q^2)\frac{1+\tau_z}{2}+G_M^n(Q^2)\frac{1-\tau_z}{2}\right]\frac{\vec{\sigma}\times(\vec{p}^f-\vec{p}^i)}{2m_N c}\right\}\ . \quad \text{(III-138)}$$

Amaro et al. performed a non-relativistic reduction for the meson exchange current up to next to leading order [122]. From their relativistic expansions for the pion-exchange currents and the transverse character of the delta current, one can observe that to lowest relativistic order the time component of the nuclear current does not receive any contribution beyond the one-body component, given by Eq. (III-137).

§4.3.2 Recoil diagrams

All two-nucleon knockout calculations, involving "heavy" ($A > 4$) target nuclei are performed in an IPM model or when corrected for the presence of short-range correlations, in a CBF approach for the nuclear wave function. Both approaches display some fundamental shortcomings which will be outlined throughout the remainder of this section.
The IPM approximation discards all correlations neglecting manifestly the short-range behavior of the nucleons. Experiments [123] advocate the necessity to incorporate short-range correlations. The CBF technique, on the other hand, incorporates the short-range correlations by folding the wave function with some correlation function. This correlation correction is considered, in the calculations, as an additional pre-operator on the IPM wave function. Or, in other words the correlations are considered as an essential part of the transition operator. This has far reaching consequences for the wave function. A correlation function makes the wave function no longer normalized and even worse the set of corrected energy-eigenstates of the target nucleus are no longer orthogonal. The latter introduces spurious contributions to the transition cross section coming from a spontaneous decay of the target nucleus due to the mere presence of the short-range correlations. A lot of present day theoretical model calculations are performed in the so-called spectator approach; meaning : the remaining $A-2$ nucleons do not participate in the reaction process whatsoever. Thereby discarding a lot of rearrangement channels in the scattering matrix. In addition both kind (IPM and CBF) of wave functions lack a proper description of the COM dynamics. Correcting the COM fallacy alters the nuclear wave function as explained in chapter II.
In general, COM or short-range correlations alter the original IPM wave function in a dramatic way which comes about when calculating the two-nucleon knockout scattering matrix. While in the common calculational schemes (no COM and spectator approach at correlation level) only a few diagrams had to be calculated, in the, along the previous lines adjusted, model a lot of additional diagrams have to be included. Those are called recoil diagrams and account for the various rearrangement channels in the scattering process. The complete range of diagrams included in our calculations are displayed in Fig. III-10. For an A-body nucleus this amounts to $A-1$ and $\frac{A(A-1)}{2}-1$ additional diagrams for respectively the one- and two-body current and this for every component in the scattering matrix(e.g.

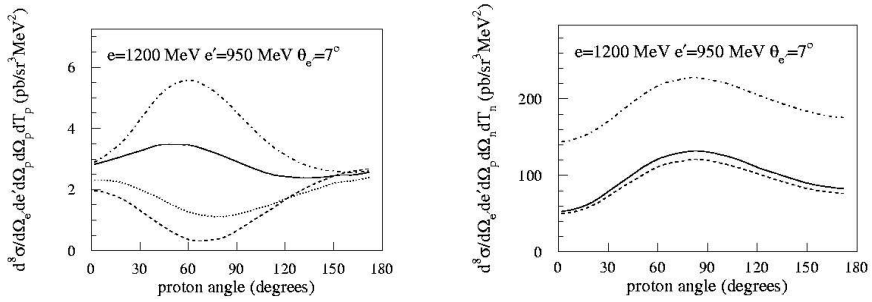

Figure III-9: *The polar angle dependence of the* $^{12}C(e,e'pp)$ *and* $^{12}C(e,e'pn)$ *differential cross section in quasi-deuteron kinematics (P = 0). The solid and dotted curve represent a calculation including final-state interactions using two different correlation functions. The dot-dashed curve represents the same calculation but in a PWA approach. For the dashed curve only the isobar current was included. These pictures are taken from Ref. [125].*

5 additional pion in-flight diagrams in the case of an ^{4}He-target etc.). The need for incorporating these recoil diagrams can be observed from the two-nucleon knockout data using ^{3}He as a nuclear target. From [124] and [14] it is clear that the recoil contribution to the *pp*- knockout cross section coming from the meson exchange current, for example, is needed in order to explain the data.

§5 Final state interactions

Towards the end of the theoretical part of this work some remarks regarding the role of FSI in two-nucleon knockout reactions are in order. Many articles have been published discussing the impact of final-state interactions on the unpolarized cross section and the polarization observables. Final-state interactions do not alter the angular dependence of the cross section considerably (see Fig. III-9). As a matter of fact, FSI mechanisms reduce the nuclear response because of rescattering effects into other final state channels (see Ref. [126]). As discussed in Sect. §3 some of the polarization observables are particularly sensitive to rescattering effects (P_i, Σ_c and A_e) (see Ref. [125]). The associated experimental observables can be used as a measure to estimate the importance of FSI-effects in their being different from zero all over phase space.
Because the aim of this work is to see whether the recoil terms give some observable contribution to the experimental quantities and to determine by which reaction mechanisms the two-nucleon knockout reaction is driven, all FSI-effects will be discarded. The final state wave function adopted, is a plane wave.

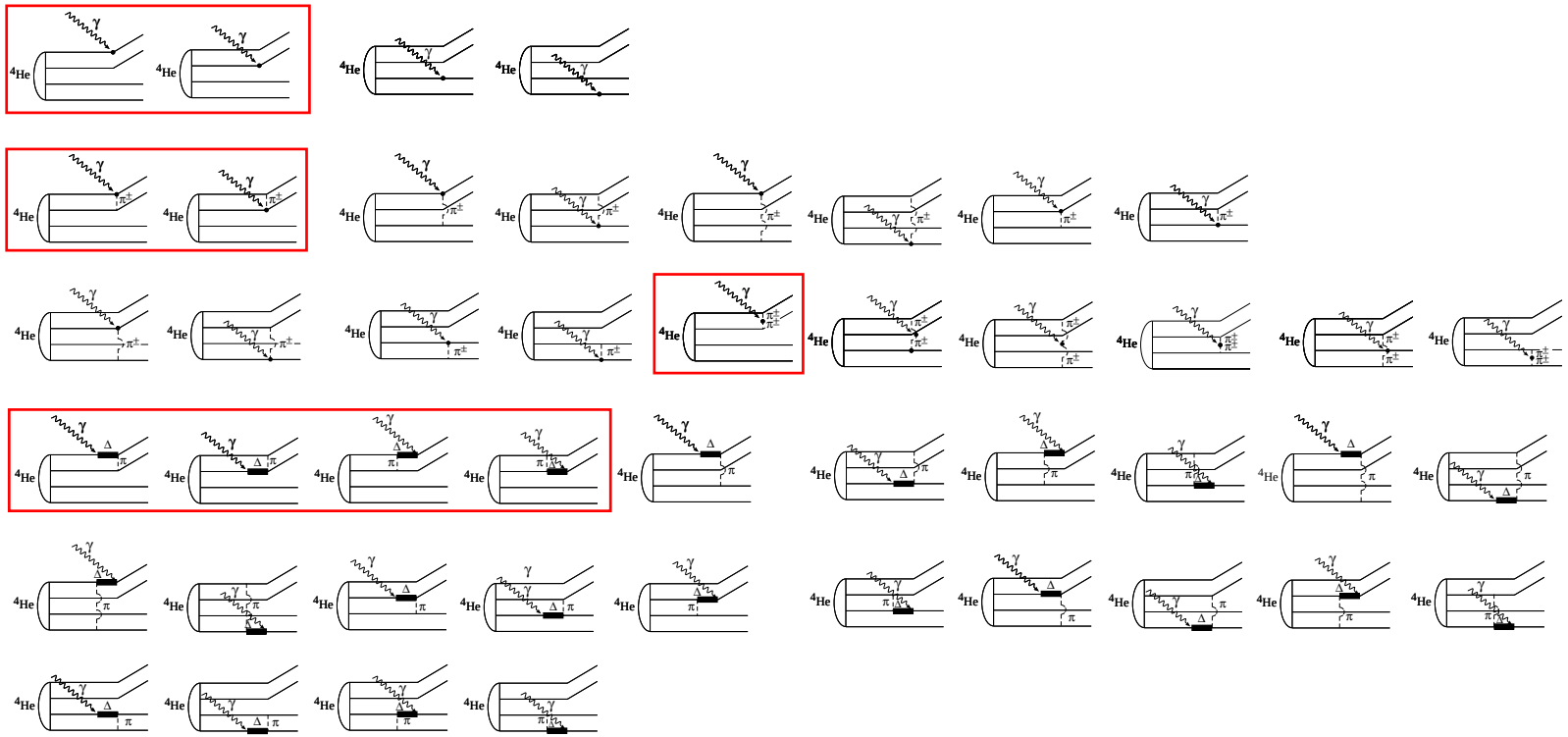

Figure III-10: *Diagrams contributing to the* $^4He(\gamma^{(*)}, NN)$ *process. The terms contained in the red boxes are the common diagrams included when adopting the spectator approximation. The others are recoil diagrams. The first row of terms corresponds with two-nucleon emission following electromagnetic coupling to the one-body current. The second and third row are related to the pion exchange diagrams while the last three rows contain the delta-current contributions.*

The reaction studied throughout this dissertation is the semi-inclusive four-body breakup channel contributing to the two-body knockout reaction on a ^{4}He nuclear target. In this particular case the final state wave function reads :

$$\begin{aligned}\Psi^f_{^4He}(x_1,x_2,x_3,x_4)^{PW} &= \mathcal{A}\left\{\frac{1}{(2\pi)^{3/2}}e^{-i\vec{p}_a.\vec{r}_1}\chi_{(1/2,m_{s_a})}(1)\zeta_{(1/2,m_{t_a})}(1).\right.\\ &\quad \frac{1}{(2\pi)^{3/2}}e^{-i\vec{p}_b.\vec{r}_2}\chi_{(1/2,m_{s_b})}(2)\zeta_{(1/2,m_{t_b})}(2).\\ &\quad \frac{1}{(2\pi)^{3/2}}e^{-i\vec{p}_c.\vec{r}_3}\chi_{(1/2,m_{s_c})}(3)\zeta_{(1/2,m_{t_c})}(3).\\ &\quad \left.\frac{1}{(2\pi)^{3/2}}e^{-i\vec{p}_d.\vec{r}_4}\chi_{(1/2,m_{s_d})}(4)\zeta_{(1/2,m_{t_d})}(4)\right\}\ ,\text{(III-139)}\end{aligned}$$

where, m_{s_i} and m_{t_i} denote the spin and isospin projections.
The above wave function is no solution of the Schrödinger equation for the realistic NN potential adopted to derive the ^{4}He bound-state wave function. The continuum and bound state solutions of the Schrödinger equation belong to different orthogonal subspaces. In order to ensure orthogonality and remove all sources of spurious overlaps, a Gramm-Schmidt procedure is adopted. Hereby, the component orthogonal to the ground state is projected out of the plane wave solution and reads as follows :

$$\Psi^f_{^4He}(x_1,x_2,x_3,x_4) = \frac{\Psi^f_{^4He}{}^{PW} - \left\langle \Psi^f_{^4He}{}^{PW}\middle|\Psi^i_{^4He}\right\rangle_P \Psi^i_{^4HeP}}{\sqrt{1-\left|\left\langle \Psi^f_{^4He}{}^{PW}\middle|\Psi^i_{^4He}\right\rangle_P\right|^2}}\ ,\text{(III-140)}$$

with, $\Psi^i_{^4HeP} = \frac{1}{(2\pi)^{3/2}}e^{-i\vec{P}\vec{R}}\Psi^i_{^4He}$.
In the most general case, a wave function constructed through such a procedure will contain components from bound and continuum states. In the ^{4}He case this projected state will lie in a vector space spanned by continuum states only. Indeed, ^{4}He has only one bound state. The momenta and spin-isospin projections for the outgoing particles remain the same as for the plane wave. The correct continuum states differ from the plane wave solution by a momentum depend phase factor. In short, we claim that this projected state will describe the correct final state rather well in the case of ^{4}He.
Some articles claim this orthogonalization procedure as being a final state interaction because it brings the newly obtained wave in closer agreement with the actual wave function. Actually it is just a necessary procedure to make the model internally consistent ($\equiv$ removing spurious transitions).

Chapter IV

Results and discussion

Differential cross sections and polarization observables are presented for both electro- and photo-induced two-nucleon knockout reactions resulting from semi-exclusive four-body break-up of ^4He. All calculations are performed in coplanar kinematics which is the preferential kinematical choice for most experiments. An orthogonality corrected plane-wave treatment for the ejected particles is adopted. This chapter focuses on short-range correlations, recoil effects and the presence of subnuclear degrees of freedom like e.g. the delta resonance. Theoretical predictions will be presented for the PIP-TOF $^4He(\gamma, NN)NN$ experiments performed at the Mainz microtron as well as for the $^4He(e, e'pp)nn$ experiment performed at the ELSA facility in Bonn.

§1 Introduction

Before turning to the problem of modeling the four-body breakup of the ^{4}He system, we will elaborate on the data and calculations available for three-body breakup of the ^{3}He nucleus. Common mean-field techniques used to study ^{16}O, ^{12}C, ^{208}Pb, ... for example are not applicable to ^{3}He, where one has to resort to few-body techniques. This is also the case for the ^{4}He system. So, by studying the qualitative features of the three-body breakup $\gamma + ^3 He \rightarrow p + p + n$, one may hope to get an idea of what to expect for ^{4}He. At present, no exclusive two-nucleon knockout calculations are available for ^{4}He.
In this section, results stemming from two different theoretical schools will be commented on. First, there are the calculations by the Bochum group (see Fig. IV-1) for a recent ^{3}He$(e, e'pp)$ experiment performed at the NIKHEF-facility [14]. Second, calculations dating from 1987, performed by J.M. Laget are available. He studied the ^{3}He$(e, e'pp)$ reaction in quasi-deuteron kinematics (See Fig. IV-2). More recently, his calculations have been compared to the data of a ^{3}He$(e, e'pp)$ experiment performed by the CLAS collaboration at TJNAF [127].

The NIKHEF ^{3}He$(e, e'pp)$ experiment [95] [128] was performed with an initial beam energy of 563.7 MeV. Fig. IV-1 shows a comparison of the data with the theoretical predictions for three different cuts in the phase space. The first panel focuses on the low missing momentum ($\vec{p}_m = \vec{p}_{\gamma^*} - \vec{p}_{p_1} - \vec{p}_{p_2} = \vec{p}_n$) side of the spec-

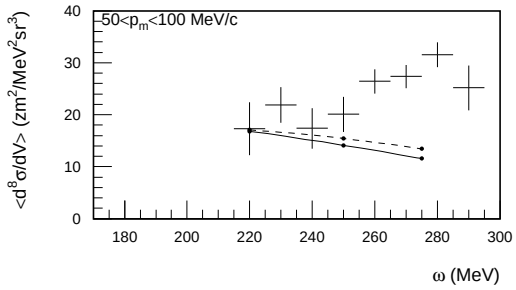

(a) *Average* $^3He(e,e'pp)$ *cross section as a function of* ω *for* $q = 375$ *MeV and* $50 < p_m < 100$ *MeV/c.*

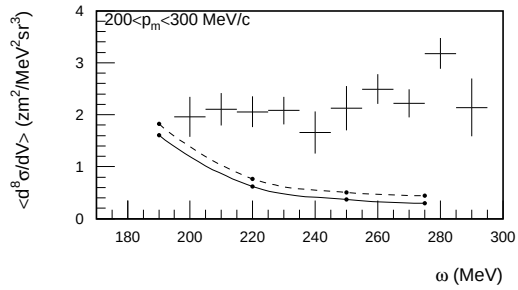

(b) *Average* $^3He(e,e'pp)$ *cross section as a function of* ω *and* $q = 375$ *MeV and* $200 < p_m < 300$ *MeV/c.*

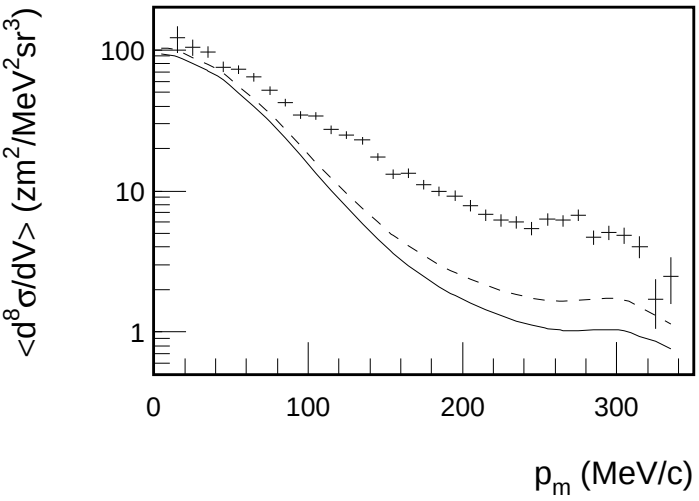

(c) *Average* $^3He(e,e'pp)$ *cross section as a function of missing momentum* p_m *for* $\omega = 220$ *MeV and* $q = 305$ *MeV.*

Figure IV-1: *Figures from the Phd-thesis of David Groep [14]. In all three pictures the solid curves represent the results of a continuum Faddeev calculation including only one-body currents while for the dashed curves also meson-exchange currents (MEC) are incorporated.*

trum where one would expect most of the strength. In this kinematical regime the photon is absorbed predominantly by the detected proton pair leaving the neutron merely as a spectator. In these circumstances, one could expect that the meson-exchange contributions to the cross section are heavily suppressed. This effect is confirmed by the Bochum calculations. At low transferred energy the cross section is determined by the one-body knockout diagrams and short-range correlations. At energy transfers approaching 250 MeV the reaction mechanisms involving intermediate delta creation become increasingly important. At 250 MeV, the transferred energy has reached the point where the incident photon can excite an intermediate delta inside the nucleus. From Fig. IV-1 one notices that the Bochum calculations badly underestimate the experimental data once intermediate Δ-excitation is expected to come into play. In the Bochum calculations, use is made of a static prescription for the delta current. It's common knowledge that the latter does not produce a pronounced delta signature in the energy dependence of cross sections.
At higher missing momenta (see panel (b) of Fig. IV-1) the deviations between the predictions and the data grow. In addition to the one-body current contribution, they predict ^{3}He$(e,e'pp)$ strength attributed to the MEC. This two-body contribution is found to be almost energy-independent and considerably smaller than the one-body part. As already mentioned by Golak [15], the lack of strength at $\omega \approx 280$ MeV, can be attributed to a three-body process where a delta is excited on a pn pair. In this reaction channel the undetected neutron carries a lot of momentum generating therefore a high missing momentum.
The above features as a function of missing momentum p_m are summarized in the lower panel of Fig. IV-1. This figure displays the cross section for a certain transferred energy and momentum as a function of missing momentum. This picture clearly shows that the lack of strength in the theoretical cross section is likely due to the three-body channel involving an intermediate delta. This statement is confirmed by the observation that at low missing momenta the theoretical predictions reproduce the experimental points within a few percent. At higher missing momenta, on the contrary, the theoretical cross section underestimates the measurements by one order of magnitude. In an attempt to improve their calculations, the Bochum group included meson exchange currents. Albeit the relative importance of the MEC contributions grows with missing momentum they are unable to bridge the gap between theory and experiment.
Summarizing, a proper description of the delta resonance, on the one hand, and including all rescattering channels on the other hand, appear indispensable to arrive at a good description of the ^{3}He$(e,e'pp)n$ reaction mechanism.

The calculations displayed in Fig. IV-2 essentially provide additional arguments to sustain the remarks made above. Laget focussed on QD kinematics in his calculations depicted in Fig. IV-2. In QD kinematics, the active nucleon pair resides in a relative S state and is assumed to be initially at rest in the nucleus.

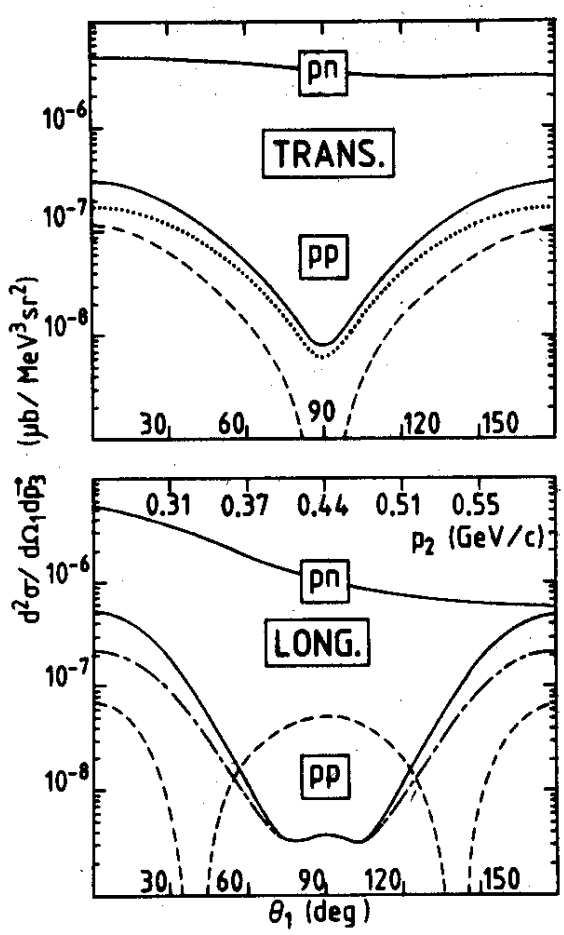

Figure IV-2: *The longitudinal and transverse contribution to the* $^3He(e,e'pp)n$ *cross section in QD kinematics for* $E_e = 570$ *MeV,* $\theta'_e = 25$ *degrees and* $\omega = 200$ *MeV. The dashed lines denote a plane-wave approximation without MEC's, the dotted lines include the MEC mechanisms in the PWA calculation, while the dot-dashed lines include pp-rescattering. The solid lines are obtained by a full calculation including MEC's and final state interactions [124]. The polar angle* θ_1 *is expressed in the COM frame.*

In addition, the missing momentum $p_m = p_n^f$ is put to zero so as to minimize the contributions stemming from the rescattering channels. In this kinematical regime the neutron does not participate in the reaction process and leaves the nucleus without any further interactions. This is a well-known regime to emphasize the contributions of the one-body current, and when selecting proton-proton knockout, to reduce the effect of two-body currents. As expected, most of the transition strength comes from the one-body current which makes up for almost the entire longitudinal part. The transverse part, on the other hand, is suppressed by adopting QD kinematics. To explain this we make the following two remarks. First, the meson exchange currents contribute marginally to the pp-knockout reaction only producing sizeable amounts of strength when approaching higher missing momenta. Second, the delta current requires P- or D-wave admixtures in the two-particle wave function which are suppressed in QD kinematics by setting p_m equal to zero.
In J.M. Laget's theoretical model, the rescattering effects in the final channel are taken into account using a partial wave analysis. They give rise to a correction in the longitudinal response as can be readily observed from the bottom panel in Fig. IV-2.

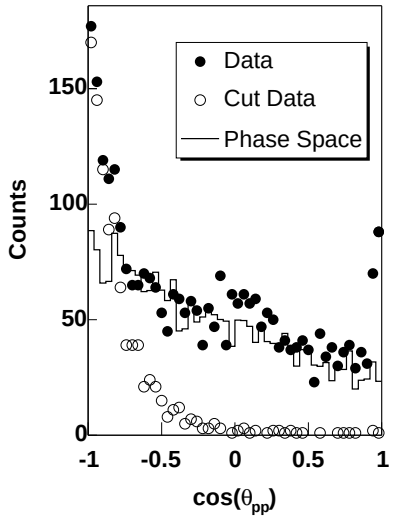

Figure IV-3: *The cosine of the pp lab frame opening angle for the events with a leading neutron and two fast protons. Filled points show the data, open points show the data with a leading neutron emitted along $\vec{q}$. The histogram shows the available phase space volume normalized to the data. Picture taken from [127].*

Whereas, in QD kinematics one focuses on $p_m \approx 0$, the $^3\mathrm{He}(e, e'pp)n$ experiment conducted by the CLAS collaboration studied, to the contrary, only those events where the photon is absorbed entirely by the third nucleon giving rise to a high missing momentum. Their goal is to study the nucleon-nucleon dynamics within the nucleus. To get a clear signal of the nuclear dynamics one should select only those events where the detected nucleon pair does not participate in the electromagnetic reaction with the photon. By selecting only high missing momentum events, one ensures that the, in the final channel, detected nucleon pair acts merely as a

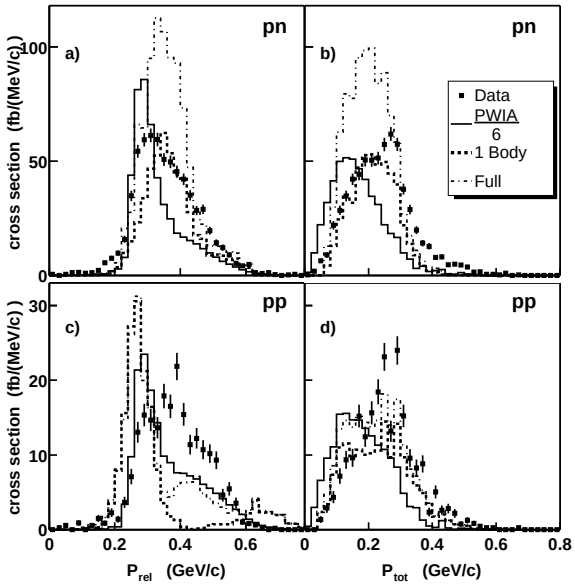

Figure IV-4: *a) Lab frame $^3He(e,e'pp)n$ cross section vs. relative momentum of the fast pn pair. Points show the data, solid histogram shows the PWIA calculations reduced by a factor of 6, thick dashed histogram shows Laget's one-body calculation, thin-dashed histogram shows Laget's full calculation; b) same data versus the total momentum; c) an d) the same for fast pp pairs. Picture taken from [127].*

spectator. In addition, of the latter only those events are selected where, on the one hand, the leading nucleon is emitted predominantly along the momentum transfer and on the other hand, the final nucleon momenta are high i.e. $p_N \geq 250$ MeV/c. These conditions will reduce the effects of FSI. Summarizing, this experiment provides a great opportunity to measure the initial pair momentum distribution in the nucleus.

Fig. IV-3 displays the angular distribution of the detected pair. One observes that the nucleons of the detected pair are preferentially emitted back-to-back. This is a clear signal for the presence of short-range correlations. Fig. IV-4 plots the cross section as a function of the relative and total momentum of the pair. Both *pn* and *pp* knockout data is reported. Both reaction cross sections display nearly the same functional dependence. This might indicate that the isospin-dependent terms in the correlation operator are rather small. In our four-body breakup calculations, the isospin dependent correlation operators have been neglected. In Ref. [127], an almost isotropically distribution in angle of the emitted correlated nucleons is reported. Such a behavior is indeed expected for a correlation operator which depends solely on the radial distance. Fig. IV-4 demonstrates that, in the kinematics of the TJNAF experiment, the one-body current is the

dominant contribution. Other diagrams have to be included though, to accurately explain the data.
When particular kinematics, i.e. QD and back-to-back kinematics, are selected, the cross section is dominated by the one-body current. The ^{3}He experiments discussed above are recorded in quite different energy regimes for the incoming virtual photon. Therefore, in drawing some overall conclusions based on these experiments, one should be cautious. The respective phase spaces spanned our quite different which will be reflected on the particular shape of the cross section. Though, some general trends can be detected. First, rescattering diagrams can't be neglected and second, the short-range correlations have a strong central part supporting the assumptions made in Chapter II.

Based on the analysis of the ^{3}He$(e, e'pp)$ reaction studied by the Bochum group and J.M. Laget, we can deduce some guidelines for our study of the four-body breakup of ^{4}He. First, it can be anticipated that at low missing momenta the ^{4}He$(e, e'pp)$ cross section will receive a sizeable contribution from one-body photon absorption mechanisms. In our approach, FSI effects are only partially included. Indeed, the FSI mechanisms where it concerns rescattering terms beyond the recoil diagrams depicted in Fig. III-10, are discarded. It will be one of our goals to make an educated guess about their share in the full set of diagrams representing final state interactions. In the PhD-thesis of David Groep [14] and subsequent papers [95] [128], calculations from the Bochum group which include a static delta current operator are shown. These calculations don't even come close in explaining the measured strength at a transferred energy of 260 MeV. We wish to investigate whether a dynamic treatment of the Δ excitation could explain this discrepancy. To this end, we will study ^{4}He(γ, NN) cross sections comparing results obtained with a static and dynamic descriptions for the Δ current. Reactions induced by real photons, which probe only the transverse part of the electromagnetic response, are considered to provide a stringent test to study the effect of MEC and IC.
In the forthcoming sections, ^{4}He(γ, pp), ^{4}He(γ, pn) and ^{4}He$(e, e'pp)$ calculations will be presented. They are obtained with the model outlined in previous chapters. We will investigate if they are subject to similar shortcomings as the ^{3}He results.

$$
\begin{aligned}
J_x^{\uparrow\uparrow\downarrow\uparrow} &= -ec\delta_{\vec{q},-(\vec{p'}_1-\vec{p}_1)}\delta_{\vec{p'}_2,\vec{p}_2}\delta_{\vec{p'}_3,\vec{p}_3}\delta_{\vec{p'}_4,\vec{p}_4}\frac{G_M^p(Q^2)}{2m_Nc^2}\times(\vec{p'}_1c-\vec{p}_1c)_z+ \\
&\quad ec\delta_{\vec{q},-(\vec{p'}_2-\vec{p}_2)}\delta_{\vec{p'}_1,\vec{p}_1}\delta_{\vec{p'}_3,\vec{p}_3}\delta_{\vec{p'}_4,\vec{p}_4}\frac{G_M^p(Q^2)}{2m_Nc^2}\times(\vec{p'}_2c-\vec{p}_2c)_z \\
J_y^{\uparrow\uparrow\downarrow\uparrow} &= ec\delta_{\vec{q},-(\vec{p'}_1-\vec{p}_1)}\delta_{\vec{p'}_2,\vec{p}_2}\delta_{\vec{p'}_3,\vec{p}_3}\delta_{\vec{p'}_4,\vec{p}_4}\frac{G_M^p(Q^2)}{2m_Nc^2}\times I(\vec{p'}_1c-\vec{p}_1c)_z- \\
&\quad ec\delta_{\vec{q},-(\vec{p'}_2-\vec{p}_2)}\delta_{\vec{p'}_1,\vec{p}_1}\delta_{\vec{p'}_3,\vec{p}_3}\delta_{\vec{p'}_4,\vec{p}_4}\frac{G_M^p(Q^2)}{2m_Nc^2}\times I(\vec{p'}_2c-\vec{p}_2c)_z \\
J_z^{\uparrow\uparrow\downarrow\uparrow} &= ec\delta_{\vec{q},-(\vec{p'}_1-\vec{p}_1)}\delta_{\vec{p'}_2,\vec{p}_2}\delta_{\vec{p'}_3,\vec{p}_3}\delta_{\vec{p'}_4,\vec{p}_4}\frac{G_M^p(Q^2)}{2m_Nc^2}\times((\vec{p'}_1c-\vec{p}_1c)_x-I(\vec{p'}_1c-\vec{p}_1c)_y)- \\
&\quad ec\delta_{\vec{q},-(\vec{p'}_2-\vec{p}_2)}\delta_{\vec{p'}_1,\vec{p}_1}\delta_{\vec{p'}_3,\vec{p}_3}\delta_{\vec{p'}_4,\vec{p}_4}\frac{G_M^p(Q^2)}{2m_Nc^2}\times((\vec{p'}_2c-\vec{p}_2c)_x-I(\vec{p'}_2c-\vec{p}_2c)_y)
\end{aligned}
$$

Table IV-1: *The explicit form of the one-body current for the isospin ppnn and spin ↑↑↓↑ channel. The $\vec{p}$ ($\vec{p}'$) denote the initial (final) momenta of the particles involved. I denotes the imaginary unit vector.*

§2 Model calculations and discussion

§2.1 Technical aspects

In this section, we will elaborate on some of the technical details of the numerical calculations. When tackling the problem of three- (threshold energy, $E_b = 26.1$ MeV) and four-body ($E_b = 28.3$ MeV) breakup of the ^{4}He nucleus, the need for a module capable of doing symbolic calculations in spin-isopsin space was realized soon. Due to the dimensions of the spin-isospin phase space, namely 16 spin channels for each of the 6 isospin channels, it would have demanded a lot of man-power to determine the complete spin-isopin dependence of the scattering matrix. As an example, table IV-1 lists the final form of the one-body current operator in the isospin *ppnn* and spin ↑↑↓↑ channel i.e. :

$$
\begin{aligned}
&< m_{t_1}=\frac{1}{2}, m_{s_1}=\frac{1}{2}; m_{t_2}=\frac{1}{2}, m_{s_2}=\frac{1}{2}; m_{t_3}=-\frac{1}{2}, m_{s_3}=-\frac{1}{2}; m_{t_4}=-\frac{1}{2}, m_{s_4}=\frac{1}{2}| \\
&\quad \sum_{l=1}^{4} ec\left\{ G_E^p(Q^2)\frac{\vec{p}_l^{\,f}c+\vec{p}_l^{\,i}c}{2m_Nc^2}\frac{1+\tau_z(l)}{2}+ \right. \\
&\qquad \left. i\left[G_M^p(Q^2)\frac{1+\tau_z(l)}{2}+G_M^n(Q^2)\frac{1-\tau_z(l)}{2}\right]\frac{\vec{\sigma}_l\times(\vec{p}_l^{\,f}-\vec{p}_l^{\,i})}{2m_Nc}\right\}
\end{aligned}
$$

$$|\frac{1}{\sqrt{4!}}\begin{vmatrix} \chi_{m_s=1/2,m_t=1/2}(1) & \chi_{m_s=1/2,m_t=-1/2}(1) & \chi_{m_s=-1/2,m_t=1/2}(1) & \chi_{m_s=-1/2,m_t=-1/2}(1) \\ \chi_{m_s=1/2,m_t=1/2}(2) & \chi_{m_s=1/2,m_t=-1/2}(2) & \chi_{m_s=-1/2,m_t=1/2}(2) & \chi_{m_s=-1/2,m_t=-1/2}(2) \\ \chi_{m_s=1/2,m_t=1/2}(3) & \chi_{m_s=1/2,m_t=-1/2}(3) & \chi_{m_s=-1/2,m_t=1/2}(3) & \chi_{m_s=-1/2,m_t=-1/2}(3) \\ \chi_{m_s=1/2,m_t=1/2}(4) & \chi_{m_s=1/2,m_t=-1/2}(4) & \chi_{m_s=-1/2,m_t=1/2}(4) & \chi_{m_s=-1/2,m_t=-1/2}(4) \end{vmatrix}>$$

The spin-isospin module alluded to above, provides us with closed expressions for the nuclear charge and current operators, in terms of particle momenta. The obtained nuclear charge and current operators are folded with the initial and final nuclear wave function expressed in momentum space. At this point, integrals over the initial momenta have to be performed in order to compute the nuclear transition matrix elements. These quadratures are challenging when attempting to evaluate them on standard computers instead of supercomputers. A well-known technique to reduce the amount of quadratures is to adopt a partial-wave expansion. This allows them to be solved analytically. Partial-wave analysis suffers from one major drawback once short-range correlations are included, namely slow convergence. Therefore, we don't resort to a partial-wave expansion technique. In order to reduce the numerical complexity without significant loss of accuracy, an expansion in terms of Gaussians is adopted for the pair correlation function. This procedure is described in more detail in Appendix C -1.2. In the PWA, this technique allows one to calculate analytically the nine-dimensional integral occurring in the matrix element for the one-body charge and current operator. The matrix elements involving a two-body current, on the other hand, cannot be computed analytically. Using the same expansion as for the one-body current, though, the initial twelve-dimensional integral can be reduced to a one or three-dimensional one depending on whether one is dealing with the pion-seagull, delta isobar or the pion-in-flight current. The remaining integrals have to be performed numerically. They are computed with a second-order Newton-Cotes quadrature technique. The integration steps are chosen so as to optimize the accuracy, at the same time keeping the computational times within reasonable limits. Whenever we integrate over a solid angle, the interpolation points are selected in a way they form a symmetrical grid on the unit sphere. This suppresses spurious contributions introduced by the oscillatory character of the phase-space volume $d\cos\theta$. Each scattering matrix element is corrected for spurious contributions stemming from the non-orthogonality deficiency of the initial and final ^{4}He wave functions. As explained in Chapter III, a Gramm-Schmidt orthogonalization correction is used. The latter does not introduce any additional integral.
As can be inferred from Eq. III-140, the orthogonalization correction exhibits two general features. First, the non-orthogonality corrections scale with the magnitude of the overlap between the initial- and final-state wave function. For out-

going nucleons with a kinetic energy $T_p \geq 50$ MeV, the overlap is small and the spurious contributions are heavily suppressed. Second, the expectation value of the nuclear current, sandwiched between the initial and final ^{4}He wave functions, decreases exponentially with transferred momentum $\vec{q}$. Therefore, with increasing transferred momentum, the plane-wave solutions approach the results obtained with the Gramm-Schmidt corrected continuum wave function. In general, for the range of photon energies and ejectile momenta we are interested in, the non-orthogonality corrections are minor. They make up less then 0.2 percent of the transition matrix element and can therefore be safely neglected.
Finally, to arrive at a semi-exclusive two-body knockout cross section, reflecting a four-body breakup process, an additional integration over the solid angle of one of the non-detected nucleons has to be performed. When comparing calculations to data, a summation over the spin and isospin quantum numbers of the non-detected nucleons is often required. E.g., determining the $^4\mathrm{He}(\gamma^*, pn)X$ cross section requires an additional sum over the two isospin channels $^4\mathrm{He}(\gamma^*, pn)pn$ and $^4\mathrm{He}(\gamma^*, pn)np$. All calculations shown throughout the following sections are performed along these lines.
Before turning to the discussion of the theoretical results a final remark has to be made. The nucleons, swirling around in the nucleus, are generally not on the mass shell. Therefore, the nucleon wave functions do not obey the Dirac equation. As a consequence, charge conservation is not necessarily fulfilled. To ensure gauge invariance, we will effectively restore current conservation. Over the years, several prescriptions have been developed to do this. In this work, we adopt the so-called Coulomb gauge in which the longitudinal component of the nuclear vector current is substituted by a charge density operator :

$$J_\mathrm{Z} \rightarrow \frac{\omega}{q}\rho \ .$$

Whereas real photons, only addresses the transverse part of the nuclear current, electro-induced two-nucleon knockout is also sensitive to the longitudinal current components. Therefore, the effects of this substitution will manifest themselves for processes involving virtual photons.

§2.2 ^{4}He$(e, e'pp)$ results in QD kinematics.

Over the last number of years, a lot of theoretical and experimental effort has been directed towards detecting signatures of short-range correlations. Kinematical conditions which have been recognized to provide great prospects for doing so, are so-called quasi-deuteron kinematics. It is defined by the requirement that the missing momentum $\vec{p}_m$ equals zero. In the impulse approximation and in the absence of all FSI mechanisms, the missing momentum $\vec{p}_m$ equals the initial COM momentum of the detected pair. Due to the finite resolution of detectors, it is experimentally not possible to select genuine QD kinematics because of the

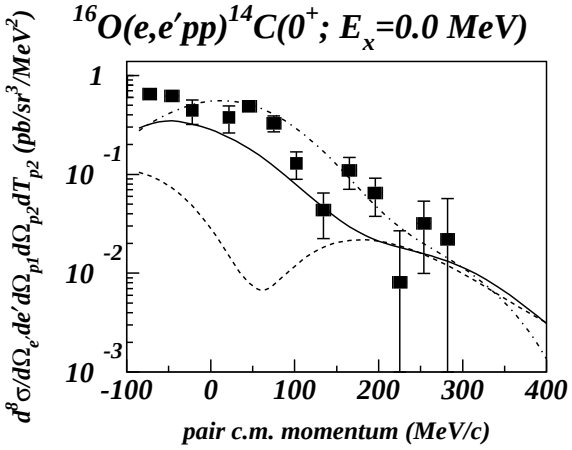

Figure IV-5: *The eightfold differential cross section for the* $^{16}O(e,e'pp)^{14}C(0^+, E_x = 0\ MeV)$ *reaction as a function of the pair COM momentum. The dashed curve shows the results of a distorted-wave calculation that include only intermediate* Δ *excitation. The solid (dot-dashed) curve is the result of a distorted-wave (plane-wave) calculation that accounts for both the intermediate* Δ *and central short-range correlations. The picture is taken from [129].*

smallness of the phase space volume. Theoretically, though, it represents a good test-case to study the impact of correlations on the physical observables. In what follows, we will present ^{4}He$(e,e'pp)$ calculations in QD kinematics and compare them with the ^{3}He$(e,e'pp)$ results of J.M. Laget.

As the two-nucleon knockout cross sections scale with the pair momentum distribution $F(\vec{P}_{\rm COM})$, and F strongly decreases with increasing $\vec{P}_{\rm COM}$, they reach a maximum for kinematical conditions approaching $\vec{p}_m \sim \vec{P}_{\rm COM} \approx \vec{0}$. Fig. IV-5 illustrates the latter remark for the ^{16}O$(e,e'pp)^{14}$C$(0^+$ (g.s.)) case.
In QD kinematics, the cross section will be dominated by the one-body current as the active pair in the target nucleus resides preferentially in a relative S state [123]. This argument is confirmed by reaction model calculations for the ^{16}O$(e,e'pp)^{14}$C(g.s.) measured at the Mainz facility by the A1 collaboration. Fig. IV-5 displays the computed differential cross section for the ^{16}O$(e,e'pp)^{14}$C reaction to a specific final state i.e. ^{14}C$(0^+, E_x = 0$ MeV) in super-parallel kinematics. In super-parallel kinematics the ejected particles are detected along the momentum transfer direction. At low values of $\vec{P}_{\rm COM}$, the detected strength is almost entirely due to the one-body current and contributions attributed to intermediate delta excitation represent only a few percent of the total strength.

Shell model		Relative	COM	Relative wave function
$(n_1,l_1)(n_2,l_2)$	$(L,S)J^\pi_{\text{pair}}$	(n,l)	(N,Λ)	$^{2S+1}l_J(T)$
$(1s)^2$	$(0,0)0^+$	$(1,0)$	$(1,0)$	$^1S_0(T=1)$
$(1p)^2$	$(0,0)0^+$	$(1,0)$	$(2,0)$	$^1S_0(T=1)$
	$(0,0)0^+$	$(2,0)$	$(1,0)$	$^1S_0(T=1)$
	$(1,1)0^+$	$(1,1)$	$(1,1)$	$^3P_1(T=1)$

Table IV-2: *Possible* 0^+ *configurations for proton-proton knockout from s- and p-shell combinations.* $\Lambda(l)$ *denotes the COM (relative) angular momentum of the pair.*

At the low missing momentum side, the nucleons are predominantly knocked out of a relative $^1S_0$ state [123]. This observation can be theoretically substantiated by means of a Moshinsky decomposition of the initial two-particle state. From Table IV-2 one notices that a relative S state is directly linked to a center-of-mass S state ($\Lambda = 0$) endorsing the observation that in QD kinematics the nucleons reside in a relative S state. All the arguments cited above, confirm the statement that QD kinematics, where $|\vec{p}_m|$ equals zero by definition, will favor the one-body reaction mechanism. When performing two-proton knockout calculations in a non-relativistic approach, the effect of meson-exchange currents (MEC) vanishes in lowest order. Indeed, in direct proton-proton knockout the MEC terms vanish as no charged meson can be exchanged. Summarizing, the two-body current strength is suppressed in QD kinematics, creating good conditions to detect signatures of short-range correlations.

Fig. IV-6 displays the ^{4}He$(e,e'pp)$ cross section in QD kinematics for a transferred energy of 250 MeV and a virtual photon momentum equal to 335 MeV/c. First, we will comment on the shift of about 20 degrees in the polar-angle distribution, observed when comparing the above model calculations with the corresponding ^{3}He$(e,e'pp)$ predictions of J.M. Laget contained in Fig. IV-2. This shift can be attributed to the particular reference frames adopted in either calculations. Laget evaluated the cross section in the COM frame, whereas throughout this work we express the measurable quantities in the LAB frame. Therefore, a Lorentz transformation has to be applied before both predictions can be com-

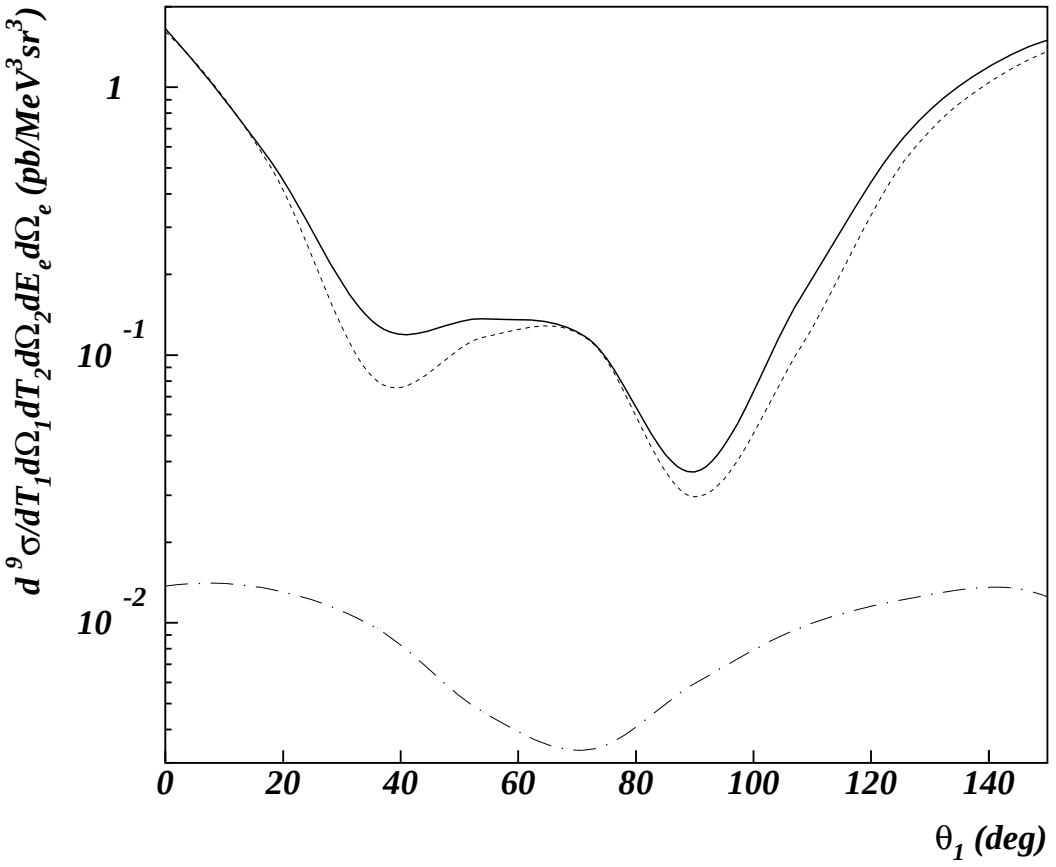

Figure IV-6: $^4He(e,e'pp)$ *cross section calculated in QD kinematics with an initial beam energy of* $E_e^i = 1200$ *MeV,* $\omega = 250$ *MeV,* $q = 335.15$ *MeV/c and* $E_m = 50$ *MeV. The dashed (dot-dashed) line depicts the result of model calculations including only the one-body (two-body) current. The solid line is obtained when both one- and two-body currents are taken into account (for the corresponding diagrams, see Fig. III-10).*

pared. The observed mirror asymmetry in the LAB system of the ^{4}He$(e, e'pp)$ cross section around a polar angle of ± 70 degrees is equally as well a consequence of the particular observation frame selected. Due to the aberration effect caused by the Lorentz transformation, the calculated cross section looses its mirror symmetry observed when expressed in the COM frame (see Fig. IV-2).

From Fig. IV-5, one notices that at $p_m = 0$ the two-body strength is almost two orders of magnitude smaller than the one-body contribution. This observation is confirmed in our ^{4}He$(e, e'pp)$ calculations in QD kinematics displayed in Fig. IV-6 where the one-body contribution makes up for almost 90% of the cross section. The peculiar angular shape of the one-body current contribution can be explained by means of the information contained in Fig. IV-7. First, Fig. IV-7 confirms the effect of the Lorentz transformation alluded to above, i.e. the loss of mirror symmetry.

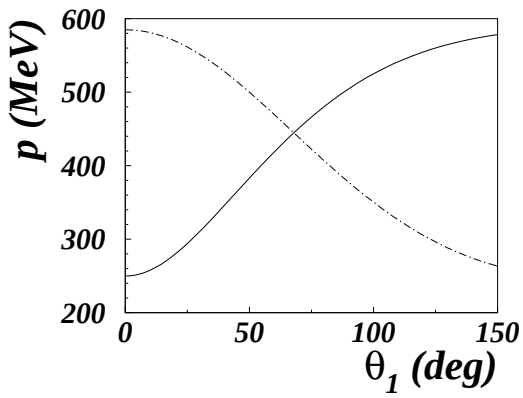

Figure IV-7: *The initial momentum of the struck nucleon as a function of the polar angle of nucleon 1 in QD kinematics and for a fixed value of ω. The solid (dot-dashed) line refers to the situation where the photon is absorbed by nucleon 1 (2).*

Second, Fig. IV-7 illustrates that the initial nucleon momentum grows with increasing polar angle when the photon is absorbed on nucleon "1", while the opposite occurs when the photon couples to nucleon "2". When selecting QD kinematics and final state interactions are neglected, one can state that the detected nucleons initially move back-to-back in their COM frame. Their respective initial momenta are equal but opposite, resulting in $P_{\rm COM} = 0$. Based on the shape of the one-body momentum density, depicted in Fig. II-6, one can conclude that the contribution of the one-body current term where the photon couples to nucleon "1" drops with polar angle. The opposite holds true for the situation whereby the virtual photon is absorbed on nucleon "2". After superimposing both contributions, one arrives at the dashed curve of Fig. IV-6.
Therefore, the observed local enhancement of the c.s., displayed in Fig. IV-6, at a polar angle of about 70 degrees is due to the presence of short-range correlations which introduce high nucleon momentum components in the nucleus. For $\theta_1 \approx 70$ degrees either absorption on nucleon "1" or nucleon "2" requires the presence of fast nucleons with an initial momentum of approximately 450 MeV/c. When

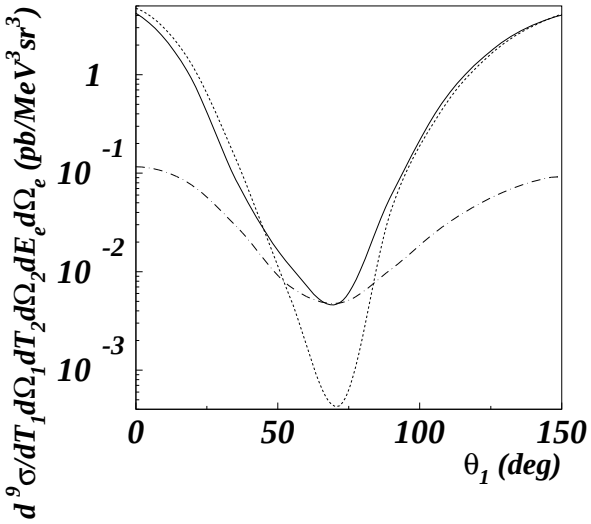

Figure IV-8: $^4He(e,e'pp)$ *cross section calculated in QD kinematics with an initial beam energy of* $E_e^i = 1200$ *MeV,* $\omega = 250$ *MeV,* $q = 335.15$ *MeV/c and* $E_m = 50$ *MeV. The results are obtained with a harmonic oscillator wave function. The same conventions are adopted as in Fig. IV-6.*

redoing the above calculations while neglecting all short-range correlations, one arrives at Fig. IV-8. The noted differences between the cross sections contained in Figs. IV-6 and IV-8, nicely illustrate the impact of short-range correlations.
Most of the above remarks rely on the assumption that the rescattering or final-state interaction effects can be neglected. To investigate to what extent the recoil terms contribute, we calculate the total cross section with and without including the recoil diagrams. These diagrams were introduced in the previous chapter and are displayed in Fig. III-10. They arise in a natural way when the COM motion of the nucleus is properly taken into account. The reaction model calculations are depicted in Fig. IV-9. One notices that the recoil diagrams only marginally contribute to the cross section in QD kinematics. This provides a strong argument that the incident photon is entirely absorbed on the hit nucleon pair leaving the remaining nucleons as mere spectators. In addition, one can state that due to the selection of QD kinematics ($p_m = 0$) and a photon momentum $q = 335$ MeV/c one selects only those events where the hit and detected nucleon pair are identical.

These observations put forward the following picture of the scattering process in QD kinematics. Initially, the four nucleons in the ^{4}He nucleus combine to highly correlated pairs residing in a relative $^1S_0$ state. The incident virtual photon cou-

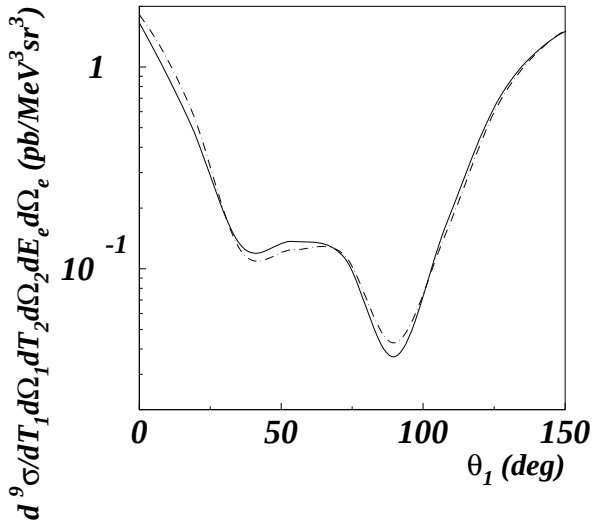

Figure IV-9: $^4He(e,e'pp)$ *cross section calculated in QD kinematics with an initial beam energy of* $E_e^i = 1200$ *MeV,* $\omega = 250$ *MeV,* $q = 335.15$ *MeV/c and* $E_m = 50$ *MeV. The solid (dot-dashed) curve shows the result of the model calculations when the recoil diagrams are (not) included.*

ples to either one of the two nucleons of a correlated pair. Without any further interaction the struck nucleon escapes from ^{4}He. The remaining system is left in an unbound state. Therefore, the other three nucleons propagate as free particles to infinity without any further mutual interactions. As a first order correction to this picture, one includes two-body reaction mechanisms in which the virtual photon four-momentum is shared by both nucleons of the detected pair.

Fig. IV-10 displays a small non-vanishing two-body contribution due to the excitation of an intermediate delta particle. A further refinement of the model consists of including rescattering terms. One important class of these consists of the meson-exchange diagrams where the photon is absorbed by a proton-neutron pair. Fig. IV-10 shows the magnitude of these contributions to the total cross section.

Summarizing, in QD kinematics the ^{4}He$(e,e'pp)nn$ results presented here exhibit identical features than the ^{3}He$(e,e'pp)n$ calculations discussed earlier. For both of the isotopes considered, the one-body current dominates in QD kinematics, creating optimum conditions to study short-range correlations. More in particular, the magnetization term generates most of the one-body strength due to its proportionality to the transferred momentum $|\vec{q}|$. The delta and meson exchange contributions account for the remaining strength which is predominantly located at $\theta = 0$ and $\theta = 180$ degrees. The seagull diagram dominates the meson-

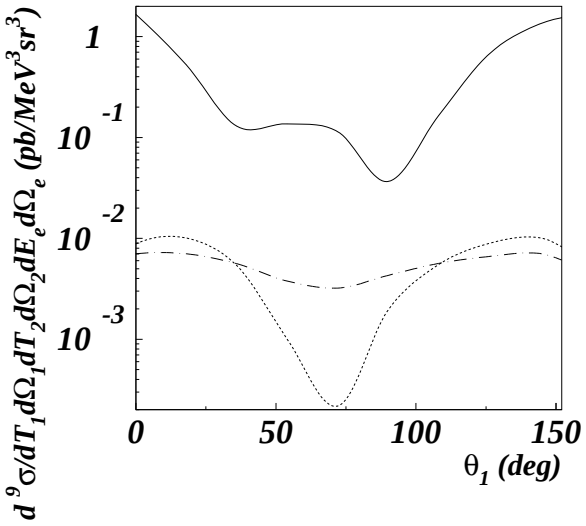

Figure IV-10: $^4He(e,e'pp)$ *cross section calculated in QD kinematics with an initial beam energy of* $E_e^i = 1200$ *MeV,* $\omega = 250$ *MeV,* $q = 335.15$ *MeV/c and* $E_m = 50$ *MeV. As in Fig. IV-6 a realistic* ^{4}*He wave function is used. The dashed (dot-dashed) curve displays the meson (delta) contributions while the solid curve represents the total cross section.*

exchange contribution, as it overshoots the pion-in-flight term by two orders of magnitude.

In QD kinematics, the two-nucleon knockout cross section is driven by the one-body current. In what follows, we will find that also the polarization observables exhibit the same behavior. The only non-vanishing polarization observables in $^4\mathrm{He}(\vec{e},e'\vec{p}p)$ are the longitudinal P_l' and transverse P_t' components of the transferred polarization as can be inferred from Table III-1. Fig. IV-11 depicts both the longitudinal and transverse transferred polarization in QD kinematics. The upper panels of Fig. IV-11 are obtained with a realistic ^{4}He wave function while for the lower panels a harmonic oscillator wave function is adopted. Despite the fact that the one-body contribution dominates the cross section, it generates a rather small transferred polarization, for both the realistic and the harmonic oscillator wave function. The absence of an explicit spin dependence gives rise to a vanishing transferred polarization induced by the convection current. Therefore, only the magnetization current generates a sizeable transferred polarization. The meson-exchange and isobar current induces a rather large transferred polarization which remains, however, suppressed in the final results due to their obviously small contributions to the matrix elements.

Comparing the realistic to the harmonic oscillator calculations, one notices an

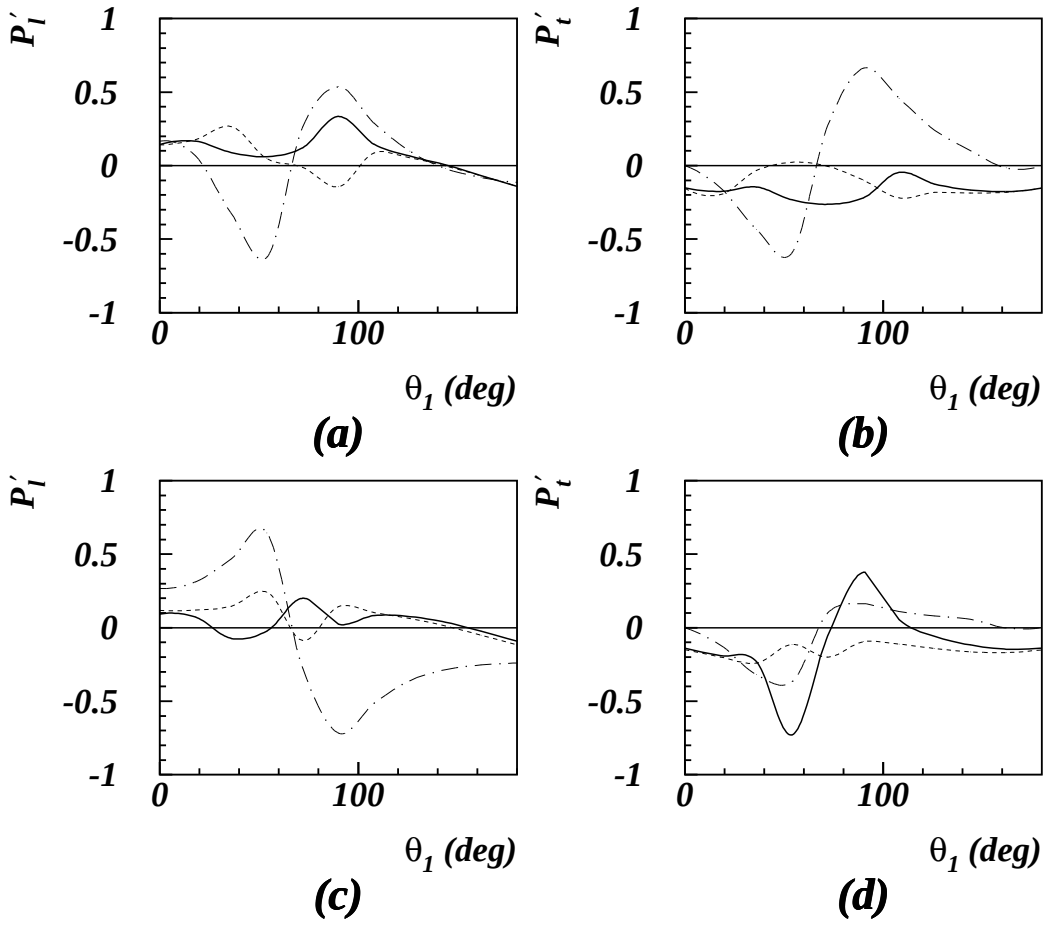

Figure IV-11: *The longitudinal P'_l and transverse P'_t components of the transferred polarization for the $^4He(\vec{e}, e'\vec{p}p)$ reaction in QD kinematics for $E = 250$ MeV, $q = 335$ MeV/c and $E_m = 50$ MeV. The panels (a) and (b) are obtained using a realistic ^4He wave function while for the pictures (c) and (d) a harmonic oscillator description is adopted. The dashed (dot-dashed) curve displays the one-body (two-body) contributions while the solid curve represents the total transferred polarization.*

almost identical longitudinal transferred polarization. Therefore, one can state that the longitudinal part of the polarization transfer is quite insensitive to the detailed form of the ^{4}He ground-state wave function. In other words, short-range correlations do not affect the longitudinal component of the transferred polarization much. The transverse component of the polarization transfer, on the other hand, emerges as a rather well suited quantity to study the effects of short-range correlations.

Another conclusion which can be drawn from Fig. IV-11 concerns the impact of rescattering effects. The rescattering effects generated by the recoil terms contribute predominantly to the two-body current. Therefore one can state that the recoil contributions will not alter the transferred polarization much. This conclusion still holds when apart from the recoil diagrams also other FSI mechanisms are included [125]. Concluding, the transverse component of the transferred polarization is particularly sensitive for the presence of short-range correlations. It has the additional advantage of being rather insensitive to FSI.

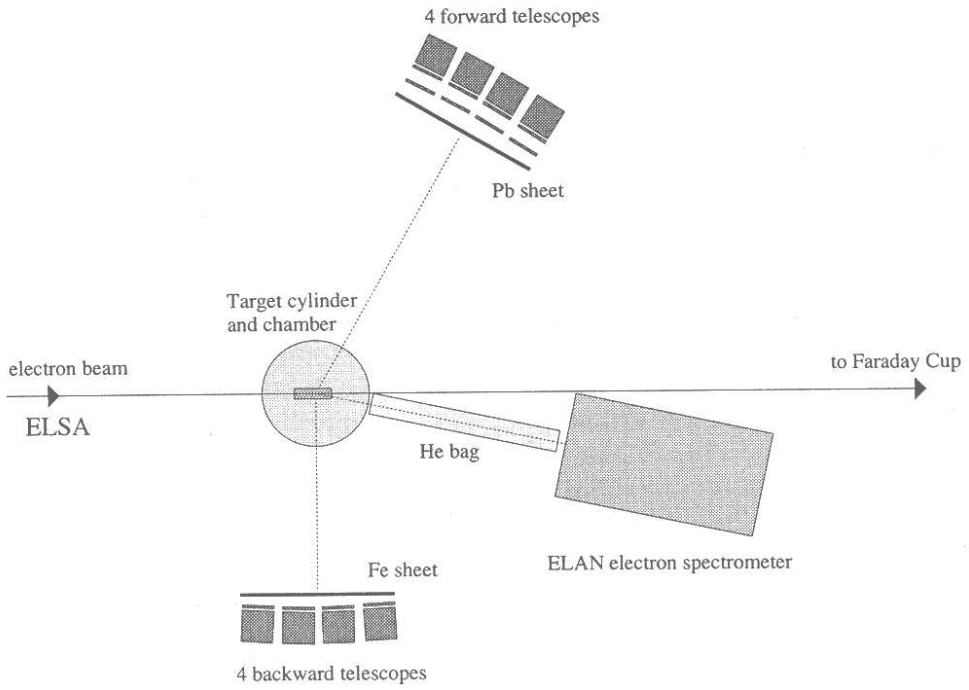

Figure IV-12: *Experimental setup for the $^4He(e, e'pp)$ experiment conducted at the ELSA facility in Bonn by R. De Vries [16]*

§2.3 The De Vries experiment: B2B-kinematics

Back in 1990, a $^4\mathrm{He}(e, e'pp)$ experiment at the ELSA facility in Bonn was conducted by R. De Vries [16]. The ELSA facility consists of a 2.5 GeV synchrotron which delivers the 1200 MeV electron beam. The scattered electrons were detected under an angle of 12 degrees in the ELAN magnetic spectrometer. Two sets of scintillator detectors were used to detect the knocked-out protons. One placed in the forward direction and one in the backward direction relative to the propagation direction of the virtual photon. The forward telescopes have an energy acceptance ranging from 90 to 185 MeV. The energy acceptance of the backward detectors lies in the range $[35, 170]$ MeV.
In the analysis of the data, a cut on low missing energies was made i.e. $E_m \leq 80$ MeV. Generally, various reaction mechanisms have been recognized to contribute to the two-nucleon knockout reaction. By cutting on low missing energies, the genuine direct two-body reactions will be enhanced while the major rescattering mechanisms are suppressed. In addition, one concentrates on the events where the protons are moving initially back-to-back in their COM frame. Keeping the relativistic aberration effect in mind, the forward and backward telescopes are not placed exactly anti-parallel, as noticed from Fig. IV-12. The recent $^3\mathrm{He}(e, e'pp)n$ results by Weinstein et al. [127], confirm that correlated nucleons are predomi-

nantly moving back-to-back (B2B) in the nucleus. In addition, for *pp*-knockout at low missing energies, no meson-exchange terms contribute. Therefore, one may expect that proton-proton knockout in B2B kinematics will be particularly sensitive to the nucleon-nucleon correlations in the ^{4}He nucleus. The features of the nucleon-nucleon dynamics give rise to the particular shape of the relative pair momentum distribution. The ^{4}He relative pair momentum distribution was derived in chapter II and shown in Fig. II-6. The elusive short range correlations reside at the high relative momentum side. When high relative pair momenta are probed, small nucleon-nucleon distances are scanned i.e.

$$\lambda \sim \frac{197.3 \text{ MeV fm}}{pc} .$$

It would be most interesting to measure the c.s. as a function of the initial relative momentum associated with the detected pair. From an experimentalist's point of view one has to seek for an accessible observable which depends almost linearly on the initial relative momentum. Alluded to above, the cut on missing energy forces the photon to couple to one of the nucleons of the detected pair. Fig. IV-13 shows the phase space scanned by the Bonn experiment. The top panels depict the accessible phase space volume, normalized to unity, as a function of the opening angle of the forward proton and the relative momentum. In the left (right) panel the initial relative momentum refers to the case where the photon is entirely absorbed by proton 1 (2). The differences in acceptance of the forward and backward detectors produce the observed asymmetry. These pictures illustrate the ability to scan the relative pair momentum just by turning the detectors around the target cell. In addition, by varying the detection angle from 0 to 90 degrees one probes higher missing momenta. Therefore the cross section will drop as a function of θ_f.
The bottom picture, on the other hand, plots the available phase space volume as a function of the relative pair momentum for the cases where the photon couples to either one of the detected protons. One notices from panel (c) that in back-to-back (B2B) kinematics the scanned relative pair momentum is at its maximum. Due to the higher relative pair momentum probed when the photon is absorbed on the backward proton, one can safely assume that for the majority of events the forward proton absorbs the incoming photon.
The simplified reaction picture looks as follows : a photon encounters a highly correlated proton-proton pair and, after absorption by one of the protons, it propagates along the direction of the photon. As a result, the nucleus entirely disintegrates without any subsequent interactions between the constituents.

Now, we will elaborate on the features of the reaction process. Fig. IV-14 depicts the pp-knockout cross section in B2B kinematics with $250 < \omega < 300$ MeV and $0 < E_m < 80$ MeV. The data are from the 1990 experiment performed at the ELSA facility by De Vries [16]. We compare the predictions obtained with a

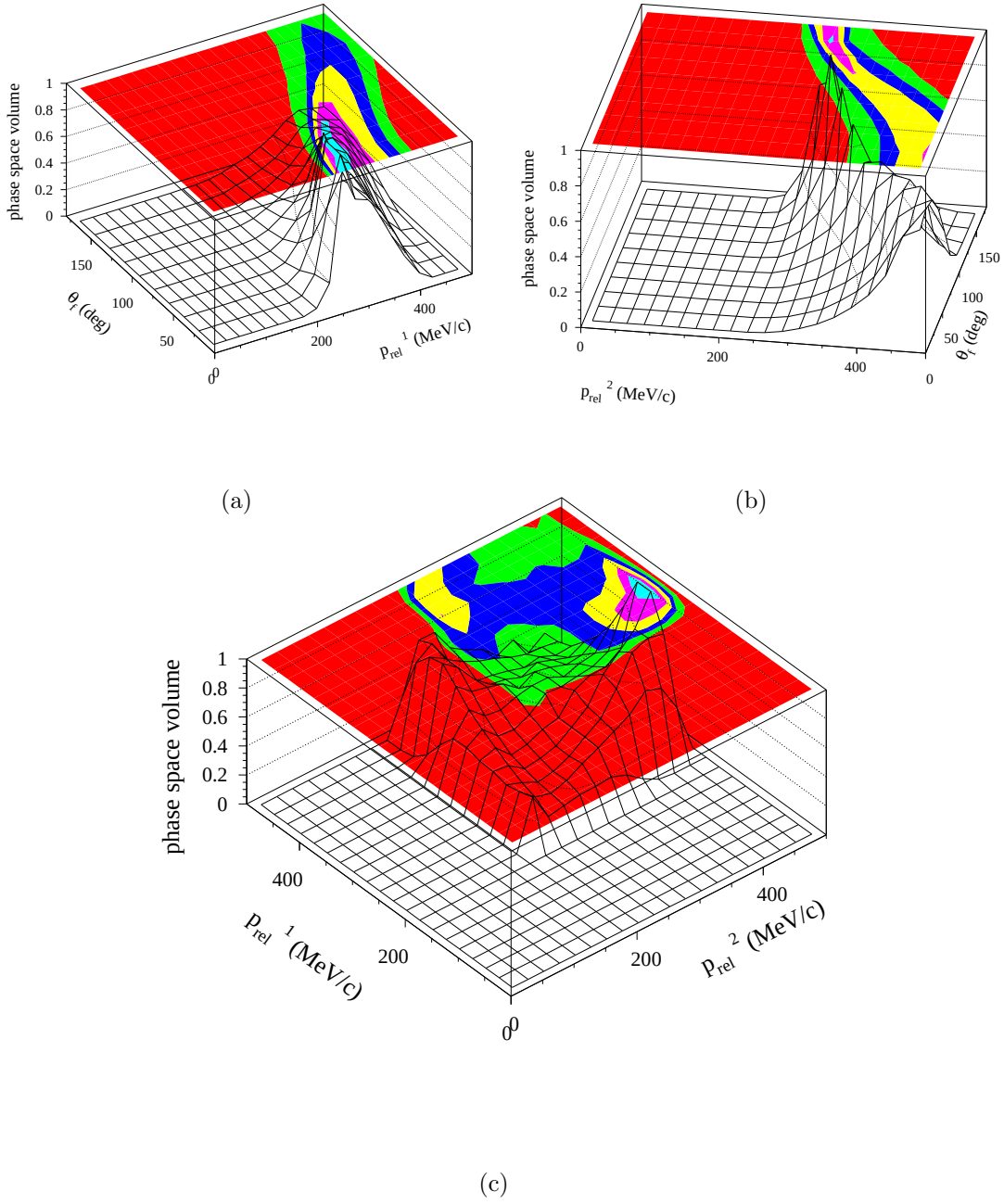

Figure IV-13: *Phase space volume available as a function of θ_f and the initial relative momentum. Both the situation where the photon couples to the forward proton (a) as where it couples to the backward going proton (a) is shown. B2B-kinematics is selected for an initial beam energy of* 1200 *MeV and with* $E_{\gamma^*} = 225$ *MeV*, $q_{\gamma^*} = 319$ *MeV/c and* $E_m = 40$ *MeV*.

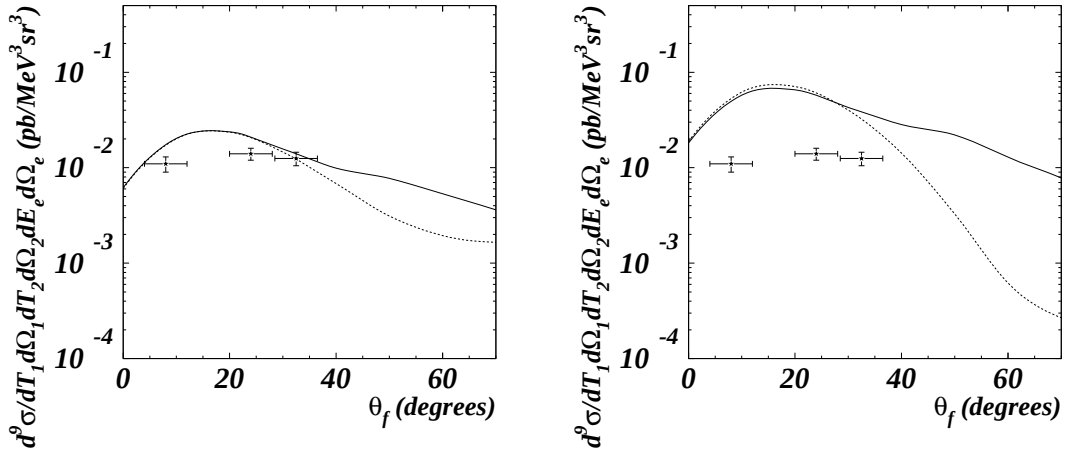

Figure IV-14: *The average $^4He(e,e'pp)$ cross section, calculated with a realistic (left panel) and a HO wave function (right panel), is plotted against the forward angle θ_f. The calculations are performed for* $200 < \omega < 250$ *MeV and for missing energies not exceeding* 80 *MeV. The dashed curve represents the one-body current while the solid one includes also the meson- and isobar exchange current. The data are taken from Ref. [16]*

realistic and a HO ^{4}He wave function. A phase-space averaging, accounting for the detector acceptances, is performed. As anticipated, for both choices of the wave function the one-body contribution accounts for almost the entire $^4\mathrm{He}(e,e'pp)$ strength. At larger opening angles θ_f, the two-body current diagrams represent the major fraction of the two-proton knockout strength. The explanation for this effect is twofold. First, the transverse character of the delta current makes it appear at larger angles. Second, when turning the detectors away from the incident beam higher missing momenta and equivalently missing energies are probed. The latter statement can be proved by the following dispersion relation :

$$E_m \approx 28.3\mathrm{MeV} + \frac{p_m^2}{4m_N} , \qquad \text{(IV-1)}$$

with m_N the mass of the nucleon. The following expressions are adopted for the missing energy and momentum in the four-body breakup channel :

$$E_m = \omega - T^f_{n_1} - T^f_{n_2} = 28.3 \text{ MeV } + T^f_{n_3} + T^f_{n_4} \qquad \text{(IV-2)}$$

$$\vec{p}_m = \vec{p}_\gamma - \vec{p}^f_{n_1} - \vec{p}^f_{n_2} = \vec{p}^f_{n_3} + \vec{p}^f_{n_4} \ , \qquad \text{(IV-3)}$$

with n_1 and n_2 the detected nucleons. In *pp*-knockout and selecting B2B-kinematics, namely, the two-body current strength resides at high missing energies.

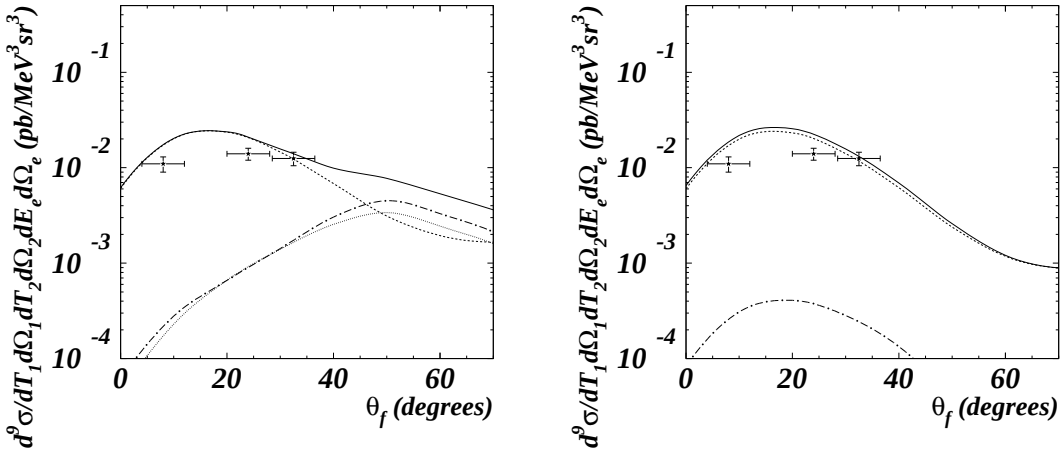

Figure IV-15: *The average* $^4He(e,e'pp)$ *cross section versus the forward angle* θ_f. *The left panel includes all reaction channels while for the right panel the recoil terms are neglected. The calculations are performed for* $200 < \omega < 250$ *MeV and with a missing energy cut equal to* 80 *MeV. The dashed curve represents the one-body current, the dotted curve displays the meson-exchange current while the dot-dashed curve represents the delta contribution. The full line includes all reaction channels. The data are taken from Ref. [16]*

It is noteworthy that with a HO wave function one obtains larger ^{4}He$(e,e'pp)$ cross sections adopting a one-body current. Nevertheless, the HO wave function cannot be expected to account properly for the effect of short-range correlations. Indeed, the one-body current contribution (dashed line in Fig. IV-14) falls steeply with increasing θ_f, or equivalently $p_{\rm rel}$, for a HO wave function. This lead us to conclude that other correlations must be present in the nucleus besides the SRC. One source of them are so-called center-of-mass correlations as defined in Section §4.3. They embody an important part of the collective behavior of the nucleons in the nucleus. In other words, the nucleons are not individually circling around an imaginary origin but they prefer to stay close to each other. Mathematically, this objective of implementing COM effects can be accomplished by making the wave function to depend on the relative coordinates only.

In this work, we will make a distinction between two kinds of correlations i.e., COM which are rather long-range and short-range correlations. Where the COM-correlations tend to hold the nucleons together, the SRC drive the nucleons out of each others vicinity. The former favor low relative pair momenta while the SRC's add strength to the high momentum side of the relative pair momentum distribution. Fig. IV-14 illustrates this feature. From Fig. IV-13 we inferred

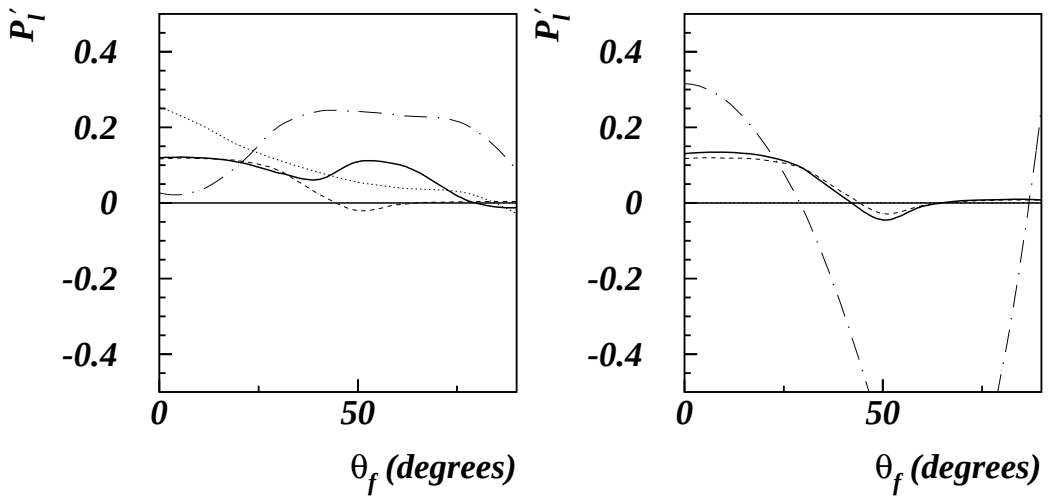

Figure IV-16: *The longitudinal component of the transferred polarization P'_l calculated with a realistic model wave function, is plotted against the forward angle θ_f. The calculations are performed for* $200 < \omega < 250$ *MeV and with a missing energy cut equal to* 80 *MeV. The dashed curve represents the one-body current, the dotted curve displays the meson-exchange current while the dot-dashed curve represents the delta contribution. The full line includes all reaction diagrams.*

that in order to probe high relative momenta, one has to turn the detectors to more perpendicular angles. The one-body strength falls as a function of forward angle, or, equivalently relative pair momentum. This feature is independent of the wave function used. Though we notice a different behavior for the realistic as for the HO calculations. The HO calculations predict more strength at low relative momenta where for a realistic wave function one notices a shift of strength to higher relative momenta. Summarizing, calculations performed with a realistic wave function predict two-proton knockout cross sections which fall gradually with increasing $\vec{p}_{\rm rel}$. For a HO wave function, on the other hand, a steep fall with growing $\vec{p}_{\rm rel}$ is noticed.

To gain additional insight in the reaction process, we plotted in Fig. IV-15 the various sub-mechanisms contributing to the cross section. A realistic model wave function is used. The left panel of Fig. IV-15 accounts for all diagrams

of Fig. III-10. The curves displayed in the right panel, on the other hand, only include direct knockout processes i.e. only the diagrams of Fig. III-10 within the red boxes are retained. The meson-exchange terms, although not present in the direct proton-proton knockout picture, start playing a role once recoil effects are included in the reaction model. One should keep in mind that while going from left to right on the θ_f-axis, the missing momenta and equivalently energies (see Eq. IV-1) grow. This observation explains why the meson exchange strength is located at larger polar angles. The majority of the delta excitation strength can be attributed to recoil terms and therefore lies at the high missing energy side of the spectrum. At forward angles, the delta current vanishes due to its transverse character as already alluded to earlier in this section. The predicted impact of the recoil terms could have been experimentally verified if the data had covered a wider range in θ_f. Indeed, at $\theta_f = 60$ degrees calculations which neglect the recoil diagrams predict a c.s. which is about one order of magnitude smaller than when including them. The one-body current, on the other hand, is only marginally altered by the presence of rescattering terms. Albeit, a small enhancement of the cross section is observed for large polar angles.

In back-to-back kinematics, the one-body diagram overwhelms all other reaction diagrams. Polarization observables come in handy to determine the sensitivity to the two-body strength. Fig. IV-16 shows the longitudinal component P'_l of the transferred polarization. At a polar angle of 50 degrees, one gets a clear signature for the presence of the delta excitation. Fig. IV-16 confirms the previous observation that the recoil terms dominate the two-body reaction mechanisms. Notice the difference in the θ_f dependence of the transferred polarization between the direct knockout and recoil terms.

Summarizing, the impact on the ^{4}He$(e, e'pp)$ cross section of COM correlations and SRC's is demonstrated for B2B-kinematics. Whereas the former reign at low relative pair momenta, the latter show up at the high relative momentum side. The recoil diagrams are shown to generate some strength at high missing momenta. Polarization measurements could select them out of the background.

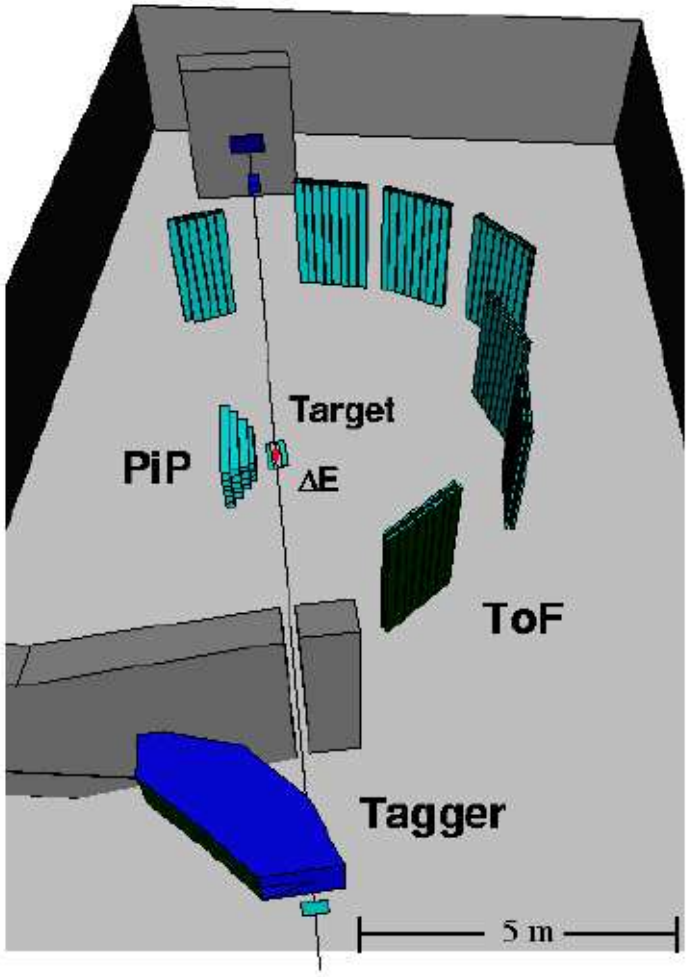

Figure IV-17: *Experimental setup for the* $^4He(\vec{\gamma}, NN)$ *experiment conducted by the A2 collaboration at the MAMI facility in Mainz [130].*

§2.4 The Mainz ^{4}He$(\vec{\gamma}, NN)$ experiment

In this section, we focus on the $^4\mathrm{He}(\vec{\gamma}, \vec{N}N)NN$ reaction. Both photo-induced pn- and pp-knockout are studied. Our calculations are performed for the specific experimental setup used for the $^4\mathrm{He}(\gamma, NN)$ measurements by the A2 collaboration in Mainz, for which a sketch is depicted in Fig. IV-17. The microtron MAMI delivers the 854.6 MeV electron beam. The accelerated electron beam is directed on a diamond crystal. This radiator produces a photon beam based on the process of Bremsstrahlung. Bremsstrahlung generated by electron scattering on a lattice structure produces a highly polarized photon beam as can be deduced from the reaction cross section :

$$d\sigma(e \to e' + \gamma) \sim \sum_{\lambda} \int \frac{d^3\vec{k}}{(2\pi)^3} \cdot \frac{e^2}{2k} \left| \vec{\epsilon}_{\lambda} \cdot \left(\frac{\vec{p}'}{p'.k} - \frac{\vec{p}}{p.k} \right) \right|^2 ,$$

	θ	ϕ	Ω
stand 1	13.98	180.	0.092
stand 2	14.52	0.	0.093
stand 3	31.50	0.	0.092
stand 4	50.71	0.	0.094
stand 5	72.13	0.	0.18
stand 6	99.65	0.	0.21
stand 7	143.54	0.	.30

Table IV-3: *The polar and azimuthal angles and associated solid angle volumes used in the calculations. The latter are taken into account to simulate the specific acceptances of TOF.*

with $\vec{\epsilon}_\lambda$ the polarization vector and $\vec{p}(\vec{p}')$ the initial (final) electron momentum. Obviously, the Bremsstrahlung photons are polarized predominantly parallel to the scattering plane and perpendicular to the photon propagation direction. The scattered electrons are detected in the Tagger. The Tagger which consists of a 1 Tesla magnet, is used to determine the energy of the scattered electrons. Due to the mechanical properties of the Tagger, polarized photons are produced with an energy ranging from 100 to approximately 700 MeV.

The reaction products of the photo-induced *pn*- and *pp*-knockout reaction are detected by the PIP-TOF detectors. The pion proton (PIP) detector is positioned behind the target and perpendicular to the photon beam. The proton, or for pp-knockout one of the protons, is detected by PIP. PIP spans a polar angle ranging from 69 to 126 degrees and has an azimuthal acceptance of $\pm$ 21 degrees. To keep the calculations manageable, the cross section will be evaluated at the center of PIP ($\theta = 90$ and $\phi = 180$ degrees) and weighted by the covered solid angle (i.e. 1.03 sr) to account for the total acceptance of PIP. The second reaction product, a proton or a neutron, is captured by the TOF detector. The time of flight (TOF) detector consists of up to 7 detector stands covering a wide polar angle extending approximately from -20 to 150 degrees. Its azimuthal acceptance varies over the several stands with an average value of $\pm$ 20 degrees. As for the PIP detector, each of the seven stands of TOF will be reduced to one single point in space when

performing the numerical calculations. The angular acceptances are implemented by means of a weight factor equal to the covered solid angle. Table IV-3 gives an overview of the angular positions of the various detector stands together with their respective solid angle acceptances. With the aid of a start and veto detector (SVD) who wraps the target cell, TOF can discriminate between a proton and a neutron.
The energy acceptance of the PIP and TOF detectors is confined to the range $[40, 250]$ MeV. The upper bound of 250 MeV for TOF was imposed so as to ensure that protons and pions could be unambiguously discriminated.
To account for the fact that the detectors have a finite resolving capability, one has to average the theoretical quantities. Meaning, before comparing the data with the model calculations a smoothing of the latter, as a function of the quantity depicted on the x-axis, has to be performed. The calculated cross sections for PIP-TOF kinematics presented in this work will be denoted as :

$$\left(\frac{d^6}{dT_1 D\Omega_1 DT_2 d\Omega_2}\right)_{\text{int}} \quad .$$

The latter is a short notation for the six dimensional cross section integrated over the available PIP-TOF phase space :

$$\left(\frac{d^6\sigma}{dT_1 d\Omega_1 dT_2 d\Omega_2}\right)_{\text{int}} \quad = \quad \int_{\text{PIP-TOF phase space}} \frac{d^6\sigma}{dT_1 d\Omega_1 dT_2 d\Omega_2} dT_1 d\Omega_1 dT_2 d\Omega_2 \quad .$$

Our model, outlined in chapter III, incorporates apart from genuine two-body absorption mechanisms also a multitude of rescattering terms, i.e. the recoil diagrams. The latter appear in a natural way when both SRC and COM correlations are included. As a consequence, our reaction model is designed to model the data over a wide range of E_m and p_m (see Eq. IV-3). Albeit some of the rescattering processes are accounted for, our theoretical description does not account for pion reabsorption and production. Neither does it account for the final state interactions (FSI) apart from the recoil terms. Fig. IV-18 shows a Monte Carlo simulation displaying the strengths stemming from the various reaction mechanisms contributing to NN knockout. The calculations fail in describing the ^{4}He data whereas for the ^{12}C data a good agreement is obtained. This can be attributed to the treatment of the nucleus as a Fermi gas, which can only be expected to be a reasonable approximation for medium heavy and heavy nuclei. Nevertheless, the Monte-Carlo calculations from the Valencia group allow to draw various conclusions about the general features and trends of the underlying reaction mechanisms to photo-induced two-nucleon knockout processes. First, the impact of FSI is much smaller for *pn*- than for *pp*-knockout. Second, for *pp*-knockout, FSI, rescattering terms and pion production account for most of the cross section. Third, a cut in missing energy at 50 MeV ensures that mostly genuine two-nucleon knockout processes are retained. Fourth, the rescattering (3N and even 4N) effects are more pronounced for *pp*- then for *pn*-knockout.

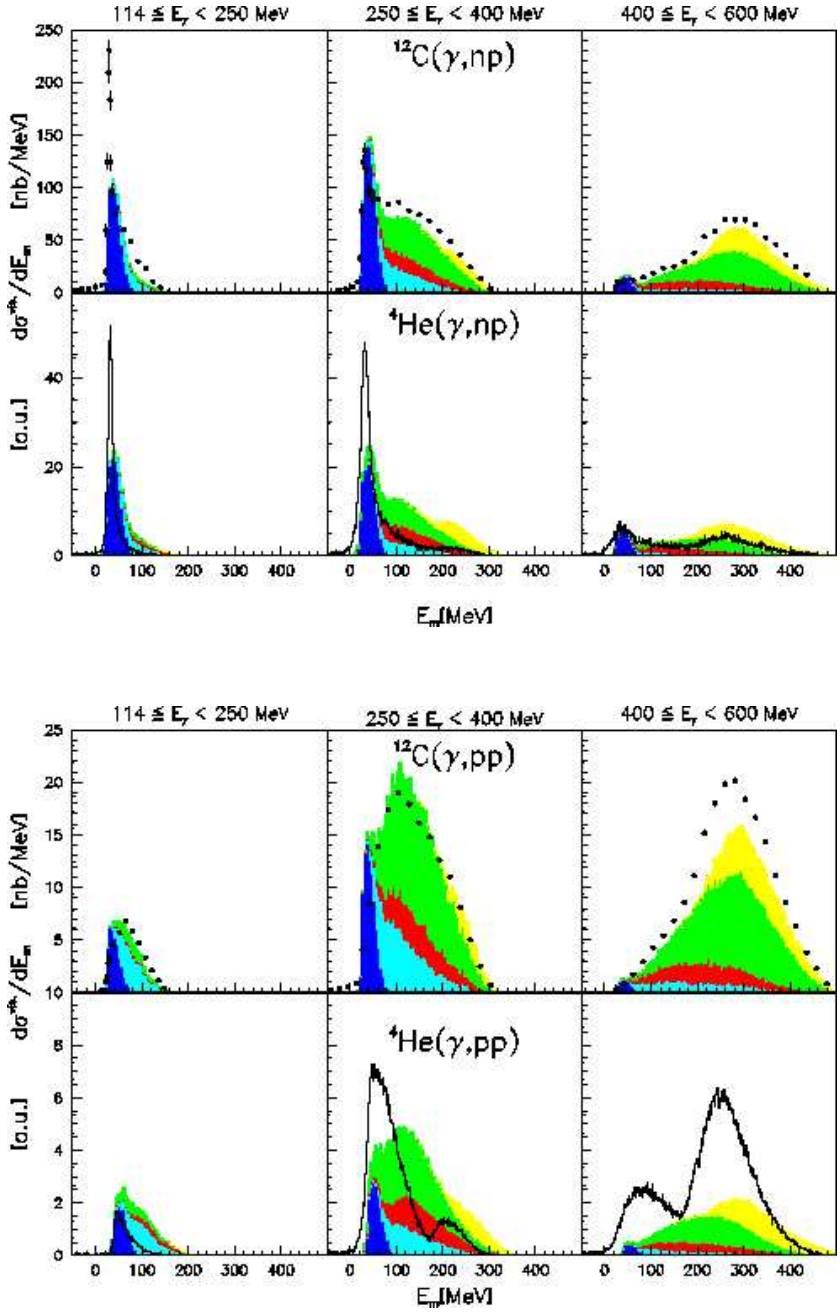

Figure IV-18: *Comparison of the (γ, np) (top) and (γ, pp) (bottom) experimental data (points) for three photon energy bins with the Valencia model (stacked histograms) for ^{12}C and ^{4}He. The different shaded regions represent : NN direct photo-absorption on a nucleon pair without (dark blue) and with FSI (light blue), 3N absorption (red), 1N absorption with pion reabsorption (green) and pion emission (yellow) [130].*

Fifth, FSI mechanisms, as such, are less important for NN-knockout from ^{4}He then they are for medium-heavy nuclei. Each of the above five remarks will be reconsidered, in the light of our theoretical results, in the course of this section.

§2.4.1 The ^{4}He$(\gamma, NN)NN$ cross section: a discussion

Fig IV-19 displays the results of the numerical calculations for *pp*- and *pn*-knockout from ^{4}He. The data acquired by the A2 collaboration are also shown. From Fig IV-19, one can conclude that the reaction model calculations are in fair agreement with the data both for *pp*- and *pn*-knockout. Although no cuts in missing energy were imposed, the model succeeds in describing the data for photon energies ranging from 100 up to 600 MeV.
Fig. IV-19 illustrates some general features. First, the deviation between the *pp* knockout data and the theoretical cross section at low photon energies, can be attributed to FSI mechanisms. Fig. IV-18 indicates that FSI mechanisms are much more important for *pp*- than for *pn*-knockout. This may explain why an equivalent mismatch at low photon energies is not observed for *pn*-knockout. On the other hand, when the transferred energy is raised FSI's lose in importance as noticed from Fig. IV-18. This explains the overall agreement between theory and experimental data once the photon energy exceeds 300 MeV. Concluding, the aforementioned remarks about the impact of FSI is in agreement with our reaction model calculations. Second, the delta contribution is rather small in both *pp*- and *pn*-knockout. This observation is in contradiction with the findings made in electromagnetically induced two-nucleon knockout reactions from nuclei like ^{12}C and ^{16}O [131] where the Δ plays a dominant role in the reaction process. Fig. IV-5 and Table IV-2 throw some light upon this issue. On the one hand, based on Table IV-2 and the observation that the nucleons in ^{4}He reside predominantly in an *s*-wave one-particle state, one might conclude that the only possible proton-proton relative wave function is a $^1S_0(T=1)$ state. For *pn*-knockout, on the other hand, apart of a $^1S_0(T=1)$ state also a relative $^3S_1(T=0)$ configuration belongs to the possibilities. In Sect. §2.2 it was printed out that relative S states produce small Δ-current contributions. The comparison of the data with the calculations contained in Fig. IV-19, seem to confirm the suppression of the delta contribution in ^{4}He, which is evidence for the dominance of relative S states. Third, although our reaction model does neither account for pion reabsorption, nor for real pion production processes it succeeds in explaining the data quite well. This observation might lead us to the conclusion that those processes are somehow suppressed in NN-knockout from ^{4}He for the kinematics under study. For *pn*-knockout this is what one already sees from the Monte Carlo simulations based on the Valencia model. However, the simulation of Fig. IV-18 fails completely when it concerns ^{4}He(γ, pp) at $400 \leq E_\gamma \leq 600$ MeV. This might indicate that other processes, apart from pion reabsorption and emission, strongly contribute. Fig. IV-19 and more in particular the ^{4}He(γ, pn) cross section at high ω,

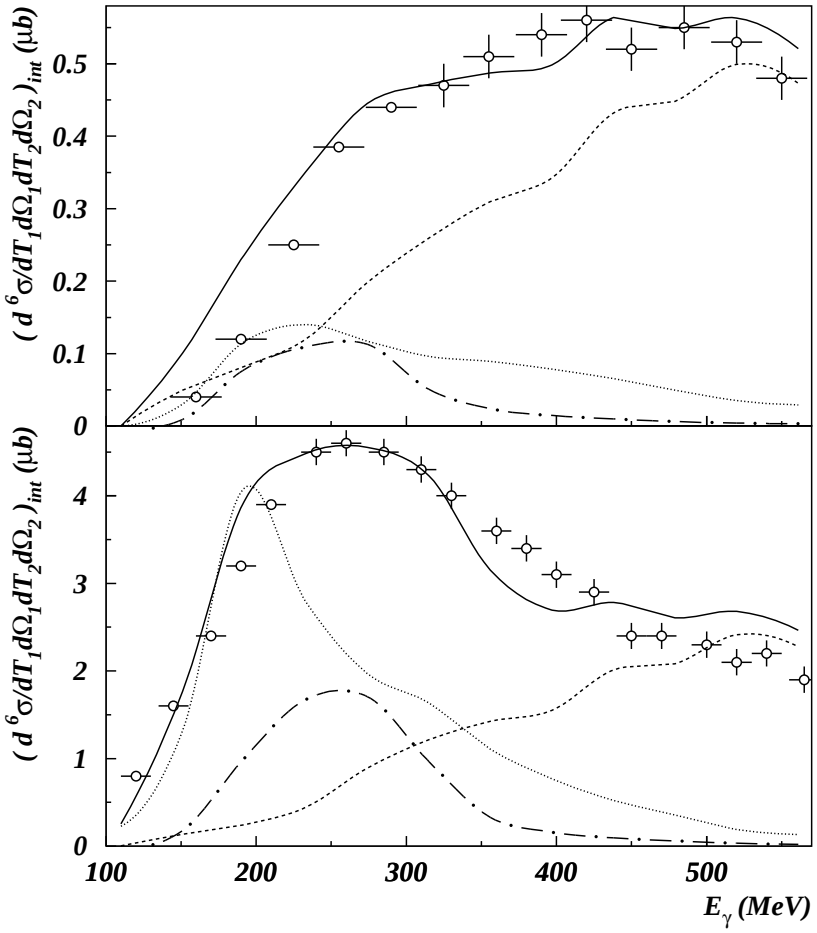

Figure IV-19: *Integrated differential* $^4He(\gamma, pp)nn$ *(upper panel) and* $^4He(\gamma, pn)NN$ *(lower panel) cross sections versus photon energy for PIP-TOF kinematics. The contribution from the different reaction mechanisms are shown : The one-body current (dashed), the meson exchange contribution (dotted), the delta isobar current (dot-dashed) and the total cross section (solid). The data are from the PIP-TOF collaboration [130].*

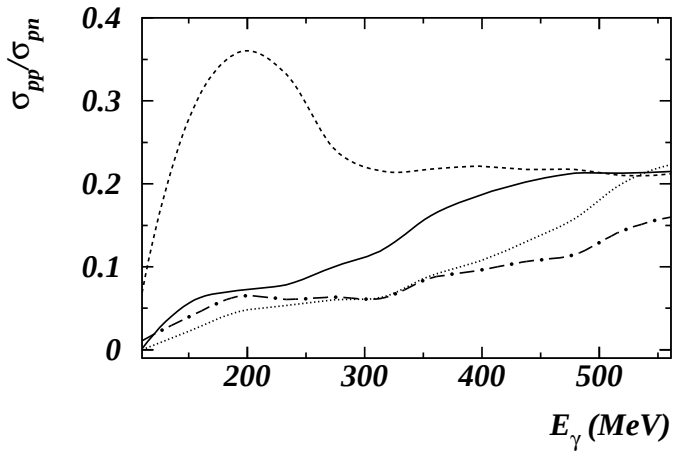

Figure IV-20: *Ratio of the* $^4He(\gamma, pp)nn$ *to the* $^4He(\gamma, pn)NN$ *cross section versus photon energy for PIP-TOF kinematics. The same conventions as in Fig. IV-19 are used.*

indicates that the rescattering diagrams of Fig. III-10 may account for this high missing energy strength. Fourth, based on a previous remark about the available relative states in ^{4}He for respectively *pp*- and *pn*-knockout, the significant difference in their respective strengths can be explained. The larger number of allowed *pn* pairs ($T = 0, S = 1$ and $T = 1, S = 0$) relative to *pp* pairs ($T = 1, S = 0$) as well as the larger number of available reaction channels (e.g. the meson exchange current), let us expect transition strengths which are a factor of 5 to 10 stronger for *pn*- than for *pp*-knockout. This feature is confirmed by the calculations. In addition, Fig. IV-20 depicts the ratio of the photo-induced *pp*- to *pn*-knockout cross section. One notices that the *pp* to *pn* cross section ratio increases steadily with photon energy. With increasing transferred momentum the delta and meson exchange contributions are suppressed due to the $1/q^2$ dependence of the pion propagator. This fall-off is at the origin of the observed steady increase of the $^4\text{He}(\gamma, pp)/^4\text{He}(\gamma, pn)$ ratio. The ratio of the one-body strengths, on the other hand, displays a broad peak at about 200 MeV. The one-body current, as derived in Eq. III-138, consists of two terms i.e. the convection and the magnetization current. Where the convection current describes the coupling of a photon to a proton, the magnetization current accounts for both photon-proton and photon-neutron coupling with a comparable coupling constant (i.e $\mu_p = 2.793$ and $\mu_n = -1.913$). Concluding, the convection current couples twice as strong to a *pp*- than it does to a *pn* pair. Second, the magnetization current makes a less pronounced distinction between a *pp*- and a *pn* pair. For PIP-TOF kinematics,

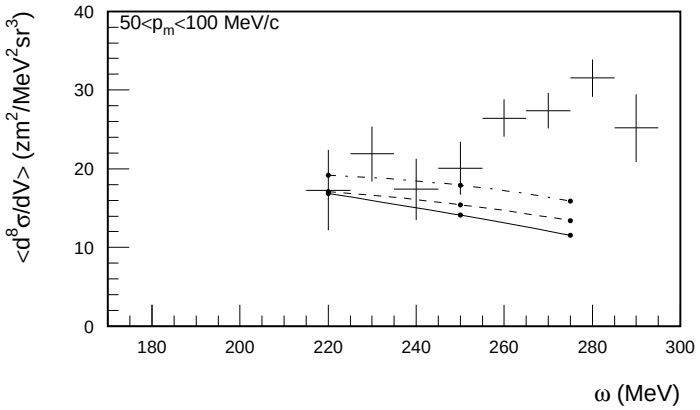

Figure IV-21: *Average* $^3He(e,e'pp)n$ *cross section as a function of transferred energy for* $q = 375MeV/c$ *and* $50 < p_m < 100MeV/c$. *The different curves represent Faddeev calculations with a one-body current only (solid), including MEC's (dashed) and including MEC's as well as static IC's (dot-dashed) [14].*

one-body photo-absorption through the convection current peaks at $E_\gamma \approx 200$ MeV, whilst the magnetization current grows in importance with increasing E_γ. Therefore explaining the enhancement of the one-body strengths ratio observed at 200 MeV. At the high photon-energy side, where essentially only the one-body current contributes, the $^4\mathrm{He}(\gamma,pp)/^4\mathrm{He}(\gamma,pn)$ ratio evolves to a value between 0.2 and 0.25. This value is roughly equal to the ratio of the total number of *pp* to *pn* pairs in the ^{4}He nucleus i.e. $\frac{1}{4}$. The $(\gamma,pp)/(\gamma,pn)$ ratio attributed to the one-body current already reaches this asymptotical value at $E_\gamma \approx 300$ MeV. Summarizing, in kinematical regions where the delta and meson exchange currents prevail the *pn* cross section is much stronger than the *pp* one. For high transferred energies, where only the one-body current survives, a constant ratio of about 0.2 is reached. This indicates that the photon couples with an equal strength to a *pp* as to a *pn* pair. The asymptotical ratio of 0.2 emerges from the mere fact that ^{4}He contains 4 times more *pn* than *pp* pairs.

§2.4.2 The Δ current

The excitation of an intermediate delta in two-nucleon knockout from a medium-heavy nucleus, gives a non-negligible contribution to the reaction cross section provided that the participating nucleons do not reside in a relative S state. Over the years, experimental evidence has been gathered which confirms this for nuclei with $A \geq 12$ [96] [97].
In light nuclei, where the nucleons predominantly populate the $1s$ single-particle states, one expects the delta strength to be small. Fig. IV-19 depicts, for both

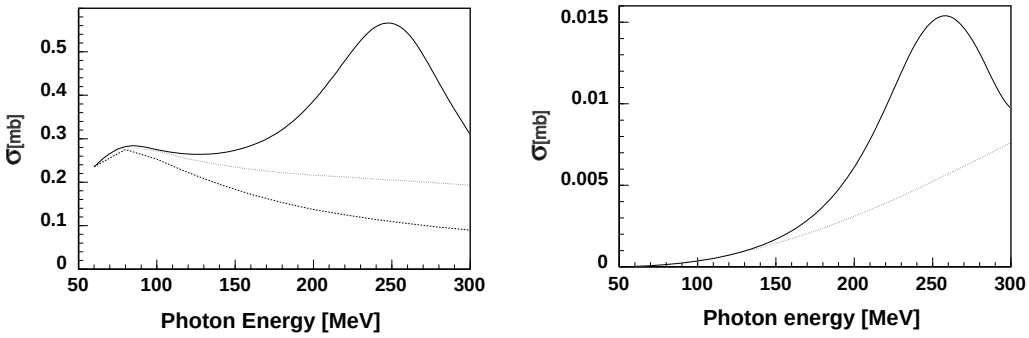

Figure IV-22: *The $^{16}O(\gamma, NN)$ cross section as a function of the photon energy. The left(right) panel depicts pn(pp)-knockout. The MEC contributions are displayed by the dashed curve, the dotted curve depicts the MEC + the static IC while the solid line shows the MEC + energy dependent IC [132].*

the ^{4}He(γ, pp) and ^{4}He(γ, pn) cross section, the contribution stemming from the various reaction mechanisms. Albeit not overshooting all other reaction mechanisms, the delta current is indispensable to arrive at a good description of the two-nucleon knockout reaction. To elaborate on this issue, the calculations performed by the Bochum group, describing the ^{3}He$(e, e'pp)$ reaction [14], will be commented on. Fig. IV-21 displays the results of the Bochum Faddeev calculations for a ^{3}He$(e, e'pp)$ experiment performed at NIKHEF [14]. The different reaction channels are disentangled, i.e. the one-body, MEC and IC current. In these calculations, the Δ excitation emerges as an insignificant background process. The ^{3}He$(e, e'pp)n$ reaction calculations from the Bochum group, however, do not stand the comparison with the data. They come not even close in explaining the observed enhancement of the data located at a transferred energy of $\pm$ 250 MeV. In Ref. [15] Golak puts forward that the static description of the delta could be at the origin of this discrepancy. In the static limit,esteemed valid at sufficiently small q and ω, the resonant and non-resonant delta propagators reduce to :

$$G_\Delta^{\text{res}}(\sqrt{s}) \rightarrow \frac{1}{(m_\Delta - m_N)c^2}$$
$$G_\Delta^{\text{non-res}}(\sqrt{s}) \rightarrow \frac{1}{(m_\Delta - m_N)c^2}$$

The static propagator G_Δ^{res} does not display a resonant behavior as a function of transferred energy explaining the rather flat Δ strength in Fig. IV-21. In 1993, L. Machenil et al. [132] investigated the impact of the choices with respect to the Δ-current propagators on the computed two-nucleon knockout cross sections. Their results are displayed in Fig. IV-22 for ^{16}O(γ, NN). Fig. IV-22 clearly demonstrates the significant difference between the delta current contribution

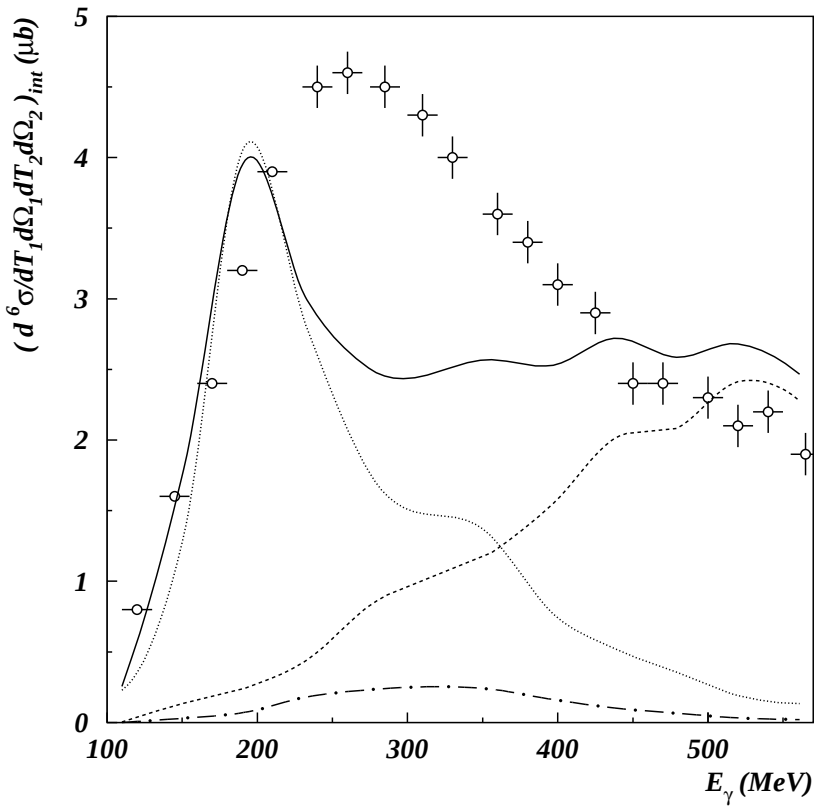

Figure IV-23: $^4He(\gamma, pn)NN$ *cross section obtained with an additional delta width* $\Sigma_I = 30$ *MeV. The same conventions are used as in Fig. IV-19.*

evaluated in the static approximation and with the energy-dependent propagators from Eqs. III-122 and III-124. Only with the latter choice one is able to predict a resonance structure at $E_\gamma \approx 250$ MeV.
An energy-dependent delta propagator (see Eqs. III-122 and III-124) is adopted in our reaction model calculations. The expression for the resonant delta propagator, as derived in Sect. §4.2, looks like :

$$G_\Delta^{res}(\sqrt{s}) \;=\; \frac{1}{m_\Delta c^2 - \sqrt{s_{res}} - i\frac{\Gamma_{\pi N} - 2.\Sigma_I}{2}} \quad ,$$

with $\Gamma_{\pi N}$ the pion-nucleon decay width and Σ_I the decay width stemming from other processes. Oset and Salcedo [114] obtained a closed expression for the latter based on an RPA calculation in nuclear matter including up to 3p3h diagrams. Fig. III-8 plots Σ_I as a function of photon energy based on the Oset and Salcedo parameterization for Σ_I after folding it with the ^{4}He one-particle density. From Fig. III-8, an average value of 30 MeV is obtained for Σ_I. Fig. IV-23 displays the $^4\mathrm{He}(\gamma, pn)$ results for the PIP-TOF experiments [130]. In the calculations, the energy-dependent delta width Σ_I from Ref. [114] has been adopted. Obviously,

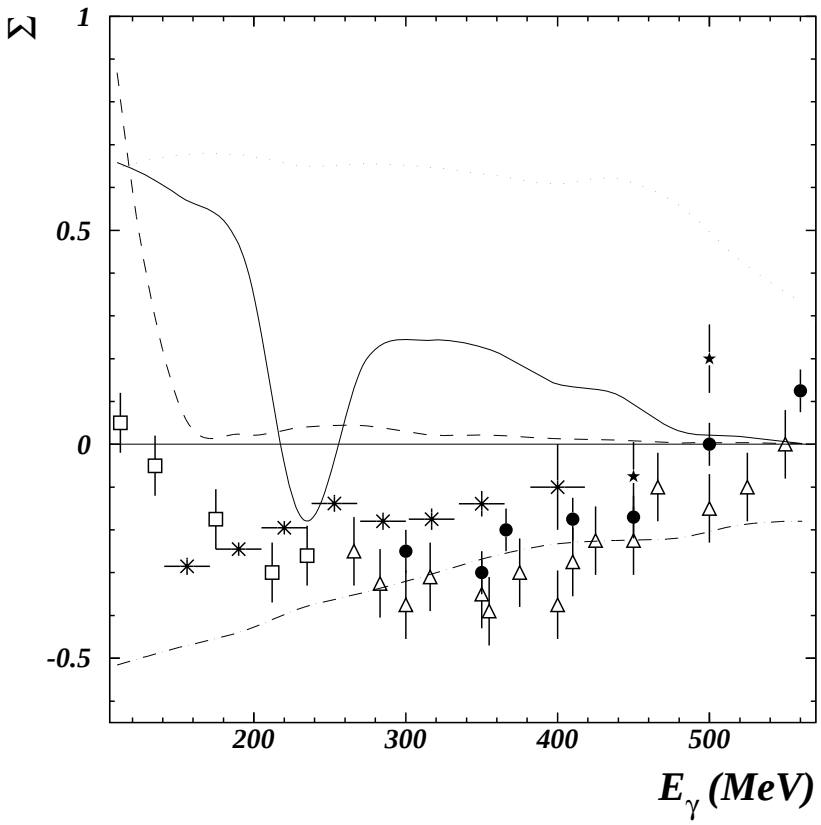

Figure IV-24: *The photon asymmetry $\Sigma_{(\vec{\gamma},pn)}$ is displayed for the different reaction channels namely : the 1-body current (dashed), the meson exchange (dotted) and the delta current (dot-dashed). The solid curve represents the total photon asymmetry. Data are taken from [133] with : $\Sigma_{^2H}$ (△), $\Sigma_{^6Li}$ (●) and $\Sigma_{^4He}$ (★). The deuteron data at low E_γ are taken from [134] (□) while the recent data for ^{4}He are from [130] (✳).*

the predicted delta contribution is small. The data exhibit a peak at $E_\gamma \approx 250$. It appears that in ^{4}He the delta has a much smaller width than expected from the nuclear matter calculations. Hjorth-Jensen et al. [135] also evaluated the width of the delta in nuclear matter at various densities. In general, they find widths smaller than those reported in Ref. [114]. For the nuclei ^{16}O, ^{40}Ca and ^{100}Sn, adopting a HO description for the bound states, they obtained a smaller width Σ_I than the typical values of Ref. [114]. In addition, they observed a decrease of the delta width for smaller mass numbers A. Based on this observation, we recalculated the $^4\mathrm{He}(\gamma, pn)NN$ cross section accounting only for the pion-nucleon decay width $\Gamma_{\pi N}$. The results are depicted in Fig. IV-19. They agree remarkably well with the data irrespective the fact that we put, somewhat artificially, Σ_I equal to zero. This obvious success may indicate that a Δ resonance created in

the ^{4}He nucleus, is not subject to additional decay mechanisms apart from the usual $\Delta \rightarrow \pi N$ decay. A possible argument can be that the $3p3h$ diagrams which are accounted for by the authors of Ref. [114] in their Σ_I calculations, are almost non-existent in light nuclei.
Concluding, the description of the delta current has a major impact on the calculated cross section. It was already recognized that a static approximation can not account for the resonant structure observed in the reaction cross section. It is clear from our analysis that also the width of the delta is an important ingredient in the model calculations.

In order to further explore the role played by the Δ, we investigated the photon asymmetry Σ for the ^{4}He$(\vec{\gamma}, pn)NN$ reaction. In Ref. [125] it is claimed that the photon asymmetry, at intermediate photon energies, is only marginally depending on the mass number. The latter was confirmed by Adamian et al. [133] who compared the available data on the photon asymmetry for ^{2}H, ^{4}He and ^{6}Li. Fig. IV-24 compares our ^{4}He$(\vec{\gamma}, pn)NN$ photon asymmetry predictions with experimental data from Refs. [133] and [130]. Whereas the measured ^{4}He$(\vec{\gamma}, pn)$ asymmetries are negative, our predictions are positive.
The delta current is known to produce a negative photon asymmetry while the one-body and meson exchange currents give rise to a positive photon asymmetry (see Ref. [125]). This is confirmed by our calculations in Fig. IV-24. In addition, some general conclusions can be drawn. First, at low energies, the photon asymmetry is dominated by the meson-exchange current and more in particular the seagull term. At $E_\gamma \approx 100$ MeV, the deuteron data display a positive photon asymmetry. Alluding to an argument made earlier, the deuteron photon asymmetry seem to confirm the dominance of the meson-exchange current at low E_γ. Second, at the high energy side, the reaction process is driven predominantly by the one-body current. For large transferred momenta, the one-body response stems almost entirely from the magnetization current. Whereas the magnetization current shows a functional dependence on $\vec{\sigma} x \vec{p}_\gamma$, the corresponding photon asymmetry vanishes once the final summation over the nucleon spins is performed. The data displayed in Fig. IV-24 seem to confirm this. Third, at $E_\gamma \approx 240$ MeV the delta current forces the photon asymmetry to become negative. Concluding, at the low and high energy side as well as at the delta peak, the calculations display the same trends as the data. Whereas, beyond these particular regions, the calculations fall short in explaining for the data. As of now, no solution has been found. Although, a few have been proposed e.g. the admixture of higher angular momentum states in the ^{4}He wave function. This would produce a stronger delta relative to the other reaction channels as alluded to above, reducing the photon asymmetry significantly. Whether this resolves the observed discrepancies still remains an open question. Future research addressing the Mainz measurements may provide more insight in this matter.

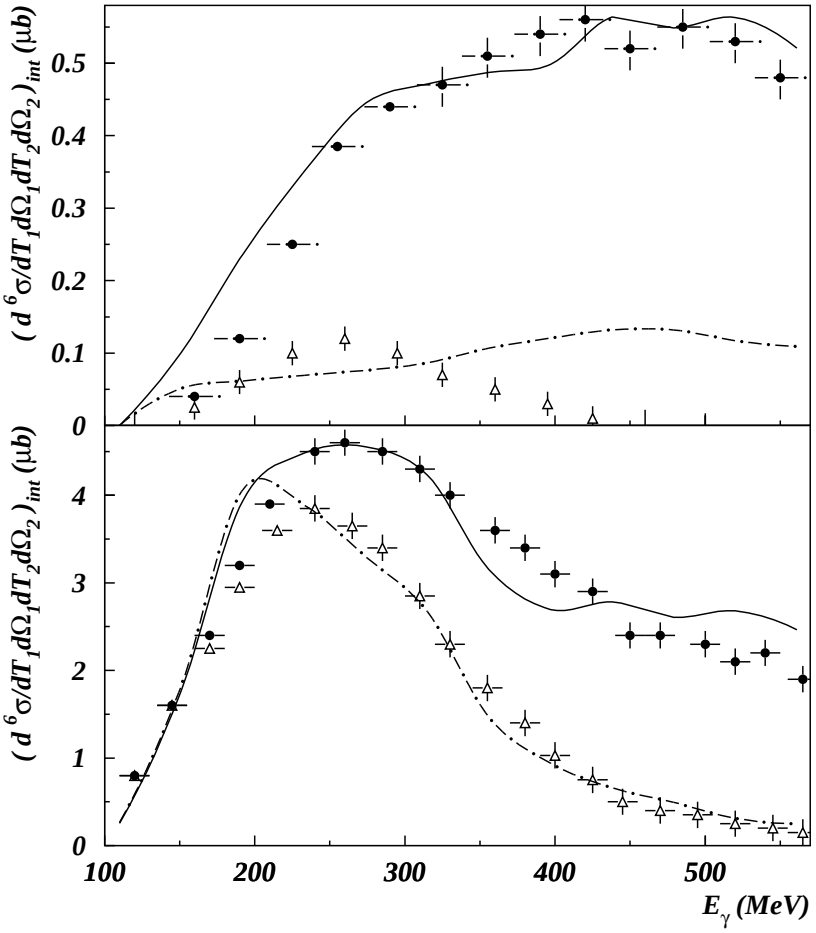

Figure IV-25: *Integrated differential* $^4He(\gamma, pp)nn$ *(upper panel) and* $^4He(\gamma, pn)NN$ *(lower panel) cross section versus photon energy for PIP-TOF kinematics. The solid lines account for all diagrams contained in Fig. III-10. The dot-dashed curves are the predicted when ignoring the recoil diagrams and including solely the diagrams of Fig. III-10 contained in the (red) boxes. The data indicated with the solid circles do not impose a cut in* E_m*, whereas for the open triangles the additional condition* $E_m \leq 45$ *MeV was demanded [130].*

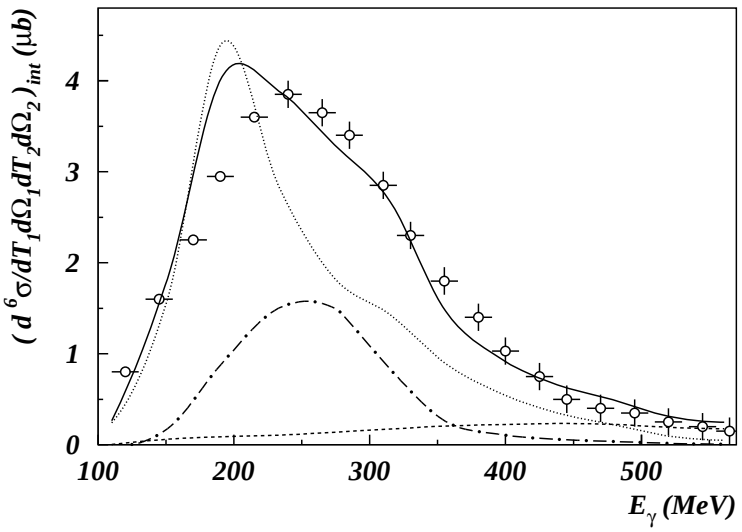

Figure IV-26: *Integrated differential* $^4He(\gamma, pn)NN$ *cross section versus photon energy for PIP-TOF kinematics including only the common two-nucleon knockout diagrams of Fig. III-10. The same conventions are used as in Fig. IV-19. For the data a cut on missing energy i.e.* $E_m < 45$ *MeV was used [130].*

§2.4.3 Recoil effects

Elucidating the role played by the recoil diagrams as defined in chapter III, is one of the major goals of this work. Whereas in medium-heavy and heavy nuclei recoil effects can be expected to be negligible, they can not by ignored when addressing light systems. The naive picture of a nucleus as a manifold of point-like nucleons swirling in an average potential doesn't suffice for light nuclei. There, the nucleus has to be described as a coupled system of mutually interacting particles. Pulling at one of the nucleons, will have its effect on the entire system. This response of the nuclear system, to an external event, is denoted by the term recoil. Fig. III-10 depicts for the two-nucleon knockout process from ^{4}He, apart of the direct knockout terms, all recoil diagrams. Long-range correlations emerge when adjusting the nuclear wave function to account for the recoil mechanisms. Thereby, the frequently adopted technique is making the nuclear wave function translationally invariant. Fig. IV-25 illustrates, for both the $^4\mathrm{He}(\gamma, pp)nn$ and $^4\mathrm{He}(\gamma, pn)NN$ reaction, the impact of the recoil effects. The data shown are taken from [130]. A constraint in missing energy, i.e. $E_m < 45$ MeV is put forward as a criterion to suppress the contributions of the recoil diagrams. It is

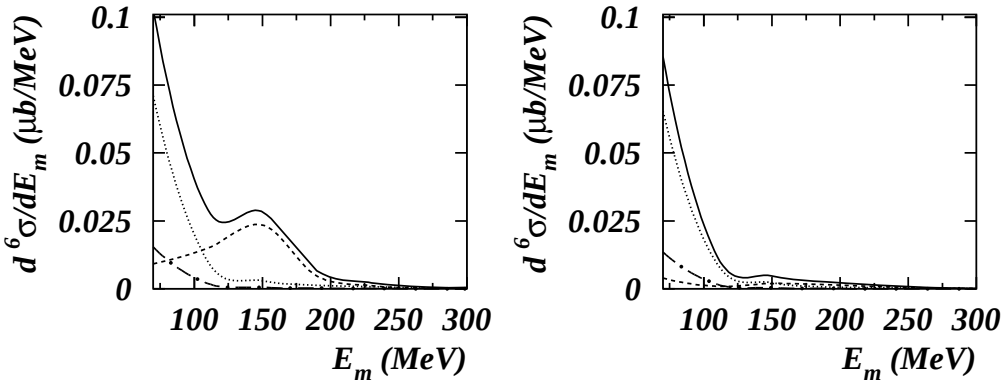

Figure IV-27: *Integrated differential* $^4He(\gamma, pn)NN$ *cross section versus missing energy for PIP-TOF kinematics at* $\omega = 400$ *MeV. The left panel implements all diagrams of Fig. III-10, whereas for the right panel the recoil diagrams are neglected. The same conventions are used as in Fig. IV-19.*

an understatement to say that the recoil diagrams are indispensable to describe the reaction cross section. For *pp*-knockout, the data and the reaction-model calculations indicate that the direct knockout diagrams contribute significantly even at relatively high missing energies $E_m > 45$ MeV. The *pn* calculations fit the data quite well. This applies to both the situations whereby no E_m-cut has been imposed (data with solid circles and theory with solid curves) and the more restricted phase-space coverage imposed by setting $E_m < 45$ MeV (open triangles and dot-dashed curves). From Fig. IV-25 one can conclude that only at low missing energies the spectator approximation, well-known from medium-heavy and heavy nuclei, is able to describe the reaction process.

The contribution of the various reaction mechanisms feeding the ^{4}He(γ, pn) cross section is shown in Fig. IV-26. We notice that when selecting events in which the undetected pn pair is left with little excitation energy, the strength stems predominantly from the meson exchange and delta current. The cross section drops with growing transferred energy due to the inverse energy dependence of the pion propagator. This is the common picture for *pn* knockout known from the study of nuclei with $A \geq 12$. The theoretical results overshoot the data at low photon energies. This effect can be attributed to the neglect of FSI rescatterings which are prevailing at low energies. From Fig. IV-19 and Fig. IV-26 some conclusions can be drawn. First, the meson-exchange and delta current

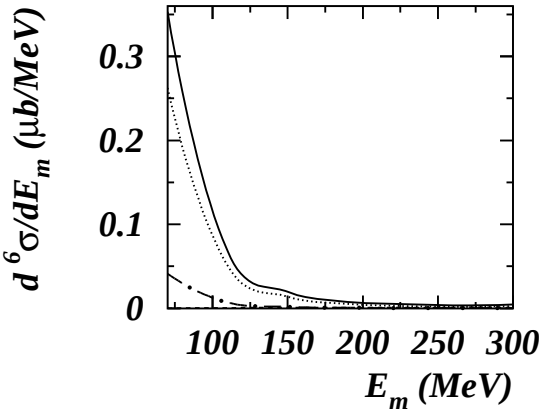

Figure IV-28: *Integrated differential* $^4He(\gamma, pn)NN$ *cross section versus missing energy for PIP-TOF kinematics and* $\omega = 400$ *MeV. A HO wave function has been used. The same conventions are used as in Fig. IV-19.*

strengths in the $^4\mathrm{He}(\gamma, pn)$ cross section are generated almost exclusively by the direct knockout diagrams. The charge exchange character of both currents, will make most of the recoil diagrams vanish in *pn*-knockout.

For the case of *pp*-knockout, the same argument explains the non-negligible contributions arising from the delta and meson currents once recoil diagrams are included. Second, the one-body channel is preferentially feeded by the recoil diagrams. The energy acceptance of the detectors (T_p in $[40, 250]$ MeV) will suppress the one-body contribution in the direct knockout response where the photon is absorbed entirely on one of the detected nucleons. This argument will definitely be true at higher photon energies. For the recoil diagrams, they do not suffer from this restraint. As a direct consequence, in PIP-TOF kinematics the recoil diagrams will dominate at higher photon energies. Fig. IV-27 displays the $^4\mathrm{He}(\gamma, pn)NN$ cross section as a function of missing energy for $E_\gamma = 400$ MeV.

$$\frac{d^6\sigma}{dE_m} = \int_{\text{PIP-TOF phase space}} \frac{d^6\sigma}{dT_p d\Omega_p dT_n d\Omega_n} \delta(E_m - 400 + T_p + T_n) dT_p d\Omega_p dT_n d\Omega_n \ .$$

In the left panel, the recoil diagrams are accounted for where in the right panel only the direct knockout terms are retained. At $E_m \leq 120$ MeV almost the complete cross section can be attributed to the direct knockout diagrams. For the recoil diagrams, they dominate the higher missing energies. Further the recoil diagrams have their largest effect in combination with the one-body current. The

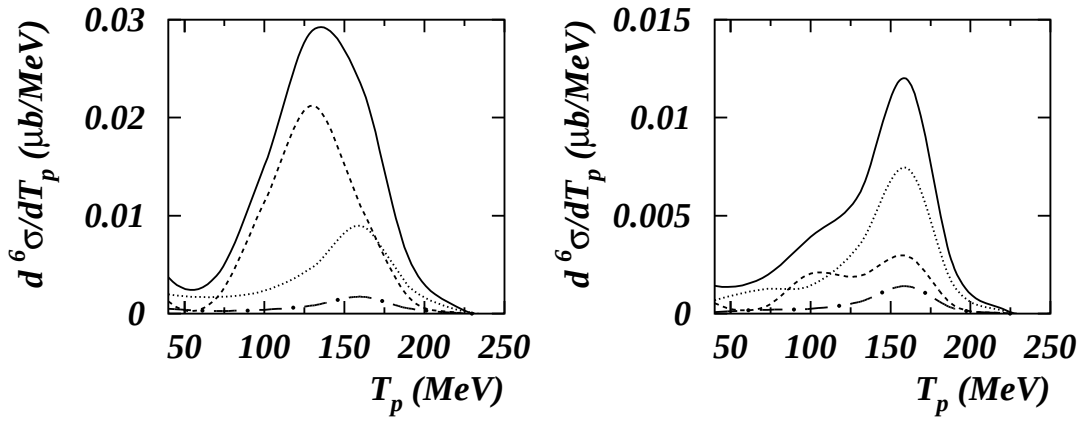

Figure IV-29: *Integrated differential* $^4He(\gamma, pn)NN$ *cross section versus kinetic energy* T_p *for PIP-TOF kinematics at* $\omega = 400$ *MeV. The left panel implements all diagrams of Fig. III-10, whereas for the right panel the recoil diagrams are neglected. The same conventions are used as in Fig. IV-19.*

latter processes give us a clear glimpse within the nucleus. No corrections accounting for the particular reaction process involved, have to be performed whilst the detected nucleons escaped from the nucleus without any external interaction. Therefore the recorded kinetic energies, T_1 and T_2, can be related to the average kinetic energy of the nucleons within the nucleus :

$$E_m \;=\; \omega - T_p^f - T_n^f \approx \omega - 2 < T^i > ,$$

with, $< T^i >$ the average nucleon kinetic energy. Based on this formulae, an average kinetic energy of 125 MeV and an average nucleon momentum of 500 MeV is obtained. This may indicate the presence of short-range correlations. Fig. IV-28 shows analogous curves as in the left panel of Fig. IV-27 but adopts a HO wave function. Despite the fact that the recoil diagrams are implemented, the one-body term (dashed curve) plays only a limited role. This confirms our statement concerning the presence of short range correlations. Concluding, one can state that by studying the two-nucleon knockout strength at high E_m, one can extract information about the nucleon dynamics. This strategy is adopted in the analysis of the ^{3}He$(e, e'p)pn$ measurements in Ref. [127].

Fig. IV-29 shows, for a transferred energy of 400 MeV, the ^{4}He$(\gamma, pn)NN$

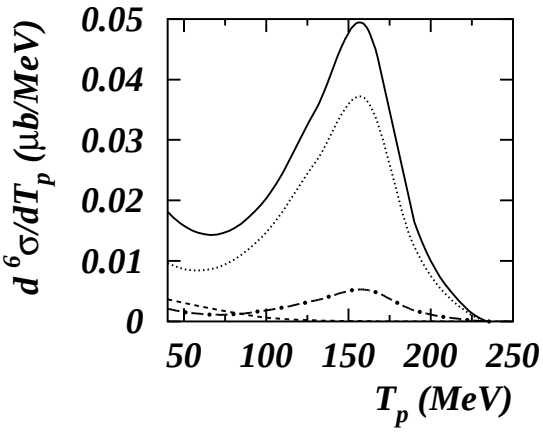

Figure IV-30: *Integrated differential* $^4He(\gamma, pn)NN$ *cross section versus kinetic energy* T_p *for PIP-TOF kinematics at* $\omega = 400$ *MeV. A HO wave function has been used. The same conventions are used as in Fig. IV-19.*

cross section as a function of the proton kinetic energy.

$$\frac{d^6\sigma}{dT_p} = \int_{\text{PIP-TOF phase space}} \frac{d^6\sigma}{dT_p d\Omega_p dT_n d\Omega_n} \delta(T_p - 400 + T_n + E_m) dT_p d\Omega_p dT_n d\Omega_n \ .$$

As in Fig. IV-27, the left panel accounts for all diagrams whereas in the right panel only the direct knockout terms are retained. The meson exchange and delta current contributions do not change significantly whether or not one adopts the spectator approximation. Most of the strength can be attributed to the one-body current stemming from the recoil terms. In the spectator approximation, one notices two broad shoulders in the one-body contribution (dashed curve). The peak at 150 MeV corresponds to photo absorption by the neutron. When the photon interacts with the proton (detected by TOF) strength appears in the smaller peak at lower T_p. The left panel shows a totally different picture. One notices just one major peak at 125 MeV. The recoil diagrams generate most of this strength. Again, one can state that the one-body strength reflects the momentum distribution of the proton in ^{4}He. Again, we arrive at a value of $T_p \approx 125$ MeV for the initial kinetic energy. In line with the observations made when studying the E_m dependence of the $^4\text{He}(\gamma, pn)$ cross sections, the one-body current is heavily suppressed when using a HO instead of a realistic wave function (see Fig. IV-30).

The recoil diagrams, commonly neglected in the study of medium and heavy

nuclei, are indispensable when light nuclei are addressed. For both pp and pn knockout they appear at transferred energies above 200 MeV. By studying the recoil effects, information about short-range dynamics can be obtained. For the recoil diagrams describe the process where a nucleon escapes from the nucleus without any additional interaction apart of FSI. So we do not have to account for the dynamics of the specific reaction process involved. The major advantages offered by this technique are already perceived by the authors of [127].

§2.4.4 Short-range correlation

In the previous subsection we made some remarks about short-range correlations and how they can be hunted with two-nucleon knockout reactions. Guided by an analysis of a $^3\mathrm{He}(\gamma,p)pn$ experiment at TJNAF [127], we computed the $^4\mathrm{He}(\gamma,pp)nn$ cross section for $\omega = 400$ MeV as a function of the opening angle between the two detected protons.

$$\frac{d^6\sigma}{d\theta_{pp}} = \int_{\text{PIP-TOF phase space}} \frac{d^6\sigma}{dT_p d\Omega_p dT_p d\Omega_p} \delta(\theta_{pp} - (\theta_{p_1} - \theta_{p_2})) dT_p d\Omega_p dT_p d\Omega_p \, .$$

One of the protons is detected by PIP which is placed perpendicular to the photon beam. The other proton has hit one of the detector stands of the TOF detector. Fig. IV-31 displays the corresponding cross section. For the left panel all diagrams are included whereas for the right panel the spectator approximation is adopted. Comparing both plots, one may conclude that, in the spectator approximation, the neutron is emitted predominantly parallel to the incident photon beam. When recoil diagrams are accounted for, a strong peak appears at an opening angle of ± 180 degrees triggered by the one-body current. In other words, whenever the detected pair acts as a spectator, the corresponding nucleons are emitted predominantly back-to-back. The suppression of the direct knockout process relative to the recoil reaction can be explained by the high momenta required in the former reaction type to compensate for the large photon momentum. From Fig. IV-31 it is clear that the entire strength located between 150 and 200 degrees stems from genuine recoil diagrams. One can conclude that the detected pair moves back-to-back in the nuclear medium. This is a well-known hinting at the presence of short-range correlations. The detected proton pair was subject to heavy repulsion forcing them to escape in a back-to-back configuration. In order to substantiate this claim, we calculate the cross section in coplanar and symmetrical kinematics. Coplanar and symmetrical kinematics corresponds with the situation where the detected nucleons escape with equal kinetic energies and polar angle with respect to the direction of the momentum transfer. For fixed energy transfer $\omega = 400$ MeV and kinetic energy of the detected nucleons $T_p = 120$ MeV, we have plotted the cross section relative to the polar angle in Fig. IV-32. By varying the polar angle from 40 to 140 degrees, the missing momentum P_m increases. For the scanned relative momentum, it

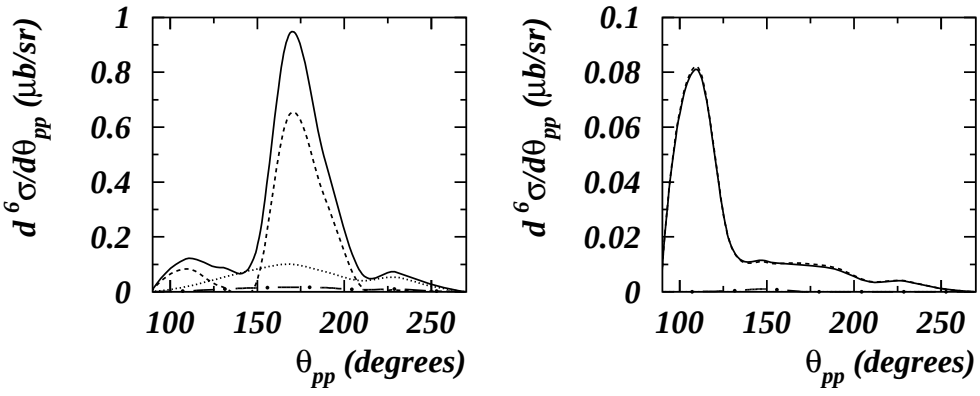

Figure IV-31: *Integrated differential* $^4He(\gamma, pp)nn$ *cross section versus the LAB-frame opening angle* θ_{pp} *for PIP-TOF kinematics at* $\omega = 400$ *MeV. The left panel includes all recoil diagrams whereas the right panel adopts the spectator approximation. The same conventions are used as in Fig. IV-19.*

reaches a maximum at 90 degrees. By selecting only those events in which the kinetic energy of the detected nucleons is high, one can hope to observe a glimpse of the elusive short-range correlations. An analogue reasoning is outlined in the paper by Weinstein et al. [127]. Fig. IV-32 displays two different reaction calculations i.e. the left panel shows the full calculations including all terms of Fig. III-10 while for the right panel the spectator approximation is adopted. At small opening angles, the transition strength can be attributed almost completly to the direct knockout diagrams. For the high kinetic energies selected, a two-body process is required to transfer part of the photon momentum to the other nucleon. The meson-exchange current fulfills this role as can be observed from Fig. IV-32. The peak observed at ± 90 degrees is generated solely by one-body mechanisms regarding recoil diagrams are included. The same signal is obtained from Fig. IV-31. To elucidate whether or not short-range correlations are at the origin of this strong response, we computed the $^4\mathrm{He}(\gamma, pn)NN$ cross section in coplanar and symmetrical kinematics using a HO wave function. Fig. IV-33 displays the results of these calculations. For a HO description inherently lacks all kinds of short-range correlations, we expect no peak at ± 90 degrees. This is confirmed by Fig. IV-33. A HO description supports apparently only the direct knockout processes for no recoil effects are observed. Therefore, one may conclude that the peak at $\theta_{pp} \approx 180$ degrees reflects the presence of SRC.

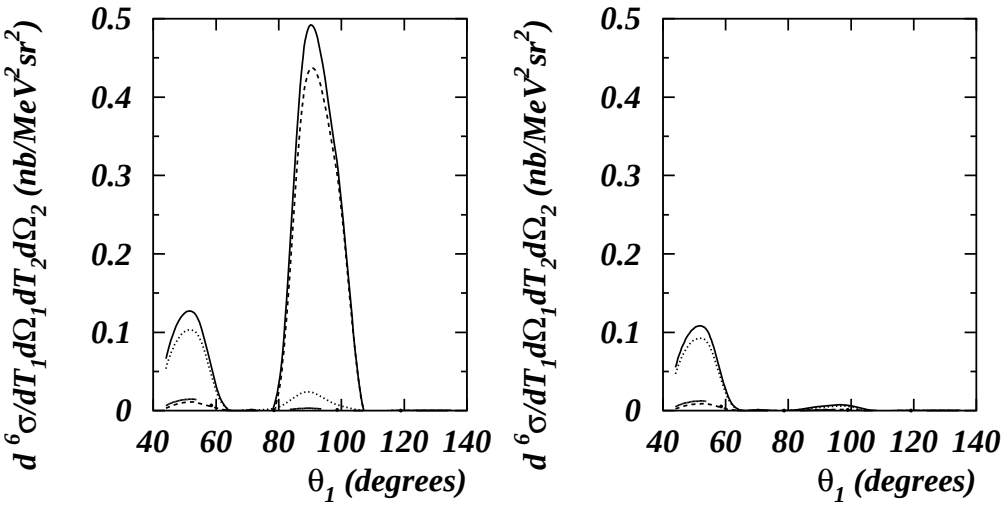

Figure IV-32: *Integrated differential* $^4He(\gamma, pn)NN$ *cross section versus opening angle* θ_{pn} *for coplanar and symmetrical kinematics with* $\omega = 400$ *MeV and* $T_p = 120$ *MeV. The left panel includes all recoil diagrams whereas the right panel adopts the spectator approximation. The same conventions are used as in Fig. IV-19.*

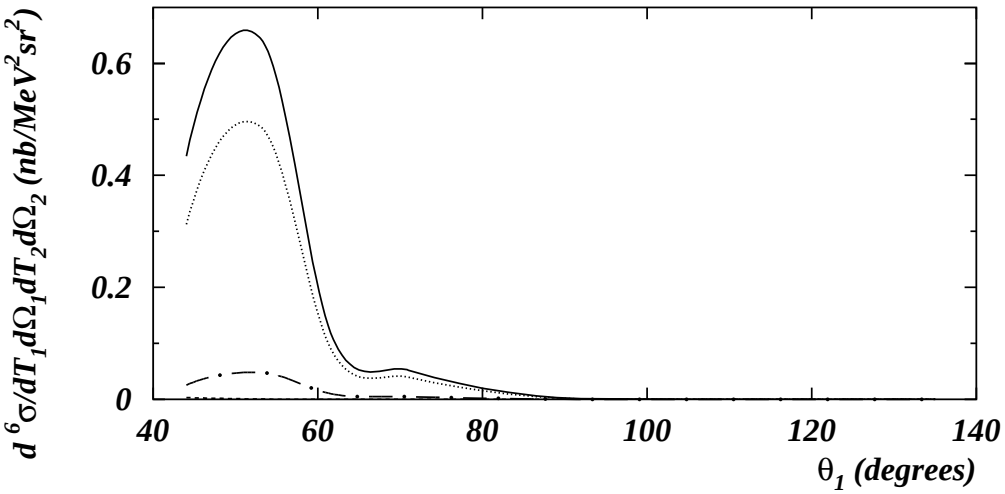

Figure IV-33: *Integrated differential* $^4He(\gamma, pn)NN$ *cross section versus opening angle* θ_{pn} *for coplanar and symmetrical kinematics with* $\omega = 400$ *MeV and* $T_p = 120$ *MeV. A HO wave function has been used. The same conventions are used as in Fig. IV-19.*

Summarizing the findings of this subsection. First, by studying the two-nucleon knockout reaction at high missing energies, a clear signal of the short range correlations can be obtained. Second, the nucleons composing ^{4}He are subject to violent repulsions triggered by the short-range correlations. Their presence can be experimentally confirmed at an opening angle of 180 degrees.

Summary

The study of nucleon-nucleon dynamics inside the nuclear medium is one of the primary goals of intermediate-energy nuclear physics. As easy as it is to formulate, as difficult it is to model the dynamics of the nucleons populating the nuclear system. For years, to solve for the exact nuclear wave function has been the holy grail in nuclear physics. Though as Walecka once said, there are two ways of doing physics. One can try to find an approximate solution for the original problem, or one can exactly solve for a related, more simplified, problem. As of today, the most successful theory to describe the nucleus (i.e. the nuclear shell model) adheres to the second point of view. The nuclear shell model reduces the original coupled N-body problem to a more simple one of N nucleons moving independently in a properly constructed average potential. Corrections on this picture are in order when probing inter-nucleon dynamics at a length scale of the order of 0.5 fm. At these short inter-nucleon distances, the strong repulsive nature of the nuclear force will show up, and the nuclear shell model description will be at stake. Over the years, all kinds of techniques have been developed to correct the shell model for the so-called short-range correlations (SRC). The correlated basis functional theory (CBF) is the most widely spread.

With the advent of increasingly fast computers, the hope to solve the nuclear problem exactly grows, at least for light nuclei. The Argonne-Urbana, Bochum, Trento and Pisa groups succeeded in solving the coupled N-body nuclear wave function for a few light nuclei like ^{3}He, ^{4}He, ... Whereas a typical nuclear shell-model wave function lacks translational invariance, the ones obtained from exactly solvable approaches depend solely on the relative coordinates. Due to the requirement of translational invariance and the Pauli exclusion principle, the nucleonic degrees of freedom are strongly intertwined in the nuclear wave function. Subsequently, it remains a challenging task to compute the transition matrix elements. In this work, a model to describe the two-nucleon knockout process from ^{4}He based on the Argonne-Urbana wave function was presented. The direct motivation for this work was to investigate whether one we could reproduce the available two-nucleon knockout data from ^{4}He. In addition, we addressed the issue of how to find signatures of the elusive short-range correlations. From the nuclear density (twice as high as in nuclear matter), one expects them to be manifestly present in ^{4}He. To preserve the translationally invariant description of ^{4}He, additional diagrams are introduced, i.e. the so-called recoil diagrams. We investigated to what extent they have an influence on the four-body breakup reaction process.

From two-nucleon knockout studies in medium-heavy nuclei, some kinematics are

known to be particularly sensitive to short-range correlations. Four kinematical regimes are treated throughout this work. First, QD-kinematics, selecting only those events with $P_m \approx 0$, is adopted to study the electro-induced two-proton knockout reaction. As no data exist for this specific part of the phase space, we compared our results with ^{3}He calculations by J.M. Laget. Up to some scaling factor, both cross sections display identical features. This observation speaks in favor of the reliability of our model calculations. In addition, short-range correlations were demonstrated to be present in the ^{4}He nucleus. Throughout this work, the effect of SRC mechanisms is estimated by comparing four-body breakup predictions obtained with a HO ^{4}He wave function to those obtained with a realistic wave function. Indeed, as a HO wave function lacks inherently short-range correlations, this is esteemed to be an unambiguous technique to quantify SRC mechanisms. In QD-kinematics, the effect of SRC's appear when high initial nuclear momenta are probed. In addition, polarization observables are studied as they are rather insensitive to FSI mechanisms. The transverse component of the transferred polarization is particularly sensitive to short-range correlations whereas the longitudinal component is rather insensitive to the details of the bound-state wave function used.

Second, we carried out calculations for an experiment performed by De Vries at ELSA in Bonn. He measured the ^{4}He$(e, e'pp)$ cross section in back-to-back kinematics as a function of the opening angle between the forward proton and the transferred momentum. In back-to-back kinematics, one probes high relative momenta. The calculations show, on the one hand, that the SRC's are located at high opening angles or, equivalently, at large relative momenta. On the other hand, the recoil diagrams which couple predominantly to the two-body currents in back-back kinematics, also appear at large relative momenta. As the recoil effects for the one-body current contribute solely at large opening angles, a clear signal for the presence of short-range correlations in ^{4}He is obtained.

Third, in a recent experiment conducted by the A2 collaboration at the Mainz facility, both photo-induced pp and pn-knockout cross sections were measured. In this specific kinematical setup, the proton is detected in a wide solid-angle detector positioned perpendicular to the photon beam, whereas the second nucleon is detected over the entire half plane opposite to the proton detector. Our model calculations succeed in reproducing the magnitude of the ^{4}He(γ, pp) and ^{4}He(γ, pn) cross sections over a wide range of photon energies. The importance of having a proper description for the in-medium delta was outlined. For a resonant Δ should emerge in the energy dependence of the cross section, an energy-dependent propagator is needed instead of the static variant used throughout the Bochum calculations for ^{3}He$(e, e'pX)$. We found that in ^{4}He an intermediate Δ preferentially decays by the well-known $\Delta \rightarrow \pi N$ reaction, whereas the other decay channels are heavily suppressed resulting in $\Sigma_I \approx 0$. Despite the success in reproducing the pp- and pn-knockout cross sections, the interpretation of the ^{4}He$(\vec{\gamma}, pn)$ photon asymmetry remains an open issue. Indeed, the overall photon

energy dependence and importance of the various reaction components contributing to the photon asymmetry (i.e. one-body, meson-exchange and delta currents) agree with what is known for medium-heavy nuclei. Their coherent sum, however, does not reproduce the experimentally determined photon asymmetries. The lack of higher angular momentum admixtures in the ^{4}He wave function, is proposed as a possible explanation. Indeed, non-central correlations are a source of higher angular momentum components entering the ground state. Further research on this topic is needed.
The predicted effects of the recoil diagrams are huge for PIP-TOF kinematics. Both in the $^4\mathrm{He}(\gamma, pp)$ and $^4\mathrm{He}(\gamma, pn)$ cross section, the recoil effects show up once $E_\gamma \geq 200$ MeV. The calculations indicate that most of the recoil strength can be attributed to the one-body current. For their charge-exchange character, the meson-exchange and delta current only weakly couple to recoil mechanisms. Proton-proton knockout, on the other hand, receives large contributions from the meson-exchange and Δ-isobar currents by means of the recoil diagrams. Where the detector acceptances (T_p in $[40, 250]$ MeV) constrain the available phase space in the direct knockout channel, the recoil triggered reactions do not suffer from this shortcoming. This explains the sudden appearance of recoil strength at large photon energies. To study the recoil effects more in detail, cross sections are computed as a function of E_m and T_p at $E_\gamma \approx 400$ MeV. In pn-knockout, the strength from the recoil terms is observed at $E_m > 120$ MeV. Whereas the direct pn-knockout strength can be mainly attributed to the two-body current, the recoil strength is preferentially generated through the one-body current. Comparing the c.s. for a realistic ^{4}He wave function to an identical calculation using a HO wave function, evidences that the recoil strength is due to the presence of short-range correlations. From the position of the recoil peak in the pn cross section plotted against missing energy, a rough estimate for the average nucleon momentum in a correlated pair in ^{4}He of approximately 500 MeV is obtained. From the $^4\mathrm{He}(\gamma, pn)$ cross section studied as a function of the detected proton kinetic energy, the same conclusions can be drawn.
The mere observation of two nucleons escaping back-to-back from the nucleus, is accepted as a clear signal for the presence of short-range correlations. Therefore, we recalculated the $^4\mathrm{He}(\gamma, pn)$ cross section as a function of the opening angle between the escaping nucleons. The obtained results confirm the previous findings : the direct knockout diagrams contribute at small angles whereas the recoil diagrams mainly generate strength at opening angles $\theta_{pn} \approx 180$ degrees. To conclude our investigations into the role of short-range correlations as the major source of the recoil strength, pp-knockout is computed in coplanar and symmetrical kinematics. As expected, the recoil strength in symmetrical kinematics, generated for back-to-back emission, requires the presence of short-range correlations.

Summarizing, the nucleons in ^{4}He are highly correlated and when modeling

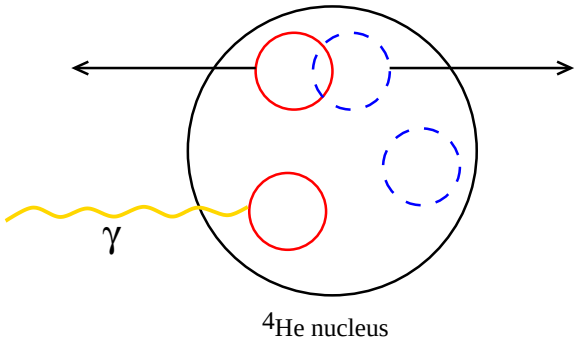

Figure IV-34: *Schematic representation of the reaction process feeding the* $^4He(\gamma, pn)$ *cross section through a recoil mechanism. The red (blue) circles depict a proton (neutron).*

the two-nucleon knockout cross section, recoil effects can not be neglected. It is outlined that identifying four-body breakup induced by a typical recoil diagram is a promising tool to study short-range correlations. Fig. IV-34 provides a simplified picture of the *pn* knockout reaction from ^{4}He, induced through mediation of one of the recoil diagrams. The SRC's are represented by the overlapping proton-neutron circles. In order to suppress the two-body currents in the recoil channel, sufficiently large energy transfers are to be selected. Then, the recoil process will give a clear signal of the genuine nucleon dynamics within the nucleus. Recently, the same strategy is adopted with success in the analysis of a ^{3}He$(e, e'p)pn$ experiment reported in Ref. [127]. When the Mainz data are analyzed accordingly, they could be used to study short-range correlations.

Appendix A

Abbreviations

In this appendix some of the commonly used abbreviations throughout this work are listed. Definitions will not be found here. They can be found in the various sections where the subjects are treated in more detail.

COM	Center of mass
QCD	Quantum Chromodynamics
SM	Shell Model
MF	Mean Field
IPM	Independent Particle Model
FY	Faddeev Yakubovski equations
VM	Variational Method
GFMC	Greens Function Monte Carlo method
SVM	Stochastic Variational Method
CHH	Correlated Hyperspherical Harmonics method
VMC	Variational Monte Carlo method

Appendix B

Definitions

This chapter contains several definitions. Though all of them are well-known and can be found in several textbooks. They are mainly included here to refresh the memory and make the reader familiar with the notations used in this work.

B-1 The Jacobi coordinates

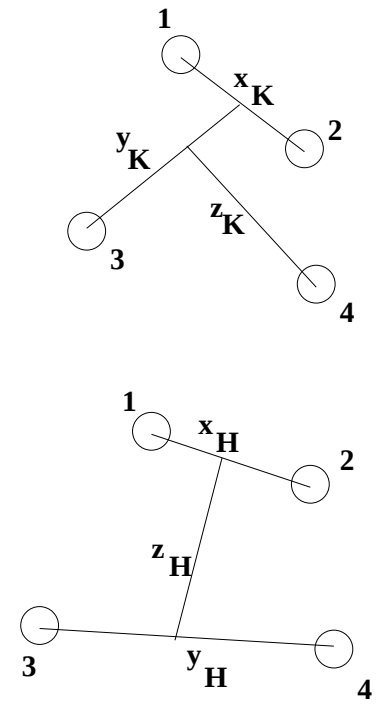

Figure B-1: Jacobi coordinates characterizing the four-body system.

The Jacobi coordinates are a generalization of the well-known relative coordinate ($\vec{r}_{12} = \vec{r}_1 - \vec{r}_2$) which is commonly introduced when tackling a two-body problem.
They characterize the topologically different two-body break-up channels of a bound A-body system. For the two- and three-body problem the definition of the Jacobi coordinates is unambiguous. There is only one two-body break-up channel available. As soon as more particles come into play various definitions of the coordinates become possible. Here, we restrict ourselves to Jacobi coordinates suitable for dealing with the four-body problem.

Two different sets are introduced and they will be referred to as K- and H-type of Jacobi coordinates. The expressions for the Jacobi coordinates for a system of four particles with coordinates $(\vec{r}_1, \vec{r}_2, \vec{r}_3, \vec{r}_4)$ and masses (m_1, m_2, m_3, m_4) look like :

K-type coordinates (3+1 break-up)

$$\begin{aligned}
\vec{x}_K &= \vec{r}_i - \vec{r}_j \\
\vec{y}_K &= \vec{r}_k - \frac{m_i\vec{r}_i + m_j\vec{r}_j}{m_i + m_j} \\
\vec{z}_K &= \vec{r}_l - \frac{m_i\vec{r}_i + m_j\vec{r}_j + m_k\vec{r}_k}{m_i + m_j + m_k}
\end{aligned}$$

H-type coordinates (2+2 break-up)

$$\begin{aligned}
\vec{x}_H &= \vec{r}_i - \vec{r}_j \\
\vec{y}_H &= \vec{r}_k - \vec{r}_l \\
\vec{z}_H &= \frac{m_i\vec{r}_i + m_j\vec{r}_j}{m_i + m_j} - \frac{m_k\vec{r}_k + m_l\vec{r}_l}{m_k + m_l}
\end{aligned}$$

For both the H- and K-type other sets can be derived by a permutation of the particles (1234). Three distinguishable sets exist for the H-type of coordinates, while there are twelve different basis sets in the K-type case.

B -2 The Spherical basis vectors

Starting from the Cartesian coordinate system and the photon propagation direction, one can define the spherical coordinate system .

$$\begin{aligned}
\vec{e}_+ &= -\frac{1}{\sqrt{2}}(\vec{e}_x + i\vec{e}_y) \\
\vec{e}_- &= \frac{1}{\sqrt{2}}(\vec{e}_x - i\vec{e}_y) \\
\vec{e}_0 &= \vec{e}_z = \frac{\vec{q}}{|\vec{q}|}
\end{aligned}$$

The spherical coordinate system is a more natural way to describe the physics of a polarized beam.
In the spherical basis, the properties for the unit vectors hold ($\lambda = 0, \pm$) :

$$\begin{aligned}
(\vec{e}_\lambda)^\dagger &= (-1)^\lambda \vec{e}_{-\lambda} \\
(\vec{e}_\lambda)^\dagger \vec{e}_{\lambda'} &= \delta_{\lambda\lambda'} \\
v_\lambda = \vec{v}.\vec{e}_\lambda &\leftrightarrow \vec{v} = v_\lambda.(\vec{e}_\lambda)^\dagger \\
v_\lambda^\dagger &= (-1)^\lambda \left[\vec{v}^{\,\dagger}\right]_{-\lambda} \\
\vec{v}\cdot\vec{w} &= \sum_{\lambda=0,\pm} (-1)^\lambda v_\lambda w_{-\lambda} \\
\vec{v}\cdot\vec{w}^{\,\dagger} &= \sum_{\lambda=0,\pm} v_\lambda (w_\lambda)^\dagger
\end{aligned}$$

$$
\begin{aligned}
&= \sum_{\lambda=0,\pm} (-1)^{\lambda} v_{\lambda} \left[w^{\dagger}\right]_{-\lambda} \\
\vec{e}_{+} \times \vec{e}_{-} &= i\vec{e}_{0} \\
\vec{e}_{-} \times \vec{e}_{0} &= -i\vec{e}_{-} \\
\vec{e}_{0} \times \vec{e}_{+} &= i\vec{e}_{+}
\end{aligned}
$$

B-3 The Dirac equation

In this section some general properties of the spin $\frac{1}{2}$ wave functions will be summarized (see Ref. [136]). The spin $\frac{1}{2}$ wave function is determined from the, by Dirac in 1928 derived, differential equation

$$
i\hbar \frac{\partial}{c\partial t} \gamma^{0} \psi(\vec{x}, t) = \left(\vec{\gamma}.\hat{\vec{p}} + mc\right) \psi(\vec{x}, t) \, , \tag{B-1}
$$

with, γ^{μ} the gamma matrices. In Bjorken and Drell conventions, they read

$$
\gamma^{0} = \begin{pmatrix} \mathbb{1} & 0 \\ 0 & \mathbb{1} \end{pmatrix} \qquad \vec{\gamma} = \begin{pmatrix} 0 & \vec{\sigma} \\ -\vec{\sigma} & 0 \end{pmatrix} \, , \tag{B-2}
$$

where, $\vec{\sigma}$ are the well-known Pauli spin matrices and $\mathbb{1}$ is the two by two identity matrix in spin space. A common practice in solving the above differential equation consists of determining the normal modes, i.e. solutions corresponding with a fixed energy and momentum eigenvalue : $\psi(\vec{x}, t) \equiv \psi(\vec{0}, 0) \frac{e^{-\frac{i}{\hbar} p.x}}{(2\pi\hbar)^{3/2}}$. The latter quantity (namely $\psi(\vec{0}, 0)$) can be written as a two-dimensional column vector, separating explicitly the positive (upper) and negative (lower) energy components :

$$
\psi(\vec{0}, 0) = \begin{pmatrix} \phi_u \\ \phi_l \end{pmatrix} \, .
$$

Inserting this parametrized form for $\psi(\vec{x}, t)$ into the Dirac equation results into a linear system of equations in (ϕ_u, ϕ_l) :

$$
\begin{cases} \frac{E}{c}\phi_u - \vec{\sigma}.\vec{p}\phi_l - mc\phi_u = 0 \\ -\frac{E}{c}\phi_l + \vec{\sigma}.\vec{p}\phi_u - mc\phi_l = 0 \end{cases} \, . \tag{B-3}
$$

This homogeneous system has two solutions depending on the sign of the energy eigenvalue $E_p = \sqrt{|\vec{p}|^2c^2 + m^2c^4}$:

$$E = E_p \qquad u(\vec{p}, m_s) = \sqrt{\frac{E_p + mc^2}{2mc^2}} \begin{pmatrix} 1 \\ \frac{\vec{\sigma}.\vec{p}c}{E_p + mc^2} \end{pmatrix} \chi_{(1/2,m_s)} \tag{B-4}$$

$$E = -E_p \qquad v(\vec{p}, m_s) = \sqrt{\frac{E_p + mc^2}{2mc^2}} \begin{pmatrix} \frac{\vec{\sigma}.\vec{p}c}{E_p + mc^2} \\ 1 \end{pmatrix} \chi_{(1/2,m_s)} \ , \tag{B-5}$$

where, $\chi_{(1/2,m_s)}$ denotes the spin wave function for a spin $\frac{1}{2}$ particle with spin projection m_s along the z-axis in its rest frame. These normal modes fulfill the following orthogonalization relations :

$$\bar{u}(\vec{p}, m_s)u(\vec{p}, m_{s'}) = \delta_{m_s,m_{s'}} \qquad \bar{v}(\vec{p}, m_s)v(\vec{p}, m_{s'}) = -\delta_{m_s,m_{s'}} \tag{B-6}$$

$$u^\dagger(\vec{p}, m_s)u(\vec{p}, m_{s'}) = \frac{E_p}{mc^2}\delta_{m_s,m_{s'}} \qquad v^\dagger(\vec{p}, m_s)v(\vec{p}, m_{s'}) = \frac{E_p}{mc^2}\delta_{m_s,m_{s'}} \ . \tag{B-7}$$

The positive energy spin-$\frac{1}{2}$ wave function fulfills the following relations :

$$\left(\frac{\not{p} + mc}{2mc}\right) u(\vec{p}, m_s) = u(\vec{p}, m_s) \tag{B-8}$$

$$\left(\frac{1 + \gamma_5 \not{s}}{2}\right) u(\vec{p}, m_s) = u(\vec{p}, m_s) \tag{B-9}$$

$$\sum_{m_s} u_\alpha(\vec{p}, m_s)\bar{u}_\beta(\vec{p}, m_s) = \left(\frac{\not{p}\, c + mc^2}{2E_p}\right)_{\alpha\beta} \ , \tag{B-10}$$

with, s^μ the relativistic continuation of the classical polarization vector $\vec{s}$. More in particular, $\vec{s}$ is the basis vector along which the spin-$\frac{1}{2}$ particle, in its rest frame, is polarized. Starting from the polarization vector : $\vec{s} = |\vec{s}|(\cos\theta\vec{e}_L + \sin\theta\vec{e}_T)$, decomposed into a component along the propagation direction and one perpendicular to it, a general polarization four vector can be defined as follows :

$$\begin{aligned} s^\mu &\overset{\vec{p}=\vec{0}}{=} (0, \vec{s}) \\ s^\mu &\overset{\vec{p}\neq\vec{0}}{=} \left(\frac{|\vec{p}|c}{\sqrt{m^2c^4 + E^2\tan\theta^2}}, \frac{E}{\sqrt{m^2c^4 + E^2\tan\theta^2}}\vec{e}_L + \frac{E}{\sqrt{m^2c^4\cot\theta^2 + E^2}}\vec{e}_T\right) . \end{aligned} \tag{B-11}$$

From Eq. B-11 the longitudinal to transverse polarization ratio of a spin $\frac{1}{2}$ particle beam can be deduced $r_{T/L} = mc^2/E$. This ratio reveals a fundamental aspect of ultra-relativistic spin $\frac{1}{2}$-particles namely the fact that they are self-polarizing more specifically along the direction of propagation. The latter can be explained as resulting from a length contraction of the longitudinal component of some internal field associated with the spin.

B-4 The Delta isobar $\Delta_{\frac{3}{2}\frac{3}{2}}$

After Ref. [137], the free Lagrangian density for a Δ-particle can be written as follows :

$$\mathcal{L}_\Delta \;=\; \bar{\Psi}^\mu_\Delta \Lambda_{\mu\nu} \Psi^\nu_\Delta \;, \tag{B-12}$$

with,

$$\begin{aligned}\Lambda_{\mu\nu} \;=\; -\Big[&(-\not{p} + m_\Delta c) g_{\mu\nu} - A(\gamma_\mu p_\nu + \gamma_\nu p_\mu) - \\ &\frac{1}{2}(3A^2 + 2A + 1)\gamma_\mu \not{p} \gamma_\nu - m_\Delta c (3A^2 + 3A + 1)\gamma_\mu \gamma_\nu \Big] \;,\end{aligned} \tag{B-13}$$

where, A is a constant. The variation in the parameter A can be identified with a gauge transformation for the spin-$\frac{3}{2}$ field. Indeed

$$A \;\rightarrow\; A' = A(1-\lambda) - \frac{A}{2} \;, \tag{B-14}$$

implies the following gauge transformation for the wave function :

$$\Psi^\mu_\Delta \;\rightarrow\; \Psi^\mu_\Delta + \frac{1}{4}\lambda \gamma_\mu \gamma_\nu \Psi^\nu_\Delta \tag{B-15}$$

This transformation does not alter the spin $\frac{3}{2}$ content of the wave function Ψ_Δ although the spinor components are changed. The original Rarita-Schwinger equations [138] are obtained for the particular choice $A = -1$:

$$\mathcal{L}_\Delta \;=\; \bar{\Psi}^\mu_\Delta \left[(\not{p} - m_\Delta c) g_{\mu\nu} + \gamma_\mu (\not{p} + m_\Delta c) \gamma_\nu - (\gamma_\mu p_\nu + \gamma_\nu p_\mu) \right] \Psi^\nu_\Delta \;, \tag{B-16}$$

and the associated free delta propagator :

$$G^{\mu\nu}_\Delta \;=\; \hbar \frac{(\not{p} + m_\Delta c)}{p^2 - m^2_\Delta c^2} \left[g^{\mu\nu} - \frac{1}{3}\gamma^\mu \gamma^\nu - \frac{2}{3}\frac{p^\mu p^\nu}{m^2_\Delta c^2} + \frac{p^\mu \gamma^\nu - p^\nu \gamma^\mu}{3 m_\Delta c} \right] \;. \tag{B-17}$$

In the nuclear medium, this propagator has to be modified to account for the unstable character of the delta particle and for its off the mass-shell behavior.
According to the original approach of Rarita and Schwinger, the delta wave function can be written as a direct product of a spin 1 with a spin $\frac{1}{2}$ constituent [138].

$$\Psi^\mu_\Delta(\vec{p}, m_{s_\Delta}) \;=\; \sum_m < \frac{3}{2}, m_{s_\Delta} | 1, m; \frac{1}{2}, m_{s_\Delta} - m > u(\vec{p}, m_s) \epsilon^\mu(m_{s_\Delta} - m, \vec{p}) \;, \tag{B-18}$$

with, $u(\vec{p}, m_s)$ and $\epsilon^\mu(m_{s_\Delta} - m, \vec{p})$ respectively a Dirac spinor and a spin 1 polarization vector. An explicit expression for the Dirac spinor has been derived in

section B-3. Using the expressions from section B-2, the general spin-1 polarization vectors look like :

$$\epsilon^{\mu}_{+1}(\vec{p}=\vec{0}) = \begin{pmatrix} 0 \\ -\frac{1}{\sqrt{2}} \\ -\frac{i}{\sqrt{2}} \\ 0 \end{pmatrix} \qquad \epsilon^{\mu}_{+1}(\vec{p}) = \begin{pmatrix} 0 \\ -(\cos\theta\cos\phi - i\sin\phi)\frac{e^{i\phi}}{\sqrt{2}} \\ -(\cos\theta\sin\phi + i\cos\phi)\frac{e^{i\phi}}{\sqrt{2}} \\ \sin\theta\frac{e^{i\phi}}{\sqrt{2}} \end{pmatrix}$$

$$\epsilon^{\mu}_{-1}(\vec{p}=\vec{0}) = \begin{pmatrix} 0 \\ \frac{1}{\sqrt{2}} \\ -\frac{i}{\sqrt{2}} \\ 0 \end{pmatrix} \qquad \epsilon^{\mu}_{-1}(\vec{p}) = \begin{pmatrix} 0 \\ (\cos\theta\cos\phi + i\sin\phi)\frac{e^{-i\phi}}{\sqrt{2}} \\ (\cos\theta\sin\phi - i\cos\phi)\frac{e^{-i\phi}}{\sqrt{2}} \\ -\sin\theta\frac{e^{-i\phi}}{\sqrt{2}} \end{pmatrix} ,$$

$$\epsilon^{\mu}_{0}(\vec{p}=\vec{0}) = \begin{pmatrix} 0 \\ 0 \\ 0 \\ 1 \end{pmatrix} \qquad \epsilon^{\mu}_{0}(\vec{p}) = \begin{pmatrix} \frac{|\vec{p}|}{m_{\Delta}c} \\ \frac{E}{m_{\Delta}c^2}\sin\theta\cos\phi \\ \frac{E}{m_{\Delta}c^2}\sin\theta\sin\phi \\ \frac{E}{m_{\Delta}c^2}\cos\theta \end{pmatrix} \tag{B-19}$$

with, $\vec{p}$ directed along the axis (θ, ϕ). In the non-relativistic limit, the energy dependence of the polarization vectors vanishes as well as their $\mu = 0$-components. In order to express the delta wave function in terms of photon, nucleon and pion degrees of freedom spin and isospin projection operators have to be defined :

$$\left\langle \frac{3}{2}, m_{s_\Delta} \middle| \vec{S}^{\dagger}_{m} \middle| \frac{1}{2}, m_s \right\rangle = \left\langle \frac{3}{2} m_{s_\Delta} \middle| 1, m; \frac{1}{2}, m_s \right\rangle \tag{B-20}$$

$$\left\langle \frac{3}{2}, m_{t_\Delta} \middle| \vec{T}^{\dagger}_{m} \middle| \frac{1}{2}, m_t \right\rangle = \left\langle \frac{3}{2} m_{t_\Delta} \middle| 1, m; \frac{1}{2}, m_t \right\rangle , \tag{B-21}$$

where, both operators have an identical impact in the spin and isospin space respectively. Making use of general angular momentum algebra rules, the following

relations for the projection operators can be derived

$$\sum_{m_{s_\Delta}} \vec{S}_i \left|\frac{3}{2}, m_{s_\Delta}\right\rangle \left\langle\frac{3}{2}, m_{s_\Delta}\right| \vec{S}_j^\dagger = \frac{2}{3}\delta_{ij}\mathbb{1} - \frac{i}{3}\epsilon_{ijk}\vec{\sigma}_k \tag{B-22}$$

$$\sum_{m_{t_\Delta}} \vec{T}_i \left|\frac{3}{2}, m_{t_\Delta}\right\rangle \left\langle\frac{3}{2}, m_{t_\Delta}\right| \vec{T}_j^\dagger = \frac{2}{3}\delta_{ij}\mathbb{1} - \frac{i}{3}\epsilon_{ijk}\vec{\tau}_k \ , \tag{B-23}$$

with $\vec{\sigma}$ and $\vec{\tau}$ the Pauli matrices acting in respectively spin and isospin space. The quantity ϵ_{ijk} is the Levi-Civita tensor.

B-5 The nuclear response functions

The elements of the hadronic tensor can be combined to the well-known nuclear response functions (see Eqs. III-62 - III-67). In order to arrive at the response functions one expresses the Cartesian components of the hadronic tensor (see Eqs. III-32 and III-33) in a spherical basis as introduced in section B-2. In this section, we report for every Cartesian component of the hadronic tensor, the explicit expressions of the hadronic response functions.

$$G^{\mu\nu} = g^{\mu\nu} - \frac{p_\gamma^\mu p_\gamma^\nu}{p_\gamma^2}$$

$$\begin{cases} W_L = -\frac{|\vec{p}_\gamma|^2}{p_\gamma^2} \\ W_T = -2 \end{cases}$$

$$V_1^\mu V_1^\nu = \left(p_1^\mu - \frac{(p_1.p_\gamma)p_\gamma^\mu}{p_\gamma^2}\right)\left(p_1^\nu - \frac{(p_1.p_\gamma)p_\gamma^\nu}{p_\gamma^2}\right)$$

$$\begin{cases} W_L = \left[\frac{E_1}{c} - \frac{E_1 E_\gamma/c^2 - |\vec{p}_1||\vec{p}_\gamma|\cos\theta_1}{p_\gamma^2}.\frac{E_\gamma}{c}\right]^2 \\ W_T = |\vec{p}_1|^2 \sin{\theta_1}^2 \\ W_{LT} = \sqrt{2}|\vec{p}_1|\left[\frac{E_1}{c} - \frac{E_1 E_\gamma/c^2 - |\vec{p}_1||\vec{p}_\gamma|\cos\theta_1}{p_\gamma^2}.\frac{E_\gamma}{c}\right]\sin\theta_1\cos\phi_1 \\ W_{TT} = -|\vec{p}_1|^2 \sin{\theta_1}^2 \cos 2\phi_1 \end{cases}$$

$$[V_1^\mu, V_2^\nu]_+ = \left(p_1^\mu - \frac{(p_1.p_\gamma)p_\gamma^\mu}{p_\gamma^2}\right)\left(p_2^\nu - \frac{(p_2.p_\gamma)p_\gamma^\nu}{p_\gamma^2}\right) + \left(p_2^\mu - \frac{(p_2.p_\gamma)p_\gamma^\mu}{p_\gamma^2}\right)\left(p_1^\nu - \frac{(p_1.p_\gamma)p_\gamma^\nu}{p_\gamma^2}\right)$$

$$
\left\{
\begin{array}{rcl}
W_L &=& 2\left[\frac{E_1}{c} - \frac{E_1 E_\gamma/c^2 - |\vec{p}_1||\vec{p}_\gamma|\cos\theta_1}{p_\gamma^2}.\frac{E_\gamma}{c}\right]. \\
& & \left[\frac{E_2}{c} - \frac{E_2 E_\gamma/c^2 - |\vec{p}_2||\vec{p}_\gamma|\cos\theta_2}{p_\gamma^2}.\frac{E_\gamma}{c}\right] \\
W_T &=& 2|\vec{p}_1|\sin\theta_1|\vec{p}_2|\sin\theta_2\cos(\phi_1-\phi_2) \\
W_{LT} &=& \sqrt{2}\Big\{\left[\frac{E_1}{c} - \frac{E_1 E_\gamma/c^2 - |\vec{p}_1||\vec{p}_\gamma|\cos\theta_1}{p_\gamma^2}.\frac{E_\gamma}{c}\right]|\vec{p}_2|\sin\theta_2\cos\phi_2 + \\
& & \left[\frac{E_2}{c} - \frac{E_2 E_\gamma/c^2 - |\vec{p}_2||\vec{p}_\gamma|\cos\theta_2}{p_\gamma^2}.\frac{E_\gamma}{c}\right]|\vec{p}_1|\sin\theta_1\cos\phi_1\Big\} \\
W_{TT} &=& -2|\vec{p}_1|\sin\theta_1|\vec{p}_2|\sin\theta_2\cos(\phi_1+\phi_2)
\end{array}
\right.
$$

$$
\begin{aligned}
[V_1^\mu, \zeta_1^\nu]_+ &= \left(p_1^\mu - \frac{(p_1.p_\gamma)p_\gamma^\mu}{p_\gamma^2}\right).\epsilon^{\nu\rho\omega\sigma}(p_\gamma)_\rho(p_1)_\omega(p_2)_\sigma + \\
& \left(p_1^\nu - \frac{(p_1.p_\gamma)p_\gamma^\nu}{p_\gamma^2}\right).\epsilon^{\mu\rho\omega\sigma}(p_\gamma)_\rho(p_1)_\omega(p_2)_\sigma
\end{aligned}
$$

$$
\left\{
\begin{array}{rcl}
W_L &=& 2|\vec{p}_\gamma|\left[\frac{E_1}{c} - \frac{E_1 E_\gamma/c^2 - |\vec{p}_1||\vec{p}_\gamma|\cos\theta_1}{p_\gamma^2}.\frac{E_\gamma}{c}\right] \\
& & |\vec{p}_1|\sin\theta_1|\vec{p}_2|\sin\theta_2\sin(\phi_1-\phi_2) \\
W_T &=& 2\Big(|\vec{p}_1|^2\sin(2\theta_1)|\vec{p}_2|\sin\theta_2\sin(\phi_1-\phi_2)\frac{E_\gamma}{c} - \\
& & 2|\vec{p}_\gamma||\vec{p}_1|\sin\theta_1|\vec{p}_2|\sin\theta_2\sin(\phi_1-\phi_2)\Big) \\
W_{LT} &=& \sqrt{2}\Big\{\frac{E_1}{c}\Big[\frac{E_\gamma}{c}(|\vec{p}_1|\cos\theta_1|\vec{p}_2|\sin\theta_2\sin\phi_2 - \\
& & |\vec{p}_1|\sin\theta_1\sin\phi_1|\vec{p}_2|\cos\theta_2) + \\
& & |\vec{p}_\gamma|\left(\frac{E_2}{c}|\vec{p}_1|\sin\theta_1\sin\phi_1 - \frac{E_1}{c}|\vec{p}_2|\sin\theta_2\sin\phi_2\right)\Big] + \\
& & |\vec{p}_\gamma||\vec{p}_1|^2\sin{\theta_1}^2\cos\phi_1|\vec{p}_2|\sin\theta_2\sin(\phi_1-\phi_2)\Big\} \\
W_{TT} &=& 2\Big[\frac{E_\gamma}{c}\Big(|\vec{p}_1|^2\sin{\theta_1}^2|\vec{p}_2|\cos\theta_2\sin(2\phi_1) - \\
& & |\vec{p}_1|^2\cos\theta_1\sin\theta_1|\vec{p}_2|\sin\theta_2\sin(\phi_1+\phi_2)\Big) + \\
& & |\vec{p}_\gamma|\Big(\frac{E_1}{c}|\vec{p}_1|\sin\theta_1|\vec{p}_2|\sin\theta_2\sin(\phi_1+\phi_2) - \\
& & \frac{E_2}{c}|\vec{p}_1|^2\sin{\theta_1}^2\sin(2\phi_1)\Big)\Big]
\end{array}
\right.
$$

$$
\begin{aligned}
V_2^\mu V_2^\nu &= \left(p_2^\mu - \frac{(p_2.p_\gamma)p_\gamma^\mu}{p_\gamma^2}\right)\left(p_2^\nu - \frac{(p_2.p_\gamma)p_\gamma^\nu}{p_\gamma^2}\right) \\
&\left\{\begin{array}{lcl}
W_L &=& \left[\frac{E_2}{c} - \frac{E_2E_\gamma/c^2 - |\vec{p}_2||\vec{p}_\gamma|\cos\theta_2}{p_\gamma^2}.\frac{E_\gamma}{c}\right]^2 \\
W_T &=& |\vec{p}_2|^2 \sin{\theta_2}^2 \\
W_{LT} &=& \sqrt{2}|\vec{p}_2|\left[\frac{E_2}{c} - \frac{E_2E_\gamma/c^2 - |\vec{p}_2||\vec{p}_\gamma|\cos\theta_2}{p_\gamma^2}.\frac{E_\gamma}{c}\right]\sin\theta_2\cos\phi_2 \\
W_{TT} &=& -|\vec{p}_2|^2 \sin{\theta_2}^2 \cos 2\phi_2
\end{array}\right. \\
[V_2^\mu, \zeta_1^\nu]_+ &= \left(p_2^\mu - \frac{(p_2.p_\gamma)p_\gamma^\mu}{p_\gamma^2}\right).\epsilon^{\nu\rho\omega\sigma}(p_\gamma)_\rho(p_1)_\omega(p_2)_\sigma + \\
&\qquad \left(p_2^\nu - \frac{(p_2.p_\gamma)p_\gamma^\nu}{p_\gamma^2}\right).\epsilon^{\mu\rho\omega\sigma}(p_\gamma)_\rho(p_1)_\omega(p_2)_\sigma \\
&\left\{\begin{array}{lcl}
W_L &=& 2|\vec{p}_\gamma|\left[\frac{E_2}{c} - \frac{E_2E_\gamma/c^2 - |\vec{p}_2||\vec{p}_\gamma|\cos\theta_2}{p_\gamma^2}.\frac{E_\gamma}{c}\right] \\
&& \qquad |\vec{p}_1|\sin\theta_1|\vec{p}_2|\sin\theta_2\sin(\phi_1-\phi_2) \\
W_T &=& 2\Big(|\vec{p}_2|^2\sin(2\theta_2)|\vec{p}_1|\sin\theta_1\sin(\phi_1-\phi_2)\frac{E_\gamma}{c} - \\
&& \qquad 2|\vec{p}_\gamma||\vec{p}_2|\sin\theta_2|\vec{p}_1|\sin\theta_1\sin(\phi_1-\phi_2)\Big) \\
W_{LT} &=& -\sqrt{2}\Big\{\frac{E_2}{c}\Big[\frac{E_\gamma}{c}(|\vec{p}_2|\cos\theta_2|\vec{p}_1|\sin\theta_1\sin\phi_1 - \\
&& \qquad |\vec{p}_2|\sin\theta_2\sin\phi_2|\vec{p}_1|\cos\theta_1) + \\
&& \qquad |\vec{p}_\gamma|\left(\frac{E_1}{c}|\vec{p}_2|\sin\theta_2\sin\phi_2 - \frac{E_2}{c}|\vec{p}_1|\sin\theta_1\sin\phi_1\right)\Big] - \\
&& \qquad |\vec{p}_\gamma||\vec{p}_2|^2\sin{\theta_2}^2\cos\phi_2|\vec{p}_1|\sin\theta_1\sin(\phi_1-\phi_2)\Big\} \\
W_{TT} &=& -2\Big[\frac{E_\gamma}{c}\Big(|\vec{p}_2|^2\sin{\theta_2}^2|\vec{p}_1|\cos\theta_1\sin(2\phi_2) - \\
&& \qquad |\vec{p}_2|^2\cos\theta_2\sin\theta_2|\vec{p}_1|\sin\theta_1\sin(\phi_1+\phi_2)\Big) + \\
&& \qquad |\vec{p}_\gamma|\Big(\frac{E_2}{c}|\vec{p}_2|\sin\theta_2|\vec{p}_1|\sin\theta_1\sin(\phi_1+\phi_2) - \\
&& \qquad \frac{E_1}{c}|\vec{p}_2|^2\sin{\theta_2}^2\sin(2\phi_2)\Big)\Big]
\end{array}\right. \\
[V_1^\mu, V_2^\nu]_- &= \left(p_1^\mu - \frac{(p_1.p_\gamma)p_\gamma^\mu}{p_\gamma^2}\right)\left(p_2^\nu - \frac{(p_2.p_\gamma)p_\gamma^\nu}{p_\gamma^2}\right) -
\end{aligned}
$$

$$\left(p_2^\mu - \frac{(p_2.p_\gamma)p_\gamma^\mu}{p_\gamma^2}\right)\left(p_1^\nu - \frac{(p_1.p_\gamma)p_\gamma^\nu}{p_\gamma^2}\right)$$

$$\begin{cases} W'_{LT} &= -\sqrt{2}i\Big\{\Big[\frac{E_1}{c} - \frac{E_1E_\gamma/c^2 - |\vec{p}_1||\vec{p}_\gamma|\cos\theta_1}{p_\gamma^2}.\frac{E_\gamma}{c}\Big]|\vec{p}_2|\sin\theta_2\sin\phi_2 - \\ & \qquad |\vec{p}_1|\sin\theta_1\sin\phi_1\Big[\frac{E_2}{c} - \frac{E_2E_\gamma/c^2 - |\vec{p}_2||\vec{p}_\gamma|\cos\theta_2}{p_\gamma^2}.\frac{E_\gamma}{c}\Big]\Big\} \\ W'_{TT} &= -2i|\vec{p}_1|\sin\theta_1|\vec{p}_2|\sin\theta_2\sin(\phi_1-\phi_2) \end{cases}$$

$$[V_1^\mu, \zeta_1^\nu]_- = \left(p_1^\mu - \frac{(p_1.p_\gamma)p_\gamma^\mu}{p_\gamma^2}\right).\epsilon^{\nu\rho\omega\sigma}(p_\gamma)_\rho(p_1)_\omega(p_2)_\sigma - \left(p_1^\nu - \frac{(p_1.p_\gamma)p_\gamma^\nu}{p_\gamma^2}\right).\epsilon^{\mu\rho\omega\sigma}(p_\gamma)_\rho(p_1)_\omega(p_2)_\sigma$$

$$\begin{cases} W'_{LT} &= \sqrt{2}i\Big\{-\frac{E_1}{c}\Big[\frac{E_\gamma}{c}(|\vec{p}_1|\sin\theta_1\cos\phi_1|\vec{p}_2|\cos\theta_2 - \\ & \qquad |\vec{p}_1|\cos\theta_1|\vec{p}_2|\sin\theta_2\cos\phi_2) + \\ & \qquad |\vec{p}_\gamma|(\frac{E_1}{c}|\vec{p}_2|\sin\theta_2\cos\phi_2 - \frac{E_2}{c}|\vec{p}_1|\sin\theta_1\cos\phi_1)\Big] + \\ & \qquad |\vec{p}_1|^2\sin{\theta_1}^2\sin\phi_1|\vec{p}_\gamma||\vec{p}_2|\sin\theta_2\sin(\phi_1-\phi_2)\Big\} \\ W'_{TT} &= 2i\Big\{\frac{E_\gamma}{c}\Big[|\vec{p}_2|\cos\theta_2|\vec{p}_1|^2\sin{\theta_1}^2 - \\ & \qquad |\vec{p}_1|^2\cos\theta_1\sin\theta_1|\vec{p}_2|\sin\theta_2\cos(\phi_1-\phi_2)\Big] + \\ & \qquad |\vec{p}_\gamma|\Big[\frac{E_1}{c}|\vec{p}_1|\sin\theta_1|\vec{p}_2|\sin\theta_2\cos(\phi_1-\phi_2) - \\ & \qquad \frac{E_2}{c}|\vec{p}_1|^2\sin{\theta_1}^2\Big]\Big\} \end{cases}$$

$$[V_2^\mu, \zeta_1^\nu]_- = \left(p_2^\mu - \frac{(p_2.p_\gamma)p_\gamma^\mu}{p_\gamma^2}\right).\epsilon^{\nu\rho\omega\sigma}(p_\gamma)_\rho(p_1)_\omega(p_2)_\sigma - \left(p_2^\nu - \frac{(p_2.p_\gamma)p_\gamma^\nu}{p_\gamma^2}\right).\epsilon^{\mu\rho\omega\sigma}(p_\gamma)_\rho(p_1)_\omega(p_2)_\sigma$$

$$
\left\{
\begin{array}{rcl}
W'_{LT} &=& \sqrt{2}i\Big\{\frac{E_2}{c}\Big[\frac{E_\gamma}{c}(|\vec{p}_2|\sin\theta_2\cos\phi_2|\vec{p}_1|\cos\theta_1 - \\
& & \qquad |\vec{p}_2|\cos\theta_2|\vec{p}_1|\sin\theta_1\cos\phi_1\Big) + \\
& & \qquad |\vec{p}_\gamma|(\frac{E_2}{c}|\vec{p}_1|\sin\theta_1\cos\phi_1 - \frac{E_1}{c}|\vec{p}_2|\sin\theta_2\cos\phi_2)\Big] + \\
& & |\vec{p}_2|^2\sin{\theta_2}^2\sin\phi_2|\vec{p}_\gamma||\vec{p}_2|\sin\theta_1\sin(\phi_1-\phi_2)\Big\} \\
W'_{TT} &=& -2i\Big\{\frac{E_\gamma}{c}\Big[|\vec{p}_1|\cos\theta_1|\vec{p}_2|^2\sin{\theta_2}^2 - \\
& & \qquad |\vec{p}_2|^2\cos\theta_2\sin\theta_2|\vec{p}_1|\sin\theta_1\cos(\phi_1-\phi_2)\Big] + \\
& & |\vec{p}_\gamma|\Big[\frac{E_2}{c}|\vec{p}_2|\sin\theta_2|\vec{p}_1|\sin\theta_1\cos(\phi_1-\phi_2) - \\
& & \qquad \frac{E_1}{c}|\vec{p}_2|^2\sin{\theta_2}^2\Big]\Big\}
\end{array}
\right.
$$

After summing all of those contributions, the response functions look like :

$$
\begin{array}{rcl}
W_L &=& -W_1\frac{|\vec{p}_\gamma|^2}{p_\gamma^2} + W_2\left[\frac{E_1}{c} - \frac{E_1E_\gamma/c^2 - |\vec{p}_1||\vec{p}_\gamma|\cos\theta_1}{p_\gamma^2}.\frac{E_\gamma}{c}\right]^2 + \\
& & 2W_3\left[\frac{E_1}{c} - \frac{E_1E_\gamma/c^2 - |\vec{p}_1||\vec{p}_\gamma|\cos\theta_1}{p_\gamma^2}.\frac{E_\gamma}{c}\right]. \\
& & \left[\frac{E_2}{c} - \frac{E_2E_\gamma/c^2 - |\vec{p}_2||\vec{p}_\gamma|\cos\theta_2}{p_\gamma^2}.\frac{E_\gamma}{c}\right] + \\
& & W_4\left[\frac{E_2}{c} - \frac{E_2E_\gamma/c^2 - |\vec{p}_2||\vec{p}_\gamma|\cos\theta_2}{p_\gamma^2}.\frac{E_\gamma}{c}\right]^2 + \\
& & 2\bar{W}_5|\vec{p}_\gamma|\left[\frac{E_1}{c} - \frac{E_1E_\gamma/c^2 - |\vec{p}_1||\vec{p}_\gamma|\cos\theta_1}{p_\gamma^2}.\frac{E_\gamma}{c}\right] \\
& & \times|\vec{p}_1|\sin\theta_1|\vec{p}_2|\sin\theta_2\sin(\phi_1-\phi_2) + \\
& & 2\bar{W}_6|\vec{p}_\gamma|\left[\frac{E_2}{c} - \frac{E_2E_\gamma/c^2 - |\vec{p}_2||\vec{p}_\gamma|\cos\theta_2}{p_\gamma^2}.\frac{E_\gamma}{c}\right] \\
& & \times|\vec{p}_1|\sin\theta_1|\vec{p}_2|\sin\theta_2\sin(\phi_1-\phi_2) \qquad \text{(B-24)} \\
W_T &=& -2W_1 + W_2|\vec{p}_1|^2\sin{\theta_1}^2 + 2W_3|\vec{p}_1|\sin\theta_1|\vec{p}_2|\sin\theta_2\cos(\phi_1-\phi_2) + \\
& & W_4|\vec{p}_2|^2\sin{\theta_2}^2 + 2\bar{W}_5\Big(|\vec{p}_1|^2\sin(2\theta_1)|\vec{p}_2|\sin\theta_2\sin(\phi_1-\phi_2)\frac{E_\gamma}{c} - \\
& & 2|\vec{p}_\gamma||\vec{p}_1|\sin\theta_1|\vec{p}_2|\sin\theta_2\sin(\phi_1-\phi_2)\Big) + \\
& & 2\bar{W}_6\Big(|\vec{p}_2|^2\sin(2\theta_2)|\vec{p}_1|\sin\theta_1\sin(\phi_1-\phi_2)\frac{E_\gamma}{c} -
\end{array}
$$

$$2|\vec{p}_\gamma||\vec{p}_2|\sin\theta_2|\vec{p}_1|\sin\theta_1\sin(\phi_1-\phi_2)\Big) \tag{B-25}$$

$$\begin{aligned}
W_{LT} &= \sqrt{2}W_2|\vec{p}_1|\left[\frac{E_1}{c}-\frac{E_1E_\gamma/c^2-|\vec{p}_1||\vec{p}_\gamma|\cos\theta_1}{p_\gamma^2}.\frac{E_\gamma}{c}\right]\sin\theta_1\cos\phi_1+\\
&\sqrt{2}W_3\left\{\left[\frac{E_1}{c}-\frac{E_1E_\gamma/c^2-|\vec{p}_1||\vec{p}_\gamma|\cos\theta_1}{p_\gamma^2}.\frac{E_\gamma}{c}\right]|\vec{p}_2|\sin\theta_2\cos\phi_2+\right.\\
&\left.\left[\frac{E_2}{c}-\frac{E_2E_\gamma/c^2-|\vec{p}_2||\vec{p}_\gamma|\cos\theta_2}{p_\gamma^2}.\frac{E_\gamma}{c}\right]|\vec{p}_1|\sin\theta_1\cos\phi_1\right\}+\\
&W_4\sqrt{2}|\vec{p}_2|\left[\frac{E_2}{c}-\frac{E_2E_\gamma/c^2-|\vec{p}_2||\vec{p}_\gamma|\cos\theta_2}{p_\gamma^2}.\frac{E_\gamma}{c}\right]\sin\theta_2\cos\phi_2+\\
&\sqrt{2}\bar{W}_5\left\{\frac{E_1}{c}\left[\frac{E_\gamma}{c}(|\vec{p}_1|\cos\theta_1|\vec{p}_2|\sin\theta_2\sin\phi_2-|\vec{p}_1|\sin\theta_1\sin\phi_1|\vec{p}_2|\cos\theta_2)+\right.\right.\\
&\left.\left.|\vec{p}_\gamma|\left(\frac{E_2}{c}|\vec{p}_1|\sin\theta_1\sin\phi_1-\frac{E_1}{c}|\vec{p}_2|\sin\theta_2\sin\phi_2\right)\right]+\right.\\
&\left.|\vec{p}_\gamma||\vec{p}_1|^2\sin{\theta_1}^2\cos\phi_1|\vec{p}_2|\sin\theta_2\sin(\phi_1-\phi_2)\right\}-\\
&\sqrt{2}\bar{W}_6\left\{\frac{E_2}{c}\left[\frac{E_\gamma}{c}(|\vec{p}_2|\cos\theta_2|\vec{p}_1|\sin\theta_1\sin\phi_1-|\vec{p}_2|\sin\theta_2\sin\phi_2|\vec{p}_1|\cos\theta_1)+\right.\right.\\
&\left.\left.|\vec{p}_\gamma|\left(\frac{E_1}{c}|\vec{p}_2|\sin\theta_2\sin\phi_2-\frac{E_2}{c}|\vec{p}_1|\sin\theta_1\sin\phi_1\right)\right]-\right.\\
&\left.|\vec{p}_\gamma||\vec{p}_2|^2\sin{\theta_2}^2\cos\phi_2|\vec{p}_1|\sin\theta_1\sin(\phi_1-\phi_2)\right\}
\end{aligned} \tag{B-26}$$

$$\begin{aligned}
W_{TT} &= -W_2|\vec{p}_1|^2\sin{\theta_1}^2\cos2\phi_1-2W_3|\vec{p}_1|\sin\theta_1|\vec{p}_2|\sin\theta_2\cos(\phi_1+\phi_2)-\\
&W_4|\vec{p}_2|^2\sin{\theta_2}^2\cos2\phi_2+2\bar{W}_5\left[\frac{E_\gamma}{c}\Big(|\vec{p}_1|^2\sin{\theta_1}^2|\vec{p}_2|\cos\theta_2\sin(2\phi_1)-\right.\\
&\left.|\vec{p}_1|^2\cos\theta_1\sin\theta_1|\vec{p}_2|\sin\theta_2\sin(\phi_1+\phi_2)\Big)+\right.\\
&\left.|\vec{p}_\gamma|\Big(\frac{E_1}{c}|\vec{p}_1|\sin\theta_1|\vec{p}_2|\sin\theta_2\sin(\phi_1+\phi_2)-\frac{E_2}{c}|\vec{p}_1|^2\sin{\theta_1}^2\sin(2\phi_1)\Big)\right]-\\
&2\bar{W}_6\left[\frac{E_\gamma}{c}\Big(|\vec{p}_2|^2\sin{\theta_2}^2|\vec{p}_1|\cos\theta_1\sin(2\phi_2)-\right.\\
&\left.|\vec{p}_2|^2\cos\theta_2\sin\theta_2|\vec{p}_1|\sin\theta_1\sin(\phi_1+\phi_2)\Big)+\right.\\
&\left.|\vec{p}_\gamma|\Big(\frac{E_2}{c}|\vec{p}_2|\sin\theta_2|\vec{p}_1|\sin\theta_1\sin(\phi_1+\phi_2)-\frac{E_1}{c}|\vec{p}_2|^2\sin{\theta_2}^2\sin(2\phi_2)\Big)\right]
\end{aligned} \tag{B-27}$$

$$W'_{LT} = -\sqrt{2}iW_7\left\{\left[\frac{E_1}{c}-\frac{E_1E_\gamma/c^2-|\vec{p}_1||\vec{p}_\gamma|\cos\theta_1}{p_\gamma^2}.\frac{E_\gamma}{c}\right]|\vec{p}_2|\sin\theta_2\sin\phi_2-\right.$$

$$
\begin{aligned}
& |\vec{p}_1|\sin\theta_1\sin\phi_1\Big[\frac{E_2}{c}-\frac{E_2E_\gamma/c^2-|\vec{p}_2||\vec{p}_\gamma|\cos\theta_2}{p_\gamma^2}.\frac{E_\gamma}{c}\Big]\Big\}+\\
& \sqrt{2}i\bar{W}_8\Big\{-\frac{E_1}{c}\Big[\frac{E_\gamma}{c}(|\vec{p}_1|\sin\theta_1\cos\phi_1|\vec{p}_2|\cos\theta_2-|\vec{p}_1|\cos\theta_1|\vec{p}_2|\sin\theta_2\cos\phi_2)\\
& +|\vec{p}_\gamma|(\frac{E_1}{c}|\vec{p}_2|\sin\theta_2\cos\phi_2-\frac{E_2}{c}|\vec{p}_1|\sin\theta_1\cos\phi_1)\Big]+\\
& |\vec{p}_1|^2\sin{\theta_1}^2\sin\phi_1|\vec{p}_\gamma||\vec{p}_2|\sin\theta_2\sin(\phi_1-\phi_2)\Big\}+\\
& \sqrt{2}i\bar{W}_9\Big\{\frac{E_2}{c}\Big[\frac{E_\gamma}{c}(|\vec{p}_2|\sin\theta_2\cos\phi_2|\vec{p}_1|\cos\theta_1-|\vec{p}_2|\cos\theta_2|\vec{p}_1|\sin\theta_1\cos\phi_1\Big)+\\
& |\vec{p}_\gamma|(\frac{E_2}{c}|\vec{p}_1|\sin\theta_1\cos\phi_1-\frac{E_1}{c}|\vec{p}_2|\sin\theta_2\cos\phi_2)\Big]+\\
& |\vec{p}_2|^2\sin{\theta_2}^2\sin\phi_2|\vec{p}_\gamma||\vec{p}_2|\sin\theta_1\sin(\phi_1-\phi_2)\Big\} \qquad \text{(B-28)}
\end{aligned}
$$

$$
\begin{aligned}
W'_{TT} \;=\; & -2iW_7|\vec{p}_1|\sin\theta_1|\vec{p}_2|\sin\theta_2\sin(\phi_1-\phi_2)+2i\bar{W}_8\Big\{\frac{E_\gamma}{c}\Big[|\vec{p}_2|\cos\theta_2|\vec{p}_1|^2\sin{\theta_1}^2\\
& -|\vec{p}_1|^2\cos\theta_1\sin\theta_1|\vec{p}_2|\sin\theta_2\cos(\phi_1-\phi_2)\Big]+\\
& |\vec{p}_\gamma|\Big[\frac{E_1}{c}|\vec{p}_1|\sin\theta_1|\vec{p}_2|\sin\theta_2\cos(\phi_1-\phi_2)-\frac{E_2}{c}|\vec{p}_1|^2\sin{\theta_1}^2\Big]\Big\}-\\
& 2i\bar{W}_9\Big\{\frac{E_\gamma}{c}\Big[|\vec{p}_1|\cos\theta_1|\vec{p}_2|^2\sin{\theta_2}^2-|\vec{p}_2|^2\cos\theta_2\sin\theta_2|\vec{p}_1|\sin\theta_1\cos(\phi_1-\phi_2)\Big]+\\
& |\vec{p}_\gamma|\Big[\frac{E_2}{c}|\vec{p}_2|\sin\theta_2|\vec{p}_1|\sin\theta_1\cos(\phi_1-\phi_2)-\frac{E_1}{c}|\vec{p}_2|^2\sin{\theta_2}^2\Big]\Big\}. \qquad \text{(B-29)}
\end{aligned}
$$

Appendix C

Calculational details

In order, to keep the line of discussion clear and not to over do the text with technicalities of the calculations, some of them are included in this chapter. These derivations, some of them in extent, will contribute to the better understanding of some of the remarks made.

C-1 The ^{4}He density functions

C-1.1 Coordinate space

The general solution of the four-body Schrödinger equation for a realistic potential can be casted in a format which serves as a starting point for CBF calculations. This realistic wave function is translationally invariant by construction as can be observed from its the expression Eq. II-26.

Starting from the expression II-26 for the ^{4}He wave function, an expansion for $\phi_c(|\vec{r}|) = f_c(|\vec{r}|).\phi_{ho}(|\vec{r}|)$ in terms of Gaussians can been adopted :

$$\begin{aligned}
\phi_c(|\vec{r}|) &= a[1]e^{-r^2/2b[1]} + a[2]e^{-r^2/2b[2]} + a[3]e^{-r^2/2b[3]} \\
&\left\{ \begin{array}{llllll}
a[1] = -0.92695023 & b[1] = 0.24725465 \\
a[2] = 0.64799724 & b[2] = 13.810559 \\
a[3] = 0.5923402 & b[3] = 2.2518416
\end{array} \right. \qquad \text{(C-1)}
\end{aligned}$$

This expansion allows us to rewrite the central part of the ^{4}He wave function as follows :

$$\Psi(\vec{r}_1,\vec{r}_2,\vec{r}_3,\vec{r}_4) = \frac{1}{\sqrt{\mathcal{N}}} \sum_{i<j=1}^{4} \sum_{t_{ij}=1}^{3} a[t_{12}]a[t_{13}]a[t_{14}]a[t_{23}]a[t_{24}]a[t_{34}]$$
$$e^{-\frac{1}{2}(|\vec{r}_1-\vec{r}_2|^2/b[t_{12}]+|\vec{r}_1-\vec{r}_3|^2/b[t_{13}]+|\vec{r}_1-\vec{r}_4|^2/b[t_{14}]+|\vec{r}_2-\vec{r}_3|^2/b[t_{23}]+|\vec{r}_2-\vec{r}_4|^2/b[t_{24}]+|\vec{r}_3-\vec{r}_4|^2/b[t_{34}])} . \qquad \text{(C-2)}$$

The tensor correlations up to first order in the cluster expansion of II-26 don't give a contribution to the nuclear densities. The coordinate space densities as

obtained after performing the integrations analytically are listed underneath.

$$\rho(\vec{r}) = \frac{4}{\mathcal{N}} \sum_{i<j=1}^{4} \sum_{t_{ij}^i, t_{ij}^f=1}^{3} \mathcal{F}_a^i \mathcal{F}_a^f \left(\frac{2\pi}{\alpha}\right)^{3/2} \left(\frac{2\pi}{\beta}\right)^{3/2} \left(\frac{4}{3}\right)^3 e^{-8\gamma r^2/9} \tag{C-3}$$

$$\begin{aligned} F_{\rm ch}(\vec{q}) &= \int d^3\vec{r}\rho(\vec{r})e^{-i\vec{q}.\vec{r}} \\ &= \frac{2}{\mathcal{N}} \sum_{i<j=1}^{4} \sum_{t_{ij}^i, t_{ij}^f=1}^{3} \mathcal{F}_a^i \mathcal{F}_a^f \left(\frac{2\pi}{\alpha}\right)^{3/2} \left(\frac{2\pi}{\beta}\right)^{3/2} \left(\frac{2\pi}{\gamma}\right)^{3/2} e^{-9q^2/32\gamma} \end{aligned} \tag{C-4}$$

$$\begin{aligned} \rho_{\rm com}(\vec{R}) &= \int d^3\vec{r}_1 d^3\vec{r}_2 \rho(\vec{r}_1, \vec{r}_2)\delta^3(\vec{R} - \frac{\vec{r}_1 + \vec{r}_2}{2}) \\ &= 6\frac{2^3}{\mathcal{N}} \sum_{i<j=1}^{4} \sum_{t_{ij}^i, t_{ij}^f=1}^{3} \mathcal{F}_a^i \mathcal{F}_a^f \left(\frac{2\pi}{\alpha}\right)^{3/2} \left(\frac{2\pi}{\delta}\right)^{3/2} e^{-\frac{1}{2}(4\zeta - \lambda^2/\delta)R^2} \end{aligned} \tag{C-5}$$

$$\begin{aligned} \rho_{\rm rel}(\vec{r}) &= \int d^3\vec{r}_1 d^3\vec{r}_2 \rho(\vec{r}_1, \vec{r}_2)\delta^3(\vec{r} - (\vec{r}_1 - \vec{r}_2)) \\ &= 6\frac{2^3}{\mathcal{N}} \sum_{i<j=1}^{4} \sum_{t_{ij}^i, t_{ij}^f=1}^{3} \mathcal{F}_a^i \mathcal{F}_a^f \left(\frac{2\pi}{\alpha}\right)^{3/2} \left(\frac{\pi}{2\zeta}\right)^{3/2} e^{-\frac{1}{2}(\delta - \lambda^2/4\zeta)r^2} \end{aligned} \tag{C-6}$$

where, the constants $\mathcal{F}_a^i$ and $\mathcal{F}_a^f$ are products of Gaussian amplitudes e.g. $\mathcal{F}_a^i = a[t_{12}^i]a[t_{13}^i]a[t_{14}^i]a[t_{23}^i]a[t_{24}^i]a[t_{34}^i]$. The one-body density function is normalized to the total number of particles (= 4), while the other two distribution functions, which are derived from the two-body density operator, are normalized to the number of pairs in the nucleus (= 6). The other variables, introduced to make the expressions for the density operators more transparent are listed in Table C-1.

C -1.2 Momentum space

The momentum space wave function can be obtained from Eq. C-2 by means of a Fourier transform :

$$\begin{aligned} &\Phi(\vec{k}_1, \vec{k}_2, \vec{k}_3, \vec{k}_4) = \\ &\quad \int d^3\vec{r}_1 d^3\vec{r}_2 d^3\vec{r}_3 d^3\vec{r}_4 \Psi(\vec{r}_1, \vec{r}_2, \vec{r}_3, \vec{r}_4) e^{-i(\vec{k}_1.\vec{r}_1 + \vec{k}_2.\vec{r}_2 + \vec{k}_3.\vec{r}_3 + \vec{k}_4.\vec{r}_4)} \end{aligned} \tag{C-7}$$

An analytical expression can be obtained for the momentum space wave function as well as for the density functions once the central correlation function is expanded in a Gaussian basis given by Eq. C-1. The key concepts in all of these derivations is the insertion of a unity operator of the form :

$$\mathbb{1} = \int d^3\vec{r} \frac{1}{(2\pi)^3} \int d^3\vec{k} e^{-i\vec{k}.\vec{r}} \tag{C-8}$$

$$
\begin{aligned}
\alpha &= \frac{1}{b[t^i_{12}]} + \frac{1}{b[t^f_{12}]} + \frac{1}{4b[t^i_{13}]} + \frac{1}{4b[t^f_{13}]} + \\
&\quad \frac{1}{4b[t^i_{14}]} + \frac{1}{4b[t^f_{14}]} + \frac{1}{4b[t^i_{23}]} + \frac{1}{4b[t^f_{23}]} + \frac{1}{4b[t^i_{24}]} + \frac{1}{4b[t^f_{24}]} \\
\beta &= \frac{1}{b[t^i_{13}]} + \frac{1}{b[t^f_{13}]} + \frac{1}{9b[t^i_{14}]} + \frac{1}{9b[t^f_{14}]} + \frac{1}{b[t^i_{23}]} + \frac{1}{b[t^f_{23}]} + \frac{1}{9b[t^i_{24}]} + \frac{1}{9b[t^f_{24}]} + \\
&\quad \frac{4}{9b[t^i_{34}]} + \frac{4}{9b[t^f_{34}]} - \frac{1}{4\alpha_1}\Big(\frac{1}{b[t^i_{13}]} + \frac{1}{b[t^f_{13}]} + \frac{1}{3b[t^i_{14}]} + \frac{1}{3b[t^f_{14}]} \\
&\quad - \frac{1}{b[t^i_{23}]} - \frac{1}{b[t^f_{23}]} - \frac{1}{3b[t^i_{24}]} - \frac{1}{3b[t^f_{24}]}\Big)^2 \\
\gamma &= \frac{1}{b[t^i_{14}]} + \frac{1}{b[t^f_{14}]} + \frac{1}{b[t^i_{24}]} + \frac{1}{b[t^f_{24}]} + \frac{1}{b[t^i_{34}]} + \frac{1}{b[t^f_{34}]} - \frac{1}{4\alpha_1}\Big(\frac{1}{b[t^i_{14}]} + \frac{1}{b[t^f_{14}]} - \frac{1}{b[t^i_{24}]} - \frac{1}{b[t^f_{24}]}\Big)^2 - \\
&\quad \frac{1}{4\alpha_2}\Big(\frac{2}{3b[t^i_{14}]} + \frac{2}{3b[t^f_{14}]} + \frac{2}{3b[t^i_{24}]} + \frac{2}{3b[t^f_{24}]} - \frac{4}{3b[t^i_{34}]} - \frac{4}{3b[t^f_{34}]} - \\
&\quad \frac{2}{4\alpha_1}\Big(\frac{1}{b[t^i_{13}]} + \frac{1}{b[t^f_{13}]} + \frac{1}{3b[t^i_{14}]} + \frac{1}{3b[t^f_{14}]} - \frac{1}{b[t^i_{23}]} - \frac{1}{b[t^f_{23}]} - \frac{1}{3b[t^i_{24}]} - \frac{1}{3b[t^f_{24}]}\Big) \\
&\quad \Big(\frac{1}{b[t^i_{14}]} + \frac{1}{b[t^f_{14}]} - \frac{1}{b[t^i_{24}]} - \frac{1}{b[t^f_{24}]}\Big)\Big)^2 \\
\delta &= \frac{1}{4b[t^i_{13}]} + \frac{1}{4b[t^f_{13}]} + \frac{1}{4b[t^i_{14}]} + \frac{1}{4b[t^f_{14}]} + \frac{1}{4b[t^i_{23}]} + \frac{1}{4b[t^f_{23}]} + \frac{1}{4b[t^i_{24}]} + \frac{1}{4b[t^f_{24}]} + \\
&\quad \frac{1}{b[t^i_{34}]} + \frac{1}{b[t^f_{34}]} - \frac{1}{4\alpha_1}\Big(-\frac{1}{2b[t^i_{13}]} - \frac{1}{2b[t^f_{13}]} + \frac{1}{2b[t^i_{14}]} + \frac{1}{2b[t^f_{14}]} + \frac{1}{2b[t^i_{23}]} + \frac{1}{2b[t^f_{23}]} - \\
&\quad \frac{1}{2b[t^i_{24}]} - \frac{1}{2b[t^f_{24}]}\Big)^2 \\
\zeta &= \frac{1}{b[t^i_{13}]} + \frac{1}{b[t^f_{13}]} + \frac{1}{b[t^i_{14}]} + \frac{1}{b[t^f_{14}]} + \frac{1}{b[t^i_{23}]} + \frac{1}{b[t^f_{23}]} + \frac{1}{b[t^i_{24}]} + \frac{1}{b[t^f_{24}]} - \\
&\quad \frac{1}{4\alpha_1}\Big(\frac{1}{b[t^i_{13}]} + \frac{1}{b[t^f_{13}]} + \frac{1}{b[t^i_{14}]} + \frac{1}{b[t^f_{14}]} - \frac{1}{b[t^i_{23}]} - \frac{1}{b[t^f_{23}]} - \frac{1}{b[t^i_{24}]} - \frac{1}{b[t^f_{24}]}\Big)^2 \\
\lambda &= -\frac{1}{b[t^i_{13}]} - \frac{1}{b[t^f_{13}]} + \frac{1}{b[t^i_{14}]} + \frac{1}{b[t^f_{14}]} - \frac{1}{b[t^i_{23}]} - \frac{1}{b[t^f_{23}]} + \frac{1}{b[t^i_{24}]} + \frac{1}{b[t^f_{24}]} - \\
&\quad \frac{2}{4\alpha_1}\Big(-\frac{1}{2b[t^i_{13}]} - \frac{1}{2b[t^f_{13}]} + \frac{1}{2b[t^i_{14}]} + \frac{1}{2b[t^f_{14}]} + \frac{1}{2b[t^i_{23}]} + \frac{1}{2b[t^f_{23}]} - \frac{1}{2b[t^i_{24}]} - \frac{1}{2b[t^f_{24}]}\Big) \\
&\quad \Big(\frac{1}{b[t^i_{13}]} + \frac{1}{b[t^f_{13}]} + \frac{1}{b[t^i_{14}]} + \frac{1}{b[t^f_{14}]} - \frac{1}{b[t^i_{23}]} - \frac{1}{b[t^f_{23}]} - \frac{1}{b[t^i_{24}]} - \frac{1}{b[t^f_{24}]}\Big)
\end{aligned}
$$

Table C-1: This table enlists the various variables introduced in the equations C-3 through C-6

and the Fubini-Tonelli theorem specifying the conditions under which it is allowed to interchange an integration sequence.

$$
\begin{aligned}
&\Phi(\vec{K}_{\rm com},\vec{k}^{1}_{\rm rel},\vec{k}^{2}_{\rm rel},\vec{k}^{3}_{\rm rel}) = \\
&(2\pi)^{3/2}\delta^{3}(\vec{K}_{\rm com})\frac{1}{\sqrt{\mathcal{N}}}\sum_{t_{12}=1}^{3}\sum_{t_{13}=1}^{3}\sum_{t_{14}=1}^{3}\sum_{t_{23}=1}^{3}\sum_{t_{24}=1}^{3}\sum_{t_{34}=1}^{3} a[t_{12}]a[t_{13}]a[t_{14}]a[t_{23}]a[t_{24}]a[t_{34}] \\
&(b[t_{12}]b[t_{13}]b[t_{14}]b[t_{23}]b[t_{24}]b[t_{34}])^{3/2}\left[\frac{2\pi}{\alpha}\right]^{3/2}\left[\frac{2\pi}{\beta}\right]^{3/2}\left[\frac{2\pi}{\gamma}\right]^{3/2} \\
&e^{-\frac{1}{2}(e_1|\vec{k}^{1}_{\rm rel}|^2+e_2|\vec{k}^{2}_{\rm rel}|^2+e_3|\vec{k}^{3}_{\rm rel}|^2-2e_{12}\vec{k}^{1}_{\rm rel}.\vec{k}^{2}_{\rm rel}-2e_{13}\vec{k}^{1}_{\rm rel}.\vec{k}^{3}_{\rm rel}-2e_{23}\vec{k}_{\rm rel}2.\vec{k}^{3}_{\rm rel})}\frac{1}{\sqrt{4!}}\Big|\ \Big|_{\text{ST-Slater}}
\end{aligned}
\tag{C-9}
$$

with

$$
\left\{\begin{array}{rcl}
\alpha &=& b[t_{13}]+b[t_{14}]+b[t_{34}] \\
\beta &=& b[t_{13}]+b[t_{14}]+b[t_{23}]+b[t_{24}]-\frac{(b[t_{13}]+b[t_{14}])^2}{\alpha} \\
\gamma &=& b[t_{12}]+b[t_{14}]+b[t_{24}]-\frac{b[t_{14}]^2}{\alpha}-\frac{(b[t_{14}]+b[t_{24}]-\frac{b[t_{14}](b[t_{13}]+b[t_{14}])}{\alpha})^2}{\beta} \\
e_1 &=& b[t_{12}](1-\frac{b[t_{12}]}{\gamma}) \\
e_2 &=& b[t_{23}](1-\frac{b[t_{23}]}{\beta}(1+\frac{(b[t_{14}]+b[t_{24}]-\frac{b[t_{14}](b[t_{13}]+b[t_{14}])}{\alpha})^2}{\beta\gamma})) \\
e_3 &=& b[t_{34}](1-\frac{b[t_{34}]}{\alpha}(1+\frac{1}{\alpha}(\frac{(b[t_{13}]+b[t_{14}])^2}{\beta}+ \\
&& \frac{(-b[t_{14}]+\frac{b[t_{13}]+b[t_{14}]}{\beta}(b[t_{14}]+b[t_{24}]-\frac{b[t_{14}](b[t_{13}]+b[t_{14}])}{\alpha}))^2}{\gamma}))) \\
e_{12} &=& \frac{b[t_{12}]b[t_{23}]}{\beta\gamma}(b[t_{14}]+b[t_{24}]-\frac{b[t_{14}](b[t_{13}]+b[t_{14}])}{\alpha}) \\
e_{13} &=& \frac{b[t_{12}]b[t_{34}]}{\alpha\gamma}(-b[t_{14}]+\frac{b[t_{13}]+b[t_{14}]}{\underline{\rm e}ta}(b[t_{14}]+b[t_{24}]-\frac{b[t_{14}](b[t_{13}]+b[t_{14}])}{\alpha})) \\
e_{23} &=& \frac{b[t_{23}]b[t_{34}]}{\alpha\beta}(b[t_{13}]+b[t_{14}]+\frac{1}{\gamma}(b[t_{14}]+b[t_{24}]-\frac{b[t_{14}](b[t_{13}]+b[t_{14}])}{\alpha}) \\
&& (-b[t_{14}]+\frac{b[t_{13}]+b[t_{14}]}{\beta}(b[t_{14}]+b[t_{24}]-\frac{b[t_{14}](b[t_{13}]+b[t_{14}])}{\alpha})))
\end{array}\right.
\tag{C-10}
$$

where, $\frac{1}{4!}\Big|\ \Big|_{\text{ST-Slater}}$ is an abbreviation for the spin-isospin Slater determinant.

The center-of-mass and relative momenta, used to describe the intrinsic dynamics for the ^{4}He-nucleus are given by the following expressions :

$$
\begin{aligned}
\vec{K}_{\rm com} &= \vec{k}_1+\vec{k}_2+\vec{k}_3+\vec{k}_4 \\
\vec{k}^{1}_{\rm rel} &= \frac{3}{4}\vec{k}_1-\frac{\vec{k}_2+\vec{k}_3+\vec{k}_4}{4} \\
\vec{k}^{2}_{\rm rel} &= \frac{\vec{k}_1+\vec{k}_2}{2}-\frac{\vec{k}_3+\vec{k}_4}{2}
\end{aligned}
$$

$$\vec{k}^3_{\rm rel} = \frac{\vec{k}_1+\vec{k}_2+\vec{k}_3}{4} - \frac{3}{4}\vec{k}_4. \quad \text{(C-10)}$$

In an analogous manner as for the coordinate-space density functions, formulas for their counterparts in momentum-space can be derived. Replacing Ψ with Φ and $\vec{r}$ by $\vec{k}$ in the formulas C-3,C-5 and C-6 leads to :

$$\rho(\vec{k}) = \frac{4}{\mathcal{N}} \sum_{i<j=1}^{4} \sum_{t^i_{ij},t^f_{ij}=1}^{3} \mathcal{F}^i_{ab}\mathcal{F}^f_{ab} \left[\frac{2\pi}{e_1}\right]^{3/2} \left[\frac{2\pi}{e_2}\right]^{3/2} e^{-\frac{1}{2}(e_3-e^2_{23}/e_2)k^2} \quad \text{(C-11)}$$

$$\rho_{rel}(\vec{q}) = \frac{6}{\mathcal{N}} \sum_{i<j=1}^{4} \sum_{t^i_{ij},t^f_{ij}=1}^{3} \mathcal{F}^i_{ab}\mathcal{F}^f_{ab} \left[\frac{2\pi}{e_1}\right]^{3/2} \left[\frac{2\pi}{e_2+e_3/4-e_{23}}\right]^{3/2} \times e^{-\frac{1}{2}(e_3-(e_3/2-e_{23})^2/(e_2+e_3/4-e_{23}))q^2} \quad \text{(C-12)}$$

$$\rho_{com}(\vec{Q}) = \frac{6}{\mathcal{N}} \sum_{i<j=1}^{4} \sum_{t^i_{ij},t^f_{ij}=1}^{3} \mathcal{F}^i_{ab}\mathcal{F}^f_{ab} \left[\frac{2\pi}{e_1}\right]^{3/2} \left[\frac{2\pi}{e_3}\right]^{3/2} \times e^{-\frac{1}{2}(e_2+e_3/4-e_{23}-(e_3/2-e_{23})^2/e_3)Q^2}, \quad \text{(C-13)}$$

where, the parameters $\mathcal{F}^i_{ab}$ and $\mathcal{F}^f_{ab}$ are mixed products of Gaussian amplitudes and widths e.g.

$$\mathcal{F}^i_{ab} = a[t^i_{12}]a[t^i_{13}]a[t^i_{14}]a[t^i_{23}]a[t^i_{24}]a[t^i_{34}](b[t^i_{12}]b[t^i_{13}]b[t^i_{14}]b[t^i_{23}]b[t^i_{24}]b[t^i_{34}])^{3/2} \left[\frac{2\pi}{\alpha^i\beta^i\gamma^i}\right]^{3/2}.$$

In order, to make the above expressions more transparent, following variables have been introduced

$$\begin{cases} e_1 = e^i_1 + e^f_1 \\ e_2 = e^i_2 + e^f_2 - \frac{(e^i_{12}+e^f_{12})^2}{e^i_1+e^f_1} \\ e_3 = e^i_3 + e^f_3 - \frac{(e^i_{13}+e^f_{13})^2}{e^i_1+e^f_1} \\ e_{12} = e^i_{12} + e^f_{12} \\ e_{13} = e^i_{13} + e^f_{13} \\ e_{23} = e^i_{23} + e^f_{23} + \frac{e_{12}e_{13}}{e_1} \end{cases}$$

Just as their coordinate space counterparts they are normalized to the total number of particles or pairs in the nucleus depending on whether one is dealing with the momentum density, the relative- or COM-pair momentum density.

C-2 Harmonic oscillator wave function

The solution of the Schrödinger equation for an harmonic oscillator potential $V_{\rm ho} = \sum_{i=1}^{4} \frac{1}{2} m_N \omega^2 |\vec{r}_i|^2$ with zero angular momentum ($L = 0$) is

$$\Psi_{\rm HO}(x_1, x_2, x_3, x_4) = \left[\sqrt{\left(\frac{\nu}{\pi}\right)^{3/2}} \right]^4 e^{-\nu \sum_{i=1}^{4} r_i^2/2} \frac{1}{\sqrt{4!}} \Big| \Big|_{\text{ST-Slater}} \quad \text{(C-14)}$$

with $\nu = \omega m_N/\hbar$ and $x_i = (\vec{r}_i, s_i, t_i)$.
The radial part of the HO-wave function factorizes into a COM- and an intrinsic part :

$$\Psi_{\rm HO}(\vec{R}_{\rm com}, \vec{r}_{\rm rel}{}^1, \vec{r}_{\rm rel}{}^2, \vec{r}_{\rm rel}{}^3) = \sqrt{\left(\frac{4\nu}{\pi}\right)^{3/2}} e^{-2\nu |\vec{R}_{\rm com}|^2} \psi^{\rm rel}_{\rm HO}(\vec{r}_{\rm rel}{}^1, \vec{r}_{\rm rel}{}^2, \vec{r}_{\rm rel}{}^3)$$

$$\text{with} \quad \psi^{\rm rel}_{\rm HO}(\vec{r}_{\rm rel}{}^1, \vec{r}_{\rm rel}{}^2, \vec{r}_{\rm rel}{}^3) = \prod_{i<j}^{4} \sqrt{2} \left[\frac{\nu}{4\pi}\right]^{3/8} e^{-\frac{\nu |\vec{r}_i - \vec{r}_j|^2}{2}} \frac{1}{\sqrt{4!}} \Big| \Big|_{\text{ST-Slater}}, \quad \text{(C-15)}$$

which allows eliminating the center-of-mass coordinate in an unambiguous way. For this HO-wave function two types of density functions can be calculated. On the one hand, the density function relative to the COM. On the other hand, relative to the center of the potential. The results of both types of calculations are listed in Table C-2. Comparing both columns, just like that, would lead to the conclusion that by eliminating the center-of-mass coordinate the width of the one-body and pair density gets reduced while the NN-separation distribution remains unaltered. This is what one would expect intuitively and so did also the authors of Ref. [43]. But instead of using the same oscillator parameter ν for both kind of densities one should determine ν as a result of fitting a theoretical expectation value to the respective experimental value. To fix the oscillator parameter, we fitted the rms charge radius $< |\vec{r}|^2_{\rm ch} >^{1/2}_{\rm exp}$ to its measured value 1.676 fm. Into lowest order, the charge density, for all particles in a $1s$-state, reads :

$$\begin{aligned} \rho^{ch}_{^4He}(\vec{r}) &= 2|\phi(\vec{r})|^2 \\ &= 2 \left| \left(\frac{\nu}{\pi}\right)^{3/4} e^{-\nu |\vec{r}|^2/2} \right|^2 \end{aligned} \quad \text{(C-16)}$$

The charge density is normalized to the total number of protons explaining the extra factor of two.
With the above charge density, the rms charge radius reads :

$$\begin{aligned} < \vec{r}^{\,2}_{ch} > &= \frac{1}{2} \int d^3\vec{r}\, \vec{r}^{\,2}\, \rho^{ch}_{^4He}(\vec{r}) \\ &= \begin{cases} \frac{3}{2\nu} & \text{HO-model} \\ \frac{9}{8\nu} & \text{com-corrected HO-model} \end{cases} \end{aligned} \quad \text{(C-17)}$$

	HO-model $(\nu = 0.534/fm^2)$	COM-corrected HO-model $(\nu = 0.4/fm^2)$
$\rho(\vec{r})$	$4\left(\frac{\nu}{\pi}\right)^{3/2} e^{-\nu r^2}$	$4\,.\,8\left(\frac{\nu}{3\pi}\right)^{3/2} e^{-4\nu r^2/3}$
$F_{ch}(\vec{q})$	$2e^{-q^2/4\nu}$	$2e^{-3q^2/16\nu}$
$\rho_{rel}(\vec{r})$	$6\left(\frac{\nu}{2\pi}\right)^{3/2} e^{-\nu r^2/2}$	$6\left(\frac{\nu}{2\pi}\right)^{3/2} e^{-\nu r^2/2}$
$\rho_{com}(\vec{R})$	$6\left(\frac{2\nu}{\pi}\right)^{3/2} e^{-2\nu R^2}$	$6\,.\,8\left(\frac{\nu}{\pi}\right)^{3/2} e^{-4\nu R^2}$

Table C-2: The one- and two-body densities and the charge form factor computed in a HO-model. The left column contains the genuine IPM densities while the distributions in the right column are obtained after eliminating the center-of-mass motion.

Solving for ν returns the oscillator parameters as given in Table C-2.

	HO-model ($\nu = 0.534/fm^2$)	COM-corrected HO-model ($\nu = 0.4/fm^2$)
$\rho(\vec{k})$	$4\left(\frac{1}{\pi\nu}\right)^{3/2} e^{-k^2/\nu}$	$4\ \left(\frac{4}{3\pi\nu}\right)^{3/2} e^{-4k^2/3\nu}$
$\rho_{rel}(\vec{q})$	$6\left(\frac{2}{\pi\nu}\right)^{3/2} e^{-2q^2/\nu}$	$6\left(\frac{2}{\pi\nu}\right)^{3/2} e^{-2q^2/\nu}$
$\rho_{com}(\vec{Q})$	$6\left(\frac{1}{2\pi\nu}\right)^{3/2} e^{-Q^2/2\nu}$	$6\ \left(\frac{1}{\pi\nu}\right)^{3/2} e^{-Q^2/\nu}$

Table C-3: The momentum density functions of ^{4}He calculated in an HO-model. The first column contains the density distributions in the LAB-frame while the momentum distributions in the COM-frame are tabulated in the second column.

The momentum space HO-wave functions (in the COM- and LAB-frame) are obtained by a suitable Fourier transform :

$$\Phi_{\rm HO}(\vec{k}_1,\vec{k}_2,\vec{k}_3,\vec{k}_4) \;=\; \int d^3\vec{r}_1 d^3\vec{r}_2 d^3\vec{r}_3 d^3\vec{r}_4 \Psi_{\rm HO}(\vec{r}_1,\vec{r}_2,\vec{r}_3,\vec{r}_4) e^{-i(\vec{k}_1.\vec{r}_1+\vec{k}_2.\vec{r}_2+\vec{k}_3.\vec{r}_3+\vec{k}_4.\vec{r}_4)} \; .$$

The previous equation can be solved in the LAB- as well as in the COM-frame of reference :

$$\Phi^{\rm LAB}_{\rm HO}(\vec{k}_1,\vec{k}_2,\vec{k}_3,\vec{k}_4) \;=\; \left[\left(\frac{4\pi}{\nu}\right)^{3/4}\right]^4 e^{-(k_1^2+k_2^2+k_3^2+k_4^2)/2\nu} \frac{1}{\sqrt{4!}}\Big| \;\Big|_{\text{ST-Slater}} \qquad \text{(C-18)}$$

$$\Phi^{\rm COM}_{\rm HO}(\vec{K}_{\rm com},\vec{k}^1_{\rm rel},\vec{k}^2_{\rm rel},\vec{k}^3_{\rm rel}) \;=\; (2\pi)^{3/2}\delta^3(\vec{K}_{\rm com}) \left[4\left(\frac{\pi}{\nu}\right)^{3/4}\right]^3$$
$$\times e^{-(|\vec{k}_{\rm rel}{}^1-\vec{k}_{\rm rel}{}^2/2|^2/\nu+|\vec{k}_{\rm rel}{}^3-\vec{k}_{\rm rel}{}^2/2|^2/\nu+|\vec{k}_{\rm rel}{}^2|^2/2\nu)} \frac{1}{\sqrt{4!}}\Big| \;\Big|_{\text{ST-Slater}}, \qquad \text{(C-19)}$$

where $(\vec{K}_{\rm com}, \vec{k}^1_{\rm rel}, \vec{k}^2_{\rm rel}, \vec{k}^3_{\rm rel})$ are defined as in Eq. C-10.
Table C-3 displays the IPM momentum densities. Ignoring the oscillator parameter differences, one concludes that the c.o.m.-corrected momentum and pair momentum distributions are narrower relative to the genuine shell model densities while the pair relative momentum function remains unaltered. This is what one would expect by simply eliminating the center-of-mass motion, These conclusions, should be looked upon along the same lines as expressed in the previous paragraph.

C-3 Lepton tensor

The lepton tensor as defined in Eq. III-15 looks like :

$$L_{\mu\nu} = \bar{u}(\vec{k^f}_e, m_{s_f})\gamma_\mu u(\vec{k^i}_e, m_{s_i})^\dagger \bar{u}(\vec{k^f}_e, m_{s_f})\gamma_\nu u(\vec{k^i}_e, m_{s_i}) \; . \qquad \text{(C-20)}$$

The electron wave function $u(\vec{k}_e, m_s)$ is a solution of the Dirac equation and as such, it has the properties outlined in Appendix B-3.
Using Eq. B-9 makes it possible to rewrite Eq. III-15 as :

$$\begin{aligned} L_{\mu\nu} = \sum_{m_{s_i}, m_{s_f} = -1/2}^{+1/2} & \bar{u}(\vec{k^f}_e, m_{s_f})\gamma_\mu \frac{1+\gamma_5 \not{s}_i}{2} u(\vec{k^i}_e, m_{s_i}) \\ & \bar{u}(\vec{k^i}_e, m_{s_i})\gamma_\nu \frac{1+\gamma_5 \not{s}_f}{2} u(\vec{k^f}_e, m_{s_f}) \end{aligned}$$

Inserting Eq. B-10 one obtains

$$\begin{aligned} L_{\mu\nu} &= \mathrm{Tr}\left[\frac{\not{p}^f_e c + m_e c^2}{2E^f_e}\gamma_\mu \frac{1+\gamma_5\not{s}_i}{2}\frac{\not{p}^i_e c + m_e c^2}{2E^i_e}\gamma_\nu \frac{1+\gamma_5\not{s}_f}{2}\right] \\ &= \frac{1}{16 E^i_e E^f_e}\mathrm{Tr}\Big[\not{p}^f_e c\gamma_\mu \not{p}^i_e c\gamma_\nu + \not{p}^f_e c\gamma_\mu \not{p}^i_e c\gamma_\nu\gamma_5\not{s}_f + \not{p}^f_e c\gamma_\mu m_e c^2\gamma_\nu + \\ &\quad \not{p}^f_e c\gamma_\mu m_e c^2\gamma_\nu\gamma_5\not{s}_f + \not{p}^f_e c\gamma_\mu\gamma_5\not{s}_i\not{p}^i_e c\gamma_\nu + \not{p}^f_e c\gamma_\mu\gamma_5\not{s}_i\not{p}^i_e c\gamma_\nu\gamma_5\not{s}_f + \\ &\quad \not{p}^f_e c\gamma_\mu\gamma_5\not{s}_i m_e c^2\gamma_\nu + \not{p}^f_e c\gamma_\mu\gamma_5\not{s}_i m_e c^2\gamma_\nu\gamma_5\not{s}_f + m_e c^2\gamma_\mu\not{p}^i_e c\gamma_\nu + \\ &\quad m_e c^2\gamma_\mu\not{p}^i_e c\gamma_\nu\gamma_5\not{s}_f + m_e c^2\gamma_\mu m_e c^2\gamma_\nu + m_e c^2\gamma_\mu m_e c^2\gamma_\nu\gamma_5\not{s}_f + \\ &\quad m_e c^2\gamma_\mu\gamma_5\not{s}_i\not{p}^i_e c\gamma_\nu + m_e c^2\gamma_\mu\gamma_5\not{s}_i\not{p}^i_e c\gamma_\nu\gamma_5\not{s}_f + m_e c^2\gamma_\mu\gamma_5\not{s}_i m_e c^2\gamma_\nu + \\ &\quad m_e c^2\gamma_\mu\gamma_5\not{s}_i m_e c^2\gamma_\nu\gamma_5\not{s}_f\Big] \\ &= \frac{c^2}{4E^i_e E^f_e}\Big\{(p^i_e p^f_e)\Big[-g_{\mu\nu} - (s_i)_\mu(s_f)_\nu - (s_i)_\nu(s_f)_\mu + \frac{g_{\mu\nu}}{2}(s_i s_f)\Big] + \\ &\quad (p^i_e s_i)\Big[-(p^f_e)_\mu(s_f)_\nu + (p^f_e)_\nu(s_f)_\mu - \frac{g_{\mu\nu}}{2}(p^f_e s_f)\Big] + \end{aligned}$$

$$
\begin{aligned}
&(p_e^i s_f)\left[(p_e^f)_\mu (s_i)_\nu + (p_e^f)_\nu (s_i)_\mu - \frac{g_{\mu\nu}}{2}(p_e^f s_i)\right] + \\
&(p_e^f s_i)\left[(p_i^e)_\mu (s_f)_\nu + (p_e^i)_\nu (s_f)_\mu - \frac{g_{\mu\nu}}{2}(p_e^i s_f)\right] + \\
&(p_e^f s_f)\left[(p_e^i)_\mu (s_i)_\nu - (p_e^i)_\nu (s_i)_\mu - \frac{g_{\mu\nu}}{2}(p_e^i s_i)\right] + \\
&(s_i s_f)\left[-g_{\mu\nu} m_e^2 c^2 - (p_e^f)_\mu (p_e^i)_\nu - (p_e^f)_\nu (p_e^i)_\mu + \frac{g_{\mu\nu}}{2}(p_e^f p_e^i)\right] + \\
&(p_e^f)_\mu (p_e^i)_\nu + (p_e^f)_\nu (p_e^i)_\mu + m_e^2 c^2 \left[(s_i)_\mu (s_f)_\nu + (s_i)_\nu (s_f)_\mu\right] + g_{\mu\nu} m_e^2 c^2 + \\
&i\epsilon_{\alpha\beta\mu\nu}\left[(p_e^f)^\alpha (s_f)^\beta + (p_e^f)^\alpha (s_i)^\beta - (p_e^i)^\alpha (s_f)^\beta - (p_e^i)^\alpha (s_i)^\beta\right] m_e c\Big\} \quad \cdot\text{(C-21)}
\end{aligned}
$$

In the relativistic limit the electron is longitudinally polarized (i.e., $s_i \to h_i \frac{p_e^i}{m_e c}$ and $s_f \to h_f \frac{p_e^f}{m_e c}$) and Eq. C-21 becomes

$$
\begin{aligned}
L_{\mu\nu} \;=\; & \frac{c^2}{4E^i{}_e E^f{}_e}\Big\{-(1+h_i h_f)(p_e^i p_e^f) g_{\mu\nu} + (1-h_i h_f) g_{\mu\nu} m_e^2 c^2 + \\
& (1+h_i h_f)\left[(p_e^f)_\mu (p_e^i)_\nu + (p_e^f)_\nu (p_e^i)_\mu\right] + i\epsilon_{\alpha\beta\mu\nu}(h_i + h_f)(p_e^f)^\alpha (p_e^i)^\beta\Big\} \quad \text{(C-22)}
\end{aligned}
$$

Electron scattering in the ultra-relativistic limit conserves helicity as can be deduced from Eq. C-22 :

$$
\begin{aligned}
L_{\mu\nu}(h_i = h_f = h) \;=\; & \frac{2c^2}{4E^i{}_e E^f{}_e}\Big\{(p_e^f)_\mu (p_e^i)_\nu + (p_e^f)_\nu (p_e^i)_\mu - \\
& \qquad g_{\mu\nu}(p_e^i p_e^f) + ih\epsilon_{\alpha\beta\mu\nu}(p_e^f)^\alpha (p_e^i)^\beta\Big\} \quad \text{(C-23)} \\
L_{\mu\nu}(h_i \neq h_f) \;=\; & \frac{2c^2}{4E^i{}_e E^f{}_e} g_{\mu\nu} m_e^2 c^2 \quad \overset{\frac{m_e}{E_e}\to 0}{\to} \quad 0\,. \qquad \text{(C-24)}
\end{aligned}
$$

The final expression for the lepton tensor in the ultra-relativistic limit reads :

$$
\begin{aligned}
&L_{\mu\nu} = \\
&\quad \frac{2c^2}{4E^i{}_e E^f{}_e}\Big\{(p_e^f)_\mu (p_e^i)_\nu + (p_e^f)_\nu (p_e^i)_\mu - g_{\mu\nu}(p_e^i p_e^f) + ih\epsilon_{\alpha\beta\mu\nu}(p_e^f)^\alpha (p_e^i)^\beta\Big\} \quad \text{(C-25)}
\end{aligned}
$$

C -4 Recoil factor

The recoil factor appears as a direct consequence of the following integral :

$$
\begin{aligned}
&\int f(|\vec{k_3}|)\delta(\omega_{\gamma^*} + \omega_{^4He} - \omega_1 - \omega_2 - \omega_3 - \omega_4) d|\vec{k_3}| \\
&= \int f(|\vec{k_3}|) \sum_i \frac{1}{\left|\partial[\Delta E(|\vec{k_3}|)]/\partial|\vec{k_3}|\right|} \delta(|\vec{k_3}| - |\vec{k_3}|_i) d|\vec{k_3}| \\
&= \sum_i f(|\vec{k_3}|_i) \frac{1}{\left|\partial[\Delta E(|\vec{k_3}|_i)]/\partial|\vec{k_3}|\right|}\,,
\end{aligned}
$$

where use have been made of a property of the Dirac delta function

$$\delta(f(x)) = \sum_i \frac{1}{|df(x_i)/dx|}\delta(x - x_i) \tag{C-26}$$

with x_i a root of the function $f(x)$. To proceed, we will first calculate $\partial[\Delta E(|\vec{k_3}|)]/\partial|\vec{k_3}|$:

$$\Delta E(|\vec{k_3}|) = \omega_{\gamma^*} + \omega_{^4He} - \omega_1 - \omega_2 - c\sqrt{|\vec{k_3}|^2 + \frac{m_N^2c^4}{(\hbar c)^2}} - c\sqrt{(\vec{k_m} - \vec{k_3})^2 + \frac{m_N^2c^4}{(\hbar c)^2}} \ ,$$

with $\vec{k_m} = \vec{q_\gamma} - \vec{k_1} - \vec{k_2}$.

$$\begin{aligned}
\partial[\Delta E(|\vec{k_3}|)]/\partial|\vec{k_3}| &= 0 + 0 - 0 - 0 - \frac{c|\vec{k_3}|}{\sqrt{|\vec{k_3}|^2 + \frac{m_N^2c^4}{(\hbar c)^2}}} - \frac{c(|\vec{k_3}| - |\vec{k_m}|cos(\theta_{3m}))}{\sqrt{(\vec{k_m} - \vec{k_3})^2 + \frac{m_N^2c^4}{(\hbar c)^2}}} \\
&= -c^2\left(\frac{|\vec{k_3}|}{\omega_3} + \frac{|\vec{k_3}| - |\vec{k_m}|cos(\theta_{3m})}{\omega_4}\right) \\
&= -c^2\left(\frac{|\vec{p_3}|}{E_3} + \frac{|\vec{p_3}| - |\vec{p_m}|cos(\theta_{3m})}{E_4}\right) \\
&= -c^2\frac{|\vec{p_3}|}{E_3}\left(1 + \frac{E_3}{E_4}\left(1 - \frac{|\vec{p_m}|cos(\theta_{3m})}{|\vec{p_3}|}\right)\right) \ .
\end{aligned} \tag{C-27}$$

The recoil factor is identified with the last part of Eq. C-27 :

$$\mathrm{f_{recoil}} = \left|\frac{1}{1 + \frac{E_3}{E_4}\left(1 - \frac{|\vec{p_m}|cos(\theta_{3m})}{|\vec{p_3}|}\right)}\right| \ . \tag{C-28}$$

C-5 The delta decay width

A decay width Γ gets defined through the following relation

$$\Gamma = \frac{1}{16}\sum\!\!\!\!\!\!\int \frac{|S_{fi}|^2}{T}d\rho_f \ , \tag{C-29}$$

with T the specific time interval during which the transition probability is calculated in a box normalization technique.
One averages over the initial spin and isospin projections and sums over the final ones. This results into an additional factor of $\Big(1/[2\times(3/2)+1]\Big)^2$. The scattering matrix S_{fi}, characterizing the decay reaction gets multiplied by the phase-space factor.

$$d\rho_f = V\frac{d^3\vec{k}_N}{(2\pi)^3}V\frac{d^3\vec{k}_\pi}{(2\pi)^3} \ ,$$

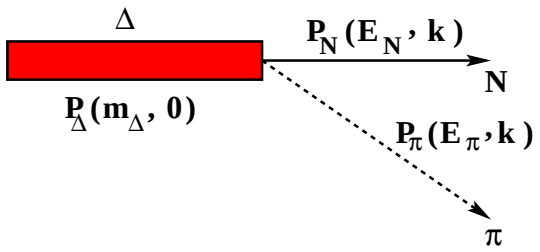

Figure C-1: The pion-nucleon decay channel of the delta resonance.

which denotes the density of final states in a volume V. The scattering matrix can be derived using the quantum field theory formalism with the interaction Lagrangian density $\mathcal{L}_{\pi N\Delta}$ of Eq. III-113 :

$$\begin{aligned}
S_{fi} &= -\frac{i}{\hbar}\int d^4x\,\langle \pi N|-\mathcal{L}_{\pi N\Delta}(x)|\Delta\rangle \\
&= -\frac{i}{\hbar}\int d^4x\left\langle \pi N|\frac{f_{\pi N\Delta}}{m_\pi}\sqrt{\frac{\hbar^3}{c}}\bar{\psi}(x)\vec{T}.(\partial_\mu\vec{\phi}(x))\Psi^\mu_\Delta(x)|\Delta\right\rangle \\
&= \lim_{V\to\infty}\frac{i}{\hbar^2}\frac{f_{\pi N\Delta}}{m_\pi}\sqrt{\frac{\hbar^3}{c}}(2\pi\hbar)^4\delta^4(p_\Delta-p_N-p_\pi)\left(\frac{1}{\sqrt{V}}\right)^3\sqrt{\frac{m_Nc^2}{E_N}}\sqrt{\frac{\hbar^2c^2}{2E_\pi}} \\
&\qquad \bar{u}(\vec{p}_N,m_s)\eta^\dagger_{(\frac{1}{2},m_t)}(\vec{T})_i(p_\pi)_\mu u^\mu_\Delta(\vec{p}_\Delta,m_{s_\Delta})\eta_{(\frac{3}{2},m_{t_\Delta})}\,. \qquad \text{(C-30)}
\end{aligned}$$

The squared scattering matrix looks like :

$$\begin{aligned}
\frac{1}{16}\sum_{s,t}|S_{fi}|^2 &= \lim_{V,T\to\infty}VT(2\pi\hbar)^4\delta^4(p_\Delta-p_N-p_\pi)\frac{1}{16}\sum\frac{f^2_{\pi N\Delta}m_Nc^3}{2m^2_\pi E_NE_\pi}\frac{\hbar}{V^3} \\
&\qquad \bar{u}(\vec{p}_N,m_s)\eta^\dagger_{(\frac{1}{2},m_t)}(\vec{T})_i(p_\pi)_\mu u^\mu_\Delta(\vec{p}_\Delta,m_{s_\Delta})\eta_{(\frac{3}{2},m_{t_\Delta})}\cdot \\
&\qquad (p_\pi)_\nu\bar{u}^\nu_\Delta(\vec{p}_\Delta,m_{s_\Delta})\eta^\dagger_{(\frac{3}{2},m_{t_\Delta})}(\vec{T})^\dagger_i u(\vec{p}_N,m_s)\eta_{(\frac{1}{2},m_t)} \\
&= \lim_{V,T\to\infty}\frac{\hbar T}{V^2}(2\pi\hbar)^4\delta^4(p_\Delta-p_N-p_\pi)\frac{1}{16}\frac{f^2_{\pi N\Delta}m_Nc^3}{2m^2_\pi E_NE_\pi} \\
&\qquad \left[\sum_{i=1}^{3}\frac{2}{3}\delta_{ii}\right]\left[\sum_{m_t=-1/2}^{1/2}\eta^\dagger_{(\frac{1}{2},m_t)}\eta_{(\frac{1}{2},m_t)}\right]|\vec{p}_\pi|^2 \\
&\qquad \left[\sum_{m_{s_\Delta}=-3/2}^{3/2}\left|\left\langle\frac{1}{2},m_{s_\Delta};1,0|\frac{3}{2},m_{s_\Delta}\right\rangle\right|^2\right. \\
&\qquad \left.\times\left[\sum_{m_s=-1/2}^{1/2}|\bar{u}(\vec{p}_N,m_s)u(\vec{p}_\Delta,m_{s_\Delta})|^2\right]\right]
\end{aligned}$$

where use have been made of the properties of the isospin projection operator defined in Appendix B-4.
In the non-relativistic limit this expression reduces to

$$\begin{aligned}\frac{1}{16}\sum_{s,t}|S_{fi}|^2 &= \lim_{V,T\to\infty}\frac{\hbar T}{V^2}(2\pi\hbar)^4\delta^4(p_\Delta - p_N - p_\pi)\frac{1}{16}\frac{f^2_{\pi N\Delta}m_N c^3}{2m_\pi^2 E_N E_\pi}\frac{2}{3}\,3\,2\,|\vec{p}_\pi|^2\,\frac{4}{3}\\ &= \lim_{V,T\to\infty}\frac{\hbar T}{V^2}(2\pi\hbar)^4\delta^4(p_\Delta - p_N - p_\pi)\frac{f^2_{\pi N\Delta}m_N c^3}{2m_\pi^2 E_N E_\pi}\frac{|\vec{p}_\pi|^2}{3}\ , \qquad \text{(C-31)}\end{aligned}$$

where we have used the property that the non-relativistic reduction of a spin $\frac{1}{2}$ spinor is momentum independent which justifies the equality

$$\bar{u}(\vec{p}_N, m_s)u(\vec{p}_\Delta, m_{s_\Delta}) \stackrel{NR}{=} 1\ \cdot \qquad \text{(C-32)}$$

To arrive at the final expression for the scattering matrix we assumed that the pion propagates along the z-axis. Inserting Eq. C-31 into the expression for the decay width gives rise to the following equation :

$$\begin{aligned}\Gamma &= \lim_{V,T\to\infty}\int(2\pi\hbar)^4\delta^4(p_\Delta - p_N - p_\pi)\frac{f^2_{\pi N\Delta}m_N c^3}{2m_\pi^2 E_N E_\pi}\frac{\hbar|\vec{p}_\pi|^2}{3}\frac{d^3\vec{p}_N}{(2\pi\hbar)^3}\frac{d^3\vec{p}_\pi}{(2\pi\hbar)^3}\\ &= \frac{2\pi}{3}\frac{f^2_{\pi N\Delta}m_N c^3}{m_\pi^2 E_N E_\pi}\frac{\hbar}{(2\pi\hbar)^2}\int\delta(E_\Delta - E_N - E_\pi)|\vec{p}_\pi|^4 d|\vec{p}_\pi|\\ &= \frac{2}{3}\frac{1}{4\pi}\frac{f^2_{\pi N\Delta}}{m_\pi^2}\frac{m_N}{m_\Delta}\frac{|\vec{p}_\pi|^3}{\hbar c}\ , \qquad \text{(C-33)}\end{aligned}$$

where we used the expression :

$$\delta(E_\Delta - E_N - E_\pi) \to \sum_i \frac{E_N E_\pi}{|\vec{p}_\pi|c^2.m_\Delta c^2}\delta(|\vec{p}_\pi| - p_0^i)\ ,$$

with the sum running over the roots of the kernel $E_\Delta - E_N - E_\pi$. The pion momentum p_π is given by :

$$|\vec{p}_\pi| = \sqrt{\frac{1}{4s}\left[(s-(m_N c + m_\pi c)^2)(s-(m_N c - m_\pi c)^2)\right]}\ , \qquad \text{(C-34)}$$

which places a cut on the Mandelstam variable s namely $s > m_N c + m_\pi c$.

C-6 The non-relativistic one-body current

We start from the relativistic one-body vertex defined in Eq. III-129

$$\Gamma^\mu_{CC2} = F_1^N(Q^2)\gamma^\mu + i\kappa_N\frac{F_2^N(Q^2)}{2m_N c}\sigma^{\mu\nu}(p_\gamma)_\nu$$

and adopt the Pauli reduction scheme [136] to derive the non-relativistic one-body nuclear current to lowest order in $\frac{p_N}{m_N}$. As explained in Section §4.3.1 the Pauli reduction method starts from the expectation value of the hadronic current for an on-shell positive-energy Dirac spinor :

$$\psi_{E=E_p}(\vec{x},t) = \sqrt{\frac{E_p + m_N c^2}{2m_N c^2}} \frac{e^{-\frac{i}{\hbar}p.x}}{(2\pi\hbar)^{3/2}} \begin{pmatrix} 1 \\ \\ \frac{\vec{\sigma}.\vec{p}c}{E_p + m_N c^2} \end{pmatrix} \chi_{(1/2,m_s)} \ .$$

The nuclear current operator in two-dimensional spin space looks like :

$$\begin{aligned} \hat{J}^{\mu}_N(0) \ = \ & \sqrt{\frac{E^f_p + m_N c^2}{2m_N c^2}} \begin{pmatrix} 1 & \frac{\vec{\sigma}.\vec{p}^{\,f} c}{E^f_p + m_N c^2} \end{pmatrix} \gamma^0 \left[F_1^N(Q^2)\gamma^{\mu} + i\kappa_N \frac{F_2^N(Q^2)}{2m_N c} \sigma^{\mu\nu}(p_\gamma)_\nu \right] \\ & \times \sqrt{\frac{E^i_p + m_N c^2}{2m_N c^2}} \begin{pmatrix} 1 \\ \\ \frac{\vec{\sigma}.\vec{p}^{\,i} c}{E^i_p + m_N c^2} \end{pmatrix} , \end{aligned} \tag{C-35}$$

with charge and vector components :

$$\begin{aligned} \hat{\rho}(0) \ = \ & \sqrt{\frac{E^f_p + m_N c^2}{2m_N c^2}} \begin{pmatrix} 1 & \frac{\vec{\sigma}.\vec{p}^{\,f} c}{E^f_p + m_N c^2} \end{pmatrix} \begin{pmatrix} F_1^N(Q^2) & -\kappa_N \frac{F_2^N(Q^2)}{2m_N c} \vec{\sigma}.\vec{p}_\gamma \\ \kappa_N \frac{F_2^N(Q^2)}{2m_N c} \vec{\sigma}.\vec{p}_\gamma & F_1^N(Q^2) \end{pmatrix} \\ & \times \sqrt{\frac{E^i_p + m_N c^2}{2m_N c^2}} \begin{pmatrix} 1 \\ \\ \frac{\vec{\sigma}.\vec{p}^{\,i} c}{E^i_p + m_N c^2} \end{pmatrix} \end{aligned} \tag{C-36}$$

$$\begin{aligned} \hat{\vec{J}}(0) \ = \ & \sqrt{\frac{E^f_p + m_N c^2}{2m_N c^2}} \begin{pmatrix} 1 & \frac{\vec{\sigma}.\vec{p}^{\,f} c}{E^f_p + m_N c^2} \end{pmatrix} \\ & \times \begin{pmatrix} i\kappa_N \frac{F_2^N(Q^2)}{2m_N c} (\vec{\sigma} \times \vec{p}_\gamma) & \left[F_1^N(Q^2) + \kappa_N \frac{E_\gamma}{2m_N c^2} F_2^N(Q^2) \right] \vec{\sigma} \\ \left[F_1^N(Q^2) - \kappa_N \frac{E_\gamma}{2m_N c^2} F_2^N(Q^2) \right] \vec{\sigma} & -i\kappa_N \frac{F_2^N(Q^2)}{2m_N c} (\vec{\sigma} \times \vec{p}_\gamma) \end{pmatrix} \\ & \times \sqrt{\frac{E^i_p + m_N c^2}{2m_N c^2}} \begin{pmatrix} 1 \\ \\ \frac{\vec{\sigma}.\vec{p}^{\,i} c}{E^i_p + m_N c^2} \end{pmatrix} . \end{aligned} \tag{C-37}$$

Starting from this expression for the charge and current operator, a perturbation expansion in $\frac{|\vec{p}^{\,(f/i)}|}{m_N}$ can be performed. Retaining only terms up to lowest

relativistic order one gets

$$\hat{\rho}_{LO}(0) = F_1^N(Q^2) \tag{C-38}$$

$$\hat{\vec{J}}_{LO}(0) = \frac{F_1^N(Q^2)}{2m_N c}\left(\vec{p}^{\,i} + \vec{p}^{\,f}\right) + i\frac{F_1^N(Q^2) + \kappa_N F_2^N(Q^2)}{2m_N c}\vec{\sigma} \times (\vec{p}^{\,f} - \vec{p}^{\,i}) \; . \tag{C-39}$$

In the lowest relativistic order an identical expression for the one-body current can be derived with the aid of a Foldy-Wouthuysen transformation [139].

Nawoord

Aan het einde van een thesis is het gepast even stil te staan bij, en een woord van dank te richten aan, de vele mensen die op directe of indirecte wijze hebben bijgedragen tot de totstandkoming ervan.

Op de eerste plaats zou ik mijn promotor Prof. Dr. Jan Ryckebusch willen danken voor het aanbrengen van dit thesis onderwerp. Zijn ervaring op het gebied van de lage- en intermediaire kernfysica is van grote waarde gebleken bij het interpreteren van de, door de computer gegenereerde, theoretische curves. Ik ben Prof. Dr. Jan Ryckebusch tevens in hoge mate erkentelijk voor het kritisch nalezen van deze thesis en voor de vele terechte correcties waardoor dit werk tot een volwaardige thesis geëvolueerd is. Dat dit niet van een leien dakje gelopen is getuige de lange doorlooptijd nl. van de aanvang in 1996 tot de finale vormgeving in 2004. Voor het grote geduld en de talrijke aansporingen om telkens weer de draad op te nemen, ben ik Jan zeer dankbaar..

Een woord van dank wil ik richten tot Prof. Dr. K. Heyde voor de kans die hij mij geboden heeft om gedurende vijf jaar, aan het instituut voor nucleaire wetenschappen, "wetenschappelijk" onderzoek te verrichten.

Theoretische fysica is een sport die gespeeld wordt met een computer wat aanleiding geeft tot allerhande triviale, maar vervelende, computer problemen. Voor de hulp mij geboden bij het oplossen van deze problemen wens ik mijn collega onderzoekers Dimitri Debruyne en Stijn Janssen te danken.

Verder wil ik Willy De Baere en Jan Deneve bedanken voor de aangename werksfeer en de vele niet wetenschappelijke babbels gedurende de afgelopen vijf jaar.

Last but not least, gaat mijn dank uit naar Rudi Verspille voor het verzorgde teken- en inbindwerk.

Samenvatting

In dit doctoraatswerk wordt een translatie invariant model voorgesteld voor de beschrijving van twee nucleon uitstoot reacties aan een helium kern. De titel haalt reeds de twee belangrijkste onderdelen in dit werk aan: nl. enerzijds een beschrijving van het reactie mechanisme en anderzijds een consistente modellering van de helium kern. Op de helium kern golffunctie wordt in hoofdstuk 2 van dit werk uitvoerig ingegaan terwijl hoofdstuk 3 volledig gewijd is aan het beschrijven van het twee nucleon uitstoot reactie proces.

Nucleon uitstoot reacties behoren tot het domein van de intermediaire energie kernfysica. De nadruk ligt hierbij vooral op de studie van de onderliggende structuur van kernmaterie en haar dynamisch gedrag op korte afstandsschaal gaande van 3 tot 0.5 fm. Bij een dergelijk resolverend vermogen begint de substructuur van de nucleonen een belangrijke rol te spelen. Het is dan ook niet verwonderlijk dat de klassieke beschrijving van de kern als een verzameling van nucleonen die onafhankelijk van elkaar bewegen en ten gevolge van elkaars aanwezigheid een gemiddelde aantrekking ondervinden, niet meer toerijkend zal zijn. Dit beeld van de kern werd in de jaren 50 door Mayer en Jensen naar voor geschoven als de schillenmodel benadering van de nucleus. De kern werd hierbij voorgesteld als bestaande uit een inerte core waarrond de valentie nucleonen cirkelen als satellieten. Voor de beschrijving van globale eigenschappen van de kern zoals bv. zijn energiespectrum, de kernstraal, lage-energie transitie sterktes etc. voldoet dit beeld wonderwel. Tal van eigenschappen zoals de stabiliteit van de magische kernen konden hiermee verklaard worden.

Wanneer we echter het gedrag van de afzonderlijke nucleonen in de kern willen beschrijven op steeds kortere afstandsschaal zal het sterk repulsieve karakter van de nucleon-nucleon wisselwerking een rol beginnen spelen. Op dat ogenblik is bovenstaand beeld van de kern niet meer toereikend daar de valentie nucleonen weliswaar nog rond de inerte core bewegen maar hierbij wel elkaars aanwezigheid zullen mijden. Fysisch, komt dit enerzijds neer op een herverdeling van de bezettingssterkten van de valentie orbitalen over hoger gelegen één-deeltjes toestanden. Dit geeft aanleiding tot experimentele spectroscopische factoren van 0.7 in plaats van 1 (in het schillenmodel) voor de één-deeltjes toestanden gelegen beneden het Fermi-niveau. Daarnaast neemt men een toename waar, in de momentum dichtheden, van de sterkte bij hoge impuls momenta als gevolg van de aanwezigheid van deze zogenaamde korte dracht correlaties. Door de sterke repulsieve kracht die twee nucleonen ondervinden op een onderling afstand van 0.5 fm zullen zij in toestanden boven het Fermi-niveau verstrooid worden. Om hiervoor te corrigeren werden aangepaste spectroscopische factoren gehanteerd in de

verstrooiings reactie berekeningen. Hiermee wordt het effect van de herverdeling van sterkten over hoger liggende één-deeltjes toestanden gesimuleerd. Recente berekeningen voor de verstrooiings reactie $^{16}\mathrm{O}(e,e'pp)^{14}\mathrm{C}$ toonden aan dat de differentiele werkzame doorsnede uitermate gevoelig is voor de gebruikte spectroscopische verdeling [129]. Men ziet zeer duidelijk hoe de vorm en de sterkte van de werkzame doorsnede afhankelijk zijn van de ruimtelijke vorm van de door de verstrooide nucleonen bezette orbitalen.
Anderzijds, zal het sterk repulsief karakter van de internucleon kracht aanleiding geven tot een deformatie van de één-deeltjes golffuncties zoals bekomen uit een Hartree-Fock berekening. Fysisch, kan men dit als volgt inzien: door de ruimtelijke uitgebreidheid van de nucleonen zullen zij elkaar wegduwen in het nucleair medium. Dit manifesteert zich als een sterke terugval in de twee-deeltjes waarschijnlijkheids distributie bij kleine internucleon afstanden. De standaard manier om voor dit effect te corrigeren is om vertrekkende van een typisch schillenmodel Slater golffunctie, een correlatie functie toe te voegen die symmetrisch is in de nucleon vrijheidsgraden. Deze techniek noemt men gecorreleerde basisfunctie theorie welke zeer populair is in o.a. de vloeistof- en atoomfysica en geïntroduceerd werd in de jaren 60 door Ristig en Clarck. Ook in deze domeinen bestaat de nood om de korte dracht effecten te modeleren zonder het N-deeltjes probleem in zijn volledige complexiteit te moeten oplossen. Weliswaar bestaat geen consensus omtrent de correcte functionele vorm van de correlatiefunctie die dient te worden gebruikt. Het experiment zal in deze laatste aangelegenheid uitsluitsel moeten brengen. Een belangrijk voordeel van deze techniek is de mogelijkheid om aan storingsrekening te doen op basis van een expansie van de correlatiefunctie.

Het schillenmodel, als typisch voorbeeld van een gemiddeld-veld benadering, vertoont nog een tekortkoming die zich des te meer zal uiten naarmate de kern ter studie lichter wordt. De standaard gemiddeld-veld golffunctie, berekend in het laboratorium coördinatenstelsel, is inherent niet-translatie invariant omwille van de bevoorrechte positie ingenomen door de oorsprong. De oorsprong wordt hierbij gelegd in het centrum van de gemiddelde potentiaal waarin de nucleonen bewegen ten gevolge van de aanwezigheid van de andere kerndeeltjes. Dit vormt geen belemmering voor de beschrijving van de statische eigenschappen van de kern op voorwaarde dat zij geen afhankelijkheid vertonen van de impuls van de kern als geheel. Zo ja, zal men vooreerst een intrinsieke golffunctie moeten distilleren uit de gemiddeld-veld golffunctie om de residuele massacentrum beweging te elimineren. Hierbij dient wel opgemerkt dat de effecten ten gevolge van het niet-translatie invariant zijn van de golffunctie schalen als $1/A^{3/2}$ met A het massagetal van de desbetreffende kern. Men kan dus gerust stellen dat deze afwijkingen kunnen verwaarloosd worden in het geval van middel-zware en zware kernen.
Als voorbeeld werden zowel de ladings vormfactor als de dichtheidsfuncties berekend voor de ^{4}He-kern. Hierbij werd vertrokken van een gemiddeld-veld en een intrinsieke golffunctie voor het specifieke geval van een harmonische oscillator

potentiaal. Enkel voor een dergelijke potentiaal is het mogelijk om de massacentrum vrijheidsgraden op een ondubbelzinnige wijze af te zonderen. We merken heel duidelijk hoe een foutieve behandeling van de massacentrum beweging fysisch meetbare grootheden kan beïnvloeden wanneer we kijken naar de figuren II-8 en II-9. Dit geeft een heel duidelijk signaal nl. een beschrijving van de kern in termen van de effectieve vrijheidsgraden is onontbeerlijk wanneer men kernprocessen wil bestuderen. Voor interactie potentialen die niet van het harmonische oscillator type zijn, werden in de loop van de jaren tal van technieken ontwikkeld, zoals de Tassie-Barker methode, die wijd toepasbaar zijn maar echter geen afdoende antwoord geven op de vraag: Hoe kan men de invloed van het massacentrum op de berekende fysische grootheden op een ondubbelzinnige manier elimineren?

De hierboven aangehaalde tekortkomingen van de klassieke gemiddeld-veld benaderingen, voor het beschrijven van kernen, hebben een nieuw onderzoeksdomein doen ontstaan nl. de weinig deeltjes natuurkunde (Few-Body Physics). Hierbij probeert men, vertrekkende van een aantal basisprincipes, tot een consistente beschrijving van het nucleair medium te komen. In de loop van de jaren zijn hiervoor een aantal technieken ontwikkeld. Deze kunnen in twee grote groepen opgedeeld worden. Vooreerst zijn er die, vertrekkende van de initiële N-deeltjes Schrödinger vergelijking, op basis van een aantal coördinaten transformaties, finaal komen tot een nog numeriek op te lossen differentiaal vergelijking. Een belangrijke vertegenwoordiger vormen de Faddeev-Yakubovski vergelijkingen. De Bochum groep heeft via dit formalisme een golffunctie bepaald voor de ^{3}He kern. Daarnaast zijn er de variationele technieken waarbij de Argonne-Urbana groep vaandeldrager is. Hierbij wordt een algemene functionele vorm voor de golffunctie vooropgesteld waarna het oorsprokelijk probleem herleid wordt tot fitten van een aantal parameters op basis van het Rayleigh-Ritz variationeel principe. Hiervoor werden een aantal methoden ontwikkeld zoals: de stochastische variationele methode, de variationele Monte-Carlo methode, de Greense functie Monte-Carlo techniek,... In dit proefschrift wordt de, op basis van de Greense functie Monte-Carlo techniek verkregen ^{4}He golffunctie gebruikt. Het was de Argonne-Urbana groep die ons deze golffunctie heeft aangereikt.
In het vervolg van hoofdstuk 2 worden een aantal dichtheidsfuncties als mede de ladingsvormfactor berekend en vergeleken met de beschikbare experimentele data. Binnen de fout marges slagen we er perfect in om de desbetreffende fysische grootheden theoretisch te beschrijven.

Nu we beschikken over een consistente beschrijving voor de grondtoestand van de ^{4}He kern kunnen we deze aanwenden bij de studie van nucleaire verstrooiings processen. Voor de studie van gelijk wel object dient men informatie over dit object in te winnen. Standaard gebeurt dit door het object te observeren en zijn gedragingen onder externe impulsen te beschrijven. Wanneer de afmetingen van de voorwerpen onder studie zeer klein zijn gebruikt men hiervoor een microscoop. In de kernfysica is een elektronen- of fotonenbundel de microscoop

bij uitstek. De gedragingen waarop we ons in dit werk gefocusseerd hebben zijn deze waarbij de helium kern twee nucleonen uitstoot ten gevolge van de impact van een reëel of virtueel foton. Beide nucleonen worden gedetecteerd waardoor we een idee krijgen van de ruimtelijke als wel als de energetische spreiding van de nucleonen zoals initieel in de kern aanwezig. Dit geeft ons de mogelijkheid om vertrekkende van QED en nucleon reactiemodellen terug te rekenen. Hierbij hopen we het beeld te reconstrueren van net voor de impact van het foton alsmede informatie te verkrijgen over het feitelijke reactieproces.
De fysisch toegankelijke grootheid is het aantal geïdentificeerde reacties waargenomen bij een bepaalde opstelling van de detectoren. Op basis van de detector acceptanties en de intensiteit van de bundel kan men deze observabele linken met de differentieel werkzame doorsnede. In hoofdstuk 3 wordt een uitdrukking afgeleid voor de werkzame doorsnede corresponderend met elektronen- als wel als fotonenverstrooiing aan een ^{4}He-kern. We spitsen onze aandacht toe op het exclusieve kanaal waarbij de 4 nucleonen na de impact vrij bewegen. Vermits ^{4}He een klein systeem is, waardoor de invloed van finale toestands interacties kan verwaarloosd worden, zullen de uitgaande nucleonen tot op zekere hoogte kunnen beschreven worden met behulp van een vlakke golf benadering. Wel zal er een Gramm-Schmidt orthogonalisatie correctie gebeuren zodoende effecten ten gevolge van het niet-orthogonaal zijn van de begin- en eindtoestand te elimineren. Bij een foton momentum van 300 MeV/c is het resolverende vermogen van de reële of virtuele fotonen zo groot dat naast nucleon vrijheidsgraden ook meson- en zelfs delta isobaar vrijheidsgraden in rekening moeten gebracht worden voor de beschrijving van het reactie proces. De relevante verstrooiings processen zijn meson uitwisselings reacties, resonante zowel als niet-resonante delta excitatie en korte dracht gecorrigeerde één-deeltjes reacties. In hoofdstuk 3 worden, vertrekkende van een effectief lagrangiaan formalisme, uitdrukkingen afgeleid voor elk van deze processen. Dit leidt dan tot een formulering van een aantal verstrooiings matrix elementen die dan kunnen aangewend worden bij de berekening van de werkzame doorsnede.
Naast de werkzame doorsnede beschikt men nog over een gamma andere experimenteel toegankelijke grootheden nl. de polarisatie observabelen. Deze grootheden bekomt men door gepolariseerde metingen te doen en vervolgens de verkregen werkzame doorsneden van elkaar af te trekken. Men onderscheid hierbij een aantal verschillende metingen, nl. metingen waarbij het inkomende foton gepolariseerd is, metingen waarbij de polarisatie van één van de uitgaande nucleonen bepaald wordt, of metingen waarbij een gepolariseerd foton binnen komt en men de polarisatie graad van een van de finale nucleonen meet. Deze verschillende opstellingen resulteren in 3 verschillende polarisatie grootheden nl. de foton asymmetrie of het electron analyserend vermogen, de terugstoot polarisatie en de overdracht polarisatie. Omwille van symmetrie redenen kunnen een aantal van deze polarisatie vrijheidsgraden verdwijnen zoals duidelijk weergegeven in tabel III-1.

Figuur III-10 toont de verschillende reactie diagrammen die opgenomen werden in de verstrooiings werkzame doorsnede. Belangrijk hierbij is op te merken dat naast de klassieke diagrammen waarbij het foton geabsorbeerd wordt door het finaal gedetecteerde nucleonen paar er nog een hele reeks andere diagrammen uitgelijst zijn. Dit zijn diagrammen die op een natuurlijke manier te voorschijn komen wanneer men werkt met een translatie invariante golffunctie. Fysisch kan men deze identificeren met een terugstoot proces waarbij het foton de 2 niet gedetecteerde nucleonen treft terwijl de waargenomen nucleonen een soort terugstoot krijgen ten gevolge van de massacentrum beweging van de kern. Deze niet-conventionele diagrammen zijn van belang om de hermiticiteit van de scattering matrix te verzekeren.

De in hoofdstuk 3 bepaalde grootheden worden vervolgens voor een aantal geselecteerde detector opstellingen uitgerekend. Een drietal opstellingen worden onderscheiden nl. quasi-deuteron kinematiek, rug-aan-rug kinematiek en een quasi rug-aan-rug kinematiek. De eerste situatie, nl. quasi-deuteron kinematiek, waarbij het initieel nucleonen paar in rust is in de kern, werd geselecteerd om de invloed van korte dracht correlaties verder te bestuderen. Om deze effecten te bestuderen werd er een vergelijkende studie gedaan nl. de berekeningen werden enerzijds uitgevoerd vertrekkende van een massacentum gecorrigeerde harmonische oscillator golffunctie en anderzijds van de realistische golffunctie zoals bekomen met behulp van de Greense functie Monte-Carlo techniek. Hieruit komt het effect van korte-dracht correlaties zeer sterk naar voren. De tweede set van berekeningen is een simulatie van het experiment uitgevoerd door R. De Vries in 1990. Dit experiment werd uitgevoerd in Bonn aan de ELSA faciliteit. Bij deze opstelling worden enkel die processen gedetecteerd waarbij de nucleonen rug aan rug worden uitgezonden. Dit maakt deze opstelling uitermate geschikt om de impact van korte-dracht correlaties te bestuderen. Uit de berekeningen blijkt echter dat naast de korte-dracht korrelaties eveneens de terugstoot diagrammen een belangrijke rol spelen. Terwille van het inrekening brengen van terugstoot effecten blijkt dat meson-uitwisselings processen eveneens bijdragen tot een reactie van het type $(e, e'pp)$. Tot slot wordt een experiment aan de Mainz faciliteit uitvoerig bestudeerd binnen het hierboven beschreven formalisme. Gelijkaardige conclusies dringen zich ook hier op nl. korte-dracht correlaties en terugstoot diagrammen zijn van belang voor een korrekte beschrijving van het reactie proces.

Tot slot kunnen we stellen dat bij de beschrijving van lichte kernen en de bijhorende reactie processen een grotere voorzichtigheid aan de dag moet gelegd worden dan bij hun zwaardere tegenhangers. Enerzijds wegen massacentrum effecten zwaarder door en zullen zij een zichtbaar teken nalaten in de fysische grootheden. Anderzijds, in het geval van ^{4}He, dient door de grote dichtheid van het nucleair medium het repulsieve karakter van de kernkracht en haar effect op de kern golffunctie in rekening gebracht te worden.

Bibliography

[1] E. Rutherford, Proceedings of the Royal Society **A 97,** 374 (1920).

[2] J. Chadwick, Proceedings of the Royal Society **A 136,** 692 (1932).

[3] W. M. Lyman, A. O. Hanson, and M.B.Scott, Phys.Rev. **84,** 626 (1951).

[4] R. Hofstadter, H. R. Fetcher, and J. A. McIntyre, Phys.Rev. **91,** 422 (1953).

[5] N. Glendenning, Atomic Data and Nuclear Data Tables 16 (1975).

[6] H. Euteneuer, J. Friedrich, and N. Vogler, Nucl. Phys. **A298,** 452 (1978).

[7] J. Cavedon *et al.*, Phys. Rev. Lett. **49,** 978 (1982).

[8] H. Müther and A.Polls, Prog.Part.Nucl.Phys. **45,** 243 (2000).

[9] J. Ryckebusch, V. Van Der Sluys, K. Heyde, H. Holvoet, W. Van Nespen, M. Waroquier, and M. Vanderhaeghen, Nucl. Phys. **A624,** 581–622 (1997).

[10] S. Boffi and F. Pacati, Nucl. Phys. **A210,** 477 (1973).

[11] K. Gottfried, Nucl. Phys. **5,** 557 (1958).

[12] G. Rosner, Prog.Part.Nucl.Phys. **44,** 99 (2000).

[13] C. Ciofi degli Atti, L. Lantto, and P. Toropainen, Phys. Lett. **B42,** 27–30 (1972).

[14] D. Groep, Ph.D. thesis, University Utrecht, 2000.

[15] W. Gloeckle *et al.*, Phys.Rep. **274,** 107 (1996).

[16] R. De Vries, Ph.D. thesis, University Utrecht, 1995.

[17] J. van den Brand *et al.*, Phys. Rev. Lett. **60,** 2006–2009 (1988).

[18] W. Eickhoff, Ph.D. thesis, University Bonn, 2003.

[19] T. Emura *et al.*, Phys. Lett. **B267,** 460–464 (1991).

[20] T. Emura *et al.*, Phys. Lett. **B286,** 229–233 (1992).

[21] S. Doran *et al.*, Nucl. Phys. **A559,** 347–367 (1993).

[22] F. Adamian *et al.*, J. Phys. **G17,** 1657–1664 (1991).

[23] V. Stoks, R. Klomp, M. Rentmeester, and J. de Swart, Phys. Rev. **C48,** 792–815 (1993).

[24] V. Stoks, R. Klomp, C. Terheggen, and J. de Swart, Phys. Rev. **C49,** 2950–2962 (1994).

[25] R. Wiringa, V. Stoks, and R. Schiavilla, Phys. Rev. **C51,** 38–51 (1995).

[26] J. Forest, V. Pandharipande, S. Pieper, R. Wiringa, R. Schiavilla, and A. Arriaga, Phys. Rev. **C54,** 646–667 (1996).

[27] H. Pirner and J. Vary, Phys. Rev. Lett. **46,** 1376 (1981).

[28] L. Wilets, M. Alberg, S. Pepin, F. Stancu, J. Carlson, and W. Koepf, Phys. Rev. **C56,** 486–490 (1997).

[29] L. Wilets, M. Alberg, S. Pepin, F. Stancu, J. Carlson, and W. Koepf, In *Proceeding International Conference on Nuclear Physics at the Turn of the Millennium*, (George, South Africa, 1996).

[30] V. Pandharipande, Nucle. Phys. **A654,** 157–177 (1999).

[31] R. Wiringa, Phys. Rev. **C43,** 1585–1598 (1991).

[32] K. Heyde, *The Nuclear Shell Model* (Springer-Verlag, 1990).

[33] K. Heyde, *Basic Ideas and Concepts in Nuclear Physics* (IOP Publishing Ltd, 1994).

[34] D. Zheng, J. Vary, and B. Barrett, Nucl. Phys. **A560,** 211–222 (1993).

[35] B. Brandow, Rev. Mod. Phys **39,** 771–828 (1967).

[36] H. J. Lipkin, Phys. Rev. **110,** 1395 (1958).

[37] S. Gartenhaus and C. Schwartz, Phys. Rev. **108,** 482–490 (1957).

[38] V. Pandharipande, I. Sick, and P. de Witt Huberts, Rev. Mod. Phys. **69,** 981–992 (1997).

[39] S. Fantoni and V. Pandharipande, Nucl. Phys. **A473,** 234 (1987).

[40] S. Fantoni and V. Pandharipande, Phys. Rev. **C37,** 1697–1707 (1988).

[41] C. Vincent, Phys. Rev. **C8,** 929–937 (1973).

[42] B. Mihaila and J. Heisenberg, Phys. Rev. **C60,** 054303 (1999).

[43] S. Dementii, V. Ogurtsov, A. Shebeko, and N. Afanas'ev, Sov. J. Nucl. Phys. **22,** 6–9 (1976).

[44] A. Dieperink and J. T. de Forest, Phys. Rev. **C10,** 543–549 (1974).

[45] D. Van Neck, M. Waroquier, A. Dieperink, S. Pieper, and V. Pandharipande, Phys. Rev. **C57,** 2308–2315 (1998).

[46] R. Bishop, M. Flynn, M. Boscá, and R. Guardiola, Phys. Rev. **C42,** 1341–1360 (1990).

[47] Kamada *et al.*, Phys. Rev. **C64,** 044001 (2001).

[48] P. Navrátil, G. Kamuntavicius, and B. Barrett, Phys. Rev. **C61,** 044001 (2000).

[49] P. Navrátil and B. Barrett, Phys. Rev. **C54,** 2986–2995 (1996).

[50] N. Barnea, V. Efros, W. Leidemann, and G. Orlandini, Phys. Rev. **C63,** 057002 (2001).

[51] N. Barnea, W. Leidemann, and G. Orlandini, Phys. Rev. **C61,** 054001 (2000).

[52] S. Merkuriev, S. Yakovlev, and C. Gignoux, Nucl Phys **A431,** 125–138 (1984).

[53] F. Ciesielski, J. Carbonell, and C. Gignoux, Nucl. Phys. **A631,** 653 (1998).

[54] F. Ciesielski and J. Carbonell, Phys. Rev. **C58,** 59–74 (1998).

[55] N. Schellingerhout, J. Schut, and L. Kok, Phys. Rev. **C46,** 1192–1202 (1992).

[56] S. Yakovlev and I. Filikhin, nucl-th/9701020 .

[57] S. Yakovlev and I. Filikhin, nucl-th/9707056 .

[58] A. Nogga, H. Kamada, and W. Glöckle, Few Body Syst. Suppl. **0,** 1–5 (1998).

[59] C. Elster, W. Schadow, A. Nogga, and W. Gloeckle, Few Body Syst. **27,** 83–105 (1999).

[60] A. Stadler, W. Glöckle, and P. Sauer, Phys. Rev. **C44,** 2319–2327 (1991).

[61] E. Harper, Y. Kim, and A. Tubis, Phys. Rev. **C2,** 877–891 (1970).

[62] M. Kamimura, Phys. Rev. **A38,** 621 (1988).

[63] K. Varga and Y. Suzuki, Phys.Rev. **C52,** 2885–2905 (1995).

[64] A. Kievsky, L. Marcucci, S. Rosati, and M. Viviani, Few Body Syst. **22,** 1–10 (1997).

[65] A. Kievsky, M. Viviani, and S. Rosati, Nucl. Phys. **A577,** 511–527 (1994).

[66] O. Benhar and V. Pandharipande, Rev. Mod. Phys. **65,** 817–828 (1993).

[67] S. Pieper and R. Wiringa, Ann. Rev. Nucl. Part. Sci. 51 (2001).

[68] J. Carlson and R. Schiavilla, Rev. Mod. Phys. **70,** 743–841 (1998).

[69] B. Pudliner, V. Pandharipande, J. Carlson, S. Pieper, and R. Wiringa, Phys. Rev. **C56,** 1720–1736 (1997).

[70] M. Ristig and J. Clark, Il Nuovo Cimento **30 A,** 609–631 (1975).

[71] J. Clark and P. Westhaus, Phys. Rev. **141,** 833–990 (1966).

[72] J. Clark, Prog. Part. Nucl. Phys. **2,** 88–199 (1978).

[73] H. Feldmeier, T. Neff, R. Roth, and J. Schnack, Nucl. Phys. **A632,** 61–95 (1998).

[74] E. Feenberg and C. Woo, Phys. Rev. **137,** 391–405 (1965).

[75] R. Guardiola and M. Portesi, Nucl. Part. Phys. **24,** 37–44 (1998).

[76] M. Gaudin, J. Gillespie, and G. Ripka, Nucl. Phys. **A176,** 237–260 (1971).

[77] S. Pieper, R. Wiringa, and V. Pandharipande, Phys. Rev. **C46,** 1741–1756 (1992).

[78] F. Dellagiacoma, G. Orlandini, and M. Traini, Nucl. Phys. **A393,** 95–108 (1983).

[79] W. Leidemann and G. Orlandini, Nucl. Phys. **A506,** 447–470 (1990).

[80] J. Ryckebusch, S. Janssen, W. Van Nespen, and D. Debruyne, Nucl. Phys. **A506,** 447–470 (1990).

[81] J. L. Goff *et al.*, Phys. Rev. **C50,** 2278–2287 (1994).

[82] C. C. degli Atti, E. Pace, and G. Salmè, Phys. Rev. **C43,** 1155–1176 (1991).

[83] S. Boffi, C. Giusti, F. Pacati, and M. Radici, *Electromagnetic Response of Atomic Nuclei* (Clarendon Press, Oxford, 1996).

[84] J. Ryckebusch, Phys. Lett. **B383,** 1–8 (1996).

[85] M. Vanderhaeghen, L. Machenil, J. Ryckebusch, and M. Waroquier, Nucl. Phys. **580,** 551–576 (1994).

[86] R. Frosch, J. McCarthy, R. Rand, and M. Yearian, Phys. Rev. **160,** 874–879 (1967).

[87] J. McCarthy, I. Sick, and R. Whitney, Phys. Rev. **C15,** 1396–1414 (1977).

[88] M. Musolf, R. Schiavilla, and T. Donnelly, Phys. Rev. **C50,** 2173–2188 (1994).

[89] http://www.phy.anl.gov/theory/research/nofk.gif.

[90] P. Ulmer *et al.*, Phys. Rev. Lett. **59,** 2259 (1987).

[91] C. M. Spaltro *et al.*, Phys.Rev. **C48,** 2385 (1993).

[92] D. Dutta *et al.*, Phys. Rev C **C61,** 061602 (2000).

[93] R. Lourie *et al.*, Phys. Rev. Lett. **56,** 2364 (1986).

[94] D. Watts *et al.*, Phys. Lett. B **553,** 25–30 (2003).

[95] D. Groep *et al.*, Phys. Rev. **C 63,** 014005 (2001).

[96] K. Blomqvist *et al.*, Phys. Lett. **B 421,** 71 (1998).

[97] R. Starink *et al.*, Phys. Lett. **B 474,** 33 (2000).

[98] D. Watts *et al.*, Phys. Rev. **C 62,** 014616 (2000).

[99] A. Picklesimer and J. V. Orden, Phys. Rev. **C35,** 266–279 (1987).

[100] A. Picklesimer and J. V. Orden, Phys. Rev. **C40,** 290–303 (1989).

[101] S. Boffi, C. Giusti, and F. Pacati, Nucl. Phys. **A476,** 617 (1988).

[102] J. Carlson, J. Jourdan, R. Schiavilla, and I. Sick, Phys. Rev. **C 65,** O24002 (2002).

[103] J. Ryckebusch, D. Debruyne, and W. Van Nespen, Phys. Rev. **C57,** 1319–1335 (1998).

[104] R. Machleidt, in *Relativistic dynamics and quark-nuclear physics*, M. Johnson and A. Picklesimer, eds., (1985).

[105] T. Sato and T. S. H. Lee, Phys. Rev. **C63,** 055201 (2001).

[106] J. Nacher and E. Oset, Nucl. Phys. **A674,** 205–228 (2000).

[107] R. Peccei, Phys. Rev. **181,** 1902–1905 (1969).

[108] R. Peccei, Phys. Rev. **176,** 1812–1821 (1968).

[109] T. Wilbois, P. Wilhelm, and H. Arenhövel, Phys. Rev. **C54,** 3311–3312 (1996).

[110] J. Ryckebusch, L. Machenil, M. Vanderhaegen, V. Van Der Sluys, and M. Waroquier, Phys. Rev. **C54,** 3313–3314 (1996).

[111] P. Wilhelm, H. Arenhövel, C. Giusti, and F. Pacati, Z. Phys. **A359,** 467–470 (1997).

[112] K. Wehrberger and R. Wittman, Nucl. Phys. **A513,** 603–620 (1990).

[113] H. Kim, S. Schramm, and S. Lee, Phys. Rev. **C56,** 1582–1587 (1997).

[114] E. Oset and L. Salcedo, Nucl. Phys. **A468,** 631–652 (1987).

[115] M. Dekker, Ph.D. thesis, University Utrecht, 1993.

[116] A. Bincer, Phys. Rev. **118,** 855–863 (1960).

[117] H. Fearing, G. Poulis, and S. Scherer, Nucl. Phys. **A570,** 657–685 (1994).

[118] H. Fearing and S. Scherer, Phys. Rev. **C62,** 034003 (2000).

[119] H. Naus and J. Koch, Phys. Rev **36,** 2459–2472 (1987).

[120] D. Debruyne, J. Ryckebusch, W. Van Nespen, and S. Janssen, Phys. Rev. **C62,** 024611 (2000).

[121] J. Kelly, Phys. Rev. **C56,** 2672–2687 (1997).

[122] J. Amaro, M. Barbaro, J. Caballero, T. Donnelly, and A. Molinari, Nucl. Phys. **A643,** 349–382 (1998).

[123] C. Onderwater *et al.*, Phys. Rev. Lett. **78,** 4893–4897 (1997).

[124] J. M. Laget, Phys. Rev. **C35,** 832–835 (1987).

[125] J. Ryckebusch, W. Van Nespen, and D. Debruyne, Phys. Lett. **B441,** 1–8 (1998).

[126] J. Ryckebusch, M. Vanderhaeghen, L. Machenil, and M. Waroquier, Nucl. Phys. A **568,** 828–854 (1994).

[127] R. Niyazov *et al.*, Phys. Rev. Lett. **92,** 052303 (2004).

[128] D. Groep *et al.*, Phys. Rev. Lett. **83,** 5443 (1999).

[129] J. Ryckebusch and W. Van Nespen, Eur. Phys. J. (2004), in press and nucl-th/0312056.

[130] F. A. Natter, private communications (unpublished).

[131] J. Ryckebusch, D. Debruyne, and W. Van Nespen, Phys. Rev. **C57,** 1319–1336 (1998).

[132] L. Machenil, M. Vanderhaeghen, J. Ryckebusch, and M. Waroquier, Phys. Lett. **B 316,** 17–22 (1993).

[133] F. Adamian *et al.*, Nucl. Part. Phys. **17,** 1657–1664 (1991).

[134] J. M. Laget, Can. J. Phys. **62,** 1046 (1984).

[135] M. Hjorth-Jensen, H. Müther, and A. Polls, Phys. Rev. **C 50,** 501–504 (1994).

[136] J. Bjorken and S. Drell, *Relativistic quantum mechanics* (McGraw-Hill Book Company, 1964).

[137] R. Davidson, M. Benmerouche, and N. Mukhopadhyay, In *Proceedings of the Excited Baryons 1988 conference*, (Troy, NY, 1988).

[138] W. Rarita and J. Schwinger, Phys. Rev. **60,** 61 (1941).

[139] K. McVoy and L. Van Hove, Phys. Rev. **125,** 1034–1043 (1962).